Deliverable 15.12: Identification of the effect of transient processes on corrosion

Work Package 15 ConCorD

http://www.ejp-eurad.eu/

EURAD (Deliverable n° 15.12) – Identification on the effect of transient processes on corrosion
Dissemination level: Public
Date of issue of this report: **29/04/2024**

Page 2

Document information

Project Acronym	**EURAD**
Project Title	**European Joint Programme on Radioactive Waste Management**
Project Type	**European Joint Programme (EJP)**
EC grant agreement No.	**847593**
Project starting / end date	**1st June 2019 – 30 May 2024**
Work Package No.	**15**
Work Package Title	**Container Corrosion under Disposal conditions**
Work Package Acronym	**ConCorD**
Deliverable No.	**15.12**
Deliverable Title	**Identification of the effect of transient processes on corrosion**
Lead Beneficiary	**CIEMAT**
Contractual Delivery Date	**31/03/2024**
Actual Delivery Date	**29/04/2024**
Type	**Report**
Dissemination level	**Public**
Authors	**Institutions in alphabetical order**
	Ana María Fernández (CIEMAT), Ursula Alonso (CIEMAT), Paula Nieto, Manuel Mingarro, Tiziana Missana (CIEMAT)
	Andres Muñoz (GRS)
	Nicolas Finck (KIT-INE), Natalie Müller (KIT-INE), Dieter Schild (KIT-INE), Ashutosh R. Singh (KIT-INE).
	Šárka Šachlová (UJV), Vlastislav Kašpar (UJV), David Dobrev (UJV), Daniel Gõtz (UJV), Kateřina Kolomá (UJV), Petr Večerník (UJV), Milan Zuna (UJV), Michaela Matulová (SURAO)

To be cited as:

Fernández A.M., Alonso U., Nieto P., Mingarro M, Missana T., Muñoz A., Finck N., Müller N., Schild D., Singh A.R., Šachlová S., Kašpar V., Dobrev D., Gõtz D., Kolomá K., Večerník P., Zuna M., Matulová M. (2024): Final version as of 29.04.2024 of deliverable D15.12 of the HORIZON 2020 project EURAD. EC Grant agreement no: 847593.

Disclaimer

EURAD (Deliverable n° 15.12) – Identification on the effect of transient processes on corrosion
Dissemination level: Public
Date of issue of this report: **29/04/2024**

Page 3

Acknowledgement

Status of deliverable		
	By	Date
Delivered (Lead Beneficiary)	Ursula Alonso (CIEMAT)	03/03/2024
Verified (WP Leader)	N. Diomidis	29/04/2024
Reviewed (Reviewers)	Fraser King, Satoru Suzuki, Guido Bracke, Christina Lilja, Valerie Maillot	31/03/2024
Approved (PMO)		
Submitted to EC (Coordinator)	Andra (Coordinator)	30/04/2024

EURAD (Deliverable n° 15.12) – Identification on the effect of transient processes on corrosion
Dissemination level: Public
Date of issue of this report: **29/04/2024**

Page 4

EURAD (Deliverable n° 15.12) – Identification on the effect of transient processes on corrosion
Dissemination level: Public
Date of issue of this report: **29/04/2024**

Page 5

Executive Summary

This document is deliverable 15.12 of the EURAD WP15 ConCorD and gathers the experimental studies carried out within Task 5, aimed to identify the role of transient conditions on corrosion of materials selected for disposal canisters in deep geological repositories for high-level radioactive waste.

The document includes four separate contributions and different set of experiments performed by CIEMAT (ES), GRS (DE), KIT-INE (DE) and UJV-SURAO (CZ) within ConCorD's Task 5.

[CIEMAT (ES)] analysed the impact of redox, hydraulic and thermal nearfield transients in the corrosion and bentonite interactions, simulating the canister / bentonite interface of a deep geological repository. Both laboratory scale and *in-situ* experiments, carried out at the Äspö Underground laboratory (Sweden), were analysed.

The samples from Äspö- ABM5 in-situ experiment were hydrated during 4.4 years with Äspo granitic groundwater and were subjected to temperature up to 250 ºC. Thus, these samples are representative of coupled hydration, temperature, redox and chemical transients. Analyses of different bentonite samples revealed that all bentonites analysed preserved their hydro-geochemical properties, after being subjected to saline groundwater infiltration, heating and interaction with corroding metals during 4.4 years. The main changes observed in all bentonites are the modification of exchangeable cation composition and the Fe increase in bentonites as a function of the distance to heater contact, due to heater corrosion. Goethite, hematite and siderite were found as corrosion products.

[CIEMAT (ES) laboratory experiments were representative of coupled thermo-hydraulic gradients and thermo-hydraulic-chemical interactions. CIEMAT activities cover a range of transient conditions affecting corrosion of metals, such as re-saturation of compacted bentonite, convective water vapour saturation fluxes, ambient and high temperature (80º C), different salinity of the infiltrating waters, and variations in oxic/anoxic conditions. The corrosion rates measured in all C-steel coupons contacted to bentonite, hydrated with different waters and subjected to 80 ºC ranged between 28 and 413 µm/year, the highest degree observed in the Nagra C-steel coupon tested with FEBEX bentonite compacted at 1.4 g/cm^3. The corrosion rates of Cu-OFP coupons subjected to the same conditions were significantly lower ranging from 3 to 9 µm/year.

[GRS (D)] analysed the effects of the consumption of oxygen enclosed in saturated bentonite on the first stages of corrosion. Electrochemical techniques such as polarisation curves (current-voltage curves) and electrochemical impedance were used to monitor the evolution of the corrosion rate for a period of time of about 3 months. The electrochemical experiments were performed in a dedicated cell containing the oversaturated Wyoming bentonite slurry (Na-bentonite like the MX-80) prepared with artificial Opalinus Clay water in a ratio of 1:10 w/w. The experiments were complemented with surface analysis including SEM-EDX and localized XPS to identify the nature of the formed corrosion products. Electrochemical experiments in Opalinus Clay water under different conditions of oxygen content and temperature were performed for obtaining additional information on the corrosion kinetics. The middle-term runs were performed at temperatures of 30 ºC and 50 °C. A miniaturized Pt-sensor was tested to follow pH-changes on the proximity of the corroding surfaces by running cyclovoltametries from time to time. Comparative experiments were carried out under gamma-irradiation conditions.

[GRS (D)] corrosion rates measured for GGG40 cast iron contacted to a slurry of bentonite hydrated with synthetic Opalinus clay were of 6 and 13 µm y^{-1} for 30 °C and 50 °C, respectively. The electrochemical investigations shown that at the corrosion potential, the oxygen reduction was mass controlled, the diffusion of oxygen being restrained by the slurry, indicating that the kinetically controlled water reduction seems to predominate. A γ-radiation dose 130 Gy h^{-1} on GGG40 in the same bentonite slurry at 50 °C. Increased the mean corrosion rate up to 52 µm y^{-1}.

[KIT-INE (DE)] performed corrosion experiments with spheroidal graphite cast iron (SGI) and cupronickel alloy (CuNi) contacted to a bentonite slurry hydrated with granitic groundwater. Ex experiments were carried out in the laboratory under anoxic conditions in a N$_2$- or Ar-filled glovebox, under static and dynamic conditions, and for contact times up to 12 months. The purpose was to provide

EURAD (Deliverable n° 15.12) – Identification on the effect of transient processes on corrosion
Dissemination level: Public
Date of issue of this report: **29/04/2024**

Page 6

information about the effect of pore water renewal on the investigated processes and performed experiments in closed vessels at 25 °C and at 50 °C. Experiments under dynamic conditions were carried out using cylindrical vessels and the flow rate was applied by using a peristaltic pump. The applied transient conditions were specific for each selected material. In the case of spheroidal graphite cast iron, a layer of a ferric compound was inserted between the metallic coupon and the bentonite. In experiments involving cupronickel coupons, the pore water was spiked with sulphide once corrosion processes already started. Reference experiments were performed separately in the absence of ferric compound or added sulphide in order to identify the effect of these parameters on the corrosion behaviour of the metallic materials.

[KIT-INE(DE)] results showed that SGI corroded upon exposure to the bentonite suspension hydrated with low saline granitic water, where the redox potential decreased in all experiments, suggesting the formation of Fe(II)-bearing secondary phases. Comparative experiments performed in presence of hematite did not significantly alter the steel degradation mechanism. After 3 months at 25°C in contact with the bentonite suspension, the corrosion rate was 4.8 µm/y, favoured by the larger amount of water available. Increasing the temperature to 50°C significantly increased the corrosion rate to 10.6 µm/y. Corrosion rates decreased systematically with increasing reaction time. Comparatively CuNi corrosion was significantly lower, being the highest value of 2.7 µm/y at 50ºC. The presence of added sulfide had no significant effect on corrosion but may have an effect at longer exposure times, or higher sulfide concentrations.

[UJV-SURAO (CZ)] studied the effect of increased temperature and gamma irradiation on acceleration of corrosion of C-steel in compacted Ca-Mg bentonite, also including MX-80 in a limited number of tests, for an insight on chemical evolution and its influence on development of the carbon steel canister – bentonite interface. Results showed that the C-steel samples heated up at 150 °C in the BCV bentonite had lower corrosion rate when irradiated compared to unirradiated samples, being the lower values around 2 µm/y and the higher corrosion measured 24.3 µm/y, combining 150 °C and irradiation. Unirradiated samples heated up to 150 °C showed the highest corrosion rate after 6 months with decreasing tendency when the loading period was prolonged up to 18 months. The decreasing corrosion rate was observed in both irradiated and unirradiated steel samples heated up at 90 °C correlating with increasing loading period.

EURAD (Deliverable n° 15.12) – Identification on the effect of transient processes on corrosion
Dissemination level: Public
Date of issue of this report: **29/04/2024**

Page 7

Table of content

EURAD (Deliverable n° 15.12) – Identification on the effect of transient processes on corrosion
Dissemination level: Public
Date of issue of this report: **29/04/2024**

Page 8

EURAD (Deliverable n° 15.12) – Identification on the effect of transient processes on corrosion
Dissemination level: Public
Date of issue of this report: **29/04/2024**

Page 9

EURAD (Deliverable n° 15.12) – Identification on the effect of transient processes on corrosion
Dissemination level: Public
Date of issue of this report: **29/04/2024**

Page 10

EURAD (Deliverable n° 15.12) – Identification on the effect of transient processes on corrosion
Dissemination level: Public
Date of issue of this report: **29/04/2024**

Page 11

List of figures

EURAD (Deliverable n° 15.12) – Identification on the effect of transient processes on corrosion
Dissemination level: Public
Date of issue of this report: **29/04/2024**

Page 12

EURAD (Deliverable n° 15.12) – Identification on the effect of transient processes on corrosion
Dissemination level: Public
Date of issue of this report: **29/04/2024**

Page 13

EURAD (Deliverable n° 15.12) – Identification on the effect of transient processes on corrosion
Dissemination level: Public
Date of issue of this report: **29/04/2024**

Page 14

EURAD (Deliverable n° 15.12) – Identification on the effect of transient processes on corrosion
Dissemination level: Public
Date of issue of this report: **29/04/2024**

Page 15

EURAD (Deliverable n° 15.12) – Identification on the effect of transient processes on corrosion
Dissemination level: Public
Date of issue of this report: **29/04/2024**

Page 16

EURAD (Deliverable n° 15.12) – Identification on the effect of transient processes on corrosion
Dissemination level: Public
Date of issue of this report: **29/04/2024**

Page 17

EURAD (Deliverable n° 15.12) – Identification on the effect of transient processes on corrosion
Dissemination level: Public
Date of issue of this report: **29/04/2024**

Page 18

EURAD (Deliverable n° 15.12) – Identification on the effect of transient processes on corrosion
Dissemination level: Public
Date of issue of this report: **29/04/2024**

Page 19

List of Tables

EURAD (Deliverable n° 15.12) – Identification on the effect of transient processes on corrosion
Dissemination level: Public
Date of issue of this report: **29/04/2024**

Page 20

EURAD (Deliverable n° 15.12) – Identification on the effect of transient processes on corrosion
Dissemination level: Public
Date of issue of this report: **29/04/2024**

Page 21

Glossary

AAS	Atomic absorption spectroscopy
BCV	Bentonite Cerny Vrch
CIEMAT	Centro de Investigaciones Energéticas, Medioambientales y Tecnológicas (Spain)
CS	Carbon steel
Ctot	Total Carbon Content
Cu-OFP	Oxygen-free phosphorus-doped copper
CZE	Capillary Zone Electrophoresis
DGR	Deep Geological Repository
DW	Deionised water
EDX	Energy dispersive X-ray spectroscopy
FEBEX	Full-scale Engineered Barriers Experiment
GRS	*Gesellschaft für Anlagen- und Reaktorsicherheit gGmbH* (Germany)
HDPE	High density polyethylene
IR	Irradiated
KIT- INE	Institute for Nuclear Waste Disposal of the Karlsruhe Institute of Technology (Germany)
LOM	Light Optical Microscopy
NAGRA	Swiss National Cooperative for the Disposal of Radioactive Waste (Switzerland)
NIR	Unirradiated
PW-1.4	Reference bentonite pore water at 1.4 g/cm^3 compaction density
RT	Room Temperature
SEM	Scanning electron microscopy
SKB	Swedish Nuclear Fuel and Waste Management Company (Sweden)
SURAO	Czech Radioactive Waste Repository Authority (Czech Republic)
Stot	Total Sulphur Content
UJV	Czech Nuclear Research Institute (ÚJV Řež, a. s., Czech Republic)
XRD	X-ray diffraction
XRF	X-ray fluorescence

EURAD (Deliverable n° 15.12) – Identification on the effect of transient processes on corrosion
Dissemination level: Public
Date of issue of this report: **29/04/2024**

Page 22

EURAD (Deliverable n° 15.12) – Identification on the effect of transient processes on corrosion
Dissemination level: Public
Date of issue of this report: **29/04/2024**

Page 23

1. Introduction

A deep geological repository (DGR) is the internationally most accepted strategy for the final disposal of high-level radioactive waste (HLRW). In a DGR, the waste is foreseen to be emplaced in metallic containers. Engineered barriers shall prevent or significantly delay access of groundwater. However, during the long-term evolution of the repository system, water will move through the barriers, reach the containers, and start altering. To evaluate the safety of a DGR, detailed information regarding metal corrosion mechanisms and rates is needed.

Degradation processes have been extensively studied in the past under many relevant conditions (Abdelouas et al 2022 and references there-in; Frankl et al., 2023). Canister corrosion will depend on the material characteristics and will be controlled by physico-chemical and specific environmental conditions established by the radioactive waste and by the other engineered barriers. These conditions will evolve over time (King and Padovani, 2011), including radiation, thermal, hydraulic, mechanical, chemical and biological processes, as well as external perturbations.

Corrosion of container materials has been extensively studied under constant conditions, commonly those reflecting the long-term period of the repository, but uncertainties still existed on the role of evolving chemical, mechanical, and redox conditions of the early post-closure period and under the coupled phenomena expected along the life of the repository. The ConCorD WP was devoted to further study these processes and, in particular, it was proposed analyse in detail the effect of near-field transient conditions on the container corrosion at the interface with the bentonite engineering barrier at varying scales.

CIEMAT (ES), GRS (DE) KIT-INE (DE) and UJV-SURAO (CZ) proposed to analyse the role of different near-field transient conditions by performing corrosion experiments at the laboratory scale in combination with in-situ experiments in underground research laboratories. The near-field conditions analysed included hydraulic, thermal redox and radiation transients.

CIEMAT aimed to study the impact of hydraulic (water saturation)/redox and thermal transients (ambient temperature and 80°C), altogether with gas evolution, to relate induced metal corrosion with gas/hydraulic and temperature conditions.

GRS in cooperation with KIT-INE proposed to analyse the temporal evolution of rate and propagation of corrosion of spheroidal graphite cast iron GGG40 and copper alloy C71500 in contact with bentonite saturated with pore water at typical near field temperatures. The influence of oxidising/reducing conditions on the growth and long-term chemical and mechanical stability of the protective oxide films will be emphasized. The redox topic will be complemented with studies at 30, 50 and 80°C and pressures of 5, 50 and 100 bar, using both accelerated and conventional corrosion techniques.

UJV-SURAO proposed to study the effect of increased temperature and irradiation on accelerated corrosion of the carbon steel canister in Ca-Mg bentonite.

The performed studies contribute to identify the physico-chemical effects of the different transients on the container material, on released corrosion products and on the engineered barrier alteration. They provide relevant information to evaluate the long-term behaviour of container materials and bentonite engineered barrier.

This report describes the experimental systems analysed by the different research groups and provides relevant experimental data on redox effects, chemical impact, temperature, bentonite saturation and gas evolution, obtained both in laboratory and in-situ.

A large part of the results obtained in Task 5 was transmitted to the modelling groups participating in Task 6, mainly to Amphos21. The results will be helpful to adequately account for these processes in performance assessment.

EURAD (Deliverable n° 15.12) – Identification on the effect of transient processes on corrosion
Dissemination level: Public
Date of issue of this report: **29/04/2024**

Page 24

1.1 Report structure

This report comprises results from independent sets of experiments performed by four organisations CIEMAT (ES), GRS (D), KIT-INE (D) and UJV-SURAO (CZ) within the Task 5 in ConCorD.

The methodology and design of the experiments carried out by each organisation are quite different from one another, as well as the materials analysed. Therefore, each contribution is separately presented as follows:

- CIEMAT experiments – Section 2, studied the impact of hydraulic (water saturation)/redox and thermal transients. It presents analyses of different bentonite samples form in-situ ABM5 experiment carried out at Aspö (Sweden) an laboratory corrosion studies of carbon steel and Cu-OFP in contact to three different bentonites, hydrated with different water type (clay pore water and granitic water) and subject to 80ºC

- GRS experiments – Section 3, focused on the corrosion behaviour of spheroidal graphite cast iron steel in contact with a slurry of bentonite prepared with saline clay porewater and Opalinus Clay water during the first 90 days. Air saturated pore water was used for the preparation of the slurry.

- KIT-INE experiments – Section 4, were devoted to analyse the corrosion on two metal systems, spheroidal graphite cast iron and copper nickel alloy, with a suspension of Na-bentonite hydrated with synthetic granitic water, at different temperatures (30ºC and 50ºC).

- UJV-SURAO experiments – Section 5, analysed corrosion of Czech C-steel in contact to compacted bentonite with respect to different gamma-irradiation dose rates, temperature, and water saturation.

EURAD (Deliverable n° 15.12) – Identification on the effect of transient processes on corrosion
Dissemination level: Public
Date of issue of this report: **29/04/2024**

Page 25

2. CIEMAT experiments: corrosion processes in different compacted bentonites subjected to hydraulic, redox and thermal transient effects.

2.1 Motivation

The studies developed by CIEMAT (ES) for WP ConCorD - Task 5 aimed to investigate corrosion and bentonite interactions during redox, hydraulic and thermal nearfield transients.

Studies were focused on analysing the effect of process occurring in compacted bentonite on corrosion processes. The impact of porewater chemistry and the presence of dissolved gases was analysed under different water saturation, salinity and temperature conditions.

CIEMAT proposed two separate activities in Task 5, analysis of samples from large-scale test and laboratory experiments (static and dynamic experiments). These activities cover a range of transient conditions affecting corrosion of metals, such as resaturation of compacted bentonite, convective water vapour saturation fluxes, ambient and high temperature (80º C), different salinity of the infiltrating waters, and variations in oxic/anoxic conditions.

Three types of reference bentonites were used in the experiments: FEBEX, SWy-3 and Czech bentonites, as well as three types of metal coupons: reference carbon steel from Nagra, reference carbon steel from SURAO and reference copper from SKB. Experiments were performed with compacted materials at two dry densities: 1.4 g/cm^3 and 1.6 or 1.65 g/cm^3.

2.2 Materials

2.2.1 Metals and coupons

2.2.1.1 Metal coupons included in the ABM5 in-situ experiment (Äspö, Sweden)

The Alternative Buffer Material ABM5 experiment is an *in situ* medium-scale experiment performed at Äspö Hard Rock Laboratory (HRL) conducted by SKB in Sweden with the aim of analysing the long-term stability of bentonites used as engineering barrier for a high-level radioactive waste repository, HLWR (Svensson et al., 2011, 2023). CIEMAT analysed five different ring-shaped Ca- and Na-bentonite blocks (Rokle, FEBEX, Ibeco, MX-80 and Asha 505), which were piled around a carbon steel cylindrical heater, subjected to a maximum temperature of 250°C and hydrated with saline Na-Ca-Cl Äspö groundwater (0.91 M ionic strength). This work allowed to identify the main corrosion products and geochemical processes involved, as well as the modifications in the physico-chemical properties and pore water composition after 4.4 years of treatment. In addition, the bentonite blocks were in contact with carbon steel (C-steel) P235TR1 Heater, and some of them were interacting with thermocouples (type K (chromel-alumel) and titanium coupons. The chemical composition of carbon steel is included in *Table 1*. More details of these materials can be found in Svensson et al. (2011).

Table 1 – Chemical composition in wt. % of carbon steel included in ABM5 experiment (steel grade P235TR1, 1.0254) EN 10216-1-2014.

Element	Fe	C	Si	Mn	P	S	Cr	Mo	Ni	Cu	Nb	Ti	V
maximum	97.2	0.16	0.35	1.20	0.025	0.02	0.30	0.08	0.30	0.30	0.01	0.04	0.02

2.2.1.2 Metal coupons used for laboratory experiments

Carbon steel

Two carbon steel materials were used by CIEMAT (ES), named *Nagra C-steel* and *Czech C-steel*, for obtaining the coupons.

![eurad logo] European Joint Programme on Radioactive Waste Management

EURAD (Deliverable n° 15.12) – Identification on the effect of transient processes on corrosion
Dissemination level: Public
Date of issue of this report: **29/04/2024**

Page 26

Nagra C-steel was provided by Jacobs (UK) consisting of a circular section of around 2 kg of C-steel ASTM A694-08 F65 (*Figure 1a*) which comes from a prototype representative of the canister material designed by the Swiss National Cooperative for the Disposal of Radioactive Waste (NAGRA). This material is ASTM A694-08 F65 with composition described in Table 2 (Patel et al, 2012).

Table 2 – Chemical composition in wt. % of reference Nagra carbon steel (Patel et al, 2012).

Element	Fe	C	Si	Mn	P	S	Cr	Mo	Ni	Cu	CE_{IIW}
maximum	98.3	0.12	0.3	0.8	0.015	0.025[2]	0.2	[1]	0.2	0.02	0.01

[1] Cr+Ni+Mo <0.25%, Nb+V <0.02%, H <1 ppm, vacuum degassed (low O,N); [2]depends on product form: for plates 0.003% max, for forgings 0.025% max; $CE_{IIW:}$ carbon equivalent content.

At CIEMAT (ES*),* cylindrical test rods of different diameters were extracted to further obtain thin flat coupons *Figure 1*b, to be used for different purposes and experiments (in Task 3 for irradiation experiments (ConCorD deliverable 15.8, 2024; and in Task 5 for evaluating the role of transients). The size of C-steel discs used for irradiation experiments was 30 mm in diameter with an average thickness of 1.5 mm.
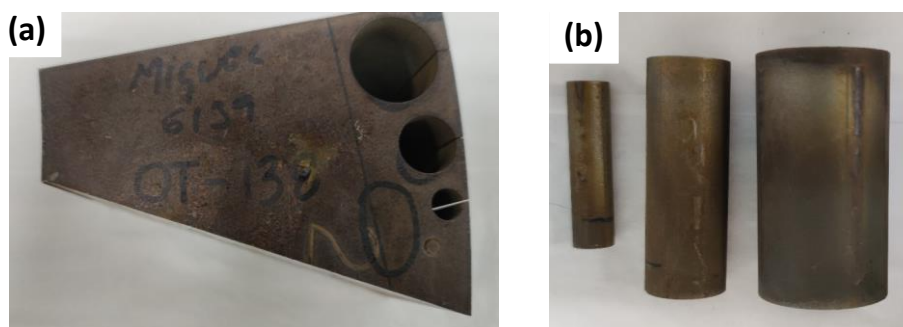
Figure 1 – (a) Carbon steel ASTM A694-08 F65 *sample sent by Jacobs (UK) of material representative of canister design by NAGRA (CH). (b) Cylindrical test rods extracted to obtain metal coupons of different diameters.*

Czech C-steel samples used are the same as that of UJV (described in Section 5.2.1). They were supplied by Škoda and are composed of carbon steel S355J2H, obtained by cutting a rod which serves as the outer casing for the Czech canister concept (Pospíšková et al. 2017, Matulová et al. 2023). The steel discs were prepared out of the steel weld by steel crosscutting and by using grinding wheel with 46K grit. The dimensions of coupons are 10 mm in diameter by 1 mm thick.

Copper

Copper samples were provided by the Swedish Nuclear Fuel and Waste Management Company (SKB, SE). Different cylindrical rods of oxygen-free phosphorus-doped copper (Cu-OFP) material were received at CIEMAT (ES). The rod used to obtain copper discs in Task 5 is referred as T77 +750 40⁰ (*Figure 2*). Obtained discs have a diameter of 27.5 mm and average thickness of 1.5 mm. The composition of the Cu-OFP material is included in *Table 3*. It is composed of 99.99 wt.% Cu with small traces of other elements.

EURAD (Deliverable n° 15.12) – Identification on the effect of transient processes on corrosion
Dissemination level: Public
Date of issue of this report: **29/04/2024**

Page 27
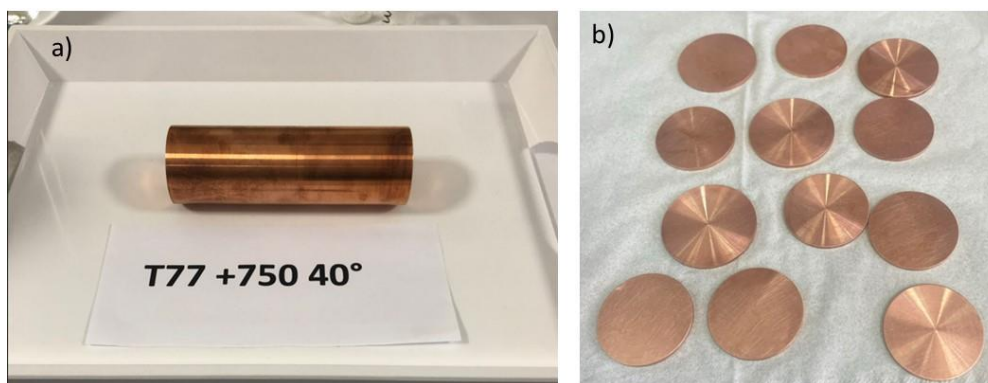
Figure 2 – (a) Cylindrical test tube reference T77 +750 40º of Cu-OFP, representative material of their canister design of SKB (SE) sent to CIEMAT (ES). (b) Example of Cu-OFP discs of 27.5 mm in diameter and 1.5 mm thickness.

Table 3 – Composition of Cu-OFP sample T77 +750 40º provided by SKB (SE).

wt.%	Traces (ppm)										
Cu	**Ag**	**Al**	**As**	**Bi**	**Cd**	**Co**	**Cr**	**Fe**	**H**	**Mn**	**Ni**
99.99	13.1	<0.08	0.3	0.6	<0.4	<0.1	0.3	0.8	0.25	<0.2	1
	O	**P**	**Pb**	**S**	**Sb**	**Se**	**Si**	**Sn**	**Te**	**Zn**	**Zr**
	0.9	56	<0.7	4.2	<1	<0.7	2.1	<0.7	<2	<0.1	<0.1

2.2.1.3 Metal cleaning procedure

Before use, all metal samples were polished and then cleaned following this procedure: metal coupons were first degreased by sonication for 5 min in a vial containing ethanol of analytical grade. Afterwards, samples were cleaned with Type I deionised water and swilled to remove any residual ethanol. Then, discs were immersed in another vial containing ~ $1 \cdot 10^{-3}$ M nitric acid (Merck, 69% for analysis EMSURE®), and subjected to 5 min of sonication. This procedure was repeated three times and finally washed with deionized water. Discs were dried with N_2 gas and stored in closed glass vessels.

This cleaning procedure was also applied after experiments dismantling, to remove corrosion and degradation products over the metal surfaces, to estimate corrosion rates by mass loss. In this case, the cleaning procedure was repeated until reaching constant weigh of the coupons. ASTM main recommendations were followed (ASTM, 2011).

2.2.2 Bentonites

2.2.2.1 Bentonites included in the ABM5 in-situ experiment (Äspö, Sweden)

At the Äspö ABM5 experiment, eleven different clays were chosen for the buffers to examine effects of smectite content, interlayer cations and overall iron content. In addition, bentonite pellets with different proportions of quartz are being tested (Svensson et al., 2011, 2023). The main purposes of the project were to characterize and compare different bentonite qualities and to identify any differences in behaviour or long-term stability of hydro-mechanical properties, mineralogy and chemical composition after groundwater saturation, heating and interaction with corroding metals, i.e., iron-bentonite interactions (Svensson et al., 2011).

CIEMAT analysed five different ring-shaped Ca- and Na-bentonite blocks (Rokle, FEBEX, Ibeco, MX-80 and Asha 505), piled around a carbon steel cylindrical heater, as well as the Asha 505 block Nº 3 in contact with thermocouples (type K (chromel-alumel) and titanium coupons. More details of the ABM5 experiment can be found in Svensson et al., (2023).

EURAD (Deliverable n° 15.12) – Identification on the effect of transient processes on corrosion
Dissemination level: Public
Date of issue of this report: **29/04/2024**

Page 28

2.2.2.2 Bentonites used for laboratory experiments

Three types of bentonites were used for the experiments:

- FEBEX bentonite, from the Cortijo de Archidona deposit (Almería) was selected. This clay takes the name form the FEBEX (*Full-scale Engineered Barriers Experiment*) project (Huertas et al., 2006). FEBEX has a montmorillonite content greater than 90 wt.%, with quartz, plagioclase, potassic feldspar, calcite and trydimite as accessory minerals. There may be illite/smectite interstratifications up to 15%. The cation exchange capacity is 100 meq/100g, and in the exchange complex 42% Ca, 33% Mg, 23% Na and 2% K are present (Fernández et al., 2004).

    For the ConCorD project, 2.5 kg of bentonite from the batch referenced as FEBEX 70-IMA-3-4-0 (Huertas et al, 2000) were separated. Prior to compaction, the FEBEX clay was ground and sieved to a fraction < 0.5 mm. Raw FEBEX clay was used in these experiments without any additional treatment or purification.

- SWy-3 bentonite, a mainly Na-bentonite from Crook County, Wyoming (USA). 1 kg of bentonite (<63 μm), was acquired from the Clay Mineral Society Source. This bentonite has a cation exchange capacity of 75 meq/100g (Na: 72%, Ca: 18%, Mg: 8%, K: 2%). Its montmorillonite content is ~87%, with quartz, plagioclases, K-feldspar, cristobalite, gypsum, mica, pyrite, as accessory minerals.

- Czech bentonite, a calcium-magnesium bentonite (BCV) from the Czech Republic (provided by KERAMOST, Plc., Czech Republic). UJV provided Ciemat with 1 Kg of this bentonite (<63 μm). This bentonite has a cation exchange capacity of 59 meq/100 g (Mg: 64%, Ca: 24%, Na: 10%, K: 2%). Its montmorillonite content is ~73%, with kaolinite, muscovite, quartz, sanidine, goethite, anatase, calcite, aragonite, ankerite and siderite, as accessory minerals.

Complete mineralogical, physical, and geochemical characterisation of these bentonites was carried out before and after experiments.

2.2.3 Waters

2.2.3.1 Water of ABM5 in-situ experiment (Äspö, Sweden)

The buffer bentonites were saturated through a natural groundwater inflow of approximately 8.5 litres/24 hours, coming from one fracture located 0.8 meter down from the floor. The chemical composition of this granitic groundwater is shown in *Table 4*.

2.2.3.2 Waters used for laboratory experiments

Different types of water were used to saturate the bentonite for analysing bentonite/coupon interactions: granitic water and synthetic FEBEX pore water corresponding to a compaction dry density of 1.4 g/cm^3 (PW-1.4), which composition is described in Fernandez & Rivas (2005). The chemical composition of this pore water is included in *Table 5*. During and after the addition of the salts for preparation the synthetic water, the solution was purged with N_2 gas.

The granitic water is a commercial water acquired in 2022 whose composition is included in *Table 6*.

For verification, aliquots of both waters were sent to the Chemical Division of CIEMAT for complete chemical analysis.

Table 4 – Typical composition of the Äspö granitic groundwater coming from borehole KA2598A.

Ion	Water-type	I (M)	Na	K	Ca	Mg	HCO$_3^-$	Cl$^-$	SO$_4^{2-}$	Br$^-$	F$^-$	Si	pH
mg/L	Ca-Na-Cl	0.91	2470	12.4	2560	64.8	51.7	8580	483	59	1.5	6.3	7.33

EURAD (Deliverable n° 15.12) – Identification on the effect of transient processes on corrosion
Dissemination level: Public
Date of issue of this report: **29/04/2024**

Page 29

Table 5 – Chemical composition (M) of synthetic pore waters prepared for FEBEX bentonite samples compacted at 1.4 (PW-1.4). Data for recipe was taken from Fernandez & Rivas (2005).

Reference 1.4 g/cm^3 dry density	Cl$^-$ (M)	SO$_4^{2-}$ (M)	HCO$_3^-$ (M)	Na (M)	K (M)	Ca (M)	Mg (M)	pH
PW-1.4	$6.36 \cdot 10^{-2}$	$4.87 \cdot 10^{-2}$	$1.10 \cdot 10^{-3}$	$1.13 \cdot 10^{-1}$	$1.01 \cdot 10^{-3}$	$1.36 \cdot 10^{-2}$	$1.48 \cdot 10^{-2}$	7.56

Table 6 – Chemical composition (M) of granitic groundwater used in dynamic and static experiments.

pH	Cl$^-$ (M)	SO$_4^{2-}$ (M)	HCO$_3^-$ (M)	Si (M)	Na (M)	Ca (M)	Mg (M)	K (M)
6.6	$1.18 \cdot 10^{-4}$	$1.67 \cdot 10^{-4}$	$1.16 \cdot 10^{-1}$	$2.60 \cdot 10^{-4}$	$2.44 \cdot 10^{-4}$	$5.99 \cdot 10^{-4}$	$3.66 \cdot 10^{-4}$	$2.12 \cdot 10^{-5}$

2.3 CIEMAT experimental description

CIEMAT proposed two separated activities in Task 5 with the aim of studying corrosion and bentonite interactions during redox, hydraulic and thermal nearfield transients:

1. In-situ experiments: Analysis of samples from ABM5 experiment (Äspö Laboratory, Sweden).
2. Dynamic and static laboratory experiments:

The types of dynamic experiments were: a) Infiltration tests, which correspond to transient conditions in which natural compacted bentonite is saturated as a function of time depending on the suction capacity of the clay material and dry density; and b) convective water-vapour fluxes tests, at 80 ºC with compacted bentonite, which simulate convective fluxes at the heater interface.

The static experiments were inside a reactor and represent transient states from natural compacted bentonite to saturated conditions, with enough amount of water for allowing bentonite/granitic water/carbon steel interactions at a high temperature (80 ºC).

2.3.1 In-situ experiment: Samples from ABM5 test (Äspö Laboratory, Sweden).

The ABM (Alternative Buffer Material) is a medium-scale experiment installed at the *Äspö Underground Research Laboratory* with the aim of analysing the long-term stability of different bentonites under similar conditions to that expected in the Swedish repository concept and considering adverse conditions regarding to high temperatures (Svensson et al., 2011).

The main purposes of the in-situ experiment were to characterize and to compare different bentonite qualities interacting with corroding metals and to identify any differences in behaviour regarding bentonite hydro-mechanical properties, mineralogy and chemical composition, after groundwater saturation, heating and on metal/bentonite interactions.

The packages were installed in boreholes (30 cm diameter and 3 m depth) drilled in the tunnel named TASD at ca. 420 m depth in the Äspö Hard Rock Laboratory. The granitic host rock consists of Äspö diorite and greenstone.

The samples analysed by CIEMAT came from package 5 (ABM5), shown *Figure 3*, deposited in the borehole named KD0098G01, where there was a groundwater inflow of around 8.5 L/d, coming from a fracture located -0.8 m.

The ABM5 contains 30 ring-shaped bentonite blocks piled around a cylindrical tube made of carbon steel P235TR1 (*Figure 3*). The ABM5 experiment includes a medium-scale test package, consisting of

EURAD (Deliverable n° 15.12) – Identification on the effect of transient processes on corrosion
Dissemination level: Public
Date of issue of this report: **29/04/2024**

Page 30

a central carbon steel tube with heaters, and a buffer of compacted clay being hydrated with natural Äspö granitic groundwater with inflow of approximately 8.5 L/day, coming from one fracture located 0.8 meter down from the floor (*Figure 3*).

An electrical heater of 1000 W was placed inside the tube as a heat source. The heating test duration was 4.4 years, starting on November 15th, 2012, and finishing on April 10th, 2017. The bentonite was heated to 50°C for the first three and half years, to support saturation and prevent water boiling, and then in 2016 the temperature was increased stepwise to 150°C and up to 250°C at the bentonite/heater interface for about the last six months of exposure. Estimated maximum temperatures at heater contact of 240-250 ºC were reached between blocks 22 and 8, decreasing temperatures both at bottom and top part of the bentonite column (<188-156 °C, blocks 3 and 27), and as a function of the granite contact (*Figure 3*). In the hottest blocks, more than 150 °C was reached at a distance of 6 cm from the heater, the thickness of the bentonite block being 10 cm.
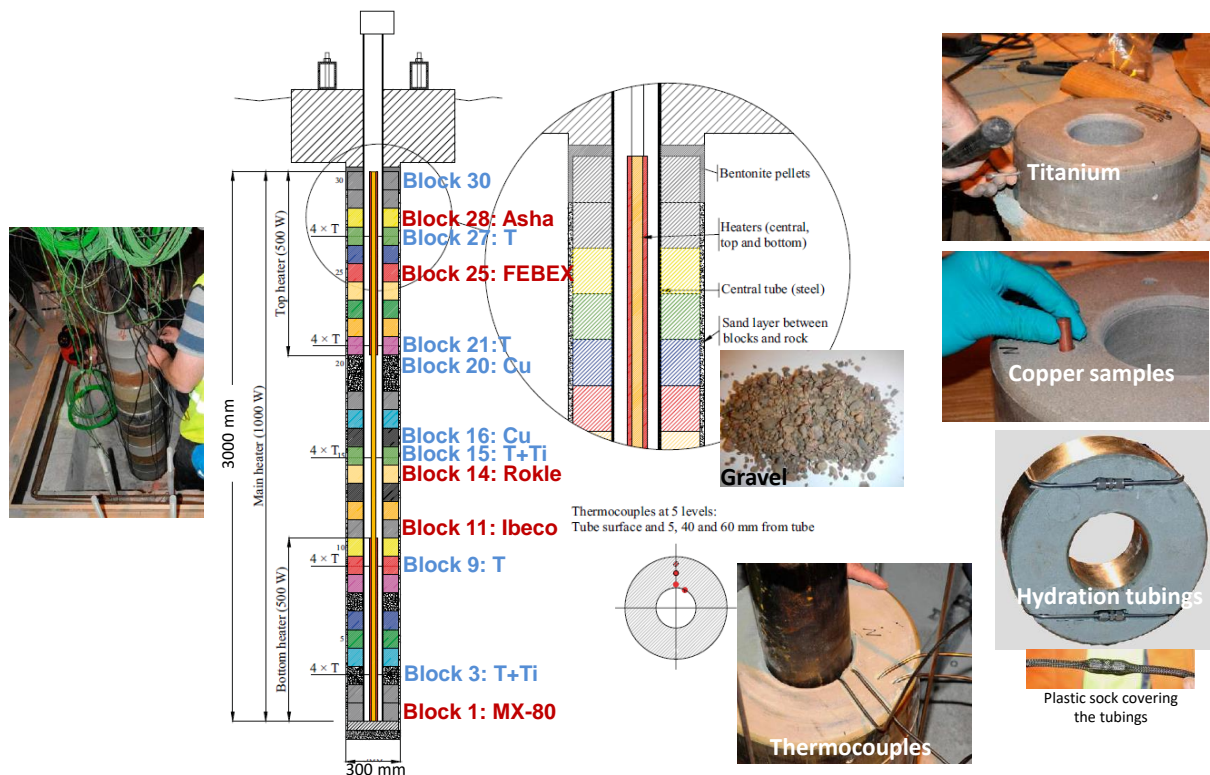
Figure 3 – ABM5 in-situ test: 30 ring-shaped bentonite blocks piled around a cylindrical tube made of carbon steel P235TR1.

Twenty thermocouples type T (chromel-alumel with a shield of cupronickel, 4.5 mm diameter) were installed in blocks numbers 3, 9, 15, 21 and 27. Four thermocouples were installed at each level in pre-drilled holes in the bentonite rings, one on the steel surface and three in the buffer at a radial distance from the heater (5, 40 and 60 mm). In addition, 8 copper specimens (10 mm diameter, 25 mm height, Cu-OFP: oxygen-free phosphorous doped) and 8 titanium specimens (tube of 6 mm outer and 4 mm inner diameters) were positioned. The specimens were installed on the surface in pre-drilled holes followed by a small bentonite cylinder. The copper specimens were positioned in blocks 16 and 20 at 3 cm distance from the heater in four directions (0º, 90º, 180º and 270º). In the case of titanium specimens, four of them were installed in each of the two chosen blocks (#3 and #15), inside holes drilled mid-height of the block periphery in four directions (0º, 90º, 180º and 270º).

The dismantling operation of the ABM5 experiment began June 2017. Some blocks looked rather intact while others were highly fractured and very fragile by the effect of water loss due to the high temperature.

EURAD (Deliverable n° 15.12) – Identification on the effect of transient processes on corrosion
Dissemination level: Public
Date of issue of this report: 29/04/2024

Page 31

Different bentonite samples were retrieved and analysed for performing different investigations. Most of the bentonite samples were preserved immediately inside vacuum-sealed aluminium-foil bags for avoiding water loss and oxidation due to their exposure to the air-atmosphere.

2.3.2 Laboratory experiments by CIEMAT

2.3.2.1 Dynamic experiments

Infiltration Tests

Infiltration tests have been performed at ambient temperature in oxic/anoxic environment (*Figure 4* and *Figure 5*). These tests correspond to transient conditions in which natural compacted bentonite (60% or 41.3% of saturation for dry densities of 1.65 or 1.4 g/cm^3, respectively) is saturated as a function of time, depending on the suction capacity of the clay material and dry density.
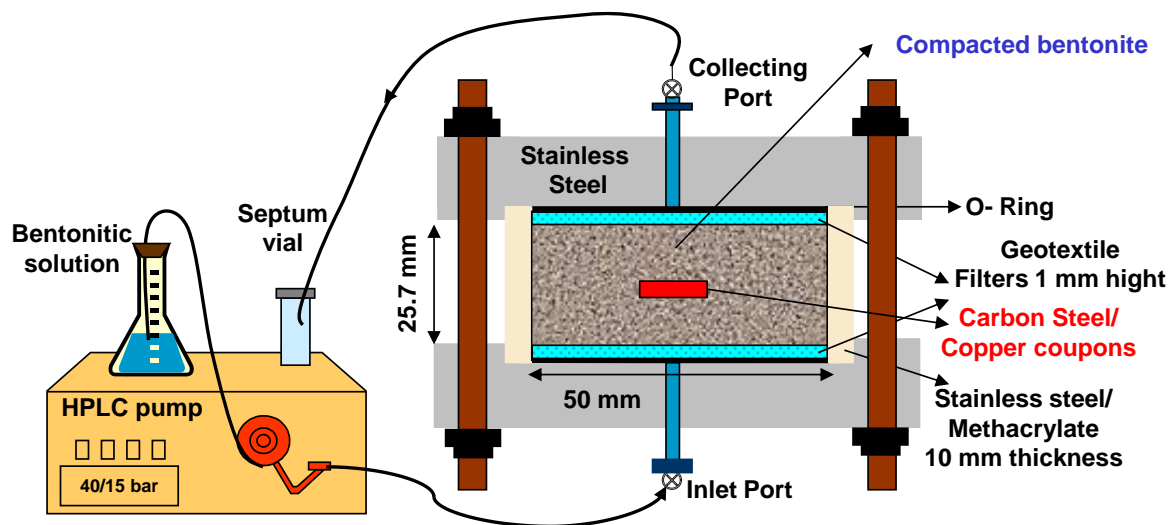
Figure 4 – Infiltration cells with compacted bentonite used for dynamic experiments: bentonite dry density at 1.4 and 1.65 g/cm^3 at oxic/anoxic conditions.

Figure 5 – Setup of the infiltration cells used for dynamic experiments.

EURAD (Deliverable n° 15.12) – Identification on the effect of transient processes on corrosion
Dissemination level: Public
Date of issue of this report: **29/04/2024**

Page 32

Figure 6 – Detail of the preparation of the compacted cells for infiltration experiments.
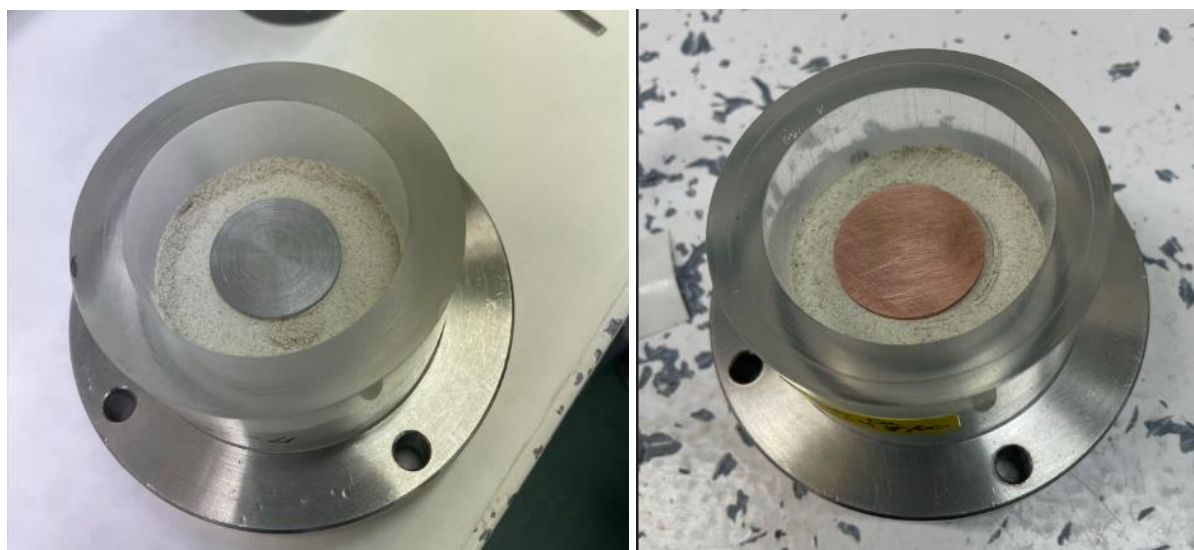
Figure 7 – Nagra carbon steel and SKB Cu-OFP coupons in the middle of the compacted bentonite for the infiltration tests in dynamic experiments.

The infiltration tests were installed in a small-scale hermetic cell- whose internal diameter is 50 mm and inner length 25.7 mm, (Figure 4). The cell has a body of methacrylate 10 mm thickness, to prevent the deformation of the cell by bentonite swelling, and the lids are made of 316L stainless steel (Figure 5, Figure 6). Two cells were completely made of stainless steel. The experimental conditions are shown in *Table 7* and *Table 8*.

EURAD (Deliverable n° 15.12) – Identification on the effect of transient processes on corrosion
Dissemination level: Public
Date of issue of this report: **29/04/2024**

Page 33

Table 7 – Experimental conditions of infiltration cells for dynamic tests.

Oxic Conditions / Degree of saturation = 60% and 41.3% for ρ_d=1.65 and 1.40 g/cm³, respectively				
Type of Cell	*Coupon*	*Type of water*	*Dry Density*	*Nº Cell*
	Nagra Carbon Steel	Granitic water	1.40 g/cm³	1
			1.65 g/cm³	2
		Bentonite Saline pore water (d=1.4 g/cm³)	1.40 g/cm³	3
			1.65 g/cm³	4
	SKB Cu	Granitic water	1.40 g/cm³	5
			1.65 g/cm³	6
		Bentonite Saline pore water (d=1.4 g/cm³)	1.40 g/cm³	7
			1.65 g/cm³	8

Table 8 – Characteristics of the infiltration cells for dynamic experiments under oxic/anoxic conditions and ambient temperature.

Methacrylate cell	Dry density	Clay mass (g)	coupon mass (g)	coupon diameter (mm)	Water-type
Cu coupon	1.40	79.35	9.1039	27.09	granitic
Cu coupon	1.65	93.51	9.0918	27.09	granitic

Stainless steel cell	Dry density (g/cm³)	Clay mass (g)	coupon mass (g)	coupon diameter (mm)	Water-type
Cu coupon	1.40	100.5	10.1763	27.09	saline
Cu coupon	1.65	118.5	9.4069	27.09	saline

Methacrylate cell	Dry density	Clay mass (g)	coupon mass (g)	Diameter coupon (mm)	Water-type
Nagra carbon steel coupon	1.40	79.35	6.6919	29.9	granitic
Nagra carbon steel coupon	1.65	93.51	6.8013	29.9	granitic

Methacrylate cell	Dry density	Clay mass (g)	coupon mass (g)	Diameter coupon (mm)	Water-type
Nagra carbon steel Coupon	1.40	79.35	6.6748	29.9	saline
Nagra carbon steel coupon	1.65	93.51	6.7175	29.9	saline

EURAD (Deliverable n° 15.12) – Identification on the effect of transient processes on corrosion
Dissemination level: Public
Date of issue of this report: **29/04/2024**

Page 34

Masses of 79.35 and 93.51 g of FEBEX bentonite were compacted at 1.4 and 1.65 g/cm^3, respectively, with its hygroscopic water content of 13.4% in each cell (*Figure 6*). Nagra carbon steel coupons were introduced inside the compacted bentonite (*Figure 7*), which is continuously hydrated with two types of waters: granitic water and saline bentonite pore water (see *Table 5* and *Table 6*). Other tests have been performed introducing reference SKB Cu-OFP coupons.

Hydration takes place at the bottom part of the cell through a geotextile filter (1 mm height). The infiltration water is injected to a pressure of 5 bars by means of a 307 Gilson® piston pump. At the top of the cell the outflowing pore water coming from the bentonite through another geotextile disk, is collected over time inside a vacuum vial closed by a septum (*Figure 5*, *Table 7*) and analysed. The inlet and outlet tubing are made of stainless steel. The temperature of the experiments was maintained at ambient temperature.

Convective water-vapour fluxes tests under dynamic conditions

Water adsorption tests have been performed at 80 ºC with compacted material (dry density of 1.4 and 1.6 g/cm^3) at constant volume. These tests simulate convective water-vapour fluxes at the heater interface.

For these tests, special cells were designed. Each cell consists of a 316L stainless steel cylindrical body, 50 mm diameter and 24 mm high, with two perforated covers joined by bolts (*Figure 8*). The clay is compacted directly inside the cell. The resulting compacted bentonite block is 24 mm length and 38 mm diameter, implying a cross section of about 11.34 cm^2 and a volume of 27.22 cm^3. At the top and at the bottom of the sample, there is a dialysis sheet X25 1.6-8K MWCO, which allows the infiltration of water and, hence, the hydration of the bentonite. This sheet is also surrounding the bentonite for avoiding the contact of the bentonite with the stainless steel of the cell.

Each cell is placed inside desiccators with a deionized water solution and vacuum is created (10^{-3} mm Hg vacuum). The dialysis sheet and the perforated covers allow for the exchange of water in the vapour phase between the clay and the relative atmosphere inside the desiccators (95-100% RH).

The types of bentonites used in these tests are: FEBEX bentonite, MX-80 (SWy-3) and Czech bentonite. In the middle of each compacted bentonite a different coupon was introduced: Nagra reference carbon steel, SKB reference copper or Czech reference carbon steel (*Figure 9*).The tests were performed at a temperature of 80 ºC, inside an oven thermostated at 353.15 K (*Figure 10*). The initial conditions are shown in *Table 9.* The duration of the tests were 286 and 326 days for cells with Nagra carbon steel and SKB Cu coupons, respectively.
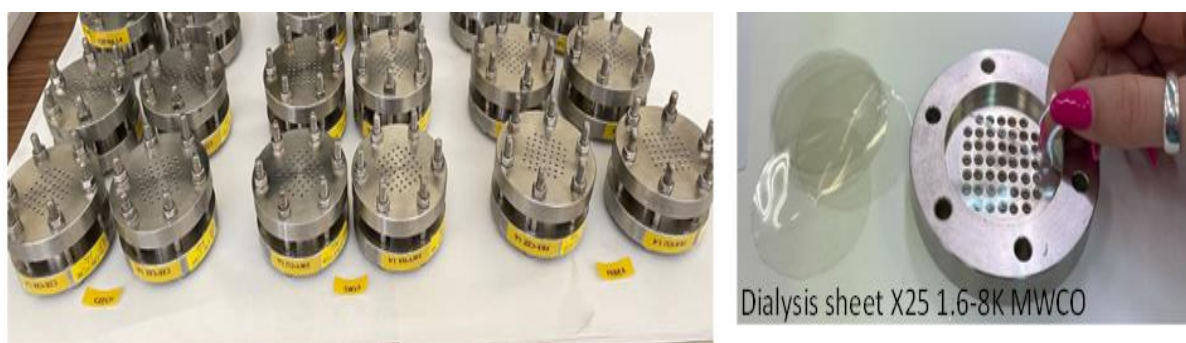
Figure 8 – Detail of cells for dynamic experiments at 80º C: Three types of bentonites at a dry density of 1.4 and 1.6 g/cm^3 at oxic conditions with Nagra, Czech and SKB metal coupons.

EURAD (Deliverable n° 15.12) – Identification on the effect of transient processes on corrosion
Dissemination level: Public
Date of issue of this report: **29/04/2024**

Page 35
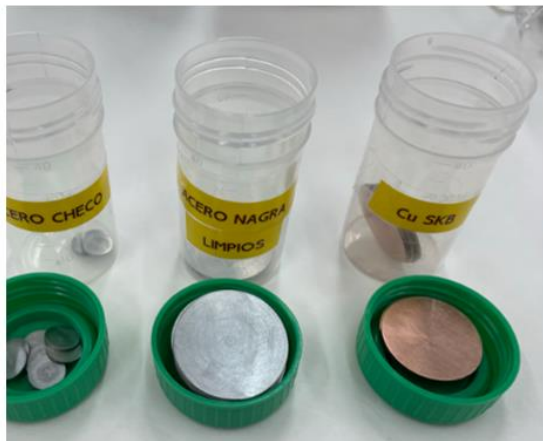
Dimensions	Diameter (mm)	Height (mm)	Volume (cm³)
Cell	38	24	27.22
Czech C Steel coupon	10	0.9	0.07
SKB Cu coupon	27.5	1.5	0.89
Nagra C Steel coupon	30	1.5	1.06

Figure 9 – Detail of coupons selected for dynamic experiments at 80º C.

Figure 10 – Experimental setup for convective water-vapor fluxes at 80 .

EURAD (Deliverable n° 15.12) – Identification on the effect of transient processes on corrosion
Dissemination level: Public
Date of issue of this report: **29/04/2024**

Page 36

Table 9 – Initial conditions of the dynamic experiments at 80 ºC.
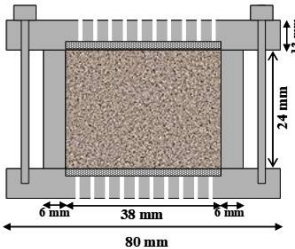
Oxic Conditions / Degree of Saturation = 55.6% and 41.3% for ρ_d=1.60 and 1.40 g/cm³, respectively / Temperature = 80 ºC / RH=100%					
Type of Cell	*Bentonite*	*Metal*	*Type of water*	*Dry Density*	*Cell*
	FEBEX	Nagra Steel	Water vapour 95-100% RH	1.4 g/cm³	1
				1.6 g/cm³	2
		SKB Cu	Water vapour 95-100% RH	1.4 g/cm³	3
				1.6 g/cm³	4
		Czech Steel	Water vapour 95-100% RH	1.4 g/cm³	5
				1.6 g/cm³	6
	SWy3	Nagra Steel	Water vapour 95-100% RH	1.4 g/cm³	7
				1.6 g/cm³	8
		SKB Cu	Water vapour 95-100% RH	1.4 g/cm³	9
				1.6 g/cm³	10
		Czech Steel	Water vapour 95-100% RH	1.4 g/cm³	11
				1.6 g/cm³	12
	Czech	Nagra Steel	Water vapour 95-100% RH	1.4 g/cm³	13
				1.6 g/cm³	14
		SKB Cu	Water vapour 95-100% RH	1.4 g/cm³	15
				1.6 g/cm³	16
		Czech Steel	Water vapour 95-100% RH	1.4 g/cm³	17
				1.6 g/cm³	18

Table 10 – Dimensions and masses used in the dynamic experiments at 80 ºC.

Dimensions	Diameter (mm)	High (mm)	Volume (cm³)
Cell	38	24	27.22
Czech coupon	10	0.9	0.07
Cu coupon	27.5	1.5	0.89
Nagra coupon	30.0	1.5	1.06

Water content	%		Coupons	Filter	Dialysis sheet
Febex <0.5 mm	14.3		Nagra Carbon Steel	X25 Spectra/PO 1.6-8K MWCO	
Czech < 63 µm	10.3		Copper SKB		
SWy3 < 63 mm	11.3		Czech Carbon Stell		

Cells Nº	Dry density (g/cm³)	Clay mass (g)	Coupons (g)		Fabrication date	Initial weight cell (g)	Temperature (ºC)	Initial test date	Final test date	Test duration (days)
1	FBX+Nagra 1,4	41.86	-		19/04/2023	1097.82	80	27/04/2023	07/02/2024	286
2	FBX+Nagra 1,6	47.84	-		19/04/2023	1098.69	80	27/04/2023	07/02/2024	286
3	FBX+Cu 1,4	42.13	-		19/04/2023	1100.27	80	27/04/2023	18/03/2024	326
4	FBX+Cu 1,6	48.15	-		19/04/2023	1102.88	80	27/04/2023	18/03/2024	326
5	FBX+Czech 1,4	41.29	-		20/04/2023	1091.96	80	27/04/2023	still running	
6	FBX+Czech 1,6	47.17	-		20/04/2023	1100.34	80	27/04/2023	still running	
7	SWy3+Nagra 1,4	40.76	8.3138		20/04/2023	1094.83	80	27/04/2023	07/02/2024	286
8	SWy3+Nagra 1,6	46.58	7.7673		20/04/2023	1106.19	80	27/04/2023	07/02/2024	286
9	SWy3+Cu 1,4	41.03	6.8022		20/04/2023	1098.85	80	27/04/2023	18/03/2024	326
10	SWy3+Cu 1,6	46.89	7.5552		20/04/2023	1101.21	80	27/04/2023	18/03/2024	326
11	SWy3+Czech 1,4	40.21	0.5426	1.0995	20/04/2023	1084.89	80	27/04/2023	07/02/2024	286
12	SWy3+Czech 1,6	45.95	0.5102	1.0493	20/04/2023	1098.44	80	27/04/2023	still running	
13	Czech+Nagra 1,4	40.40	7.7713		20/04/2023	1097.41	80	27/04/2023	07/02/2024	286
14	Czech+Nagra 1,6	46.17	7.7476		20/04/2023	1099.78	80	27/04/2023	still running	
15	Czech+Cu 1,4	40.65	8.4522		20/04/2023	1103.55	80	27/04/2023	18/03/2024	326
16	Czech+Cu 1,6	46.46	7.3394		20/04/2023	1101.68	80	27/04/2023	18/03/2024	326
17	Czech+Czech 1,4	41.92	0.5304	1.0471	20/04/2023	1092.98	80	27/04/2023	still running	
18	Czech+Czech 1,6	47.91	0.497	1.0408	26/04/2023	1097.33	80	27/04/2023	still running	

EURAD (Deliverable n° 15.12) – Identification on the effect of transient processes on corrosion
Dissemination level: Public
Date of issue of this report: 29/04/2024

Page 37

2.3.2.2 Static experiments

Static experiments represent transient states from the initial compacted bentonite at oxic conditions to saturated and anoxic conditions, with enough amount of water for allowing compacted bentonite/granitic water/carbon steel interactions at a high temperature (80 ºC).

In this case, FEBEX bentonite < 0.5 mm particle size was compacted inside special cells designed for this purpose at two dry densities: 1.4 and 1.6 g/cm^3, the initial degree of saturation being 41.3 and 55.6%, respectively. The bentonite mass was 65.57 g and 74.93 g, respectively (*Figure 11*, *Table 11*). In the middle of the compacted cell, two coupons of Nagra carbon steel were inserted. Between the sample and the covers there is a dialysis sheet X25 1.6-8K MWCO, which allows the infiltration of water and, hence, the hydration of the bentonite. These cells were introduced inside a PARR reactor (model 4600) at 80 ºC where 120 mL of granitic water was added for the hydration of the bentonite during the experiment (*Figure 12*).

For the compacted sample at 1.4 g/cm^3, the cell at contact with the granitic water was heated for 135 days, so the conditions were of a relative humidity of 100%, i.e., at a relative water pressure of 0.4619 bar (absolute 1.4569 bar).

At the end of the test (135 days of experiment for density 1.4 g/cm^3 test), and prior to open the reactor, gas and water samples were collected after several cycles of Ar flushing and vacuum inside the sampling lines (*Figure 13*). Then, the cell was dismantled and the compacted bentonite block was transferred to an anoxic glove box for sampling both the coupons and the bentonite.

Table 11 – Initial and final characteristics of the static experiments in reactor at 80 ºC.

Materials used			
Dimensions	Diameter (mm)	Height (mm)	Volume (cm^3)
Cell (Delrin)	38	38	43.10
Nagra Carbon steel coupon	30	1.5	1.06
Bentonite conditions			
Dry density (g/cm^3)	1.4	1.6	
Bentonite mass (g)	65.57	74.93	
Clay Initial water content (%)	14.3	14.3	
Initial saturation degree (%)	41.3	55.6	
Test Temperature (ºC)	80	80	
Granitic water at contact (mL)	200	200	
Mass of the Coupons (g/each)	7.7713	7.7713	
Final mass of the coupons (g)	7.5163		
Intitial Water vapour pressure (relative, bar)	0.4619		
Total Final pressure (absolute, bar)	1.472		
Test duration (days/months)	135 / 4.35		
Corrosion rate (☐m/year)	53.2		

EURAD (Deliverable n° 15.12) – Identification on the effect of transient processes on corrosion
Dissemination level: Public
Date of issue of this report: **29/04/2024**

Page 38

Figure 11 – Detail of the bentonite, Nagra C-steel coupon and cell used for static experiments.

Figure 12 – Setup of the static experiments.

Figure 13 – Collection of gas and water samples at the end of the static experiment in the reactor at 80 ºC: FEBEX bentonite at 1.4 g/cm³ of dry density.

EURAD (Deliverable n° 15.12) – Identification on the effect of transient processes on corrosion
Dissemination level: Public
Date of issue of this report: **29/04/2024**

Page 39

2.4   Sample analyses after dismantling the experiments

For the samples simulating the canister /bentonite interface, main analyses were focused on determining the corrosion rates of coupons by mass loss, the identification of the main corrosion products, and also on bentonite analyses.

Characterisation and analytical techniques were applied, whose main characteristics are below described.

2.4.1   Disassembling and visual inspection

The disassembling and sampling procedure was adapted to the type of samples and experiments.

2.4.1.1 Disassembling of the cells

The procedure for disassembling the samples simulating the metal canister/bentonite interface required additional care. Photographs were taken of the samples throughout the procedure to better evaluate induced changes or damage.

The sample extraction from the cells required the use of the same press used to compact the bentonite samples. After sample extraction from the cells, the compacted sample was cut by the middle part. The metal discs were usually stuck to the surface of the hydrated bentonite and were carefully separated from the bentonite with tweezers. Once metal and bentonite surfaces were separated, the alteration and degradation products (mixture of corrosion products and bentonite phases or salts) could be seen over both surfaces.

First attempt aimed to analyse these degradation products directly on the metal or clay surfaces, by applying non-destructive characterization techniques.

Later on, the degraded/corroded surface layers were carefully retrieved from the metal samples with a spatula and stored for further analyses.

2.4.1.2 Metal discs

Metal discs (coupons) were extracted from the compacted bentonite and photographed to visually compare their degradation, and then analysed by SEM. When appreciable alteration was detected on the disc surface, the altered surface layer was carefully retrieved with a spatula and stored for analyses. After analysis, metal samples were cleaned a few times with the same procedure described in section 2.2.1.3, to eliminate degradation products, following standard practices (ASTM, 2011). After cleaning, samples were weighed to estimate corrosion rate by mass loss.

2.4.1.3 Bentonite and corrosion products at bentonite/coupon interface

The bentonite at direct contact with the metal was recovered by using a knife and analysed by different techniques (XRD, FTIR, TG-DSC, SEM, etc.). All powder and compacted samples were characterised before and after the experiments, to identify relevant changes induced by studied coupled processes and the nature of bentonite degradation and corrosion products.

2.4.2   Water analyses

The *pH* was measured by means of an ORION 720A pH-meter equipped with a Metrohm 6.0224.100 combined pH micro-electrode. Merck pH buffer solutions of pH 4.00 and 7.00 were used for pH-meter calibration.

Electrical Conductivity measurements (EC) were performed by means of an ORION 115 conductimeter. The conductivity cell was checked/calibrated with a standard solution of 1413 µS/cm or 12.6 mS/cm (NaCl). The measurements were automatically adjusted to a temperature of 25 ºC.

EURAD (Deliverable n° 15.12) – Identification on the effect of transient processes on corrosion
Dissemination level: Public
Date of issue of this report: **29/04/2024**

Page 40

The *redox potential* (Eh) was measured by means of a combined platinum-ring electrode (Metrohm, ref. 6.0451.100) with a built-in Ag/AgCl reference electrode. The standardisation was carried out by using a redox buffer, $Fe(CN)_6^{4-}/Fe(CN)_6^{3-}$ (10^{-3} M), at +250 ± 5 mV vs the Ag-AgCl 3 M KCl electrode.

The total *alkalinity* of the water samples was determined with a specific Dynamic Equivalence point Titration (DET) method for analysing samples of 1-2 mL. The instrumentation consists of a Metrohm 888 Titroprocessor equipped with a 5 mL burette and a 6.0224.100 Metrohm combined pH micro-electrode.

The *major, trace cations and silica* were analysed by Inductively Coupled Plasma-Optical Emission Spectrometry (ICP-OES) with a Varian 735ES spectrometer. Sodium and potassium were determined by atomic absorption spectrometry with an Agilent AA 240 FS spectrometer, and *ultratrace elements* were determined by ICP-MS (Finnigan Mat SOLA).

A*nions* were analyzed by ion chromatography (Dionex ICS-2000).

Fe(II)/Fe(III) ratio was determined by UV-Vis spectrophotometry with the ferrozine method after acidification of the samples to pH <1 with HCl. Spectrometric determination of the Fe(II)-ferrozine complex was performed on separated aliquots before and after reduction step with hydroxylamine. Fe (III) was obtained from the difference between total Fe and Fe(II).

The NPOC (non-purgable organic carbon) which refers to organic carbon present in a non-volatile form was analysed with a TOC-V$_{CSH}$ analyzer (Shimadzu Scientific Instruments, Kyoto, Japan). Samples were acidified with HCl 2 M and sparged with synthetic compressed air (99.999% purity) to remove inorganic carbon. The samples were then injected into a reaction chamber heated at 720⁰C packed with platinum catalyst. The CO_2 formed was transported to the detector by a carrier gas stream (high-purity oxygen) and measured directly by a non-dispersive infra-red (NDIR) gas analysis system. The water samples were filtered through 0.45 □m syringe filters, except those for pH and EC measurements.

2.4.3   Gas analyses

The gas samples were taken inside gas cylinders of 50 cm^3 for analysis and inside Al-gas/water sampling bags (SuperTM–Inert Foil Gas sampling bags, 1 L). The total pressure of the sampling lines was measured with a high precision digital manometer Keller LEX-1. The samples were sent to Hydroisotop Gmbh laboratory (Germany), where the gas composition was determined via gas chromatography (GC), by using various detectors: GC-TCD detector for He, H_2, O_2, N_2, Ar, and CO_2; and GC-FID detector for methane, ethane, i-butane, n-butane, ethane and propene.

2.4.4   Mass loss and corrosion rates estimations

To calculate the average corrosion rate of the specimens, the mass loss concept was applied.

All metal discs were weighed (initial mass) and measured with a digital caliper (diameter and thickness) prior to assembly. After dismantling, the metal discs were cleaned with the same procedure used for cleaning the specimens prior to installation (section 2.2.1.3), following ASTM recommendations (ASTM, 2011). After cleaning the metal disc were reweighed. This procedure was repeated until the masses from successive cleaning steps, measured with two different high precision balances (average final mass), were the same.

The mass loss due to corrosion of the metal coupons was calculated by difference between the initial mass and the average final mass. The density considered for Cu-OFP and C-steel samples was determined with a high precision density kit adapted to a AX224 Sartorius high precision balance. The measured average densities were 9.2 ± 0.1 g/cm^3 for Cu-OFP and 8.2 ± 0.2 g/cm^3 for the C-steel sample.

2.4.5   X-ray diffraction (XRD)

XRD patterns were obtained from random powders in order to identify the mineralogical species. The powders were analysed with a Philips X'Pert –PRO MPD diffractometer, using an anticathode Cu-Kα at

EURAD (Deliverable n° 15.12) – Identification on the effect of transient processes on corrosion
Dissemination level: Public
Date of issue of this report: **29/04/2024**

Page 41

45 kV and 40 mA, equipped with a fixed divergence slit (0.1245º size), Scientific X´celerator detector. The samples were investigated from 2º to 70º 2θ with a step size 0.017º 2θ, and a scan rate of 50 s per step for the powder samples. The XRD database used for mineral identification has been the Power Diffraction File from the International Center for Diffraction Data (ICDD).

2.4.6   Fourier transform IR spectra (FT-IR)

To detect structural changes, Fourier transform IR (FT-IR) spectra were obtained on powder samples by transmission in the mid-IR region (4000-400 cm^{-1}), using a Nicolet iS50 with a DTGS KBr detector (resolution 4 cm^{-1}, 32 scans) in an atmosphere continuously purged from water and atmospheric CO_2. Two milligrams of powder air-dried samples were dispersed in 200 mg of KBr and pressed to a clear disc. The pressed samples were analysed at room temperature after heating in an oven overnight at 110 ºC. The spectra were examined in the OH stretching region (3400-3800 cm^{-1}) and the region below 1200 cm^{-1}, where intense Si-O absorptions and OH bending bands are present (Kloprogge, 2005; Madejová and Komadel, 2001; Van der Marel and Beutelspacher, 1976; Farmer, 1974). The spectral analysis interpretation was performed with the Thermo Scientific™ OMNIC™ Spectra Software.

2.4.7   Thermal analysis (TG-DSC)

Thermal Analysis (TG/DSC) of the samples was performed in a Setaram Themys equipment at a heating rate of 10 ºC/min and under a dynamic argon atmosphere (20 mL/min) at temperatures between 20 ºC and 1100 ºC (Mackenzie, 1957).

2.4.8   Scanning electron microscopy (SEM).

A JEOL 6400 JSM scanning electron microscope coupled to a X LINK LZ_5 energy dispersive X-ray energy spectrometer (XEDS), which allows for the qualitative analysis of light elements from boron (resolution of 133 eV), was used to define the microstructural morphology of clay minerals, possible alteration products and accessory minerals. Most of the clay samples were dried at 40-60 □C in an oven overnight, and then subjected to a gold metallization by applying 5·10^{-2} Torr vacuum and a gold coating of 300 to 400 Å thickness, using a BALZERS SCD 004 sputter coater for the scanning electron microscopy analysis. The calculation of the structural formula for smectites from the chemical composition analysed by XEDS was based on the assumption of tetrahedral occupation by 4.0 cations ($^{IV}Si+^{VI}Al$) and complete oxygen/hydroxyl framework of $O_{10}(OH)_2$, resulting in 22 negative anionic charges per half unit cell (p.h.u.c.) according to Newman (1987).

EURAD (Deliverable n° 15.12) – Identification on the effect of transient processes on corrosion
Dissemination level: Public
Date of issue of this report: **29/04/2024**

Page 42

2.5   CIEMAT results

2.5.1   Analysis of in situ samples from ABM5 experiment (Sweden)

Geochemical modifications of different bentonites (Asha 505, FEBEX, Rokle, IBECO and MX-80) used as engineered barriers were studied in the ABM5 experiment. Detailed results can be found in Fernández et al. (2022).

The main change observed in all bentonites is the modification of exchangeable cation composition, explained on the basis of equilibration with Äspö saline groundwater enriched with Ca and Na salts. Calcium bentonites (FEBEX, Rokle, IBECO) increased their sodium content, and sodium bentonites (Asha 505, MX-80) increased their calcium content. Exchangeable magnesium decreased in all the samples, except in MX-80 block 1 located at the bottom of the column. The variation of the type of exchangeable cations in all bentonites seems to indicate that concentration tends to equilibrium with groundwater/pore water and to be homogeneous in the whole bentonite column, with predominance of bivalent cations at exchange sites.

Cation exchange variations and/or salinity of the pore waters may explain the decrease of the external surface area values observed in all samples. However swelling capacity is not affected due to total surface area data is not modified.

A decrease on CEC values is observed towards heating surface, which may be related to the high salinity of the pore water, a modification of the crystal structure of the smectite clay particles, increasing the layer charge, and the drying. These factors are driven by temperature, water vapor fluxes and water saturation.

In spite of available and increased magnesium content in the pore water, no other additional magnesium-bearing mineral phases and/or trioctahedral smectites were detected, as found in ABM1 and ABM2 experiment. Furthermore, transformation of montmorillonite to illite is discarded, probably due to the potassium low concentrations both in pore waters and exchange sites.

Fe increased as a function of the distance to heater contact. Heater corrosion provoked the increase of iron in the bentonite, and goethite, hematite and siderite were found as corrosion products. No magnetite was detected. Although the ratio of ferrous to ferric iron increased in the close vicinity of the C-steel heater, major Fe content is as Fe(III). No indications of Fe-montmorillonite have been detected (*Table 12*).

The initial bentonite pore water was modified in all bentonite blocks after their interaction with the saline Na-Ca-Cl groundwater. Pore waters changed from mainly an initial Na-Cl or Na-SO$_4$ water type towards a Na-Ca-Cl pore water in all bentonite blocks analysed, except for MX-80 block 1, which changes from Na-SO$_4$ to Na-Cl water-type. Probably water-vapour fluxes increased the salinity of the pore waters at the top part of the package, since the final ionic strength (0.82-0.91 M) are similar in the upper bentonite blocks (Asha 505, FEBEX, Rokle) but lower at the bottom part of the package (IBECO and MX-80), with values of 0.69 and 0.26 M, respectively. Pore water chemistry of bentonites evolved as a function of the diffusive transport of the saline infiltrating groundwater (anions being affected by anion exclusion), the chemical equilibrium of cations at exchange sites and mineral dissolution/precipitation processes. These reactions are in turn dependent on temperature and water vapour fluxes. All bentonites preserved their hydro-geochemical properties, after being subjected to saline groundwater infiltration, heating and interaction with corroding metals during 4.4 years of experiment.

EURAD (Deliverable n° 15.12) – Identification on the effect of transient processes on corrosion
Dissemination level: Public
Date of issue of this report: **29/04/2024**

Page 43

Table 12 – Mineral phases detected in the bentonite samples from ABM5 in-situ experiment(by XRD, FTIR and SEM) (Fernández et al., 2022).

Type of mineral phases	Mineral phases	Original Samples	Granite contact	Medium part	Heater contact
Fe-oxyhydroxides	Goethite (weak FM) (Gth)	Asha 505 Rokle	Asha B28 Rokle B14	Asha B28 Febex B25 Rokle B14 MX-80 B1	Asha B28 Febex B25 Rokle B14 MX-80 B1
	Hematite (AFM) (Hem)	Asha 505 MX-80	Asha B28 MX-80 B1	Asha B28 MX-80 B1	Asha B28 Rokle B14 MX-80 B1
	Magnetite (FM) (Mag)	NO	NO	NO	NO
	Titanomagnetite (Tmag)	NO	NO	NO	NO
	Maghemite (FM) (Mgh)	NO	NO	NO	NO
	Ferrihydrite (Fhy)	NO	NO	NO	NO
Carbonates	Calcite (Cal)	All	All	All	All
	Monohydrocalcite (MhCal)	NO	NO	NO	MX-80 B1
	Dolomite (Dol)	Rokle	Rokle B14	Rokle B14	Rokle B14
	Magnesite (Mgs)	NO	NO	NO	NO
	Siderite (Sd)	Rokle MX-80	Rokle B14 MX-80 B1	Febex B25 Rokle B14 MX-80 B1	Febex B25 Rokle B14 MX-80 B1
Sulfides	Pyrrhotite (Pyh)	NO	NO	NO	NO
	Mackinawite (Mkw)	NO	NO	NO	NO
	Pyrite (Py)	MX-80	MX-80 B1	Asha B28 Rokle B14 MX-80 B1	Asha B28 Rokle B14 MX-80 B1
	Sphalerite (Sp)	NO	NO	NO	MX-80 B1
Sulfates	Gypsum (Gp)	MX-80	MX-80 B1	Asha B28 MX-80 B1	Asha B28 MX-80 B1
	Barite (Ba)				Febex B25 Rokle B14
Silica oxides	Quartz (Qz)	All	All	All	All
	Cristobalite (Crs)	All	All	All	All
	Tridymite (Trd)				Rokle B14
Feldspars	K-felspars (KFs)	All	All	All	All
	Plagioclases (Pl)	All	All	All	All
Titanium oxides	Anatase (Ant)	Rokle	Rokle B14	Asha B28 Rokle B14	Rokle B14
Mg-hydroxides	Brucite (Brc)	No	No	No	No
Zeolites	Clinoptilolite (Cpt)	No	No	Asha B28	Asha B28
Smectites	Montmorillonite (Mnt)	All	All	All	All
	Saponite (Sap)	No	No	No	No
Illite/Muscovite	Illite (Ilt)/Muscovite (Ms)	Febex B25 Rokle MX-80	Febex B25 Rokle B14 MX-80 B1	Febex B25 Rokle B14 MX-80 B1	Febex B25 Rokle B14 MX-80 B1
Kaolinites	Kaolinite (Kln)	Asha 505 Rokle	Asha B28 Rokle B14	Asha B28 Rokle B14	Asha B28 Rokle B14
Chlorites	Clinochlore(Clc)/ Chamosite (Chm)	No	No	No	No

![eurad logo] European Joint Programme on Radioactive Waste Management

EURAD (Deliverable n° 15.12) – Identification on the effect of transient processes on corrosion
Dissemination level: Public
Date of issue of this report: **29/04/2024**

Page 44

2.5.2 Dynamic experiments: infiltration tests

Eight water infiltration experiments are still running with Cu and C-steel coupons embedded in compacted bentonite at two dry densities (1.4 and 1.65 g/cm^3), by using both saline pore water and granitic groundwater as saturating waters. The degree of water saturation of the bentonite depends on time, suction capacity and the dry density of the bentonite, being higher for a lower dry density of 1.4 g/cm^3. *Figure 14*a and *Figure 14*b show the advance of the saturation front through the bentonite compacted at 1.4 and 1.65 g/cm^3, respectively, from the bottom to the top of the cell at the beginning of the experiment, being higher at 1.4 g/cm^3, so more water could be collected during the experiment at this dry density.

During the 173 days of the experiment (up to date), water aliquots could be sampled inside septum vials from the compacted samples at 1.4 g/cm^3: five times after 57, 111, 119, 127, and 139 days. Some water could be observed in septum vials from bentonite compacted at 1.65 g/cm^3 after 119 days. The volumes extracted ranged from drops to 13 mL. The amount of water collected can be seen in *Table 13*. The water is being chemically analysed. These tests are still running due to the long time needed for the saturation of the compacted bentonite. The dismantling of the cells at 1.4 g/cm^3 is scheduled for April 2024. The cells compacted at 1.65 g/cm^3 will be dismantled in 2025 for a long interaction time of the bentonite pore water with metals.

Information about a test performed at a dry density of 1.65 g/cm^3, without any coupon and using granitic water for saturation is available. Outcoming water at the opposite side was collected and chemically analysed over time. Since a complete chemical analysis can be only performed from 2 mL aliquots, the water expelled by each cell was recovered inside a septum vial. When at least 2 mL of water were obtained, a chemical analysis was carried out (*Table 13*). The permeability of the bentonite during each infiltration test at different dry densities is calculated by the Darcy´s law. As can be seen at the initial states of the experiment, the flow of water that passed through the bentonite column, Q, was very low. However, the water flow increased over time, which can be also observed by the change of the permeability or hydraulic conductivity value, which approaches with time to the reference FEBEX permeability value (*Figure 15*).

Figure 14 – Detail of the degree of saturation of the bentonite: a) compacted at 1.4 g/cm^3, and b) compacted at 1.65 g/cm^3.

EURAD (Deliverable n° 15.12) – Identification on the effect of transient processes on corrosion
Dissemination level: Public
Date of issue of this report: **29/04/2024**

Page 45

Table 13 – Data obtained from the analysis of infiltration cells performed with FEBEX bentonite compacted at two dry densities (1.4 and 1.65 g/cm^3) at oxic/anoxic conditions using coupons of Nagra carbon steel and SKB Cu-OFP.

Date	Dry density	Coupon	Infiltrating water	Collected water (mL)
15/12/2023 (57 days)	1.4 g/cm^3	Nagra Carbon steel	Granitic	5
	1.4 g/cm^3	Nagra Carbon steel	PW-1.4	4.5
	1.4 g/cm^3	Cu-OFP	Granitic	4
	1.4 g/cm^3	Cu-OFP	PW-1.4	2
7/2/2024 (111 days)	1.4 g/cm^3	Nagra Carbon steel	Granitic	6
15/2/2024 (119 days)	1.4 g/cm^3	Nagra Carbon steel	Granitic	5.5
	1.4 g/cm^3	Nagra Carbon steel	PW-1.4	3.8
	1.4 g/cm^3	Cu-OFP	Granitic	3
	1.4 g/cm^3	Cu-OFP	PW-1.4	--
	1.65 g/cm^3	Nagra Carbon steel	Granitic	1
	1.65 g/cm^3	Nagra Carbon steel	PW-1.4	1
	1.65 g/cm^3	Cu-OFP	Granitic	drops
	1.65 g/cm^3	Cu-OFP	PW-1.4	1
23/2/2024 (156 days)	1.4 g/cm^3	Nagra Carbon steel	Granitic	5
	1.4 g/cm^3	Nagra Carbon steel	PW-1.4	2
	1.4 g/cm^3	Cu-OFP	Granitic	1.8
	1.4 g/cm^3	Cu-OFP	PW-1.4	1.8
	1.65 g/cm^3	Nagra Carbon steel	Granitic	1
	1.65 g/cm^3	Nagra Carbon steel	PW-1.4	1.8
	1.65 g/cm^3	Cu-OFP	Granitic	--
	1.65 g/cm^3	Cu-OFP	PW-1.4	1
6/3/2024 (167 days)	1.4 g/cm^3	Nagra Carbon steel	Granitic	9.8
	1.4 g/cm^3	Nagra Carbon steel	PW-1.4	4
	1.4 g/cm^3	Cu-OFP	Granitic	3
	1.4 g/cm^3	Cu-OFP	PW-1.4	2
	1.65 g/cm^3	Nagra Carbon steel	Granitic	1.2
	1.65 g/cm^3	Nagra Carbon steel	PW-1.4	2
	1.65 g/cm^3	Cu-OFP	Granitic	0.8
	1.65 g/cm^3	Cu-OFP	PW-1.4	--
3/4/2024 (167 days)	1.4 g/cm^3	Nagra Carbon steel	Granitic	13.5
	1.4 g/cm^3	Nagra Carbon steel	PW-1.4	5
	1.4 g/cm^3	Cu-OFP	Granitic	4.2
	1.4 g/cm^3	Cu-OFP	PW-1.4	3
	1.65 g/cm^3	Nagra Carbon steel	Granitic	2
	1.65 g/cm^3	Nagra Carbon steel	PW-1.4	2.2
	1.65 g/cm^3	Cu-OFP	Granitic	1
	1.65 g/cm^3	Cu-OFP	PW-1.4	--

EURAD (Deliverable n° 15.12) – Identification on the effect of transient processes on corrosion
Dissemination level: Public
Date of issue of this report: **29/04/2024**

Page 46
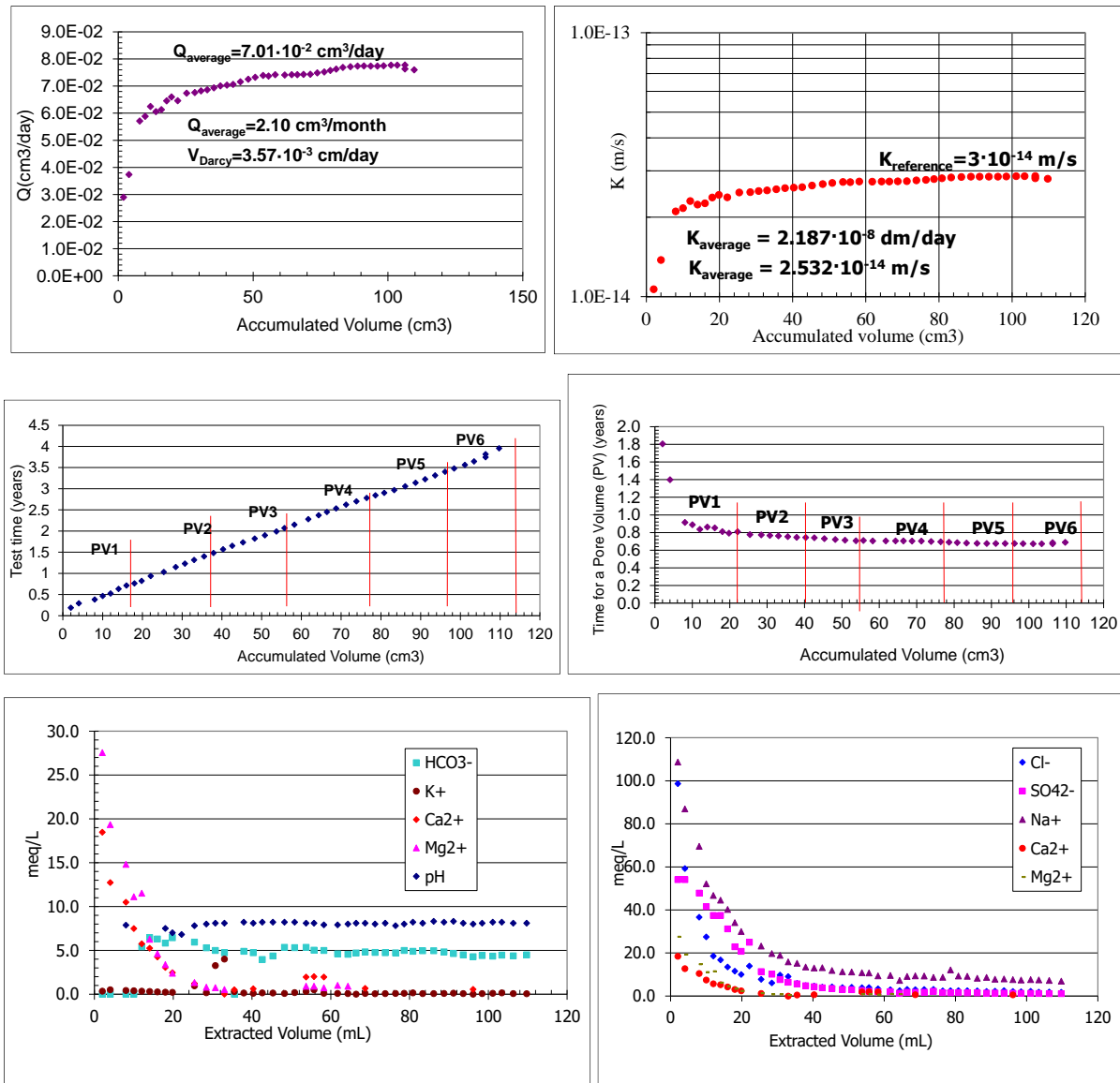
Figure 15 – Results from infiltration cells in dynamic experiments: bentonite compacted at a dry density of 1.65 g/cm³ without any coupon and hydrated with granitic water.

2.5.3 Dynamic experiments: convective water-vapour fluxes tests

Corrosion experiments with compacted bentonite at 1.4 g/cm³ and 1.6 g/cm³ were performed under relative humidity of 95-100% at 80 ºC. The samples were introduced inside a desiccator filled with distilled water, and close at vacuum. Then, they were maintained thermostated at 353.15 K in an oven (*Figure 10*). Three types of bentonites were used in these experiments: FEBEX, SWy-3 and Czech bentonites, as well as three types of metal coupons: Reference carbon steel from Nagra, Reference copper from SKB and Reference carbon steel from SURAO. Experiments were performed with compacted materials at two dry densities: 1.4 g/cm³ and 1.6 g/cm³.

The initial conditions are shown in *Table 9* and *Table 10*. The samples were subjected to convective water-vapour fluxes at a temperature of 80 ºC, simulating the conditions at the bentonite/canister interface.

The duration of the tests performed with carbon steel coupons was 286 days, when some cells were dismantled. The duration of the tests performed with SKB Cu-OPF coupons was 326 days, when some

EURAD (Deliverable n° 15.12) – Identification on the effect of transient processes on corrosion
Dissemination level: Public
Date of issue of this report: **29/04/2024**

Page 47

cells were dismantled. The bentonites and metal coupons were analysed by XRD, FTIR, TG-DSC, Raman and SEM techniques.

2.5.3.1 Cells with C-steel coupons

After 286 days of experiment, all the bentonite samples were completely saturated. Some photographs from the dismantling are shown from *Figure 16* to *Figure 21*. The metal coupons present a degree of corrosion, being higher when the dry density of the bentonite is lower due to the higher O_2 diffusivity through the pore space (initial porosity of 48.5 and 41.2% for dry densities of 1.4 and 1.6 g/cm^3, respectively). After dismantling, the corrosion rate measured is shown in *Table 14*. The highest degree of corrosion was observed in the Nagra C-steel interacting with FEBEX bentonite compacted at 1.4 g/cm^3 (*Figure 22*, *Figure 23*), probably due to the high salinity of the FEBEX pore water, which is higher with respect the other bentonites. However, the extent of alteration inside the bentonite was < 2 mm in all bentonite samples (*Figure 16*), showing an increase of iron content.

Table 14 – Corrosion rate observed in the metal carbon steel coupons (Nagra: C-steel; Czech: Czech)

Sample	Material	Dry density (g/cm^3)	Initial weight (g)	Thickness (mm)	Diameter (mm)	Coupon density (cm^3)	Final weight (g)	Mass Loss (g)	Loss (µm)	Contact time (days)	Corrosion rate (µm/year)
FEBEX	C-steel	1.4	7.7713	1.5	30.0	8.2	5.8938	1.8775	323.92	286	413
FEBEX	C-steel	1.6	7.7713	1.5	30.0	8.2	7.5163	0.2550	43.99	286	56
SWy3	C-steel	1.4	8.3138	1.5	30.0	8.2	7.9539	0.3599	62.09	286	79
SWy3	C-steel	1.6	7.7673	1.5	30.0	8.2	7.6408	0.1265	21.82	286	28
SWy3	Czech	1.4	0.5426	0.9	10.0	8.2	0.5072	0.0232	36.02	286	46
Czech	C-steel	1.4	7.7713	1.5	30.0	8.2	6.6312	1.1401	196.70	286	251

EURAD (Deliverable n° 15.12) – Identification on the effect of transient processes on corrosion
Dissemination level: Public
Date of issue of this report: **29/04/2024**

Page 48

Figure 16 – Dismantling of the FEBEX bentonite compacted at 1.4 g/cm³ with Nagra carbon steel coupon: altered bentonite and corroded corrosion is shown.

EURAD (Deliverable n° 15.12) – Identification on the effect of transient processes on corrosion
Dissemination level: Public
Date of issue of this report: **29/04/2024**

Page 49
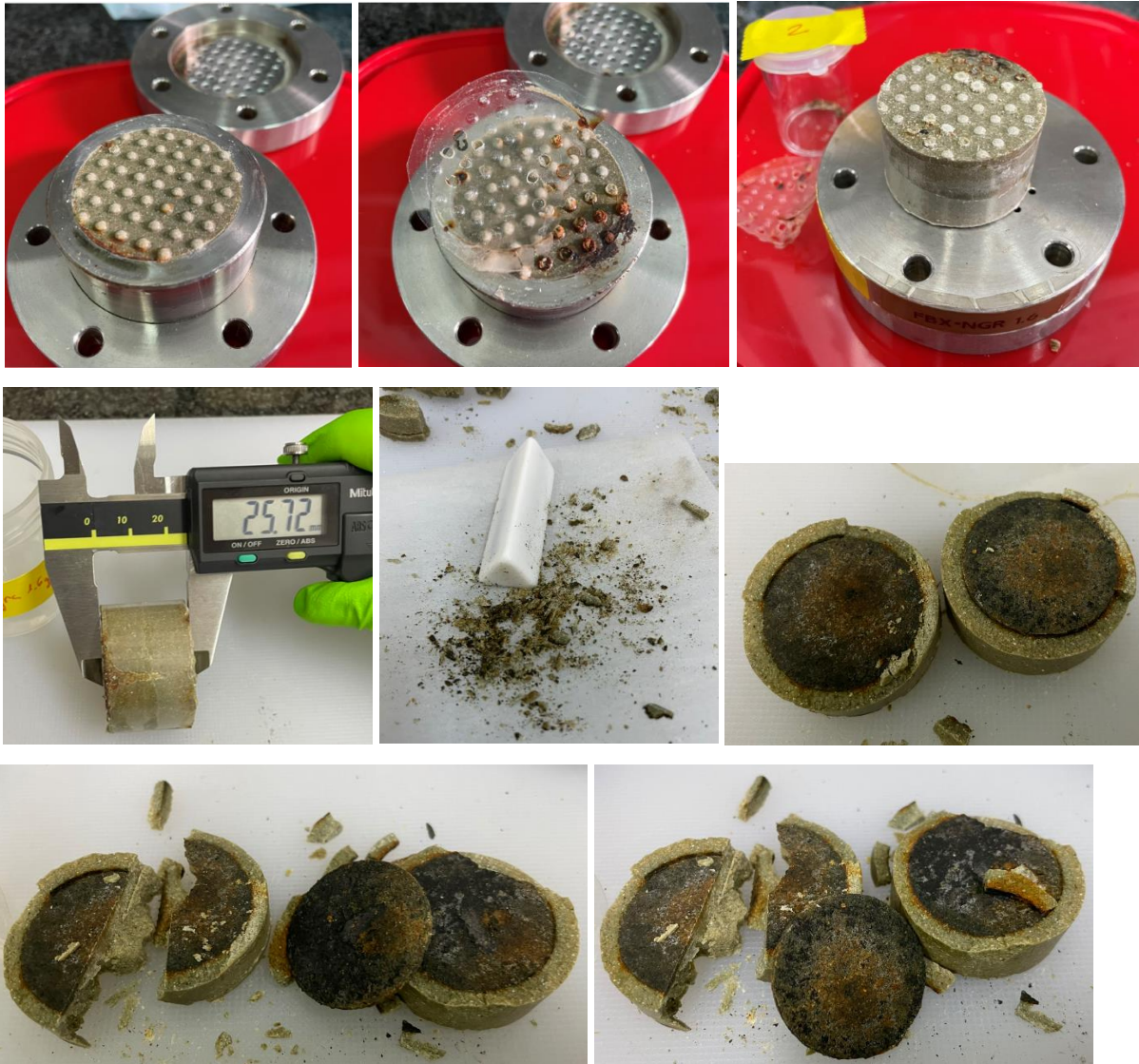
Figure 17 – Dismantling of the FEBEX bentonite compacted at 1.6 g/cm³ with Nagra carbon steel coupon showing the corroded C-steel coupon and the compacted bentonite.

EURAD (Deliverable n° 15.12) – Identification on the effect of transient processes on corrosion
Dissemination level: Public
Date of issue of this report: **29/04/2024**

Page 50

Figure 18 – Dismantling of the SWy3 bentonite compacted at 1.4 g/cm³ with Nagra carbon steel coupon showing the alteration of the bentonite and the corroded coupon.

EURAD (Deliverable n° 15.12) – Identification on the effect of transient processes on corrosion
Dissemination level: Public
Date of issue of this report: **29/04/2024**

Page 51

Figure 19 – Dismantling of the SWy3 bentonite compacted at 1.6 g/cm^3 with Nagra carbon steel coupon showing the corroded coupon and the compacted bentonite.

EURAD (Deliverable n° 15.12) – Identification on the effect of transient processes on corrosion
Dissemination level: Public
Date of issue of this report: **29/04/2024**

Page 52
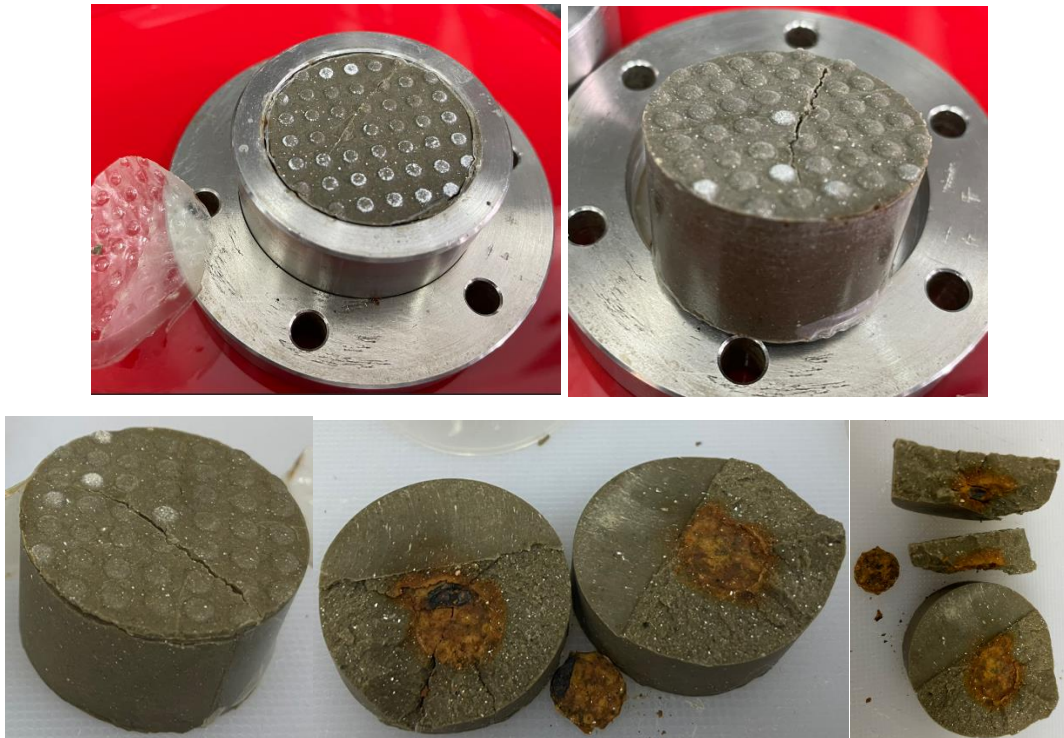
Figure 20 – Dismantling of the SWy3 bentonite compacted at 1.4 g/cm³ with Czech carbon steel coupon showing the alteration of the bentonite and the corroded coupon.

EURAD (Deliverable n° 15.12) – Identification on the effect of transient processes on corrosion
Dissemination level: Public
Date of issue of this report: **29/04/2024**

Page 53

Figure 21 – Dismantling of the Czech bentonite compacted at 1.4 g/cm3 with Nagra carbon steel coupon showing the alteration of the bentonite and the corroded coupon.

EURAD (Deliverable n° 15.12) – Identification on the effect of transient processes on corrosion
Dissemination level: Public
Date of issue of this report: **29/04/2024**

Page 54

FEBEX - 1.4 g/cm³ - Nagra (1)

FEBEX - 1.6 g/cm³ - Nagra (2)

SWy-3 - 1.4 g/cm³ - Nagra (4)

SWy-3 - 1.6 g/cm³ - Nagra (6)

Czech - 1.4 g/cm³ - Nagra (5)

SWy-3 1.4 g/cm³ - Czech (3)
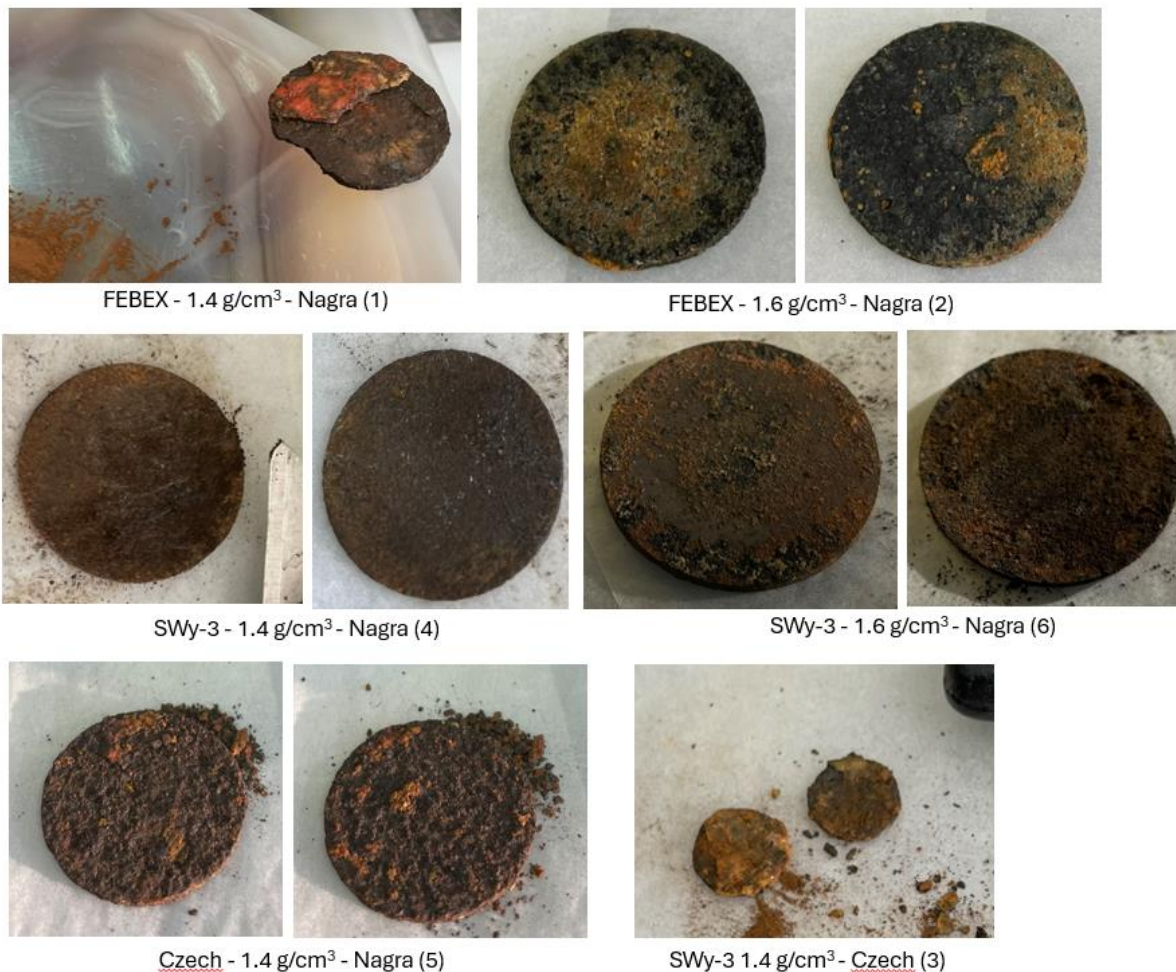
Figure 22– Visual aspect of the corroded coupons (Nagra carbon steel and Czech) after dismantling of the cells.
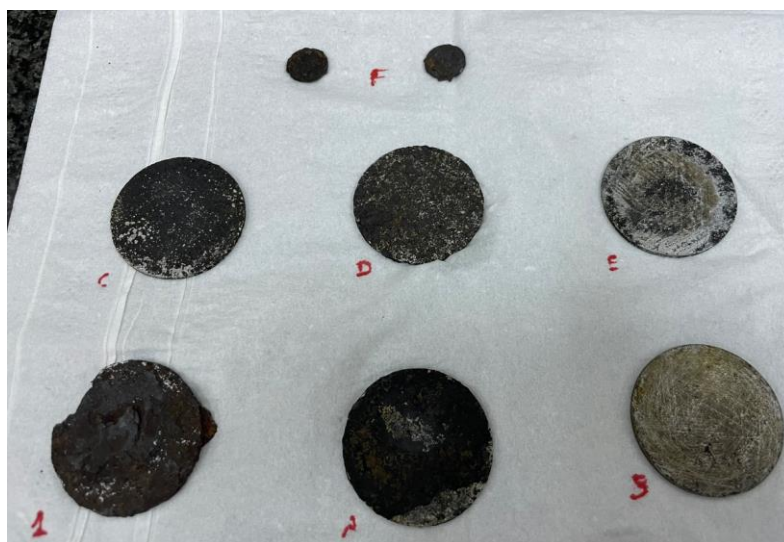
Figure 23 – Visual aspect of the corroded coupons (Nagra carbon steel and Czech) after the sixth washings prior to determining corrosion rate.

EURAD (Deliverable n° 15.12) – Identification on the effect of transient processes on corrosion
Dissemination level: Public
Date of issue of this report: **29/04/2024**

Page 55

Corrosion of coupons

The degree of corrosion of the Nagra and Czech carbon steel coupons were analysed by XRD (*Figure 24*, *Figure 27*, *Figure 29*, *Figure 31*, *Figure 33*, *Figure 36*), and SEM analyses. The highest degree of corrosion was observed in the Nagra coupon tested with FEBEX bentonite compacted at 1.4 g/cm^3, which presents the highest mass loss (*Figure 22*, *Figure 23*). The corrosion rates measured in all the coupons are shown in *Table 14*, which ranged between 28 and 413 µm/year, being lower for bentonites compacted at a higher dry density of 1.6 g/cm^3.

The main corrosion product observed in the coupons is magnetite, although there are other Fe oxy-hydroxides, such as: hematite, goethite, lepidocrocite and akaganeite. Calcite, aragonite and dolomite were the carbonates observed by XRD. Siderite was only observed by SEM. Gypsum and anhydrite were also detected. Sulfurs were only detected in SWy-3 and czech bentonites. The aspect of the Fe-oxy-hydroxides formed after corrosion of the metal coupons are shown in Figure 25, Figure 26, Figure 28, Figure 30, Figure 32 and Figure 35. In some samples, iron calcium silicates, e.g., hedenbergite type, were observed, as seen in Figure 35. This finding suggests that dissolved silica must have been available in the system (Kaufhold et al., 2020), certainly favoured by the elevated temperature.
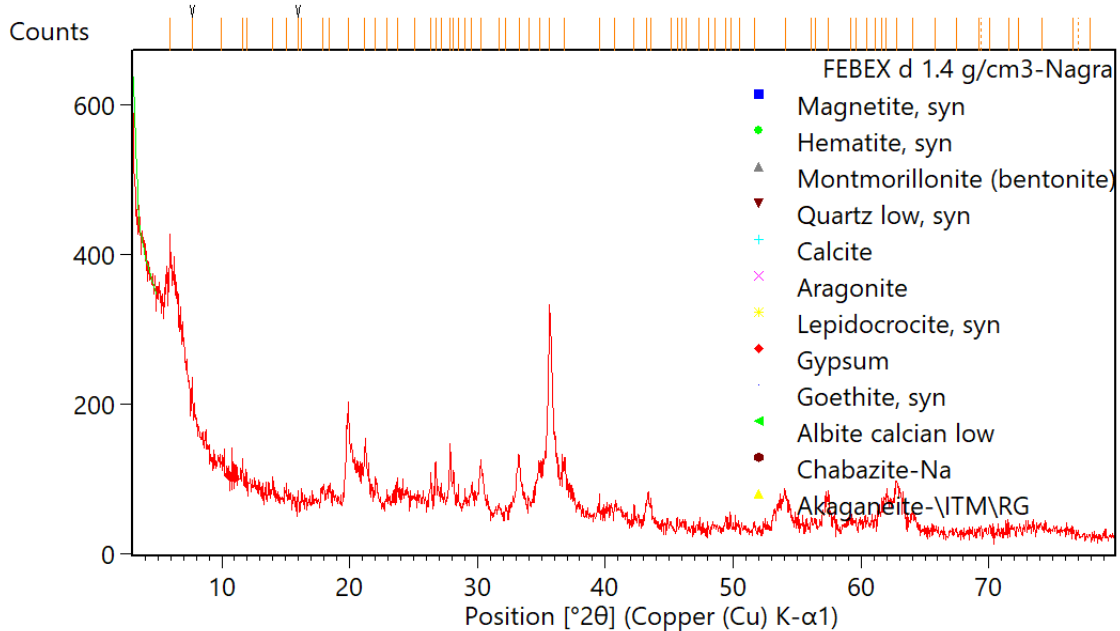
Figure 24 – XRD pattern of material attached to the Nagra carbon steel coupon in the test performed with FEBEX bentonite compacted at 1.4 g/cm^3. The main mineral phases identified are indicated.
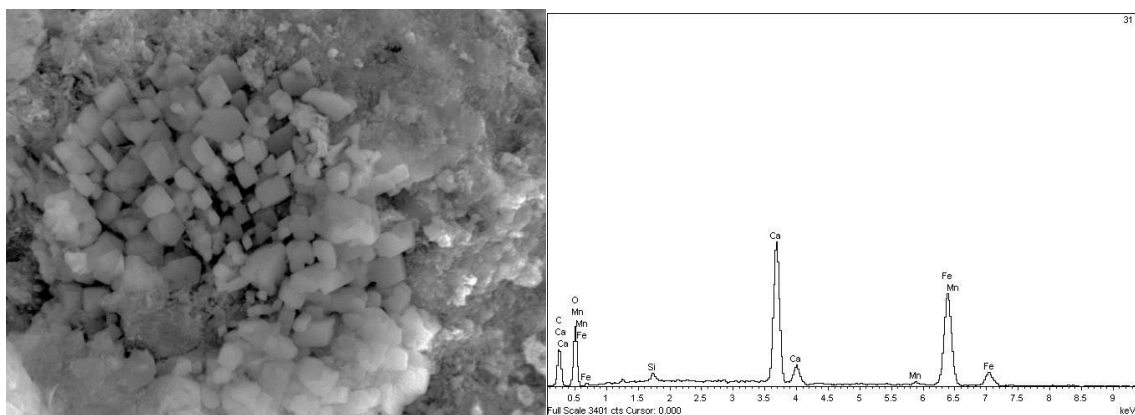
Figure 25 – SEM photomicrographs and EDX spectrum of material attached to the Nagra carbon steel coupon in the test performed with FEBEX bentonite compacted at 1.4 g/cm^3: Fe-carbonate (siderite).

EURAD (Deliverable n° 15.12) – Identification on the effect of transient processes on corrosion
Dissemination level: Public
Date of issue of this report: **29/04/2024**

Page 56
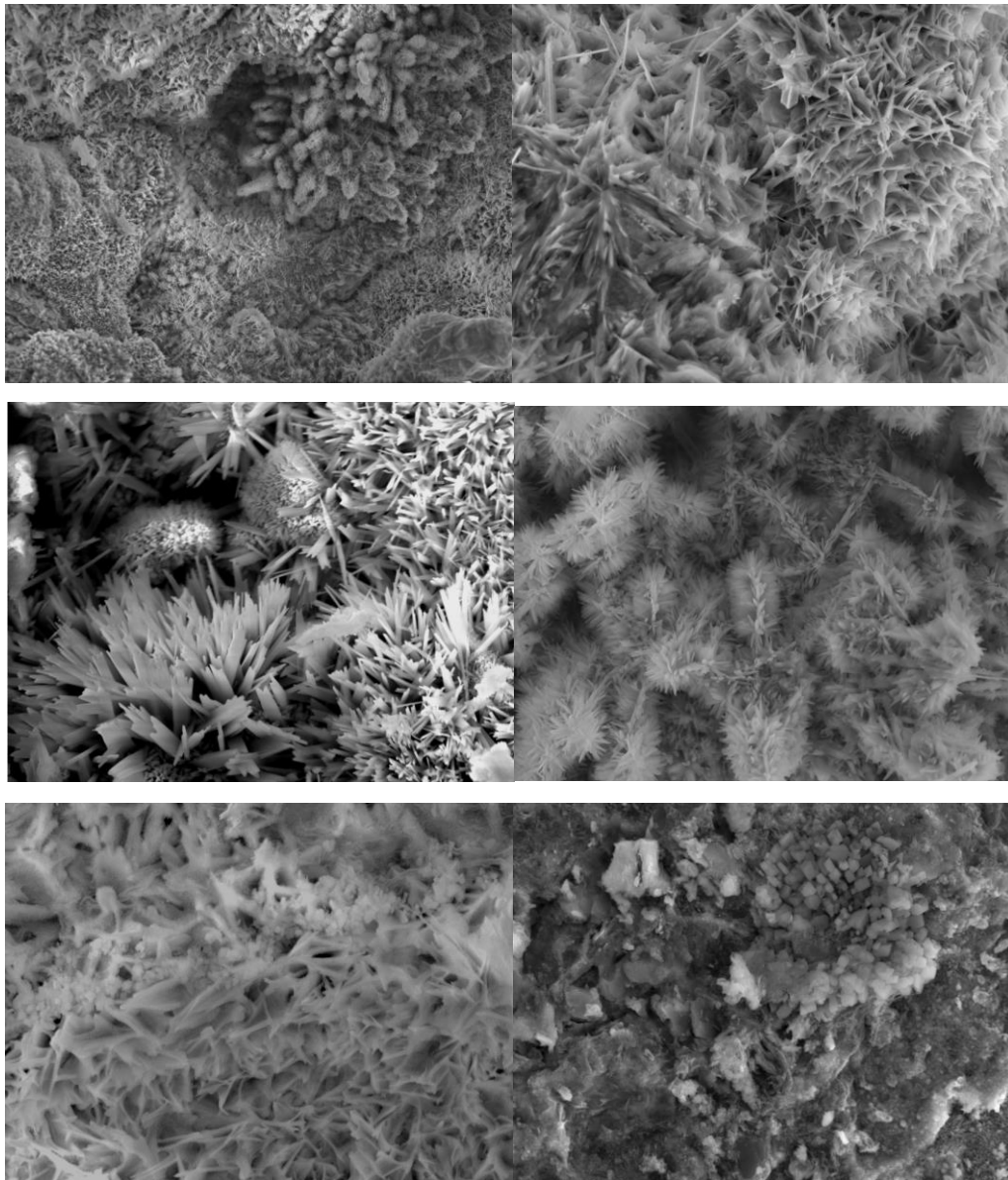
Figure 26 – SEM photomicrographs of material attached to the Nagra carbon steel coupon in the test performed with FEBEX bentonite compacted at 1.4 g/cm³: Fe-(oxy-)hydroxides.

EURAD (Deliverable n° 15.12) – Identification on the effect of transient processes on corrosion
Dissemination level: Public
Date of issue of this report: **29/04/2024**

Page 57
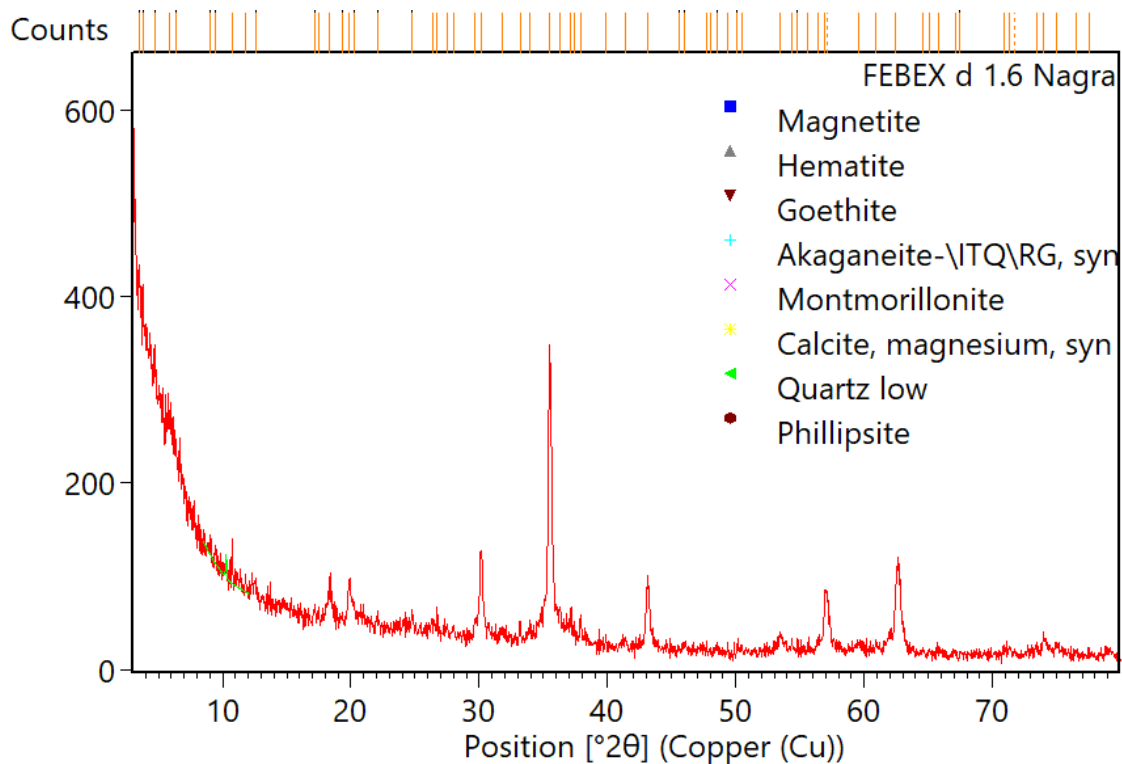
Figure 27 – XRD pattern of material attached to the Nagra carbon steel coupon in the test performed with FEBEX bentonite compacted at 1.6 g/cm³. The main mineral phases identified are indicated.
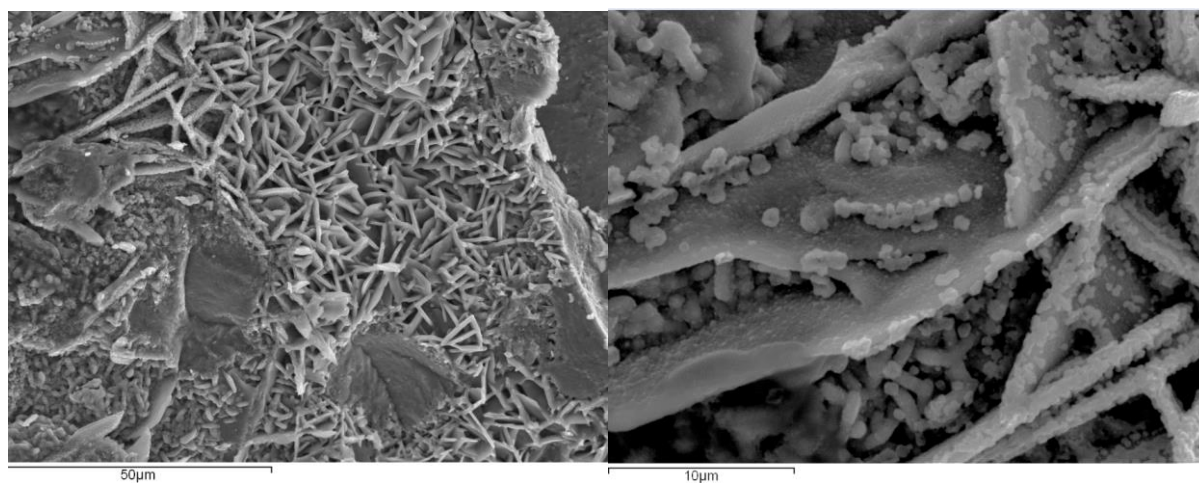
Figure 28 – SEM photomicrographs of material attached to the Nagra carbon steel coupon in the test performed with FEBEX bentonite compacted at 1.6 g/cm³: Fe-(oxy-)hydroxides.

EURAD (Deliverable n° 15.12) – Identification on the effect of transient processes on corrosion
Dissemination level: Public
Date of issue of this report: **29/04/2024**

Page 58
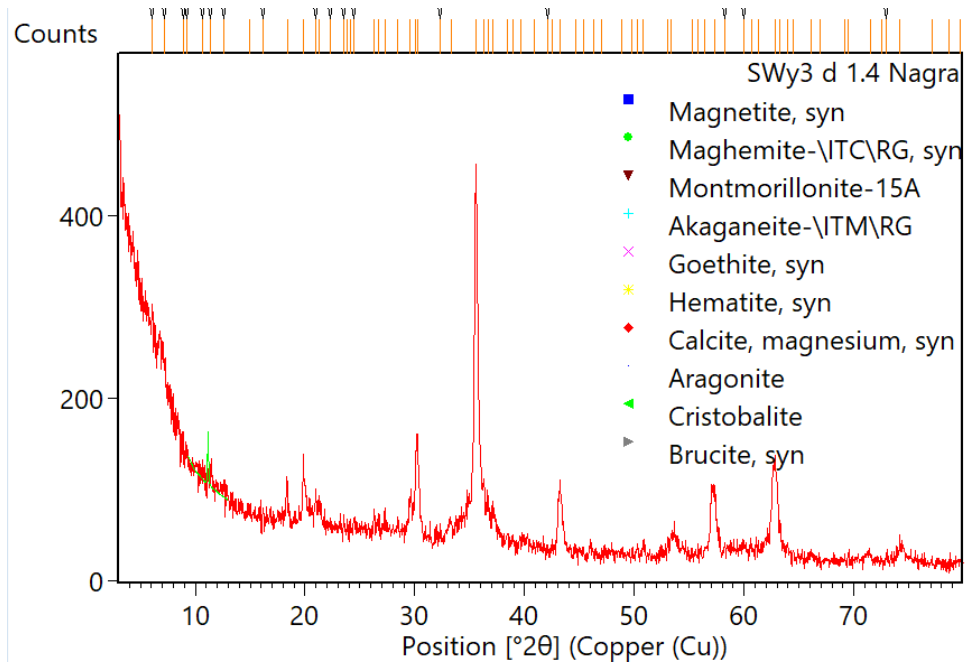
Figure 29 – XRD pattern of material attached to the Nagra carbon steel coupon in the test performed with SWy-3 bentonite compacted at 1.4 g/cm³. The main mineral phases identified are indicated.
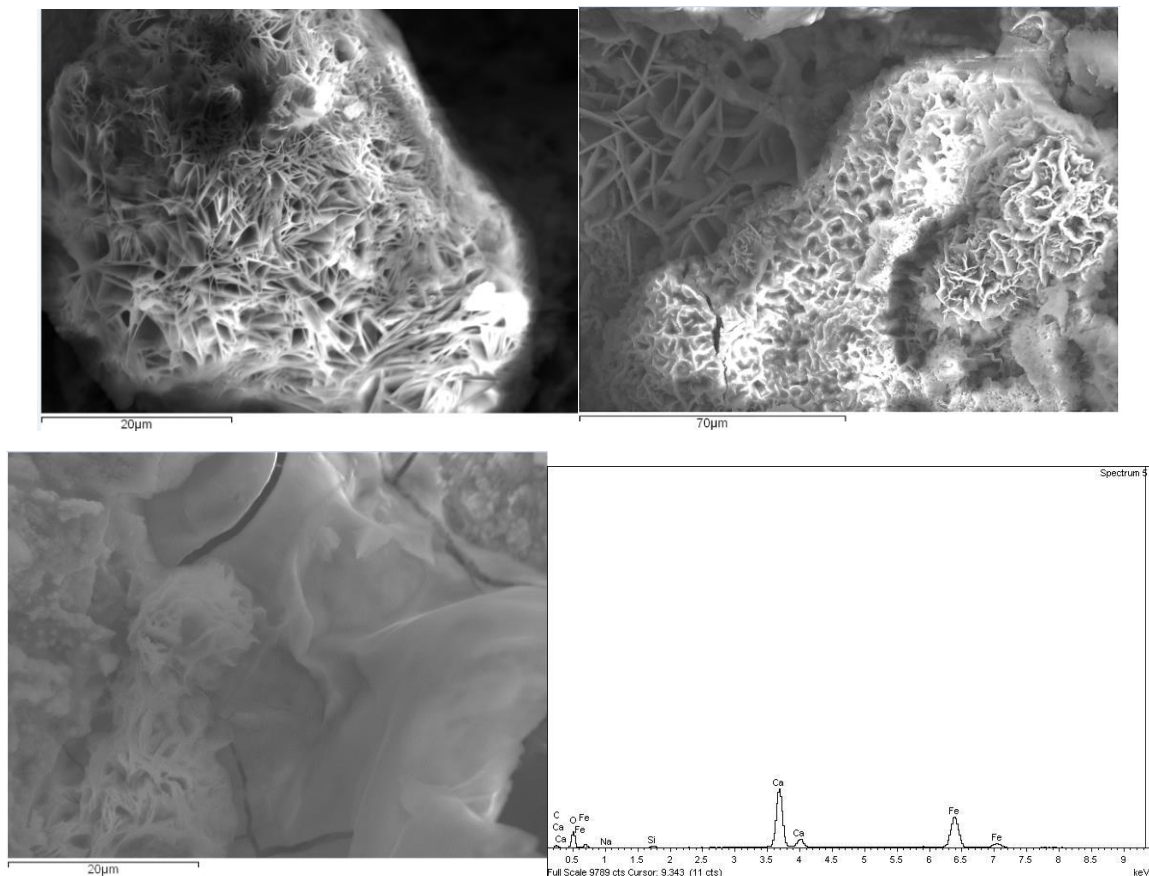
Figure 30 – SEM photomicrographs and EDX spectrum of material attached to the Nagra carbon steel coupon in the test performed with SWy-3 bentonite compacted at 1.4 g/cm³: a) Fe-oxyhydroxides, b) Fe-carbonate (siderite).

EURAD (Deliverable n° 15.12) – Identification on the effect of transient processes on corrosion
Dissemination level: Public
Date of issue of this report: 29/04/2024

Page 59
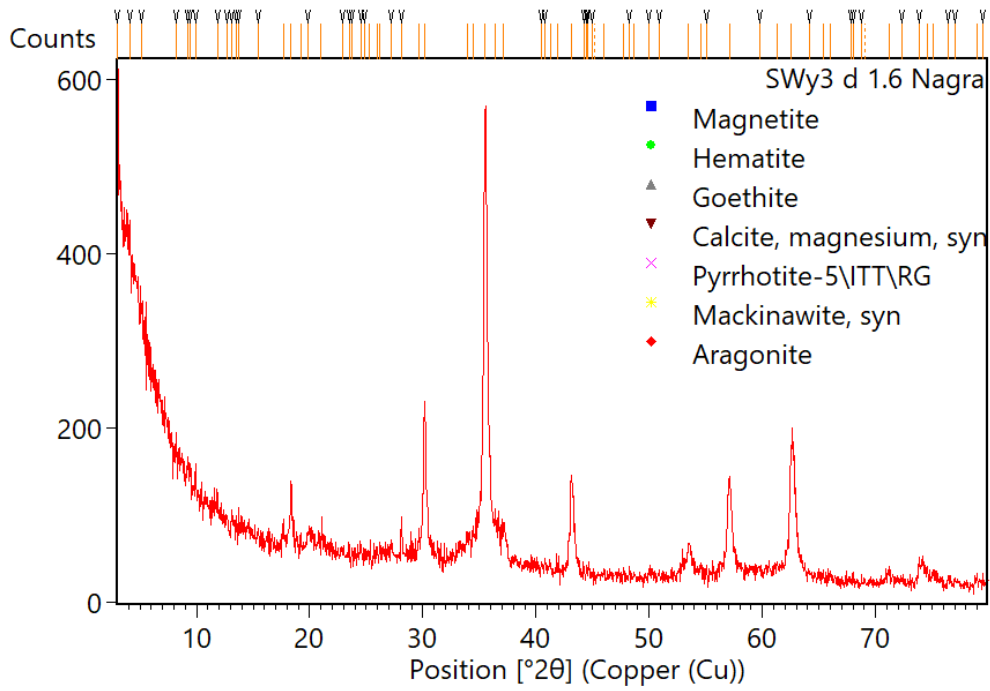
Figure 31 – XRD pattern of material attached to the Nagra carbon steel coupon in the test performed with SWy-3 bentonite compacted at 1.6 g/cm³. The main mineral phases identified are indicated.
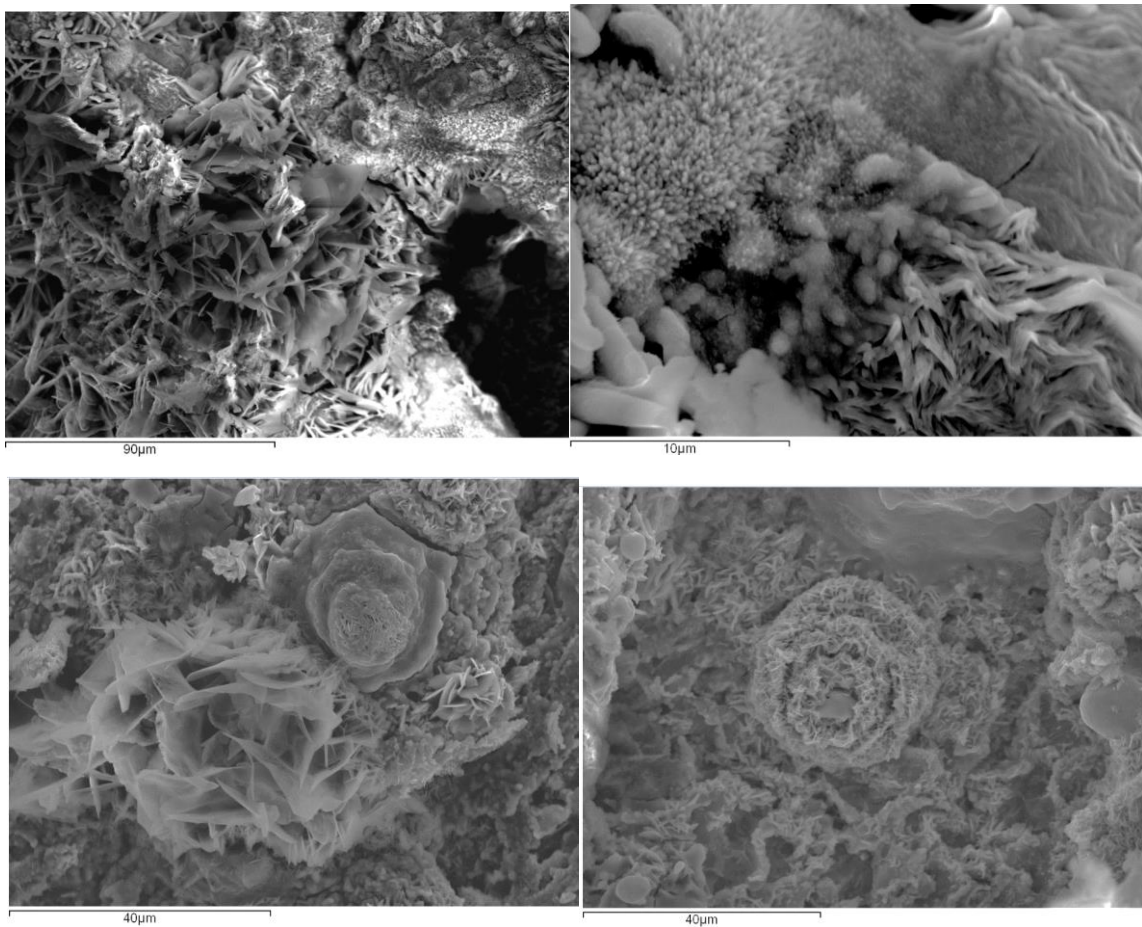
Figure 32 – SEM photomicrographs of material attached to the Nagra carbon steel coupon in the test performed with SWy-3 bentonite compacted at 1.6 g/cm³: Fe-oxyhydroxides.

EURAD (Deliverable n° 15.12) – Identification on the effect of transient processes on corrosion
Dissemination level: Public
Date of issue of this report: **29/04/2024**

Page 60
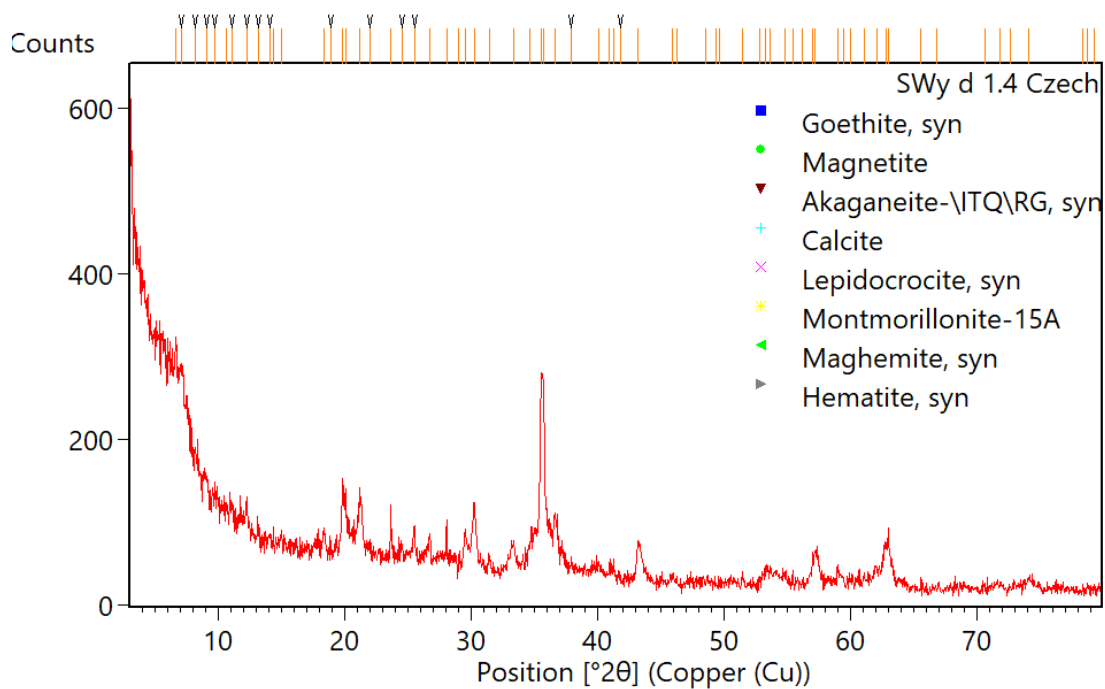
Figure 33 – XRD pattern of material attached to the Czech carbon steel coupon in the test performed with SWy-3 bentonite compacted at 1.4 g/cm³. The main mineral phases identified are indicated.
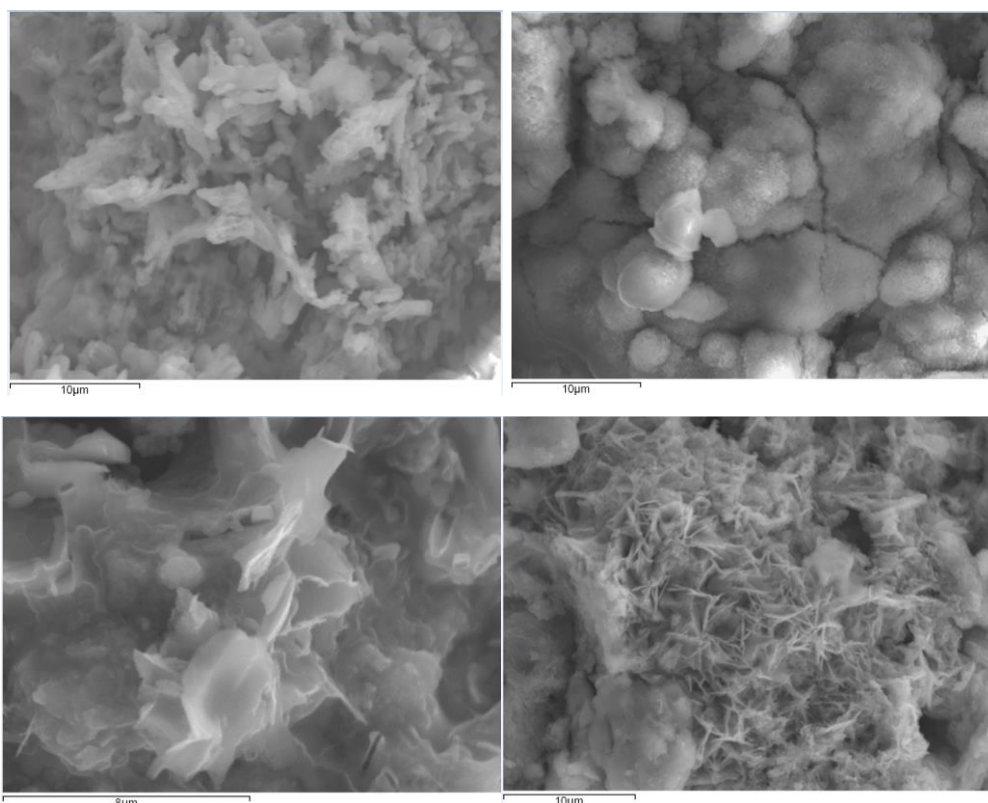
Figure 34 – SEM photomicrographs of material attached to the Czech carbon steel coupon in the test performed with SWy-3 bentonite compacted at 1.4 g/cm³: Fe-oxyhidroxides.

EURAD (Deliverable n° 15.12) – Identification on the effect of transient processes on corrosion
Dissemination level: Public
Date of issue of this report: **29/04/2024**

Page 61
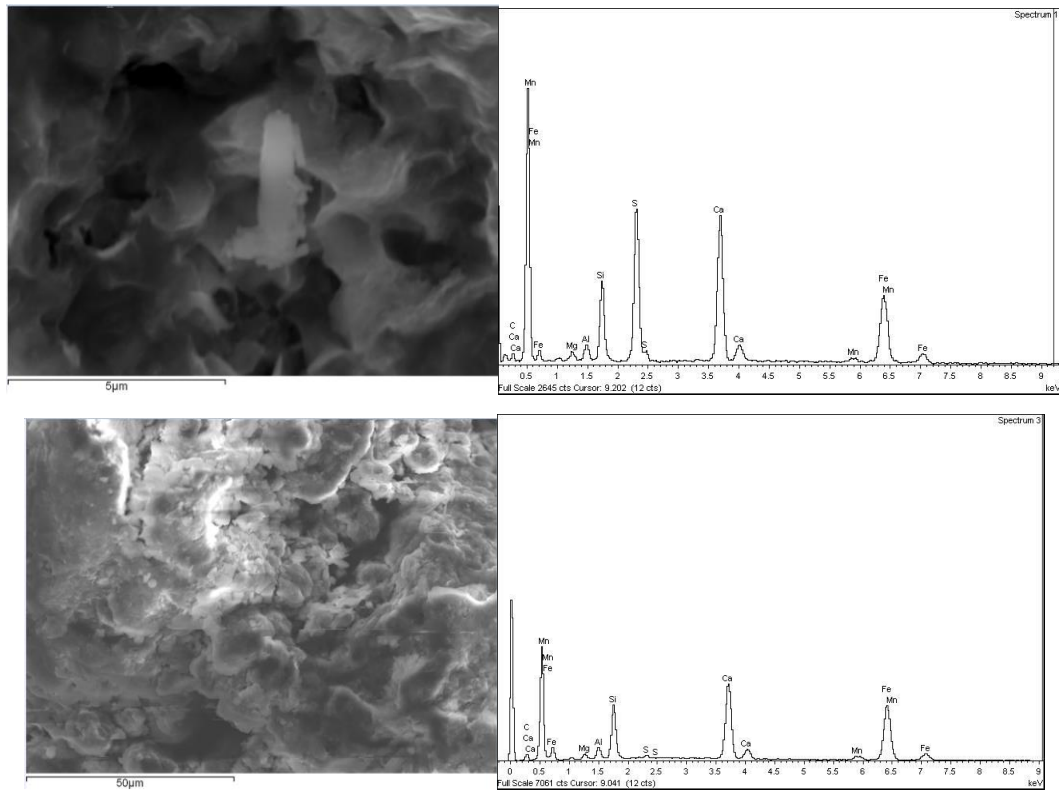
Figure 35 – SEM photomicrographs and EDX spectrum of material attached to the Czech carbon steel coupon in the test performed with SWy-3 bentonite compacted at 1.4 g/cm³: a) Ca-sulfates, b) Calcium iron silicate (Hedenbergite type).
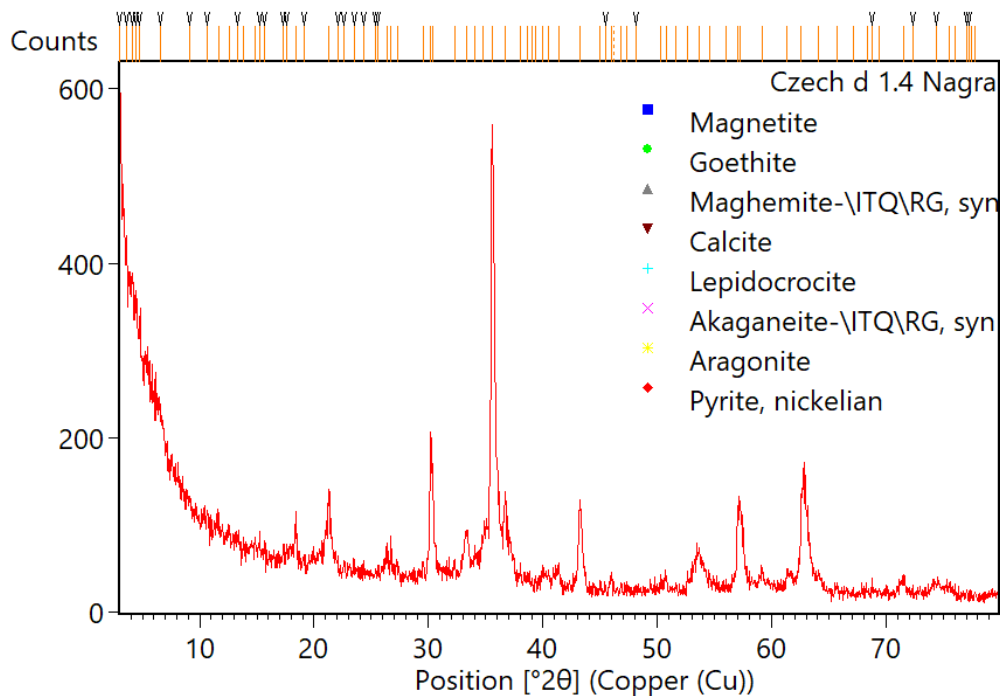
Figure 36 – XRD pattern of material attached to the Nagra carbon steel coupon in the test performed with Czech bentonite compacted at 1.4 g/cm³. The main mineral phases identified are indicated.

EURAD (Deliverable n° 15.12) – Identification on the effect of transient processes on corrosion
Dissemination level: Public
Date of issue of this report: **29/04/2024**

Page 62

Bentonite alteration

The bentonite at direct contact with the coupon was analysed by XRD (*Figure 37*), FTIR (*Figure 38* to *Figure 40*), TG-DSC (*Figure 41*), and SEM (*Figure 42* to *Figure 46*).

The extent of visual alteration inside the bentonite was < 1-2 mm, corresponding to an increase of the iron content. Most of the bentonites remains unaltered, as seen in XRD and FTIR spectra, with signals similar to the reference bentonite samples. However, the major impact of corrosion inside the bentonite is observed in samples compacted at a lower dry density of 1.4 g/cm^3, especially in FEBEX and Czech bentonites. In these samples, magnetite and goethite are observed in the XRD patterns, as well as aragonite (*Figure 37*, *Figure 38*). Aragonite is also observed in the Czech bentonite in contact with Nagra carbon steel (*Figure 40*). DSC signals show also such alterations (*Figure 41*), indicating the presence of hematite, magnetite and carbonates, and changes in the dehydroxylation peak of smectite. FEBEX at 1.4 g/cm^3 presents two peaks at 630 and 530 ºC, instead of one peak at 650 ºC. This implies an increase of trans-vacant sites, i.e., an increase of iron at octahedral sites of the smectite particles. All the bentonite samples show a band located around 1317 cm^{-1} (and at 1543 cm^{-1} at FEBEX bentonite), which is indicative of the presence of organics. By SEM analysis, Fe-oxyhydroxides and Fe-carbonates are observed in these samples (*Figure 42*, *Figure 46*). In FEBEX bentonite compacted at 1.6 g/cm^3, other mineral phases are observed, such as Cl-green rush and chlorites (*Figure 43*, *Figure 44*), as well as a double dehydroxylation peak at 500 and 638 ºC (*Figure 41*). However, the FTIR spectra do not show any alteration, this being similar to the reference FEBEX sample.

According to XRD patterns and FTIR spectra, SWy-3 bentonite is not altered in contact with the Nagra carbon steel coupon. Only at 1.4 g/cm^3, and in contact with Czech carbon steel, lepidocrocite is observed by DSC (*Figure 41*).

EURAD (Deliverable n° 15.12) – Identification on the effect of transient processes on corrosion
Dissemination level: Public
Date of issue of this report: **29/04/2024**

Page 63
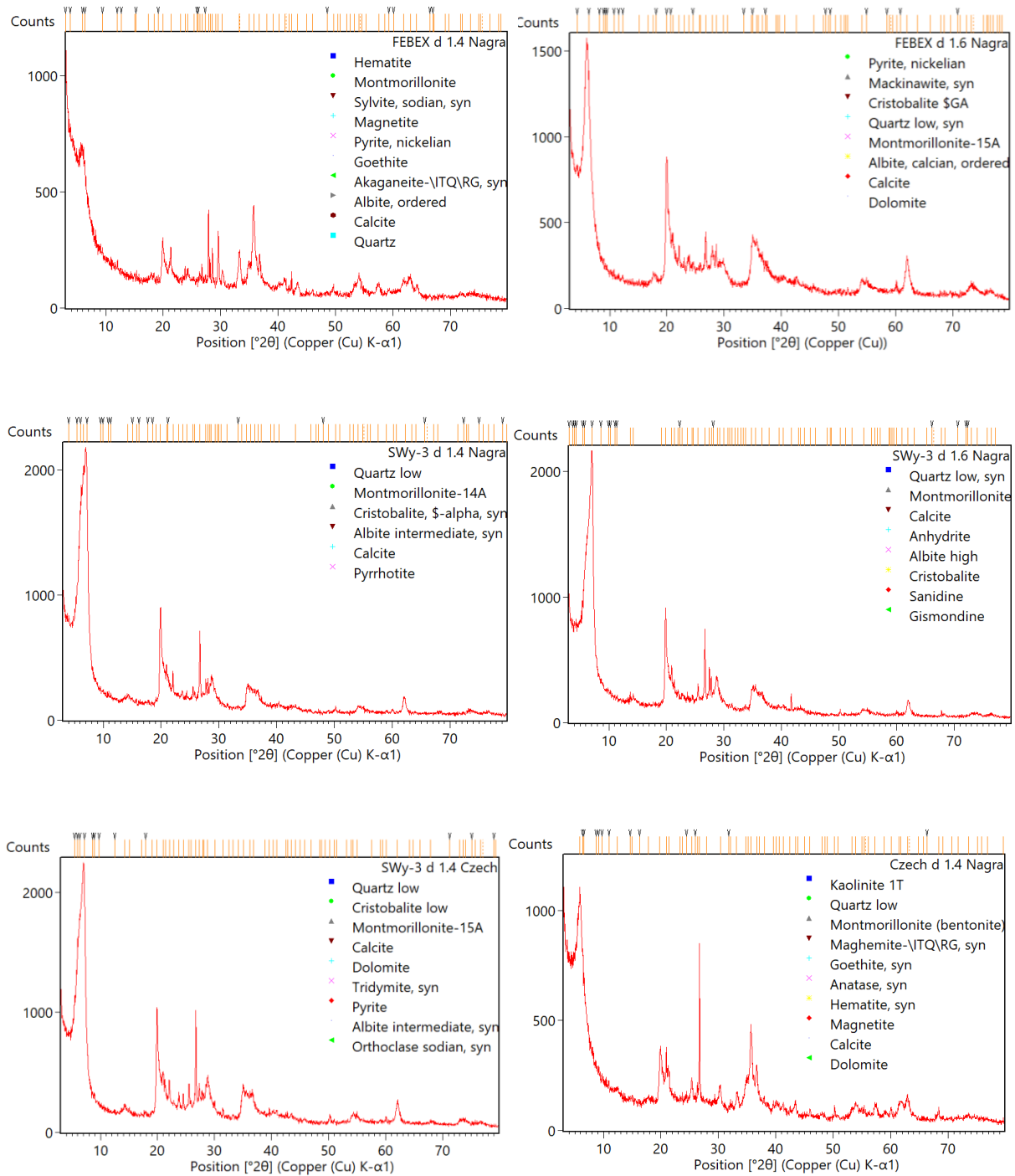
Figure 37 – XRD pattern of bentonite at direct contact to the carbon steel coupons in the different tests. The main mineral phases identified are indicated.

EURAD (Deliverable n° 15.12) – Identification on the effect of transient processes on corrosion
Dissemination level: Public
Date of issue of this report: 29/04/2024

Page 64
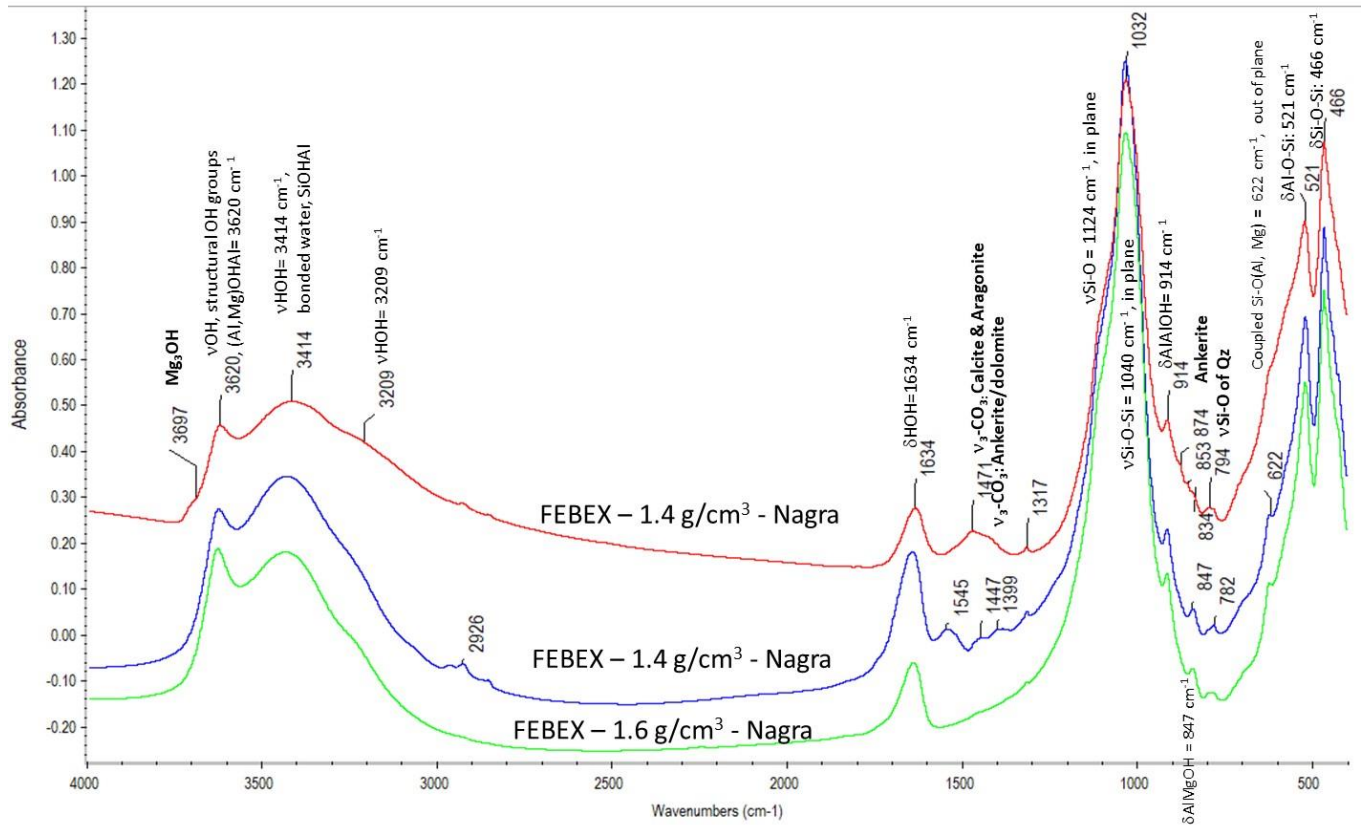
Figure 38 – FTIR spectrum of FEBEX bentonite compacted at 1.4 and 1.6 g/cm³ at contact with Nagra carbon steel coupon.
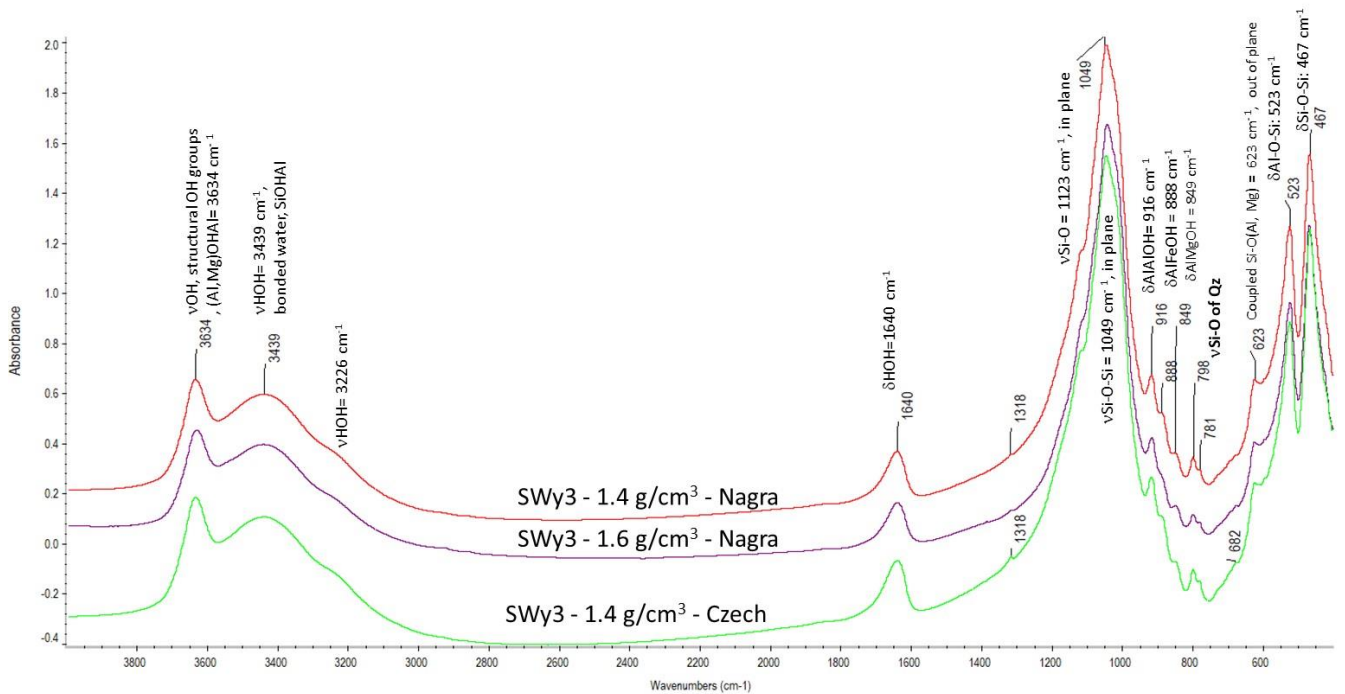
Figure 39 – FTIR spectrum of SWy-3 bentonite compacted at 1.4 and 1.6 g/cm³ at contact with Nagra carbon steel and two Czech coupons.

EURAD (Deliverable n° 15.12) – Identification on the effect of transient processes on corrosion
Dissemination level: Public
Date of issue of this report: **29/04/2024**

Page 65

Figure 40 – FTIR spectrum of Czech bentonite compacted at 1.4 g/cm³ at contact with Nagra carbon steel coupon.

Figure 41 – DSC curves from bentonite samples at contact with the coupon.

EURAD (Deliverable n° 15.12) – Identification on the effect of transient processes on corrosion
Dissemination level: Public
Date of issue of this report: **29/04/2024**

Page 66

Figure 42 – SEM photomicrographs of FEBEX bentonite compacted at 1.4 g/cm³ at contact with Nagra carbon steel coupon: a) and b) Fe-oxyhydroxides, c) Fe-carbonates, d) Ca-Mg-carbonates.

EURAD (Deliverable n° 15.12) – Identification on the effect of transient processes on corrosion
Dissemination level: Public
Date of issue of this report: **29/04/2024**

Page 67
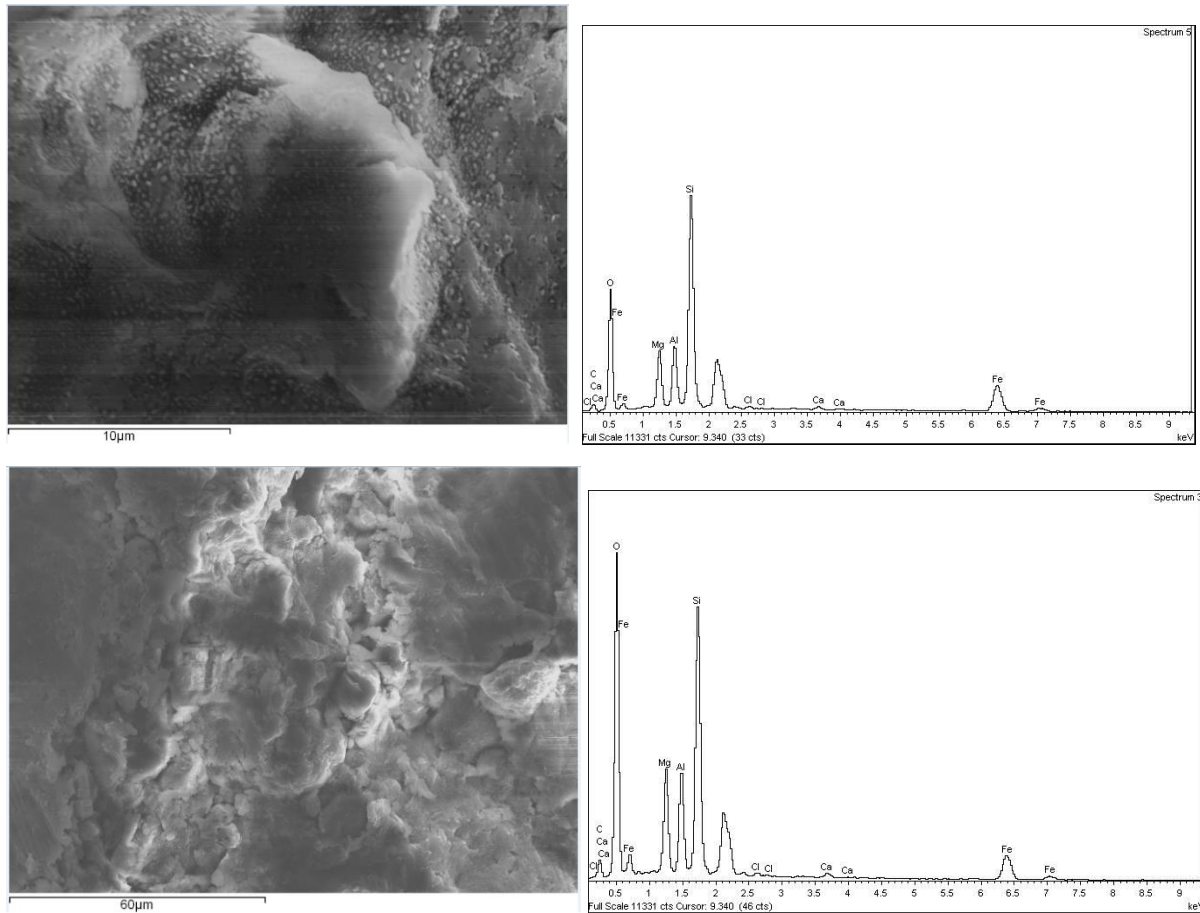
Figure 43 – SEM photomicrographs and EDX spectrum of FEBEX bentonite compacted at 1.6 at contact with Nagra carbon steel coupon: chlorites.
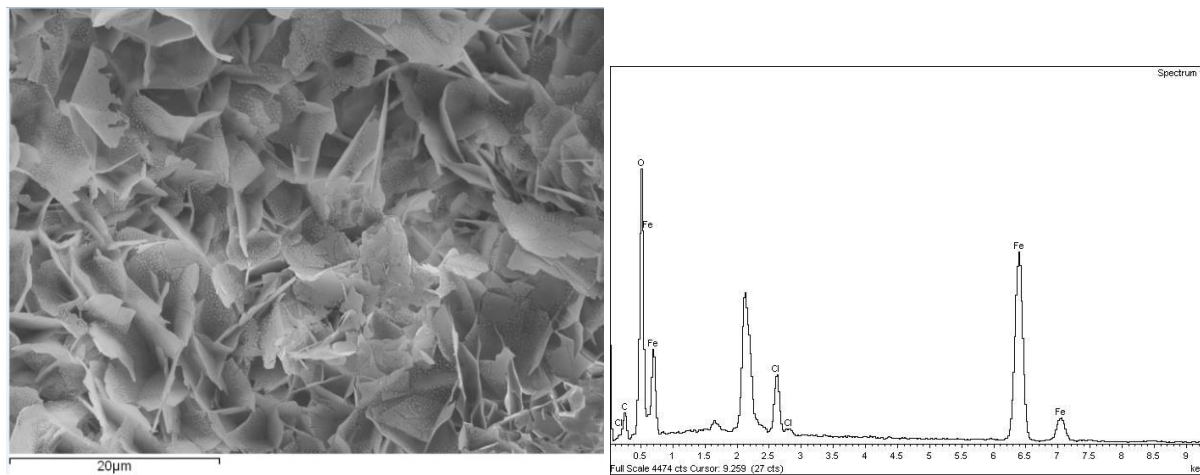
Figure 44 – SEM photomicrographs and EDX spectrum of FEBEX bentonite compacted at 1.6 g/cm³ at contact with Nagra carbon steel coupon: Cl-green-rush (akaganeite?).

EURAD (Deliverable n° 15.12) – Identification on the effect of transient processes on corrosion
Dissemination level: Public
Date of issue of this report: **29/04/2024**

Page 68
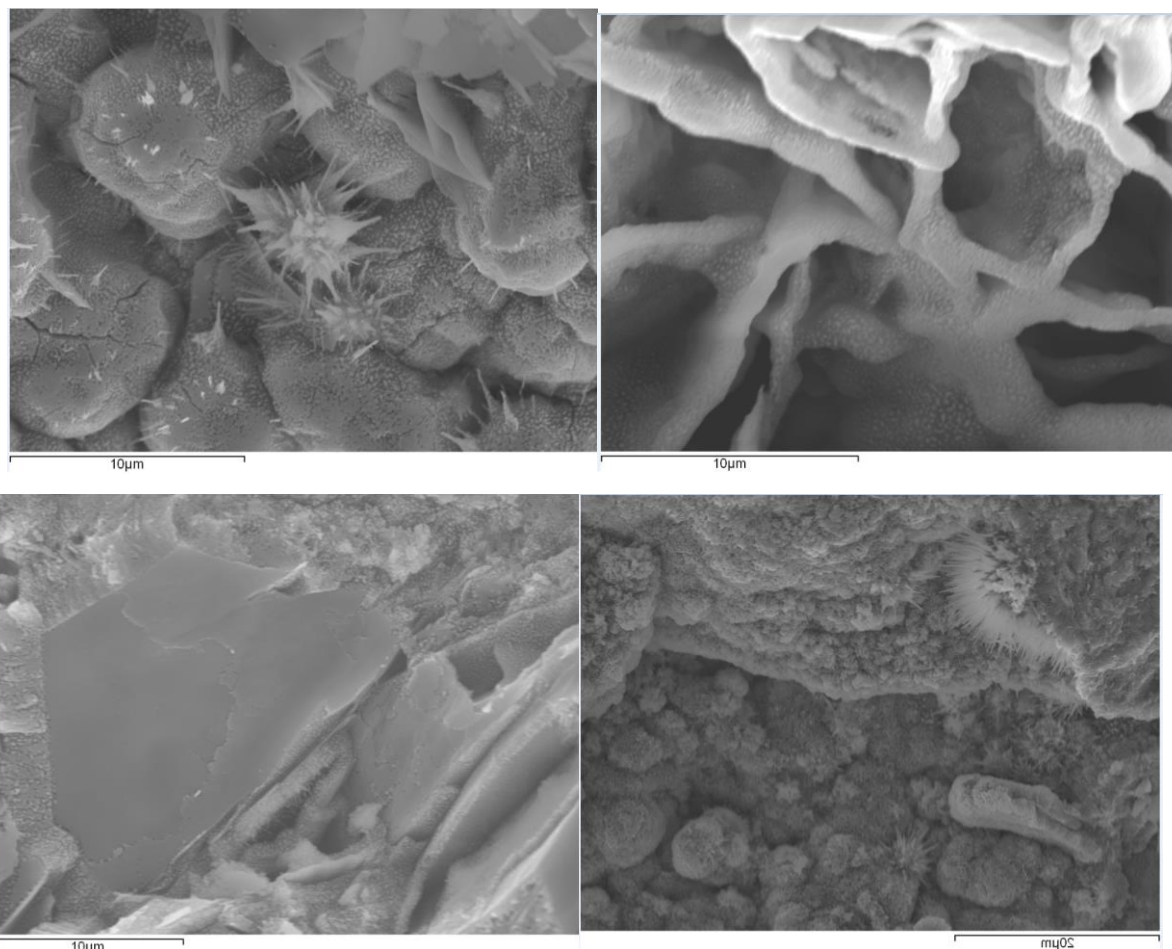
Figure 45 – SEM photomicrographs of FEBEX bentonite compacted at 1.6 g/cm³ at contact with Nagra carbon steel coupon: Fe-(oxy-)hydroxides.
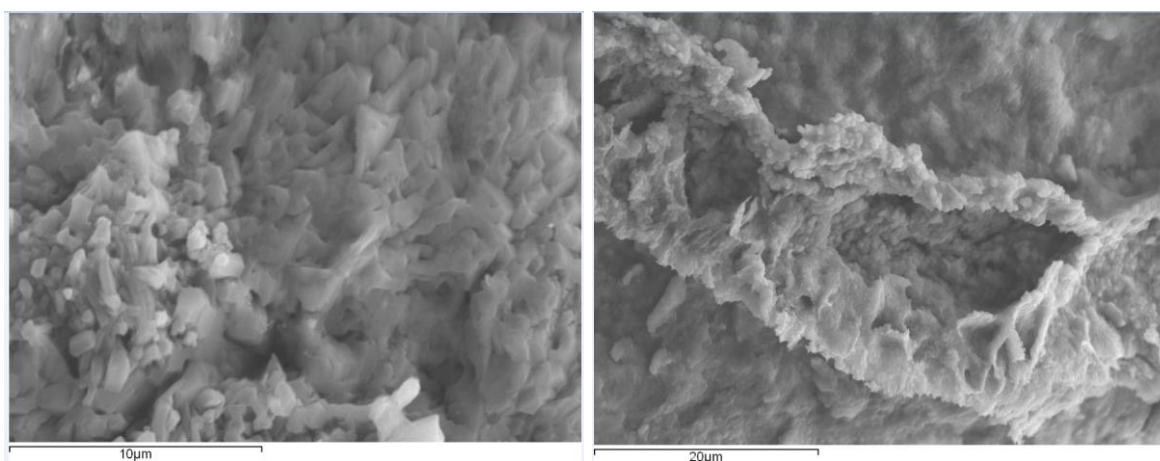
Figure 46 – SEM photomicrographs of Czech bentonite compacted at 1.4 g/cm³ at contact with Nagra carbon steel coupon: a) Fe-carbonates and Ca-carbonates, and b) Fe-carbonates and Ca-carbonates.

EURAD (Deliverable n° 15.12) – Identification on the effect of transient processes on corrosion
Dissemination level: Public
Date of issue of this report: **29/04/2024**

Page 69

2.5.3.2 Cells with SKB Cu-OFP coupons

After 326 days of experiment, all the bentonite samples were completely saturated. Some photographs from the dismantling are shown from *Figure 47* to *Figure 52*. The metal coupons present a degree of corrosion, which depends more on the type of bentonite than on the dry density (*Figure 53*). After dismantling, the coupons were observed by SEM, and then washed according to ASTM procedure described above (*Figure 54*). In principle, no signs of dissolution of Cu metal were observed during the cleaning. The corrosion rates measured are shown in *Table 15*. The highest degree of corrosion seems to be in the Cu coupon interacting with the Czech bentonite, with corrosion rate of 8-9 µm/year. However, the variation in the corrosion rate measured in all bentonite is low, ranging from 3 to 9 µm/year, compared to the corrosion rates measured in bentonites interacting with C-steel coupons (*Table 14*). In addition, the extent of bentonite alteration at the bentonite/coupon contact was < 0.5-1 mm in all samples (*Figure 47* to *Figure 52*), also much lower than that observed from C-steel coupons. It is interesting to note the change of color of the Cu-coupons prior and after the tests (*Figure 53*, *Figure 53*), which is different in all bentonite samples, and changes from yellowish orange to dusky red (FEBEX 1.4 g/cm^3), moderate reddish brown (FEBEX 1.6 g/cm^3), moderate and dark reddish brown (SWy-3 1.4 g/cm^3), moderate brown and reddish brown (SWy-3 1.6 g/cm^3), or brownish black (Czech bentonite 1.4 g/cm^3 and 1.6 g/cm^3). This seems to indicate the presence of both Cu phase minerals: cuprite (red, Cu_2O, Cu(I)) and tenorite (black, CuO, Cu(II)).

Table 15 – Corrosion rate observed in the Cu-OFP metal coupons

Sample	Metal	Dry density (g/cm^3)	Initial weight (g)	Thickness (mm)	Diameter (mm)	Coupon density (cm^3)	Final weight (g)	Mass Loss (g)	Loss (µm)	Contact time (days)	Corrosion rate (µm/year)
FEBEX	Cu-OFP	1.4	7.6489	1.5	27.5	9.2	7.6291	0.0198	3.623	326	4
FEBEX	Cu-OFP	1.6	7.8243	1.5	27.5	9.2	7.809	0.0153	2.800	326	3
SWy3	Cu-OFP	1.4	6.8022	1.5	27.5	9.2	6.7711	0.0311	5.691	326	6
SWy3	Cu-OFP	1.6	7.5552	1.5	27.5	9.2	7.5251	0.0301	5.508	326	6
Czech	Cu-OFP	1.4	8.4522	1.5	27.5	9.2	8.4091	0.0431	7.887	326	9
Czech	Cu-OFP	1.6	7.3394	1.5	27.5	9.2	7.3023	0.0371	6.789	326	8

EURAD (Deliverable n° 15.12) – Identification on the effect of transient processes on corrosion
Dissemination level: Public
Date of issue of this report: **29/04/2024**

Page 70
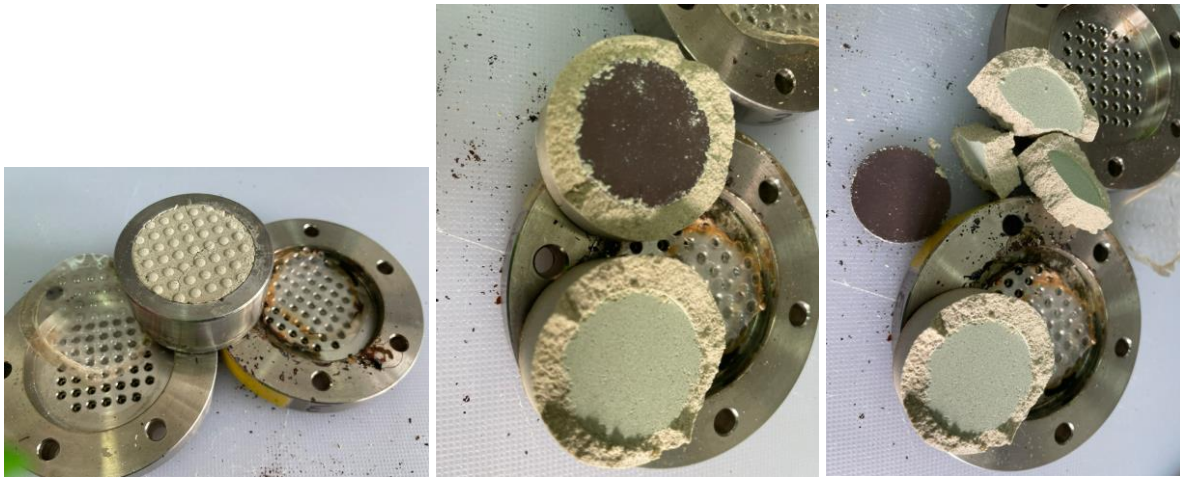
Figure 47 – Dismantling of the FEBEX bentonite compacted at 1.4 g/cm³ with SKB Cu-OFP coupon.
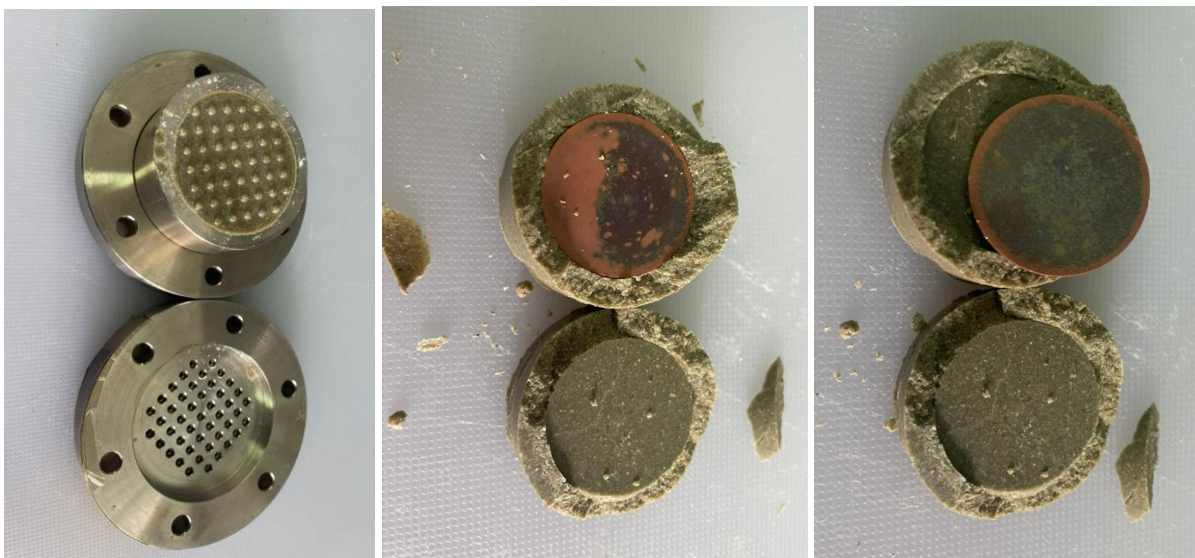
Figure 48 – Dismantling of the FEBEX bentonite compacted at 1.6 g/cm³ with SKB Cu-OFP coupon.

Figure 49 – Dismantling of the SWy-3 bentonite compacted at 1.4 g/cm³ with SKB Cu-OFP coupon.

EURAD (Deliverable n° 15.12) – Identification on the effect of transient processes on corrosion
Dissemination level: Public
Date of issue of this report: **29/04/2024**

Page 71
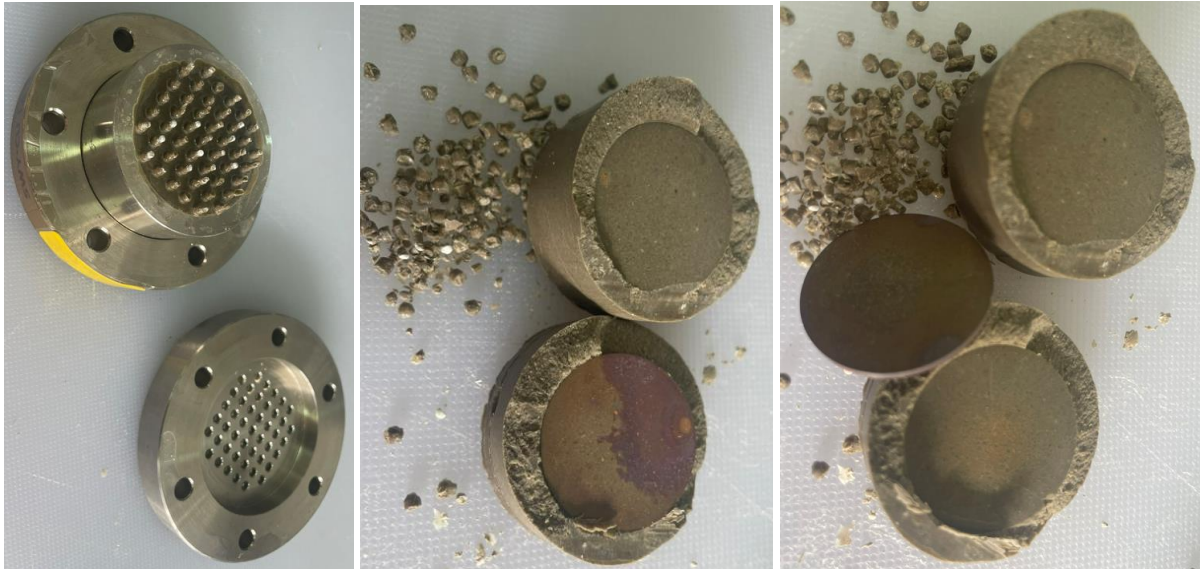
Figure 50 – Dismantling of the SWy-3 bentonite compacted at 1.6 g/cm³ with SKB Cu-OFP coupon

Figure 51 – Dismantling of the Czech bentonite compacted at 1.4 g/cm³ with SKB Cu-OFP coupon.
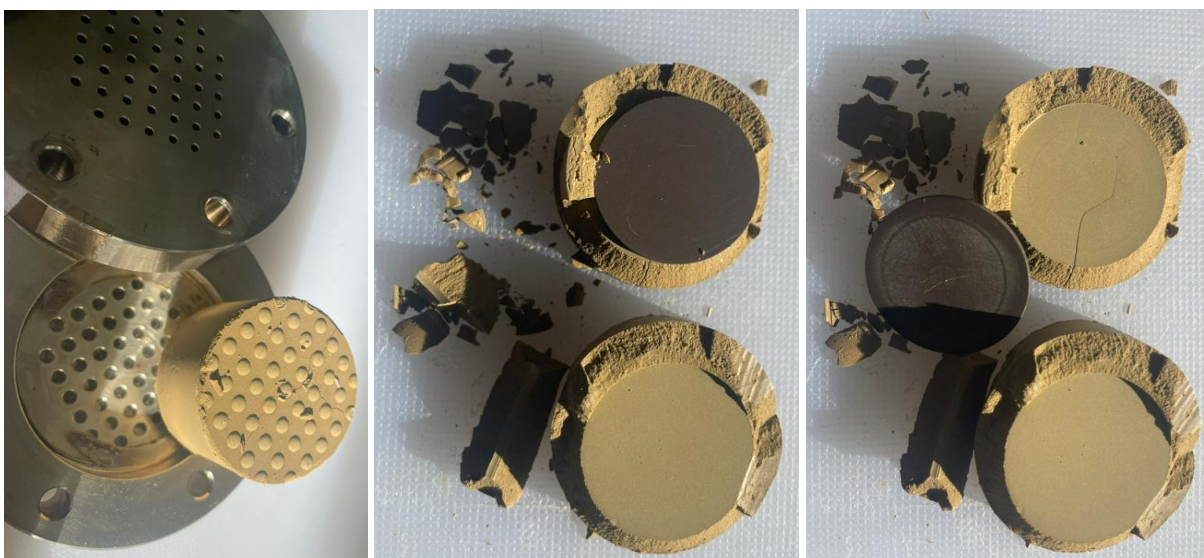
Figure 52 – Dismantling of the Czech bentonite compacted at 1.6 g/cm³ with SKB Cu-OFP coupon.

EURAD (Deliverable n° 15.12) – Identification on the effect of transient processes on corrosion
Dissemination level: Public
Date of issue of this report: **29/04/2024**

Page 72
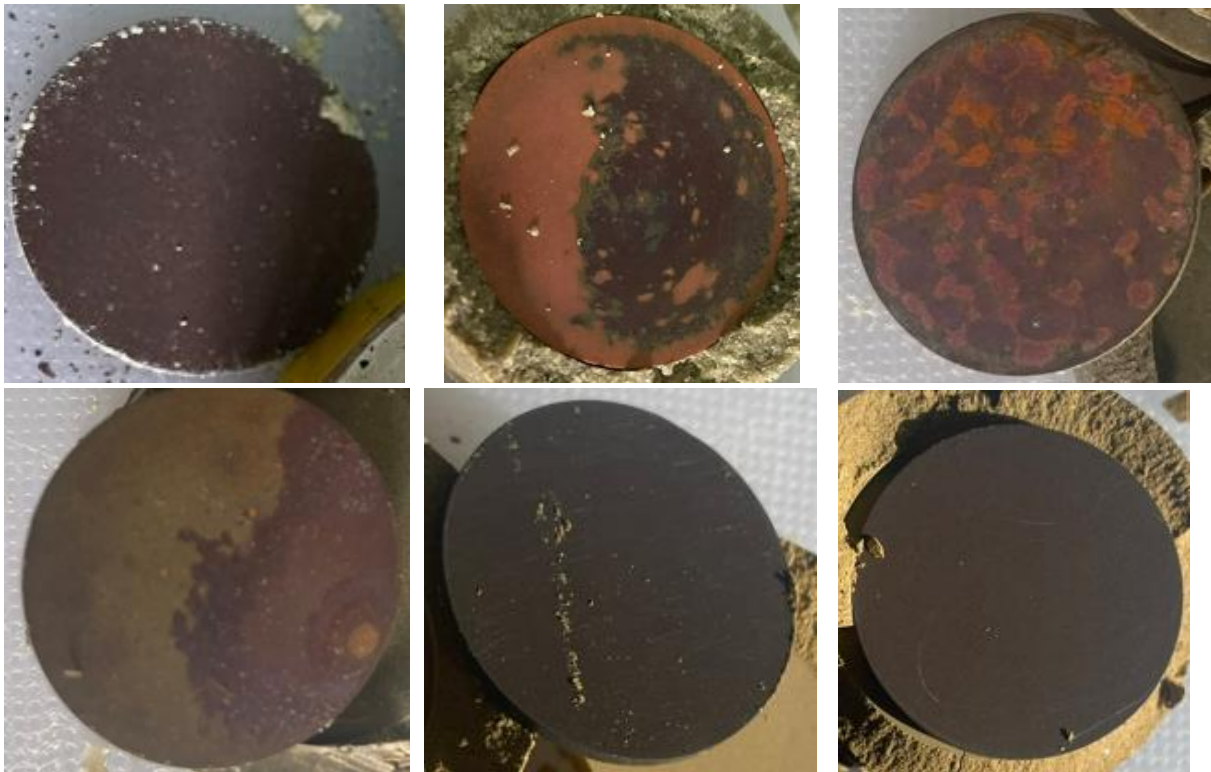
Figure 53 – Visual aspect of the corroded Cu-coupons after dismantling of the cells interacting with different bentonites: a) FEBEX 1.4 g/cm³, b) FEBEX 1.6 g/cm³, c) SWy-3 1.4 g/cm³, d) SWy-3 1.6 g/cm³, e) Czech 1.4 g/cm³, f) Czech 1.6 g/cm³.

Figure 54 – Visual aspect of the corroded Cu-coupons after the five washings prior to determining corrosion rate.

EURAD (Deliverable n° 15.12) – Identification on the effect of transient processes on corrosion
Dissemination level: Public
Date of issue of this report: **29/04/2024**

Page 73

Corrosion of Cu coupons

The degree of corrosion and corrosion products of Cu coupons were analysed by XRD (*Figure 55* to *Figure 59*), and SEM analyses (*Figure 60* to *Figure 67*). The corrosion rates measured in all the coupons ranged from 3 to 9 µm/year (*Table 15*), being higher in tests performed with Czech bentonite. In this case, Cu corrosion seems to depend more on the type of bentonite than on degree of compaction of the bentonite (although is slightly different for samples compacted at 1.6 g/cm^3 than for 1.4 g/cm^3).

The main corrosion products observed in the coupons were cuprite (and copper, probably extracted during scraping of the adhered material), although tenorite was detected in minor amount in the Czech samples compacted at 1.4 and 1.6 g/cm^3. Mineral phases of Cu and C were also detected by SEM in SWy-3 and Czech bentonite samples; and in FEBEX bentonite by XRD.
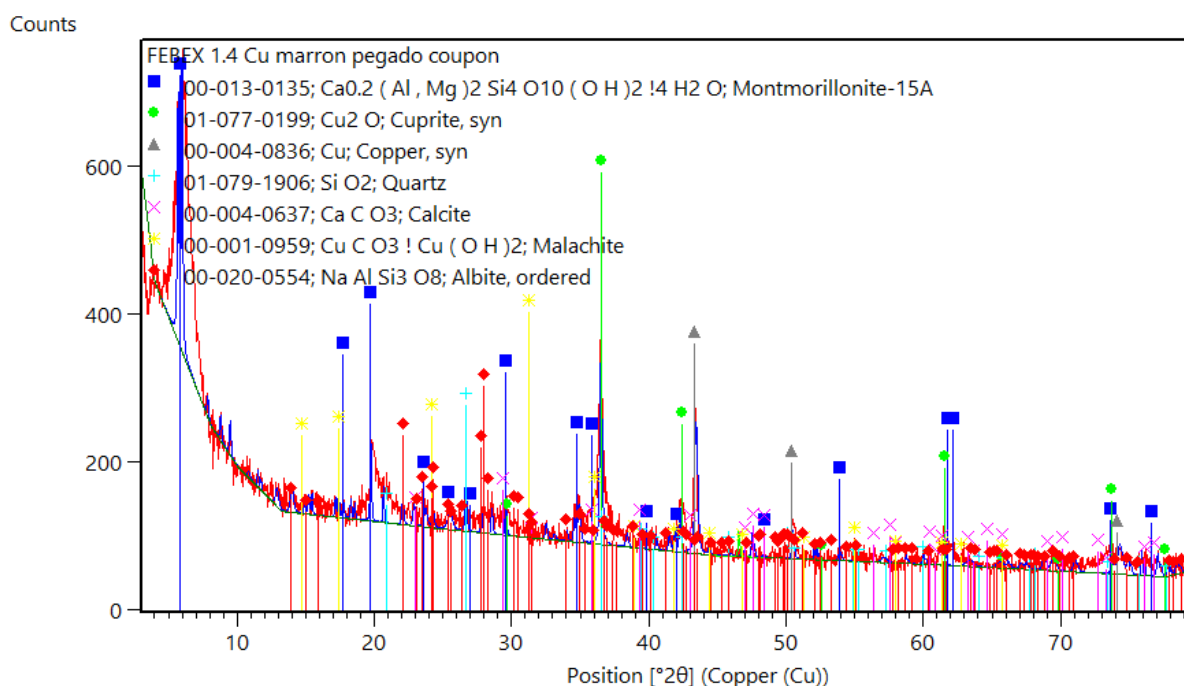
Figure 55 – XRD pattern of material adhered to the SKB Cu-OFP coupon in bentonite FEBEX 1.4 g/cm^3. The main mineral phases identified are indicated.

EURAD (Deliverable n° 15.12) – Identification on the effect of transient processes on corrosion
Dissemination level: Public
Date of issue of this report: **29/04/2024**

Page 74
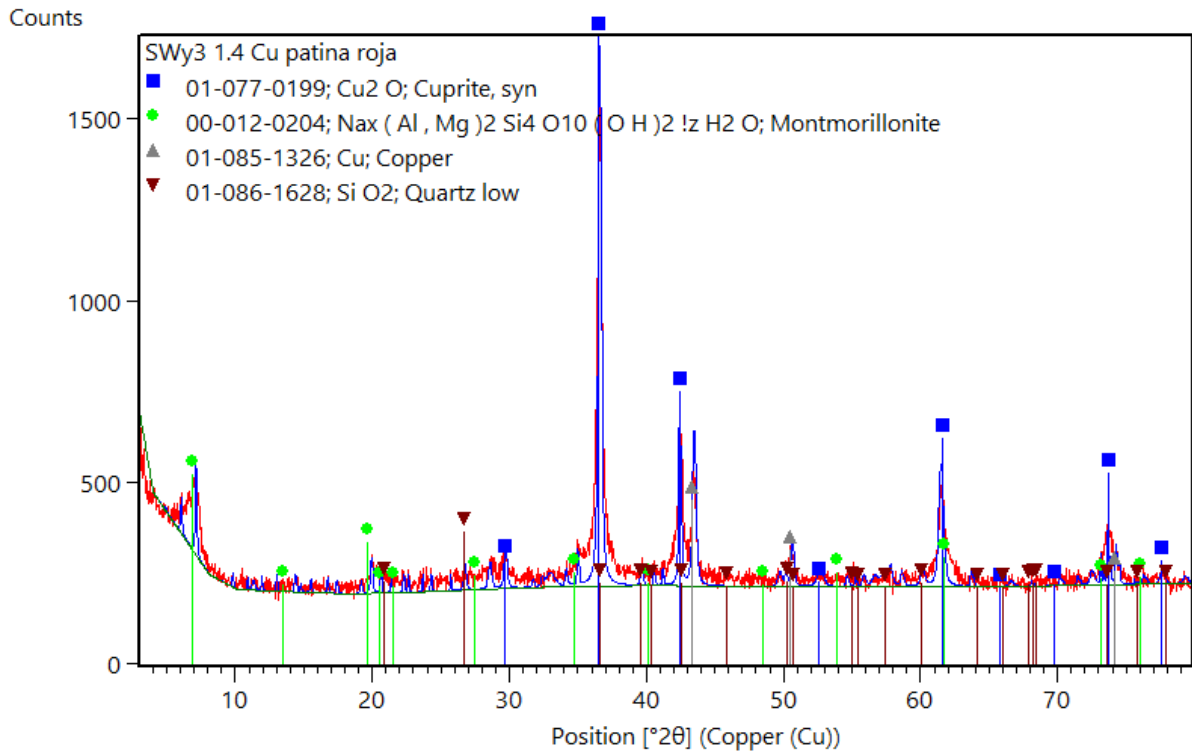
Figure 56 – XRD pattern of material adhered to the SKB Cu-OFP coupon in bentonite SWy-3 1.4 g/cm³. The main mineral phases identified are indicated.
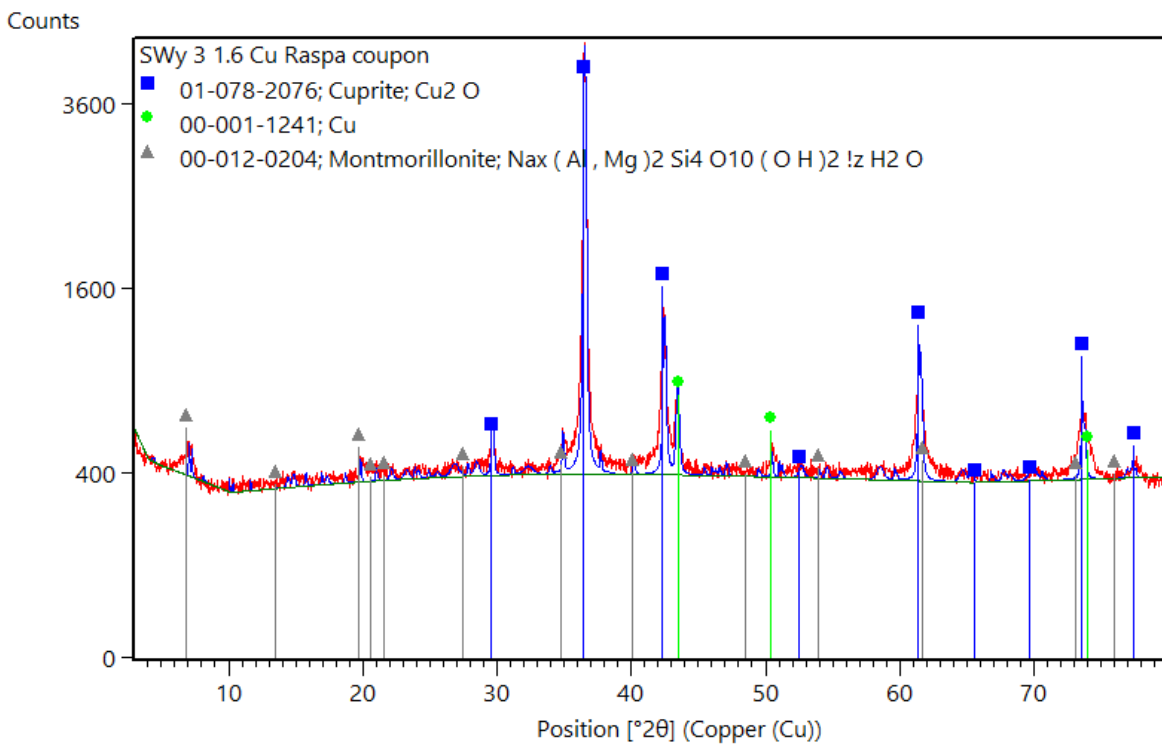
Figure 57 – XRD pattern of material adhered to the SKB Cu-OFP coupon in bentonite SWy-3 1.6 g/cm³. The main mineral phases identified are indicated.

EURAD (Deliverable n° 15.12) – Identification on the effect of transient processes on corrosion
Dissemination level: Public
Date of issue of this report: **29/04/2024**

Page 75
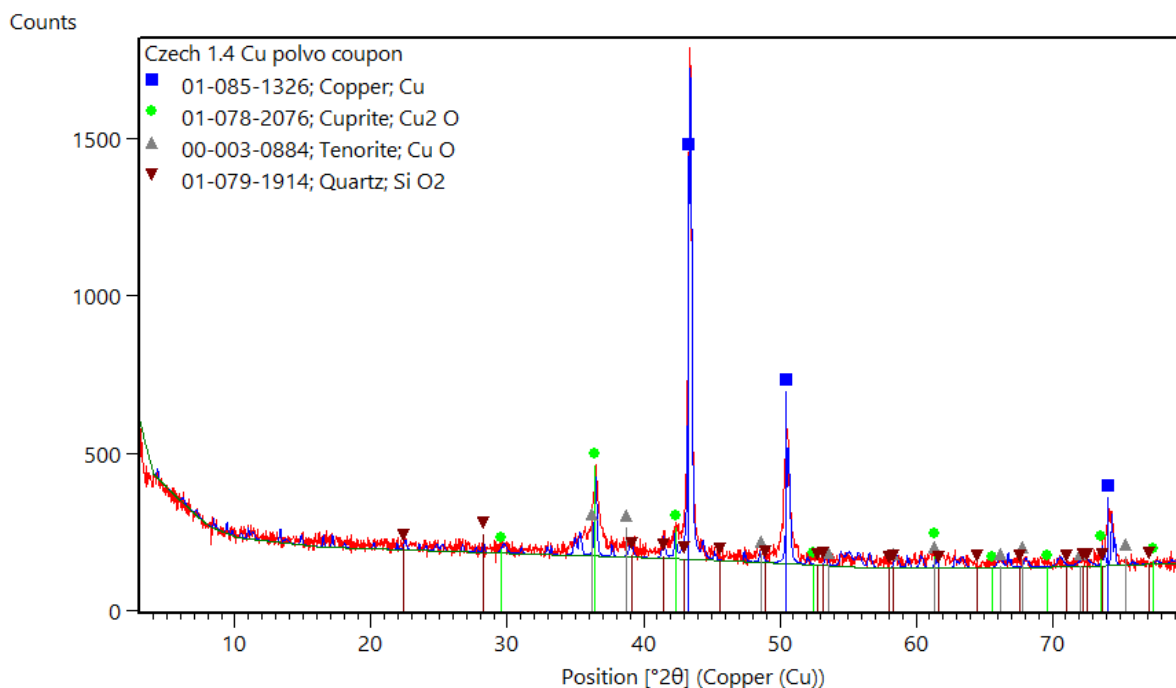
Figure 58 – XRD pattern of material adhered to the SKB Cu-OFP coupon in bentonite Czech 1.4 g/cm^3. The main mineral phases identified are indicated.
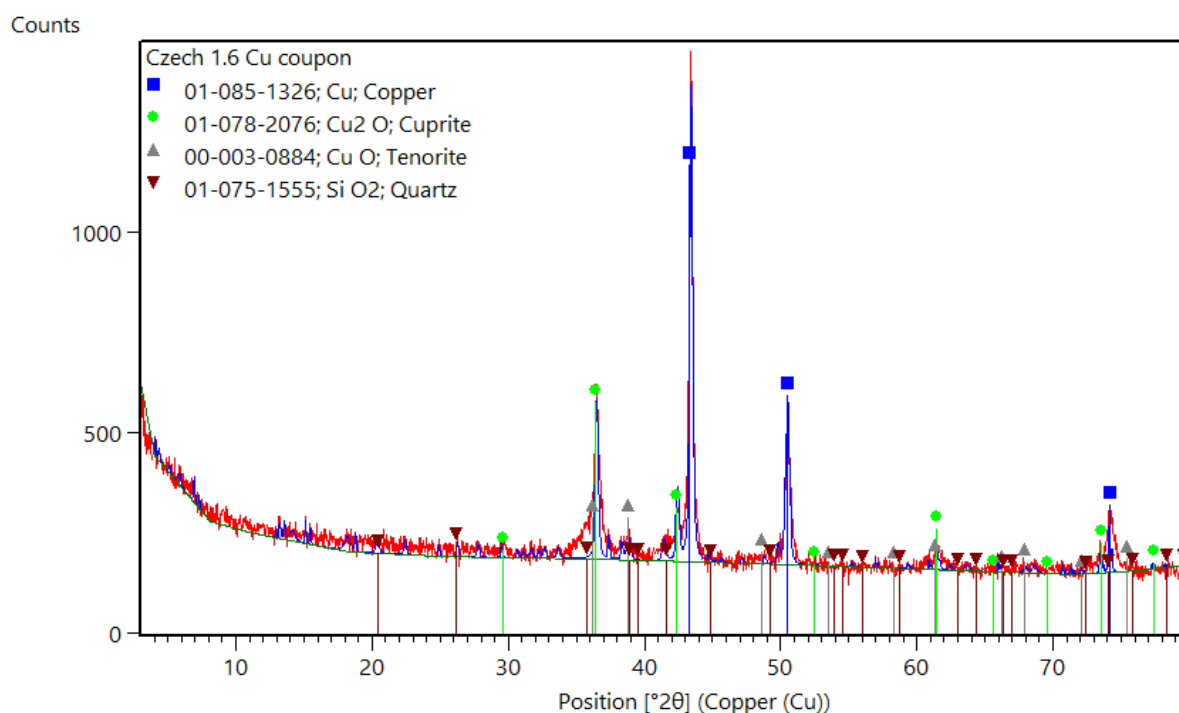
Figure 59 – XRD pattern of material adhered to the SKB Cu-OFP coupon in bentonite Czech 1.6 g/cm^3. The main mineral phases identified are indicated.

EURAD (Deliverable n° 15.12) – Identification on the effect of transient processes on corrosion
Dissemination level: Public
Date of issue of this report: **29/04/2024**

Page 76
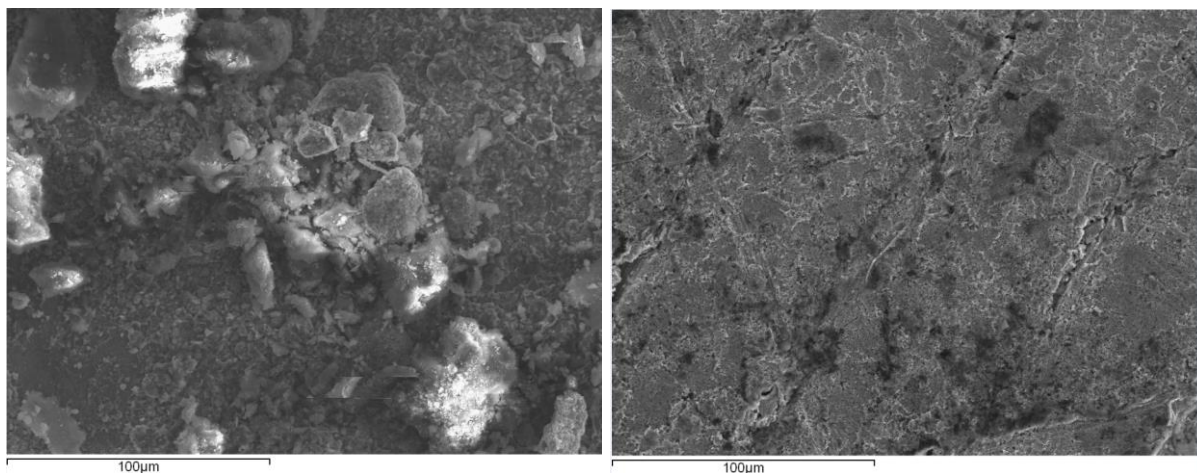
Figure 60 – SEM photomicrograpsh from the Cu coupon inside: a) bentonite SWy-3 1.4 g/cm³: Cu-oxides with bentonite particles; b) bentonite Czech 1.6 g/cm³: general view.
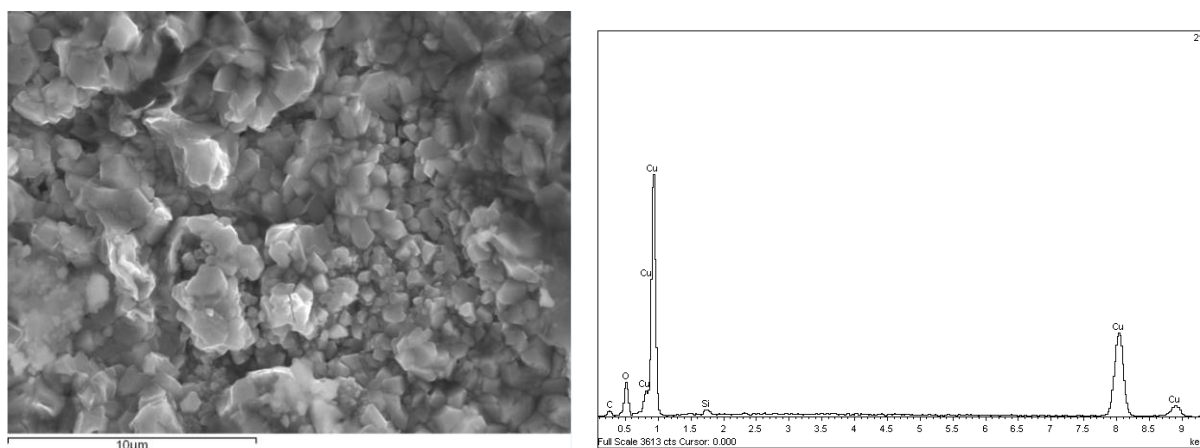
Figure 61 – SEM photomicrograph and EDX spectrum from the Cu coupon inside bentonite SWy-3 1.4 g/cm³: Cu-oxides with 2:1 Cu:O ratio (cuprite).

EURAD (Deliverable n° 15.12) – Identification on the effect of transient processes on corrosion
Dissemination level: Public
Date of issue of this report: **29/04/2024**

Page 77
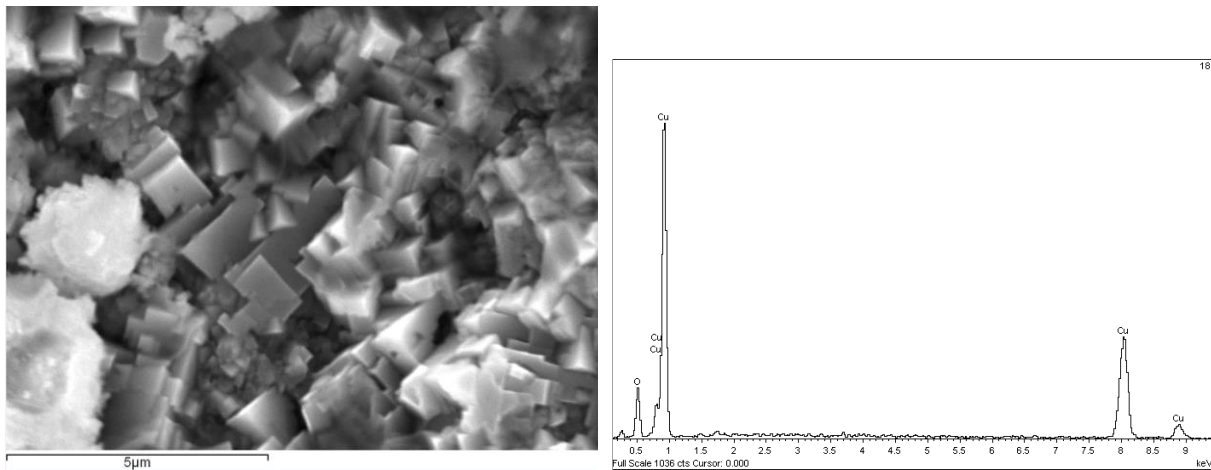
Figure 62 – SEM photomicrograph and EDX spectra from the Cu coupon inside bentonite SWy-3 1.4 g/cm³: Cu-oxides with 4:1 Cu:O ratio.
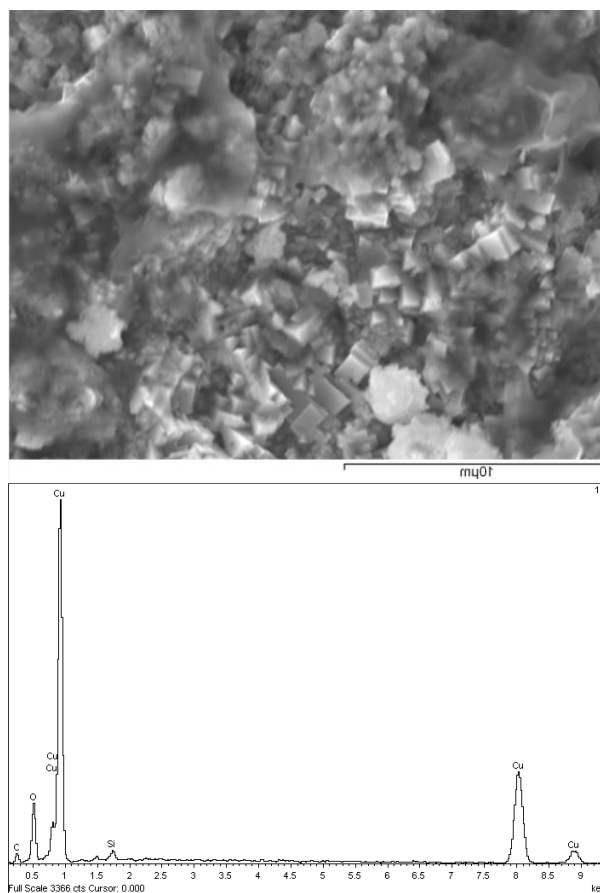
Figure 63 – SEM photomicrograph and EDX spectrum from the Cu coupon inside the SWy-3 1.4 g/cm³: Cu-oxides with 2:1 Cu:O ratio and with carbon.

EURAD (Deliverable n° 15.12) – Identification on the effect of transient processes on corrosion
Dissemination level: Public
Date of issue of this report: **29/04/2024**

Page 78
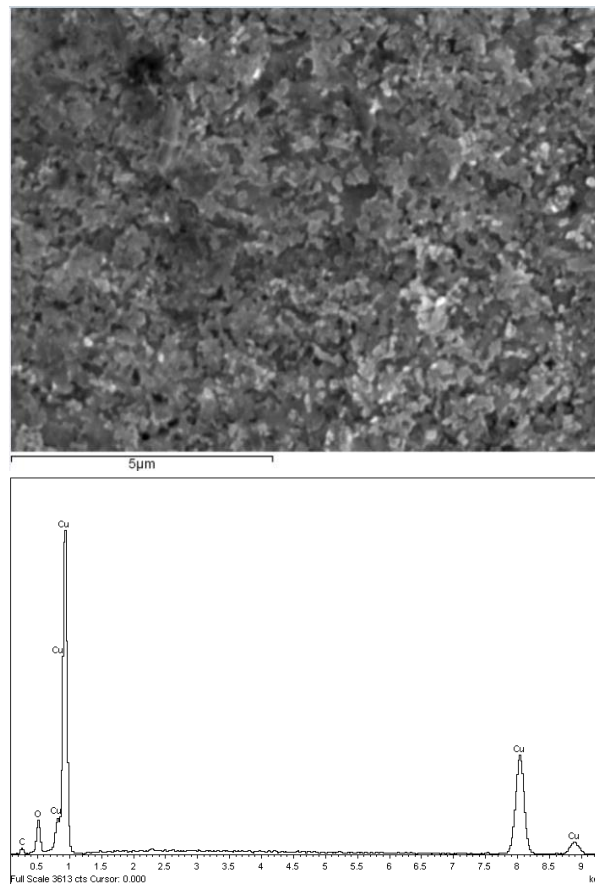
Figure 64 – SEM photomicrograph and EDX spectrum, from the Cu coupon inside bentonite SWy-3 1.6 g/cm³: Cu-oxides with 2:1 Cu:O ratio (cuprite).

EURAD (Deliverable n° 15.12) – Identification on the effect of transient processes on corrosion
Dissemination level: Public
Date of issue of this report: **29/04/2024**

Page 79
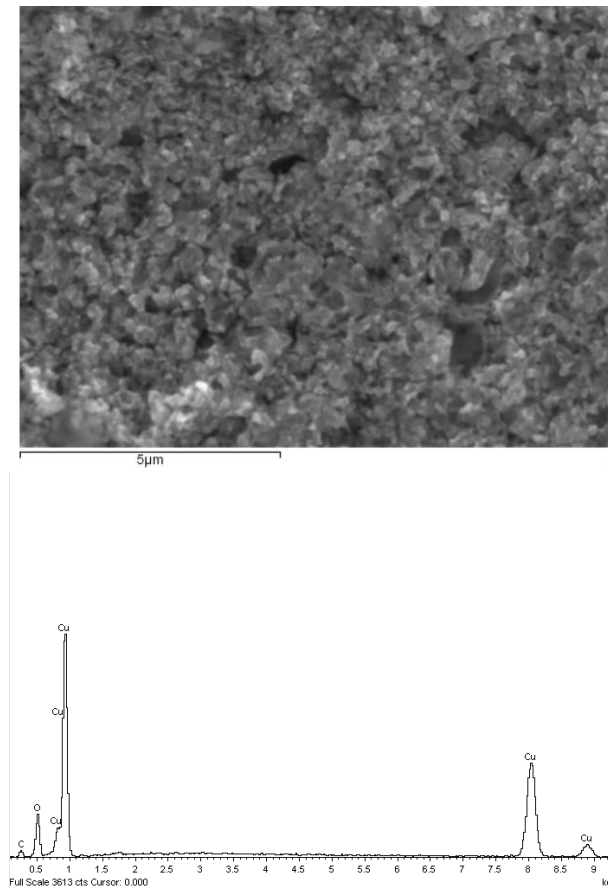
Figure 65 – SEM photomicrograph from the Cu coupon inside bentonite Czech 1.4 g/cm³: Cu-oxides with 2:1 Cu:O ratio.
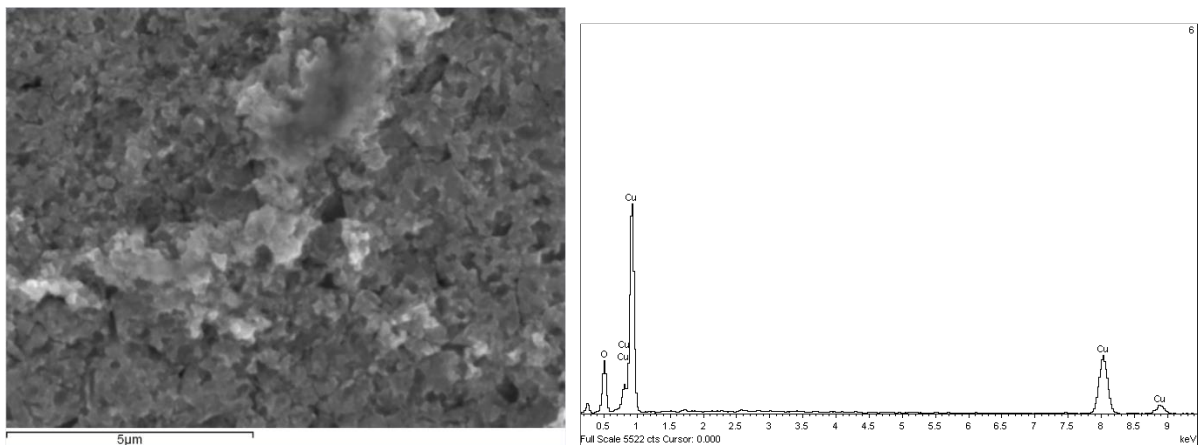
Figure 66 – SEM photomicrograph from the Cu coupon inside bentonite Czech 1.6 g/cm³: Cu-oxides with 4:1 Cu:O ratio.

EURAD (Deliverable n° 15.12) – Identification on the effect of transient processes on corrosion
Dissemination level: Public
Date of issue of this report: **29/04/2024**

Page 80
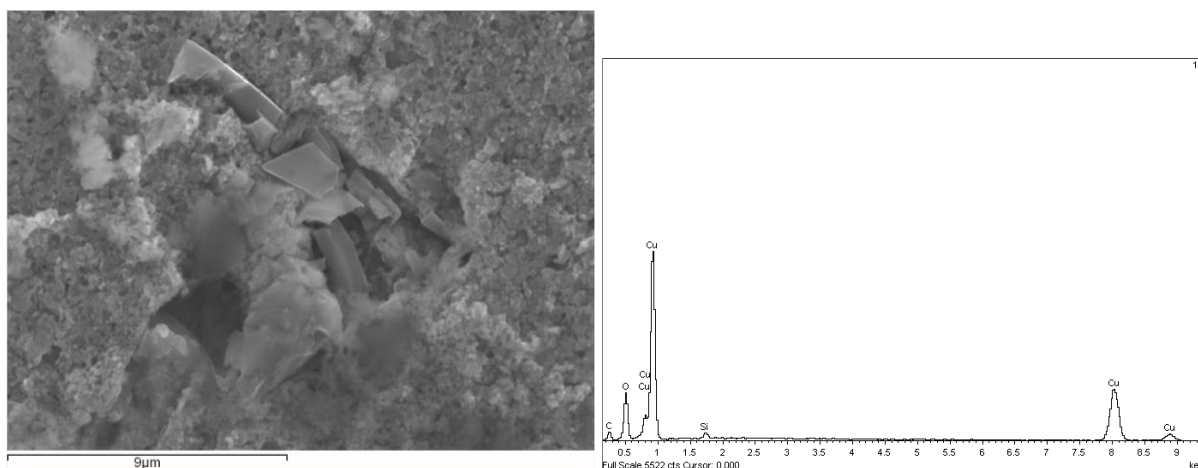
Figure 67 – SEM photomicrograph from the Cu coupon inside bentonite Czech 1.6 g/cm³: mineral phases with Cu-oxides and crystal particles with C (10%), Cu (48%) and O (42%).

Bentonite alteration

The bentonite at direct contact with the coupon was analysed by XRD (*Figure 69* to *Figure 74*).

The extent of visual alteration inside the bentonite was < 0.5-1 mm, only detected visually by a change of the colour in the bentonite FEBEX at 1.4 g/cm³, were azurite and cuprite were detected (*Figure 47*, *Figure 69*). Most of the bentonites remains unaltered, as seen by XRD, with signals similar to the reference bentonite samples. However, malachite is observed in some samples at the bentonite/Cu coupon interface: FEBEX samples compacted at 1.4 and 1.6 g/cm³, and SWy-3 compacted at 1.6 g/cm³ (*Figure 69*, *Figure 70*, *Figure 72*).
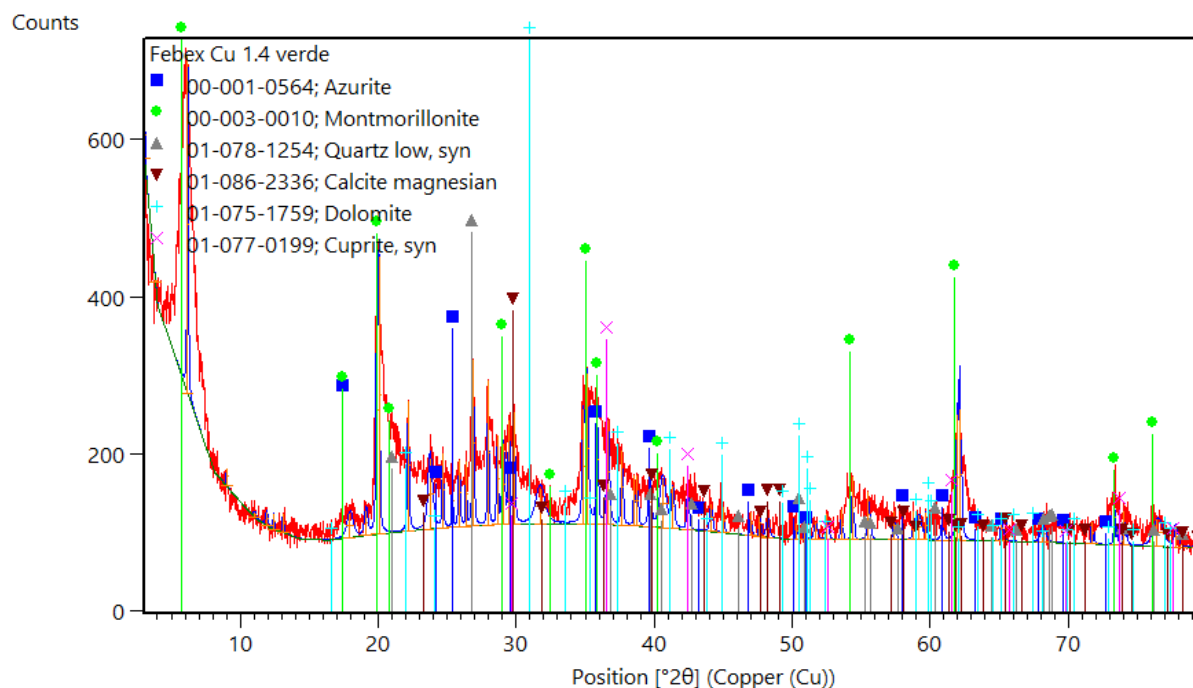
Figure 68 – XRD pattern of bentonite FEBEX 1.4 g/cm³ greenish coloured at contact with Cu coupon.

EURAD (Deliverable n° 15.12) – Identification on the effect of transient processes on corrosion
Dissemination level: Public
Date of issue of this report: **29/04/2024**

Page 81
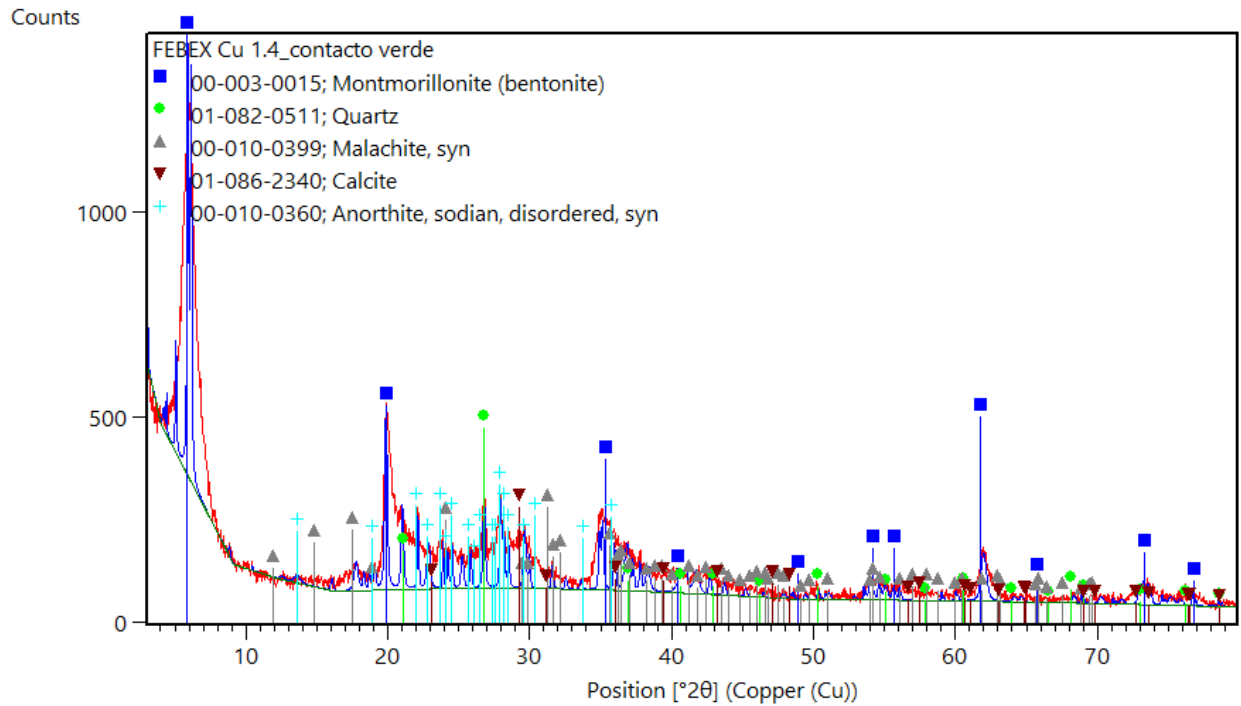
Figure 69 – XRD pattern of bentonite FEBEX 1.4 g/cm³ at contact with Cu coupon.
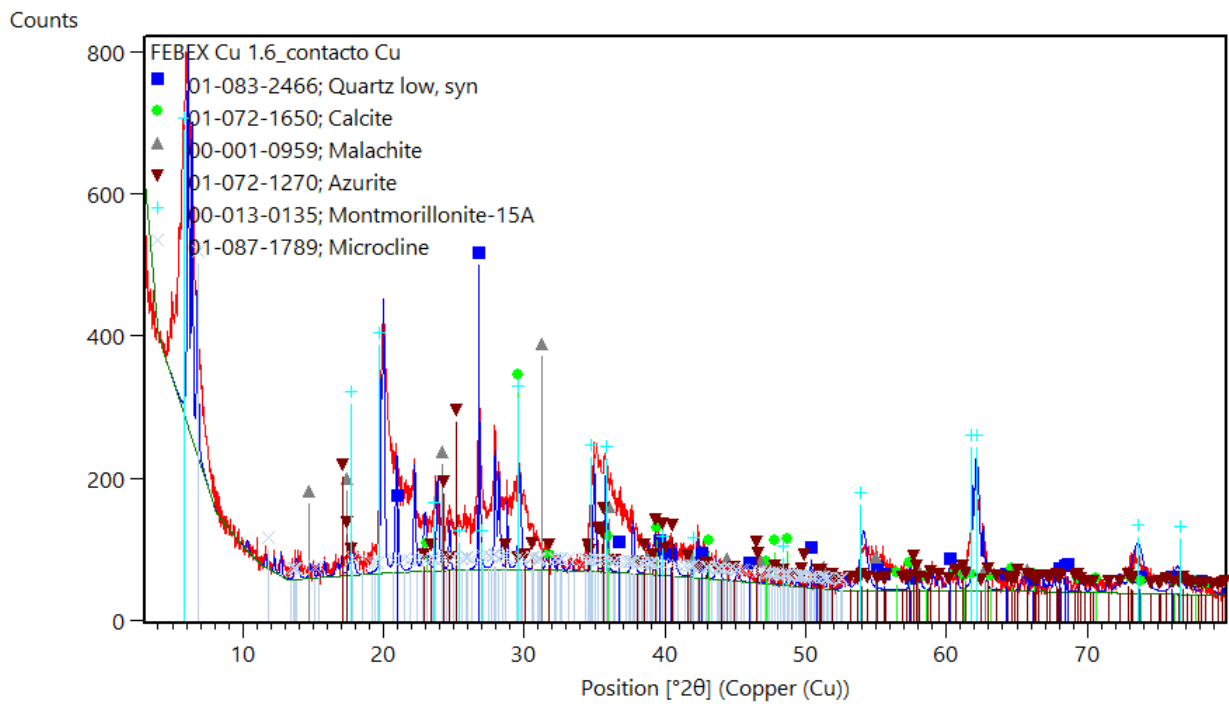
Figure 70 – XRD pattern of bentonite FEBEX 1.6 g/cm³ at contact with Cu coupon.

EURAD (Deliverable n° 15.12) – Identification on the effect of transient processes on corrosion
Dissemination level: Public
Date of issue of this report: **29/04/2024**

Page 82
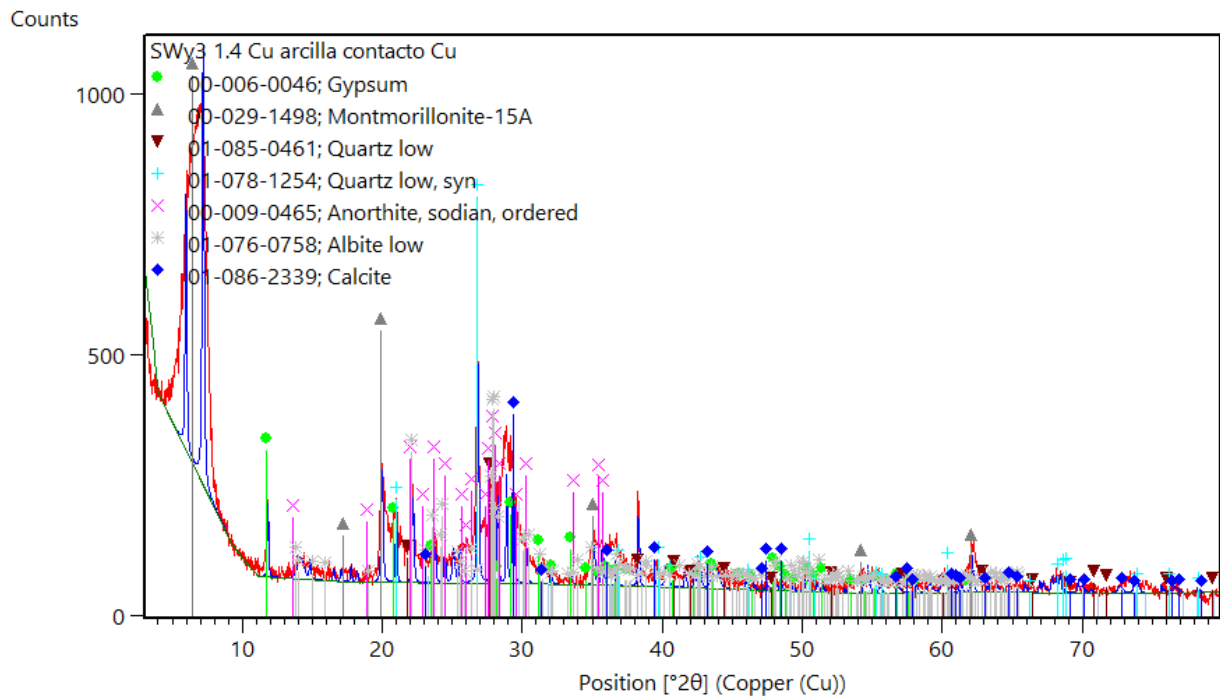
Figure 71 – XRD pattern of bentonite SWy-3 1.4 g/cm³ at contact with Cu coupon.
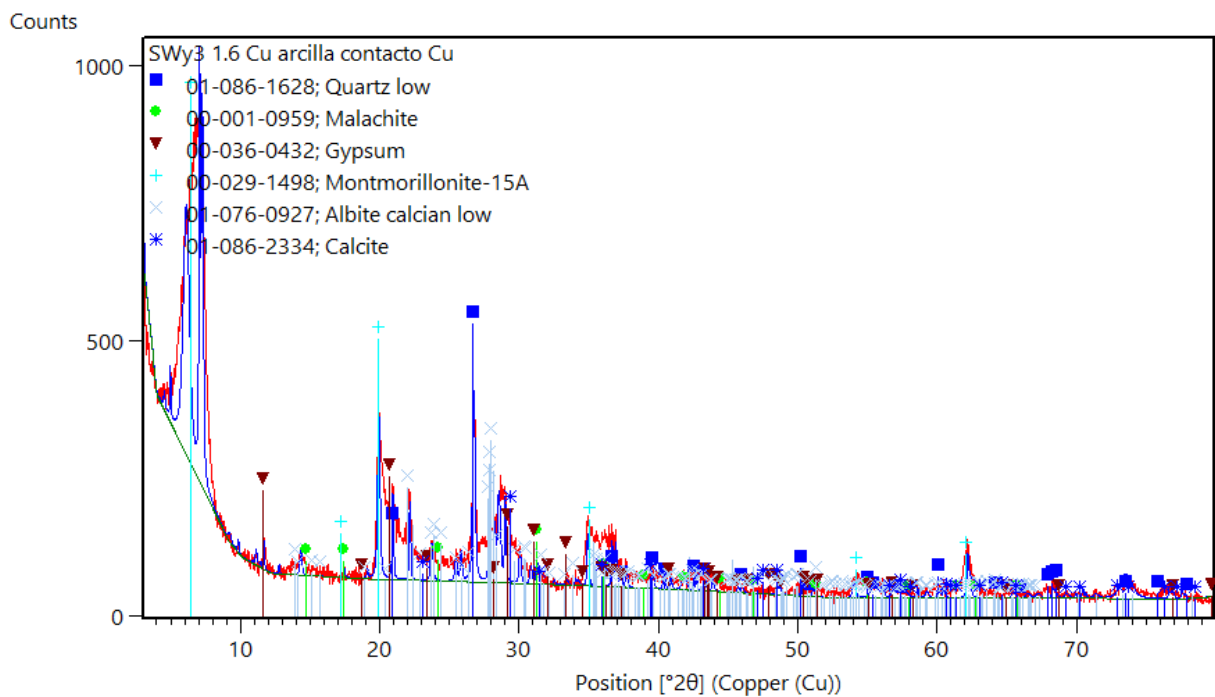
Figure 72 – XRD pattern of bentonite SWy-3 1.6 g/cm³ at contact with Cu coupon.

EURAD (Deliverable n° 15.12) – Identification on the effect of transient processes on corrosion
Dissemination level: Public
Date of issue of this report: **29/04/2024**

Page 83
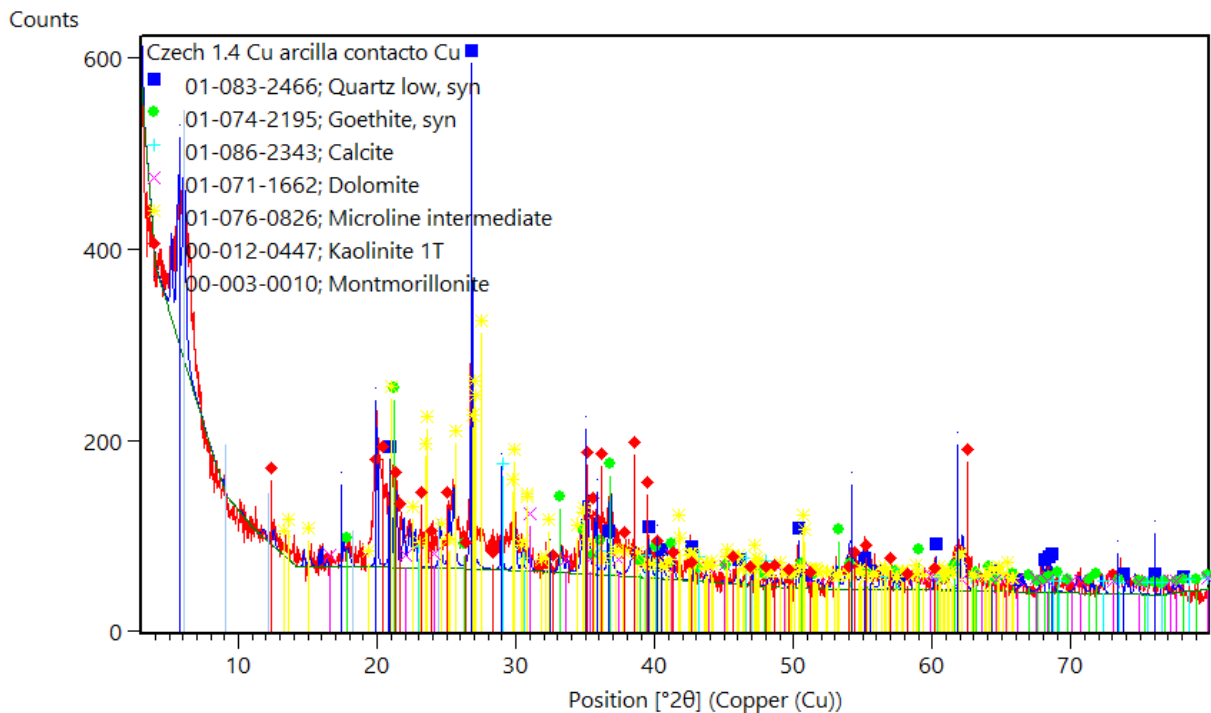
Figure 73 – XRD pattern of bentonite Czech 1.4 g/cm³ at contact with Cu coupon.
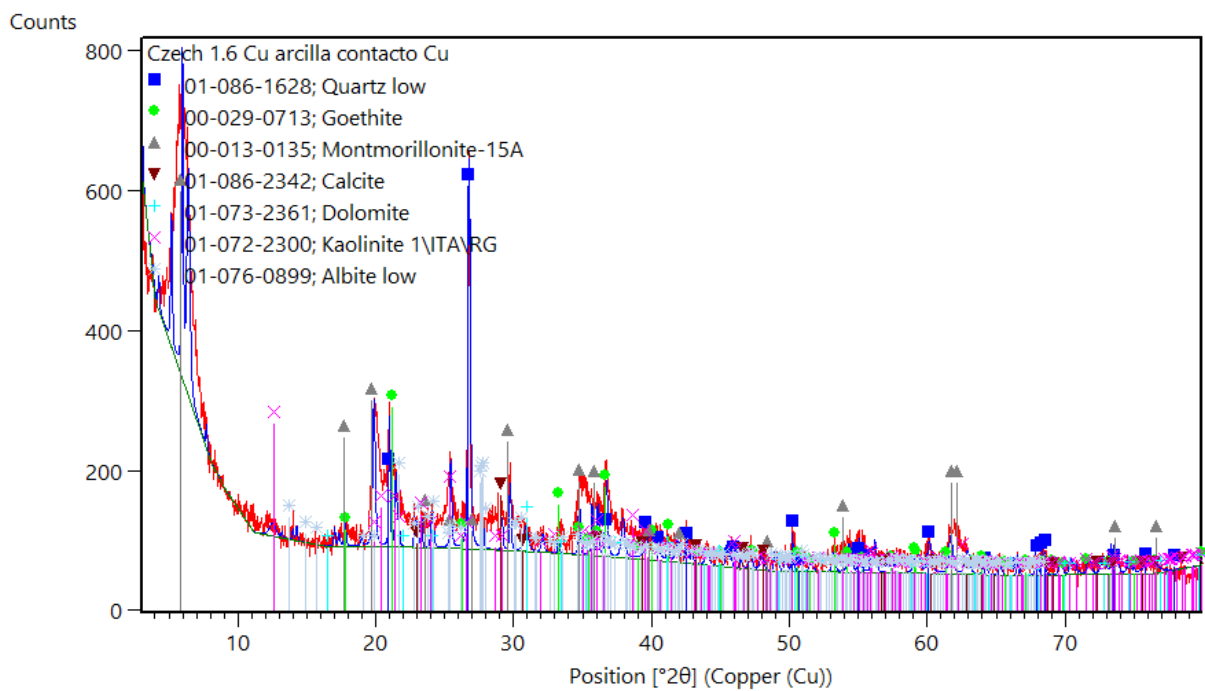
Figure 74 – XRD pattern of bentonite Czech 1.6 g/cm³ at contact with Cu coupon.

EURAD (Deliverable n° 15.12) – Identification on the effect of transient processes on corrosion
Dissemination level: Public
Date of issue of this report: **29/04/2024**

Page 84

2.5.4 Static experiments

A cell with compacted FEBEX bentonite sample (1.4 g/cm^3) was placed at contact with granitic water (200 mL) inside a reactor, which was heated at 80 ^{o}C during 135 days. After closing the reactor, the starting conditions were oxic. Reaching the temperature of 80 ^{o}C, the reactor was at the water pressure of 0.4619 bar (absolute 1.4569 bar).

At the end of the test, and prior to open the reactor, gas and water samples were collected after several cycles of Ar flushing and vacuum inside the sampling lines (*Figure 13*). Then the cell was dismantled and the compacted block bentonite was introduced inside an anoxic glove box for sampling both the coupon and the bentonite (*Figure 75*, *Figure 76*). The degree of the two corroded Nagra carbon steel coupons embedded in the middle of the bentonite are shown in *Figure 76*.

2.5.4.1 Analysis of metal coupons

The corroded coupons were analysed by scanning electron microscopy (SEM), and afterwards, corroded material was separated from the coupon surface and analysed by XRD (*Figure 77*). The texture of the corroded coupon can be observed in the SEM photomicrographs (*Figure 78*). Magnetite, siderite, calcite, aragonite, pyrrhotite, anhydrite, gypsum and a carbonate green rush were found as corrosion products. The formed Fe(II) from corrosion can hydrolyze and precipitate as Fe(OH)$_2$, and with time can convert into magnetite according to the Schikorr reaction. Fe(II) can also be transported away by porewater through the bentonite. In principle, the corrosion rate increase with temperature and time, and hint at the formation of a protective passivation layer at the metal surface. No other Fe-oxy-hydroxides were found, except magnetite. In this test, the corrosion rate of the Nagra carbon steel is 53.2 μm/year, which was obtained according to the ASTM G1-90 Standard (ASTM G1-90, 2011). The coupons seem to present an uniform generalized corrosion.

2.5.4.2 Analysis of gases and hydration water

At the end of the experiment, gas and water samples were taken through the sampling circuit (*Figure 12* and *Figure 13*). The gas samples were taken inside gas cylinders of 50 cm^3 for analysis and the water was collected inside Al-gas/water sampling bags (SuperTM–Inert Foil Gas sampling bags, 1 L). The total pressure of the sampling lines was measured with a high precision digital manometer Keller LEX-1. The samples were sent to Hydroisotop Gmbh laboratory (Germany), where the gas composition was determined via gas chromatography (GC), by using various detectors: GC-TCD detector for He, H$_2$, O$_2$, N$_2$, Ar, and CO$_2$; and GC-FID detector for methane, ethane, i-butane, n-butane, ethane and propene.

The total gas pressure in the sampling lines was of 1.477 bar (absolute), therefore, a slight increase of pressure with respect to water vapour pressure at 80 ^{o}C (0.46 bars, relative) was found.

The gas composition obtained is shown in *Table 16*. It is observed H$_2$, CO$_2$ and methane, apart from other hydrocarbons (C2 to C4). There is a decrease of oxygen and nitrogen with respect to reference atmospheric values (78.08 vol% N$_2$, 20.95 vol% O$_2$ and 0.93 vol.% Ar), and due to the presence of hydrogen and methane, these contents may be due to a contamination during sampling or to the presence of different local redox conditions inside the cell: a) oxic, oxygen being consuming over time, and b) reduced, at the bentonite/coupon contact where H$_2$ is generated. The presence of hydrogen is an indication of metal coupon corrosion under anoxic conditions and that oxygen is probably due to air contamination during sampling. Argon gas was used for flushing the gas lines.

CO$_2$ increased from the atmospheric value of 10$^{-3.5}$ bar to 10$^{-1.0}$ bar, indicating a production of CO$_2$. Dissolved CO$_2$ concentrations in the porewater depend on pH and temperature. The major dissolved carbon species are represented by the two carbon redox end-members: CO$_2$ and CH$_4$. CO$_2$ may be derived from: a) inorganic sources (carbonates decomposition), and b) organic sources (organic matter degradation), which include both aerobic and anaerobic oxidation of organic matter, and abiogenic thermal decarboxylation reactions. The initial alkalinity of the interacting groundwater was 1.9 meq/L and the final value was 2.24 meq/L (*Table 17*). Three sources of carbon supply can be considered in this test: groundwater/porewater (dissolved CO$_2$), carbon from C-steels during corrosion, and

![eurad logo](European Joint Programme on Radioactive Waste Management)

EURAD (Deliverable n° 15.12) – Identification on the effect of transient processes on corrosion
Dissemination level: Public
Date of issue of this report: **29/04/2024**

Page 85

degradation of organic materials. CO_2 may be reduced to CH_4 at anoxic conditions biotic or abiotically, although abiotic reaction is kinetically slow..

Fe(s) is unstable in the presence of water. The corrosion of metals, which is a destructive attack of a metal by an electrochemical process, may produce significant amounts of gas. The rate of gas production is strongly dependent on different factors and on the local geochemical conditions (Féron et al., 2008; King, 2008, 2009; Wersin et al., 2007): 1) the amount of oxygen initially present, 2) the volume of water in contact with the metals (at the time of emplacement and due to water inflow from the host rock into the tunnels); i.e., the water saturation degree and porosity, 3) the quantity of corrodible metals present and the exposed metallic surface area, 4) the temperature, 5) the pH/Eh of the system (e.g., at pH<6 corrosion rates increases sharply), and 6) the chemical composition of the contacting porewater, increasing with salinity and chlorides and sulfate contents.

The depletion of dissolved O_2 inside the reactor is controlled by molecular diffusion and the kinetics of reduction reactions. The O_2-consumption points to reactions with reducing compounds; i.e., electron donors seem to have controlled oxygen concentrations. Most probably inorganic reactions: oxic metal corrosion ($4Fe + 3O_2 \rightarrow 2Fe_2O_3$), fermentative microbially-mediated degradation of organic matter (aerobic respiration: $CH_2O+O_2 \rightarrow CO_2+H_2O$) or its abiotic oxidation, and Fe(II) oxidation from octahedral sites inside smectite clay mineral structure. There is no any evidence of microbial activity in this experiment. However, a high amount of formate is detected in the equilibrium hydration water, as well as NH_4^+ (*Table 17*), Methane (methanogenesis) can be produced by both abiotic (CO_2 reduction) and biotic (e.g., acetate fermentation) mediated processes. The process is controlled by the absence of oxygen and the amount hydrogen and/or easily degradable organic matter. CO_2 reduction is dependent on a supply of dissolved H_2, whereas acetate fermentation is usually limited by the amount of acetate available. The presence of light hydrocarbons (C2, C3, iC4), may indicate that fermentative/oxidation processes of organics are responsible for oxygen consumption.

Hydrogen is produced during anoxic corrosion. Since Fe(s) is thermodynamically unstable in water and, in absence of any other oxidant, metals corrode through water reduction, with subsequent hydrogen generation and the transformation of Fe into magnetite:

$$3Fe(s) + 4H_2O \rightarrow Fe_3O_4 \ (magnetite \ ) + 4H_2 \qquad\qquad \text{Equation 1}$$

These reactions are thermodynamically favourable towards the right and practically irreversible. Under anoxic conditions Fe(III)-oxides (hematite or goethite), may be reduced to magnetite.

After depletion of oxygen initially present in the system, anoxic corrosion will dominate. This produces hydrogen and consumes water at rates that will depend on the amount of water present. In general, the corrosion rate at oxic conditions is higher than under anoxic conditions and increases with temperature following an Arrhenius relationship and decreases when pH increases. The presence of oxygen at the end of the tests may be indicative that not all the oxygen could be consumed and of local reducing conditions at the bentonite/metal coupon interface. However, most probable is an air contamination of the gas sample during sampling.

The hydration interacting water indicates a decrease of pH and calcium, and increase of carbonates, chloride, sulfate ammonium and formate (*Table 17*).

EURAD (Deliverable n° 15.12) – Identification on the effect of transient processes on corrosion
Dissemination level: Public
Date of issue of this report: **29/04/2024**

Page 86

Table 16 – Gas analysis at the end of the static experiment

O_2	N_2	He	Ar	CO_2	H_2	CH_4 methane	C_2H_6 ethane	C_3H_8 propane	i-C_4H_{10} i-butane	n- C_4H_{10} n-butane	C_2H_4 ethene	C_3H_6 propene
vol %	vol %	vol %	vol %	vol %	vol %	vpm	vpm	vpm	vpm	vpm	vpm	vpm
12.7	68.3	<0.05	0.8	9.3 (pCO_2 =10^{-1} bar)	8.3	71	3	1	<1	2	5	1

Table 17 – Analysis of the hydration water prior and after interaction with the two Nagra carbon steel coupons embedded in compacted FEBEX bentonite at 1.4 g/cm^3 of dry density during 135 days (in mg/L).

Sample	pH	HCO_3^-	Br^-	Cl^-	SO_4^{2-}	NO_3^-	NO_2^-	Na	K	Ca	Mg	Sr	NH_4^+	Formate
Initial	6.6	115.9	<0.1	4.2	16	4.0	--	5.6	0.83	24	8.9	0.09	--	--
Final	4.97	136.6	1.2	358	266	6.5	0.38	656	17.7	13.9	7.7	0.19	0.23	1788

2.5.4.3 Bentonite analysis

The bentonite at contact with the coupons were also analysed. However, apart from the visual Fe(II) front, the smectite clay particles seems to remain unaltered, as observed by XRD, FTIR, and SEM analyses (*Figure 79*, *Figure 80* and *Figure 81*).

The bentonite showed a change of colour from slight brownish to greenish, indicating a redox from the middle to both ends of the compacted bentonite, i.e., a diffusion profile of Fe(II) though the compacted bentonite (*Figure 75*). Also, at one end of the bentonite sample, some orange brownish spots we found (siderite? (yellowish brown colour); whereas at the opposite site this was not observed (*Figure 75*). Reducing conditions developed as a consequence of steel corrosion forms Fe(II)-bearing compounds. The green coloration of the bentonite suggests a possible reduction of structural Fe(III) within smectite, since colour is among properties of smectites that is greatly affected by redox reactions (Stucki, 2011). Indeed, Mössbauer studies with the greenish bentonite at direct contact with the corroded coupons shows Fe(II) at octahedral sites. However, FTIR spectrum does not show an increase of iron in the smectite clay particles. Dissolved Fe(II) may react with dissolved Si at high temperature and form iron silicates (e.g., berthierine, odinite, greenalite), but in this sample only a Fe-Ca-Si phase was found by SEM.

EURAD (Deliverable n° 15.12) – Identification on the effect of transient processes on corrosion
Dissemination level: Public
Date of issue of this report: **29/04/2024**

Page 87

Figure 75 – Detail of sampling of bentonite at the end of the static experiment in the reactor at 80ºC: FEBEX bentonite at 1.4 g/cm^3 of dry density.

EURAD (Deliverable n° 15.12) – Identification on the effect of transient processes on corrosion
Dissemination level: Public
Date of issue of this report: **29/04/2024**

Page 88
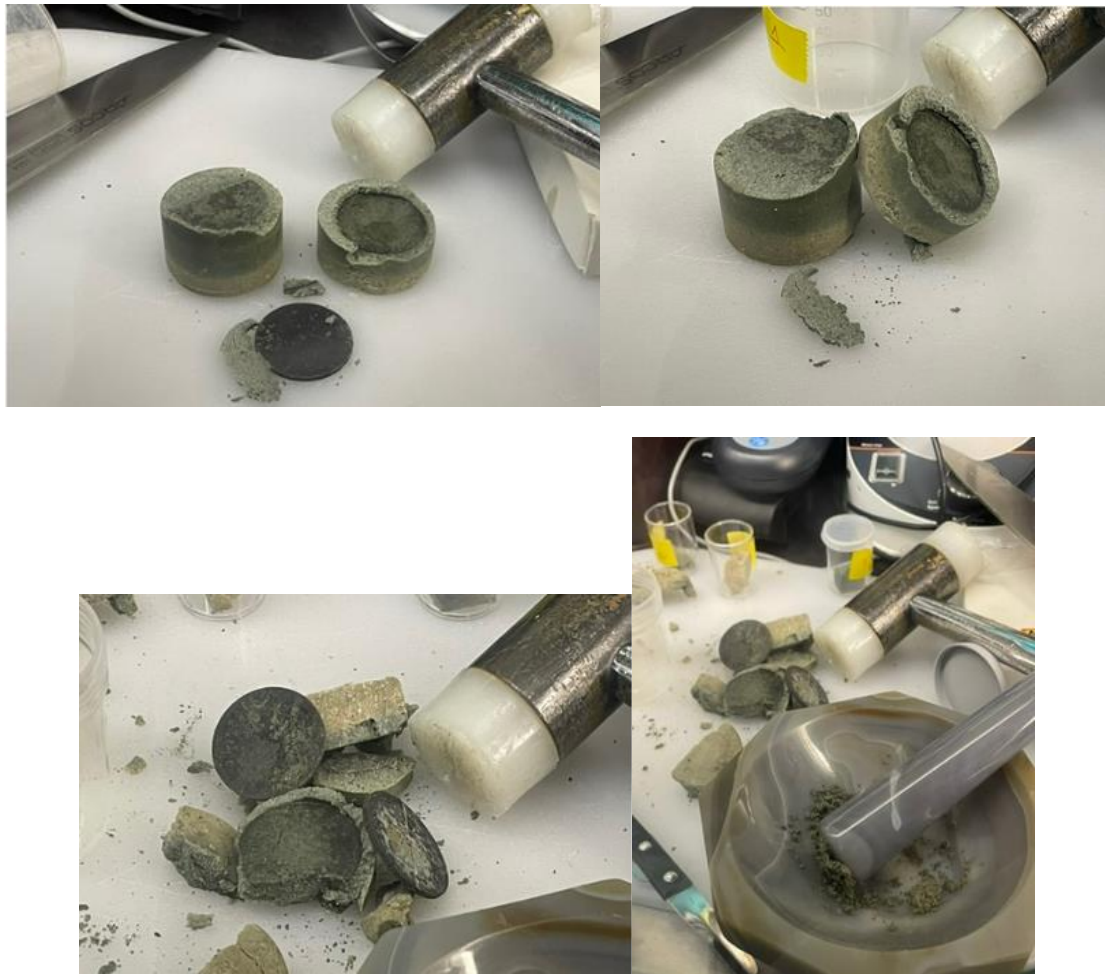
Figure 76 – Detail of sampling of the corroded coupons and the bentonite inside and anoxic glove box: static experiment in the reactor at 80 □C with FEBEX bentonite at 1.4 g/cm³ of dry density.
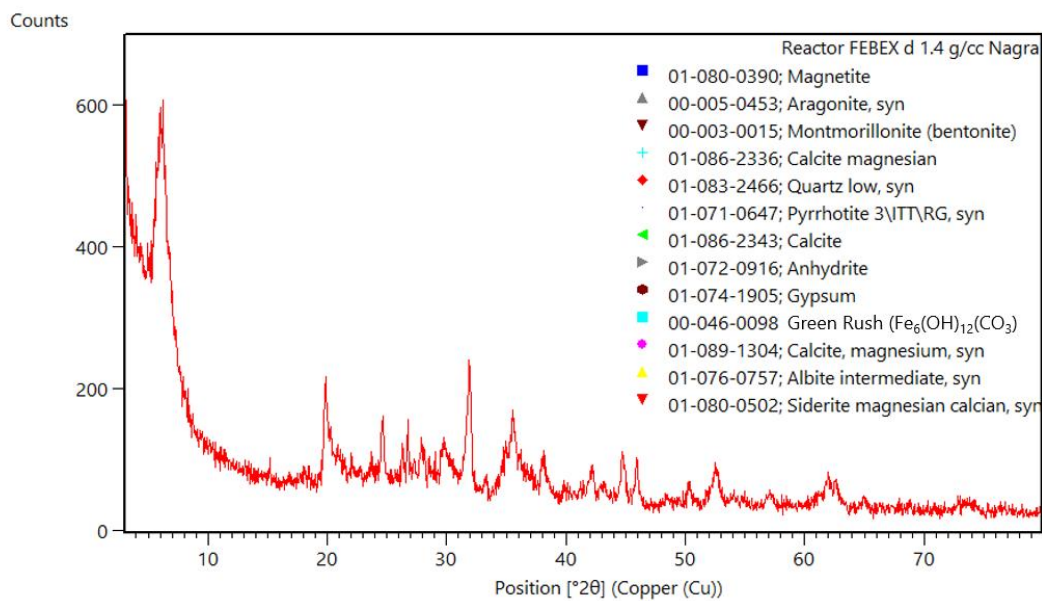
Figure 77 – XRD pattern of material adhered to the Nagra carbon steel coupon. The main mineral phases identified are indicated.

EURAD (Deliverable n° 15.12) – Identification on the effect of transient processes on corrosion
Dissemination level: Public
Date of issue of this report: **29/04/2024**

Page 89
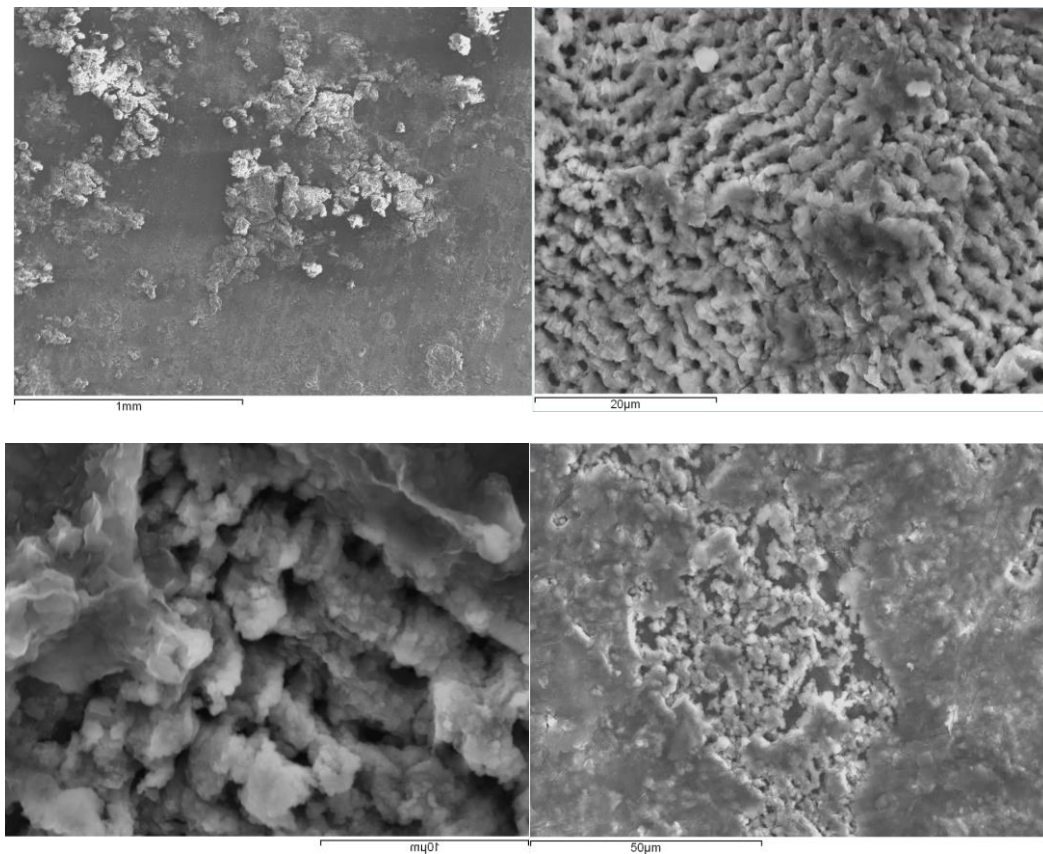
Figure 78 – SEM photomicrographs of Nagra carbon steel coupon surface: a) general aspect, b) Fe-oxy-hydroxides, c) Fe-oxides, and c) smectite clay particles with carbonates, iron sufides, iron oxy-hydroxides (with V, Cr, Mn and Cu).

EURAD (Deliverable n° 15.12) – Identification on the effect of transient processes on corrosion
Dissemination level: Public
Date of issue of this report: **29/04/2024**

Page 90
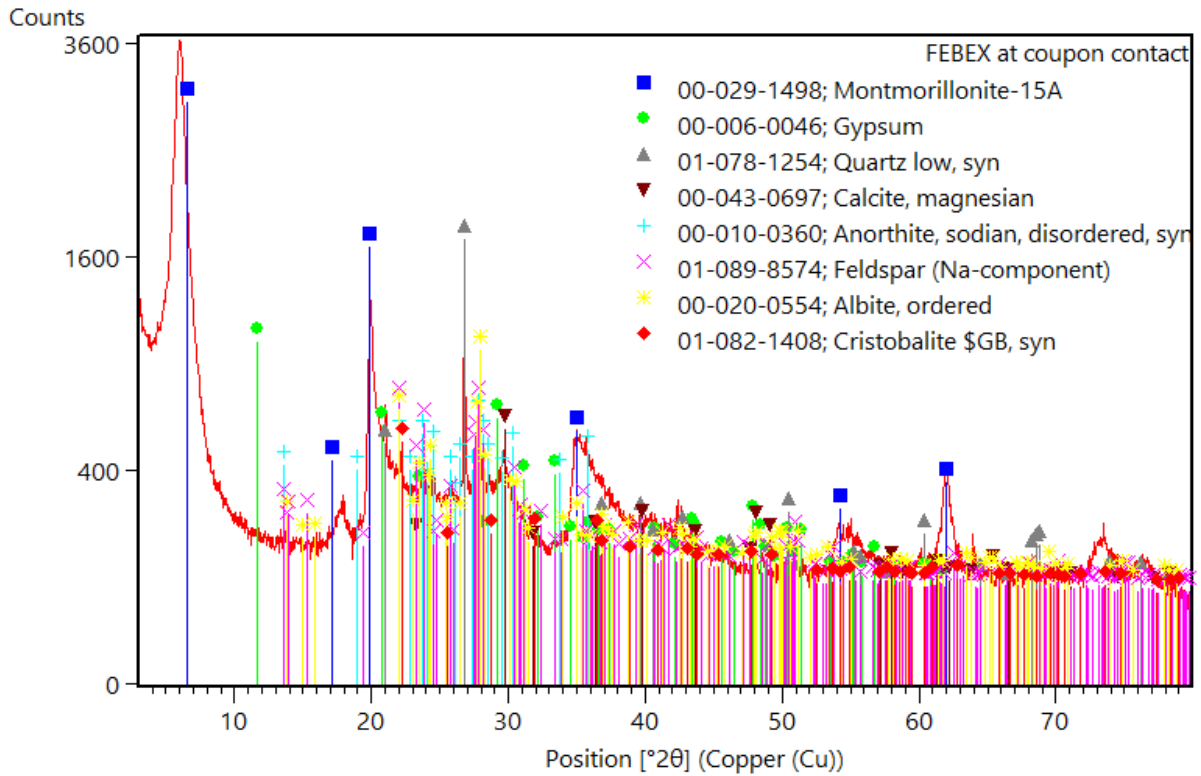
Figure 79 – XRD pattern of bentonite at contact with the Nagra carbon steel coupon. The main mineral phases identified are indicated.
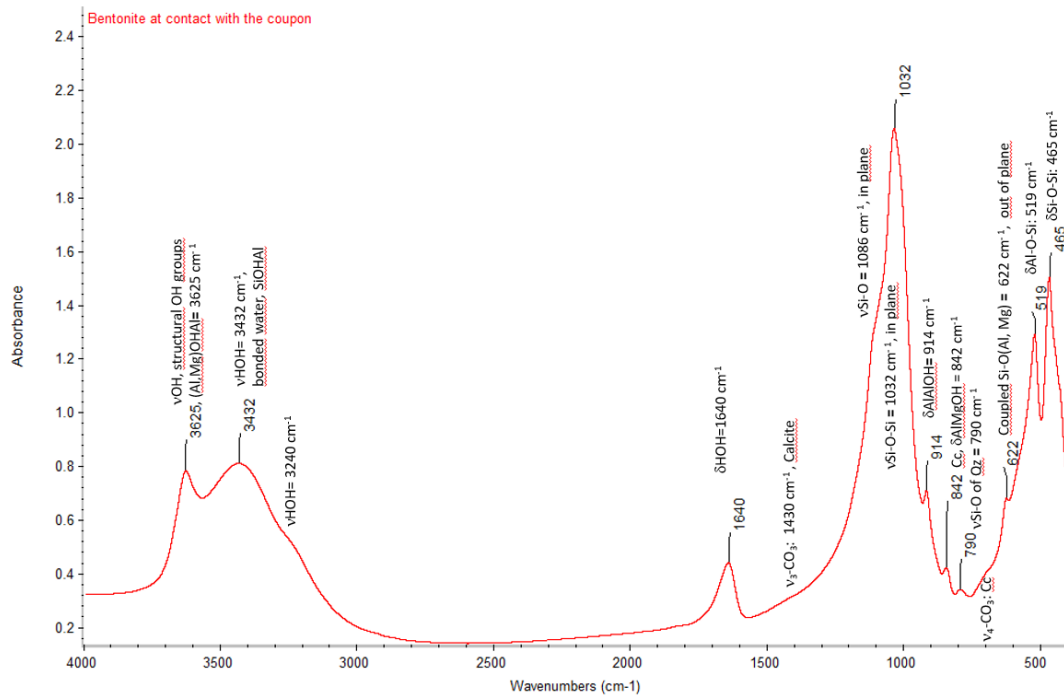
Figure 80 – FTIR spectrum of bentonite at contact with the Nagra carbon steel coupon.

EURAD (Deliverable n° 15.12) – Identification on the effect of transient processes on corrosion
Dissemination level: Public
Date of issue of this report: **29/04/2024**

Page 91
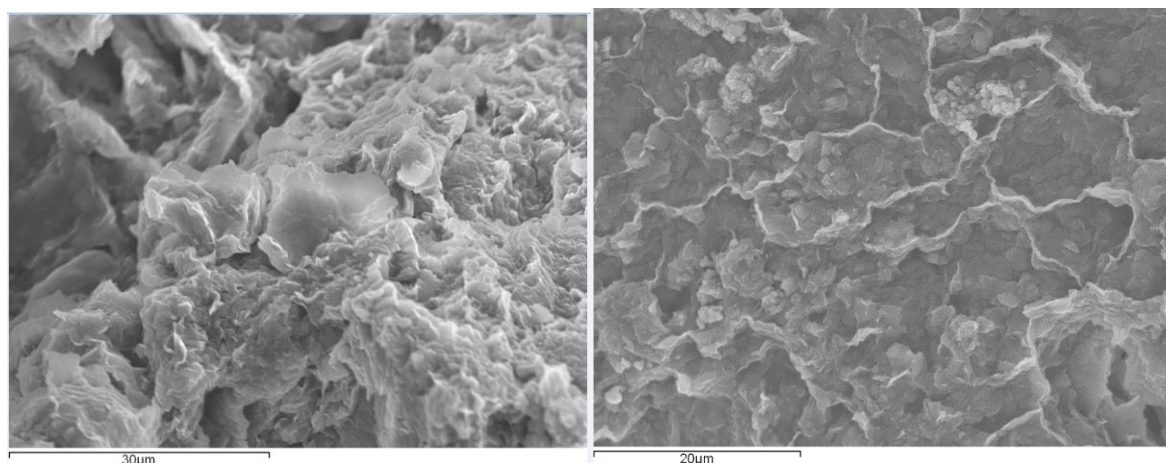
Figure 81 – SEM photomicrographs of bentonite at contact with the Nagra carbon steel coupon: a) smectite clay particles, and b) smectite particles surrounding iron oxyhydroxides particles.

2.6   CIEMAT summary and conclusions

CIEMAT carried out different experiments to analyse the impact of transients in the corrosion and bentonite interactions during redox, hydraulic and thermal nearfield transients, simulating the canister / bentonite interface of a deep geological repository within the framework of Task 5 - ConCorD.

CIEMAT experiments were designed to simulate canister/bentonite interface, considering a representative repository scenario at the early stage in which bentonite is not fully water saturated and conditions are still aerobic, usually defined as Phase 2 – Aerobic unsaturated phase (oxic and unsaturated conditions).

CIEMAT performed two separate activities in Task 5: a) Analysis of samples from large-scale test, and b) laboratory experiments (static and dynamic experiments). These activities cover a range of transient conditions affecting corrosion of metals, such as resaturation of compacted bentonite, convective water vapor saturation fluxes, ambient and high temperature (80 ºC), different salinity of the infiltrating waters, and variations in oxic/anoxic conditions.

Three types of bentonites were used in the experiments: FEBEX, SWy-3 and Czech bentonites, as well as three types of metal coupons: Reference carbon steel from Nagra, Reference copper from SKB and Reference carbon steel from SURAO. Experiments were performed with compacted materials at two densities: 1.4 g/cm^3 and 1.6 g/cm^3.

In the large scale *in situ* ABM5 experiment, all bentonites preserved their hydro-geochemical properties, after being subjected to saline groundwater infiltration, heating and interaction with corroding metals during 4.4 years of experiment. The main change observed in all bentonites is the modification of exchangeable cation composition, explained on the basis of equilibration with Äspö saline groundwater enriched with Ca and Na salts. The initial bentonite pore water was modified in all bentonite blocks after their interaction with the saline Na-Ca-Cl groundwater. Pore waters changed from mainly an initial Na-Cl or Na-SO$_4$ water type towards a Na-Ca-Cl pore water in all bentonite blocks analysed, except for MX-80 block 1, which changes from Na-SO$_4$ to Na-Cl water-type. Probably water-vapor fluxes increased the salinity of the pore waters at the top part of the package.

Fe increased as a function of the distance to heater contact. Heater corrosion provoked the increase of iron in the bentonite, and goethite, hematite and siderite were found as corrosion products. No magnetite was detected. Although the ratio of ferrous to ferric iron increased in the close vicinity of the C-steel heater, major Fe content is as Fe(III).

EURAD (Deliverable n° 15.12) – Identification on the effect of transient processes on corrosion
Dissemination level: Public
Date of issue of this report: **29/04/2024**

Page 92

The main corrosion product detected in all the laboratory experiments performed with C-steel metals is magnetite, which is transformed in other Fe(III) mineral phases as a function of the oxygen content in the environment. Overall, results for experiments under dynamic conditions are comparable to that obtained under static conditions when reducing conditions prevail. The corrosion rates increase with temperature, the degree of salinity of the porewater and decrease with the dry density. The corrosion rates obtained in these transient experiments with carbon steel coupons ranged from 28 to 413 µm/year, depending on the salinity of the pore water and the dry density of the bentonite. Higher corrosion rates were observed for high saline pore waters and lower dry densities, as observed for FEBEX bentonite compared to SWy-3 and Czech bentonites. In any case, the extent of alteration inside the bentonite was < 2 mm in all bentonite samples, smectite clay particles being preserved.

In the case of laboratory experiments performed with SKB Cu-OFP metal, the main corrosion product is cuprite, although a minor amount of tenorite was detected in interactions with Czech bentonite. Azurite and mainly malachite also was observed at the bentonite/coupon contact. The corrosion rates obtained were much lower than those obtained in experiments with carbon steel coupons, with values ranging from 3 to 9 µm/year. The extent of alteration inside the bentonite was < 0.5-1 mm in all bentonite samples, and no alteration of smectite clay particles were detected.

EURAD (Deliverable n° 15.12) – Identification on the effect of transient processes on corrosion
Dissemination level: Public
Date of issue of this report: **29/04/2024**

Page 93

3. GRS experiments and results in Task 5

The experiments performed at GRS were designed for obtaining more mechanistic information about the reaction processes during the first stages of the corrosion triggered after contact of spheroidal graphite cast iron with bentonite saturated with geologic water. In this case, the oxygen enclosed during sealing process is expected to dissolve in the geological waters percolating through the bentonite barrier. The evolution of the dissolution rate and corrosion potential were monitored by applying electrochemical techniques, such as potentio-dynamic polarisations (current-voltage curves) and electrochemical impedance with minimal perturbation of the interfacial reaction system. The interpretation of electrochemical results was aided with topographic and chemical surface analysis.

Answers to the questions referred to the relevance of the oxygen reduction reaction at the initial stages of corrosion and the influence of graphite spheres in the building of local galvanic elements are targeted. The influence of gamma-radiation during these first corrosion stages was also analysed aiming at a more complete picture of the possible reaction scheme in real conditions. These experiments can be categorised as model experiments because the affecting factors, such as oxygen content and radiation dose rate were set beyond typical values expected for a repository. This is expected to enhance long-term features in the comparatively short test times.

3.1 Middle-term corrosion experiments of GGG40 cast iron in saturated Wyoming bentonite

These experiments were designed for monitoring of the corrosion of spheroidal graphite cast iron (GGG40) in contact with a slurry of Wyoming bentonite and Opalinus Clay water during a period 90 days. Naturally air saturated synthetic pore water was used for the preparation of the slurry. Thus, these conditions are thought to reproduce the very initial corrosion processes upon intrusion of water in the steel-bentonite interface in the cooling-down phase after repository closure. Dissolved oxygen in the disposal is provided by air trapped in voids of the closure filling materials.

The experiments were performed in a so-called bentonite-cell (see *Figure 82*). The slurry and the supernatant liquid with their original content of dissolved oxygen are separated from each other by a perforated plate which maintains a constant slurry porosity and avoids turbulences. Further incoming of oxygen from the surrounding is avoided by fluxing argon at the upper part of the cells connected to water traps.

The corrosion process was monitored by measuring:

(i)   the corrosion or open circuit potential (OCP),
(ii)   impedance spectra in the frequency region of 10^5 to 10^{-3} Hz at the OCP and
(iii)   polarization curves at 0.166 mV s^{-1} from -0.1 V vs OCP until reaching an anodic current of 15 µA.

3.1.1 Experimental details

Figure 82 shows a schematic of the bentonite cell used for the corrosion experiments without including the electrodes for electrochemical measurements. 80 g of Wyoming bentonite were mixed with 800 g of artificial Opalinus Clay pore water, the composition of which is given in *Table 18*. The suspension was allowed to decant for 24 h. The supernatant liquid was separated from the slurry. This latter was introduced in the bottom part of the cell. Thereafter, the supernatant solution was introduced from the upper part of the cell. According to the volumes before and after decantation observed in a separate experiment, the ratio Vsolution/(Vparticles + Vsolution) in the slurry is about 0.93.

The concentration of dissolved oxygen measured in the supernatant liquid at the beginning of the experiment was 8.21 mg l^{-1}. At the end of experiment, the concentration of the sample taken near to the separating plate was 7.56 mg l^{-1}. During the whole experiment, the upper empty region over the liquid was flooded with Ar (no bubbling).

EURAD (Deliverable n° 15.12) – Identification on the effect of transient processes on corrosion
Dissemination level: Public
Date of issue of this report: 29/04/2024

Page 94

The used Wyoming bentonite was characterized by (Kaufhold et al, 2008, 2015a). The composition of the bentonite is reproduced in *Table 18*.
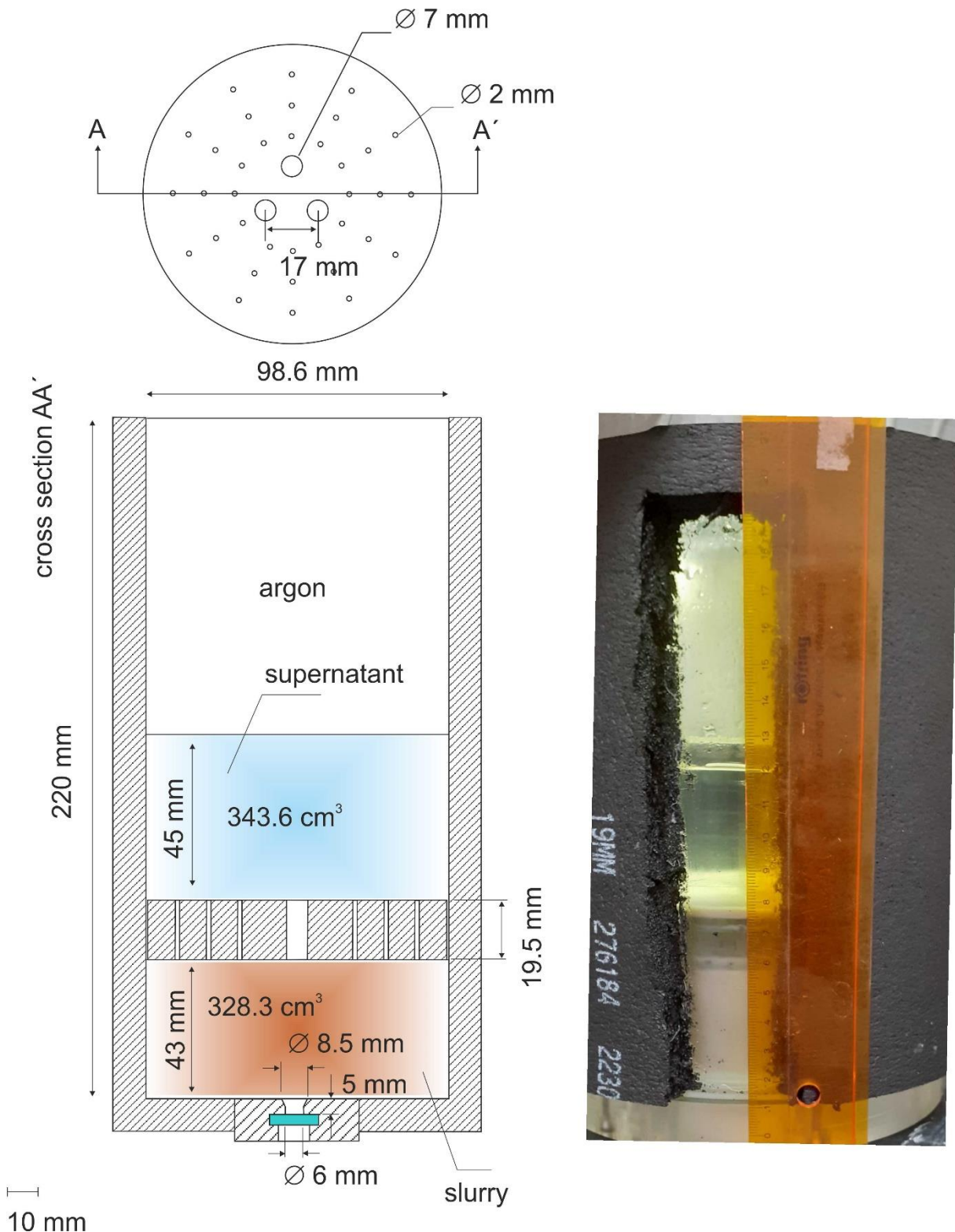
Figure 82 – (Left) Schematic of the bentonite-cell showing geometrical dimensions; (Right) Picture of the cell.

EURAD (Deliverable n° 15.12) – Identification on the effect of transient processes on corrosion
Dissemination level: Public
Date of issue of this report: **29/04/2024**

Page 95

3.1.2   Corrosion rate

The corrosion process was monitored by measuring the corrosion potential, the polarization resistance and polarization curves at regular intervals. Originally, the corrosion rate was intended to be calculated from the polarization resistance, measured by Nyquist impedance diagrams, using the Stern-Geary equation. The results obtained in this way, however, deviate considerably from those obtained from polarization curves. After an analysis of the impedance spectra, it was found, that the impedance signal is dominated by the dielectric and conducting properties of the bentonite. The diffusion of dissolved oxygen in the slurry should also complicate the ongoing interpretation of the impedance spectra. Therefore, corrosion rate cannot be simply calculated by the well-known Stern-Geary equation, were the cathodic and anodic reactions are assumed to follow a Butler-Volmer kinetics and an evaluation of the specific kinetic aspects are still necessary.

*Figure 83*a shows as an example one of the measured polarization curves. The polarisation was run by -100 mV respective the corrosion potential in the anodic direction. The cathodic-anodic transition defines the zero-current point, from which the corrosion potential and the corrosion rate can be derived. This transition, however, cannot be directly defined because of the noisy signal characterizing these curves, which cannot be attributed to a technical artefact. The random oscillation of the current defines an upper and lower current limit (see enlargement in *Figure 82*b). This indicates a metastable system which alternated between to dissolution mechanisms as discussed below. Because the experiment is a potential-controlled one, the net oscillating current is the sum of the kinetically controlled anodic dissolution of iron, the kinetically controlled water reduction, and the transport-controlled oxygen reduction. Both reduction reactions, however, bring about a strong local alkalisation, which can perturb the system by a precipitation of passivating products. The mean current values and the maximal diffusion-controlled corrosion limit were extracted from the measured polarization curve and presented as log I vs V diagrams in *Figure 84*a. The corrosion potential and the corrosion current were measured by extrapolating the cathodic and the anodic branches to the zero-current point. The values are presented in *Figure 84*b and c for temperatures of 30 °C and 50 °C.
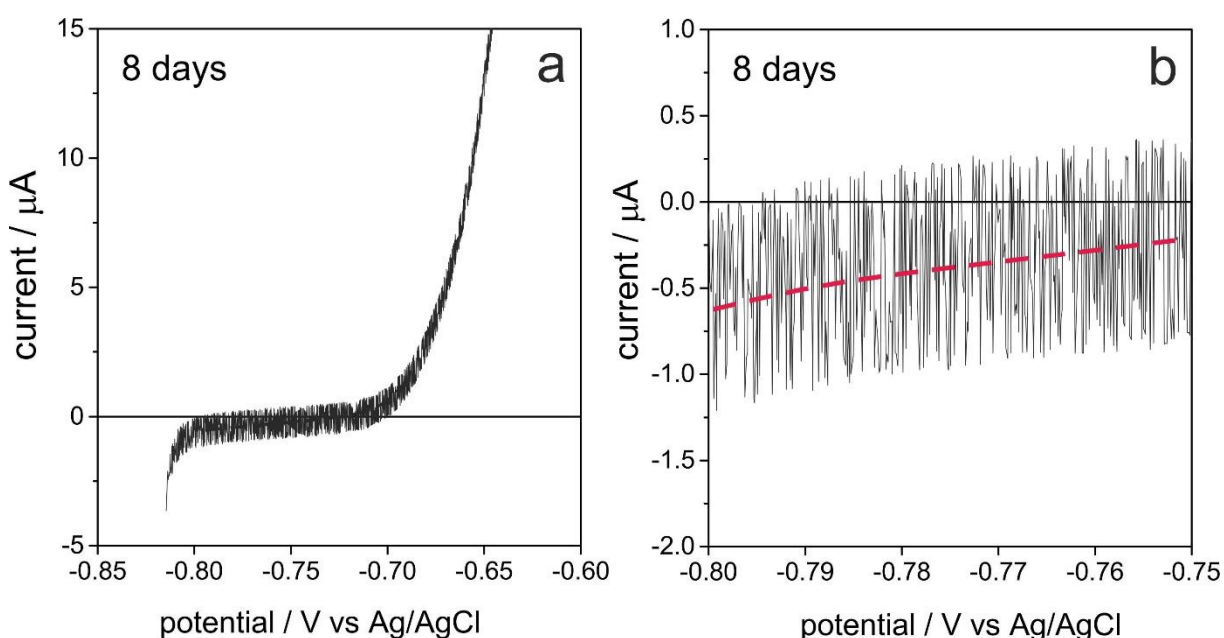
Figure 83 – (a) Polarization curve of GGG40 after 8 days in contact with saturated bentonite at 30 °C. v: 0.166 mV s^{-1}; (b) enlargement of a part of the polarization curve in (a) with indication of the mean value (red dashed line).

EURAD (Deliverable n° 15.12) – Identification on the effect of transient processes on corrosion
Dissemination level: Public
Date of issue of this report: **29/04/2024**

Page 96
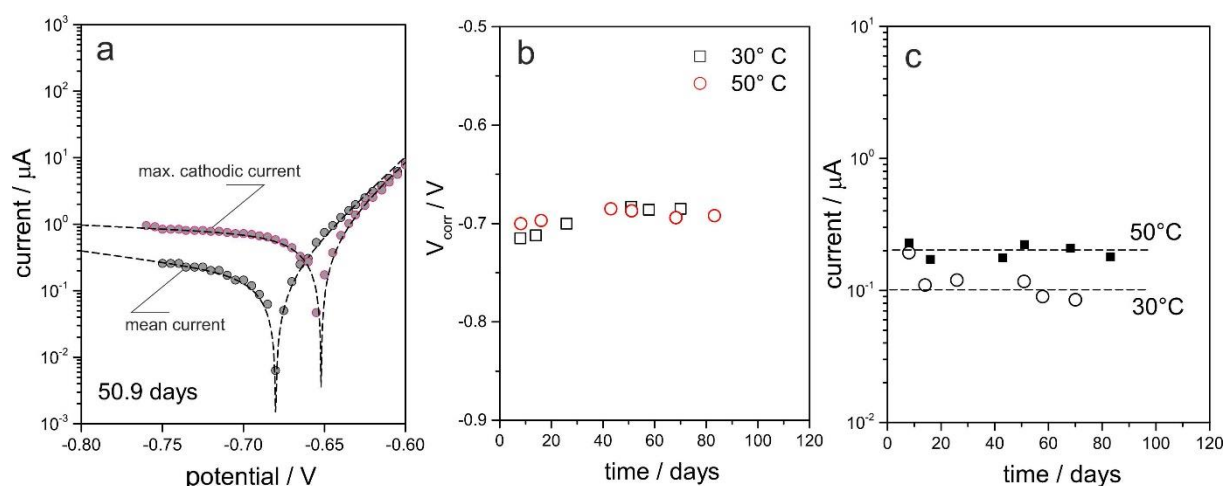
Figure 84 – (a) Mean and maximum current values as log I vs. V extracted from the polarization curve of GGG40 after 50.9 days in contact with saturated bentonite at 30 °C. v: 0.166 mV s⁻¹; (b) and (c) corrosion potential and corrosion current, respectively, obtained from the log I vs. V curves for the mean polarization currents.

The corrosion currents calculated from the mean values of the polarisation curves oscillate around mean values of 0.1 µA and 0.2 µA for GGG40 in contact with saturated bentonite at 30 °C and 50 °C respectively. The GGG40 cast iron has an iron content of w/w % 92.69 and a density of 7.3 g cm⁻³. Assuming a dissolution reaction Fe → Fe(II) + 2 e⁻, it is possible to calculate the corrosion rate as µm/y by:

$$[\mu m/y] = I_{corr} \cdot 3.154 \cdot 10^7 \text{ s y}^{-1} \cdot 55.85 \text{ g mol}^{-1}/ (2 \cdot F \cdot [w/w\%Fe / 100] \cdot \rho \cdot A) \qquad \text{Equation 2}$$

where I_{corr} is the corrosion current in Ampere, F is the Faraday constant (96500 C mol⁻¹), ρ is the density of the cast iron in g cm⁻³ and 55.85 g mol⁻¹ is the molar mass of iron. Applying (1) we obtain corrosion rates of 6 ± 1µm/y and 13 ± 1 µm/y at 30°C and 50°C respectively. These values are in line with those obtained by mass loss measurements in coupon experiments carried out by KIT-INE (see section 3).

Figure 85 a shows the polarization of GGG40 and graphite in anoxic and air saturated Opalinus Clay water at 30°C. The electrochemical behaviour should reflect that expected for the cast iron surface free of bentonite. The cathodic branches of the curves of GGG40 resemble those for the maximum and mean current values for the polarization at the bentonite-cast iron interface. Thus, it is feasible that the random current oscillations observed in the polarization curves arise from surface instabilities generated by counteracting dissolution and passivation events. The adhesion of bentonite particles in the form of smectite and various silicates creates small cavities on the surface which limit the inward and outward mass transport of reactants and corrosion products. The strong alkalization resulting from the oxygen reduction is supposed to bring about a local precipitation of iron oxide/hydroxide which blocks further reaction. The passivity, however, is rapidly distorted by diffusion/migration processes and by the presence of chloride. A metastable situation, like that observed before pitting arises.

The current transient obtained by applying a potentiostatic pulse at the cathodic side (shown in *Figure 85*b shows a tendency to a linear course at long times when represented as I vs $t^{1/2}$. This indicates a diffusion-controlled process, described by the Cottrell equation:

$$I = I_k + zF \, A \, D^{1/2} \, C \, \pi^{-1/2} \, t^{-1/2} \qquad \text{Equation 3}$$

Where I_k is the current of a kinetically surface reaction, z is the number of electrons involved in the diffusion-controlled reaction, C and D are the concentration and the diffusion coefficient of the active species (oxygen) respectively. *Figure 85*b shows the linear Cottrell relation we would obtain assuming

EURAD (Deliverable n° 15.12) – Identification on the effect of transient processes on corrosion
Dissemination level: Public
Date of issue of this report: **29/04/2024**

Page 97

a D_{O2} = 2.236·10^{-5} cm^2 s^{-1} (30 °C) (Han & Bartels, 1996) and a C_{O2} = 8.6 mg l^{-1} (2.68·10^{-7} mol cm^{-3}). Assuming that the diffusion-controlled reaction is the oxygen reduction (see *Figure 86*):

$$O_2(aq) + 4\ e^- + 2\ H_2O \rightarrow 4\ OH^- \qquad\qquad \text{Equation 4}$$
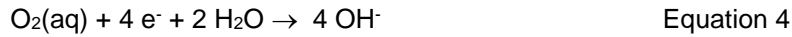
the ratio of the electro-active area free of bentonite to the geometric electrode area is given by A_{elect} /A_{geom} = $p_{bentonite}$ /p_{free} =1 / 6.7, where A_{geom} is the geometric area of the electrode: 0.282 cm^2; $p_{bentonite}$ and p_{free} are the slopes of the I vs t$^{-1/2}$ curves for the electrode in bentonite and for a free diffusion, respectively.
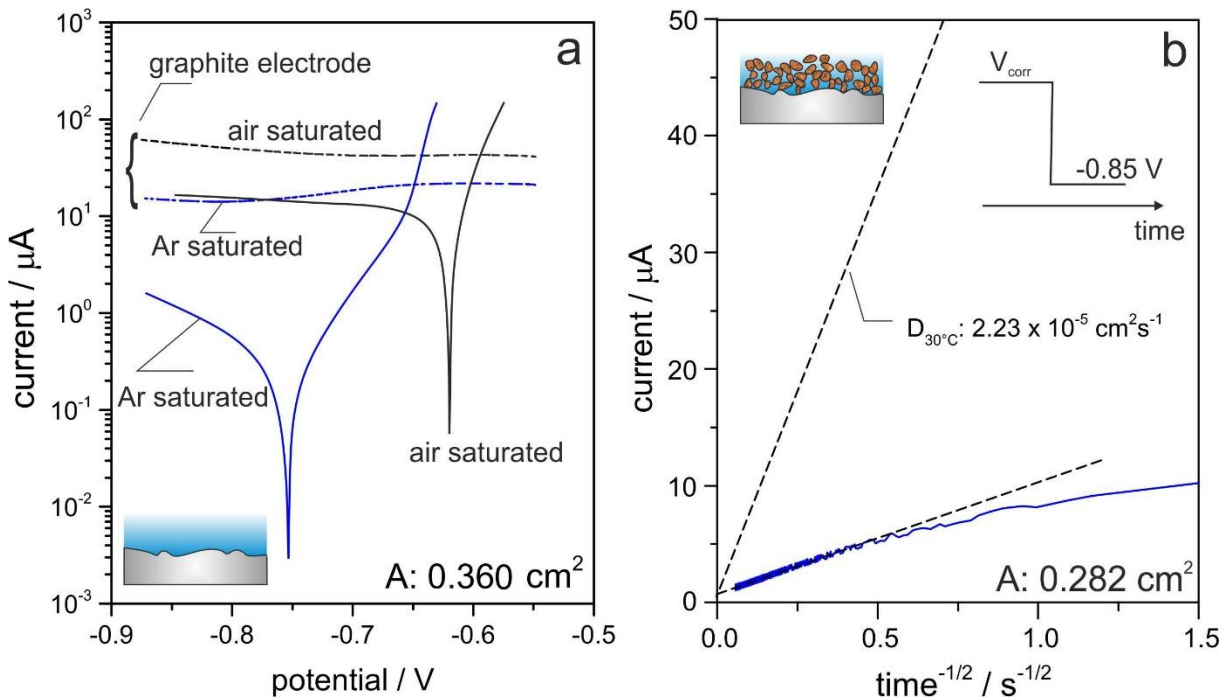
Figure 85 – (a) Polarization curves of GGG40 and graphite in Opalinus Clay water at 30 °C in anoxic and air saturated solutions (ca. 8.6 mg l^{-1} of O$_2$); (b) current transient recorded on applying a potentiostatic pulse for GGG40 in contact with saturated bentonite at 30 °C.
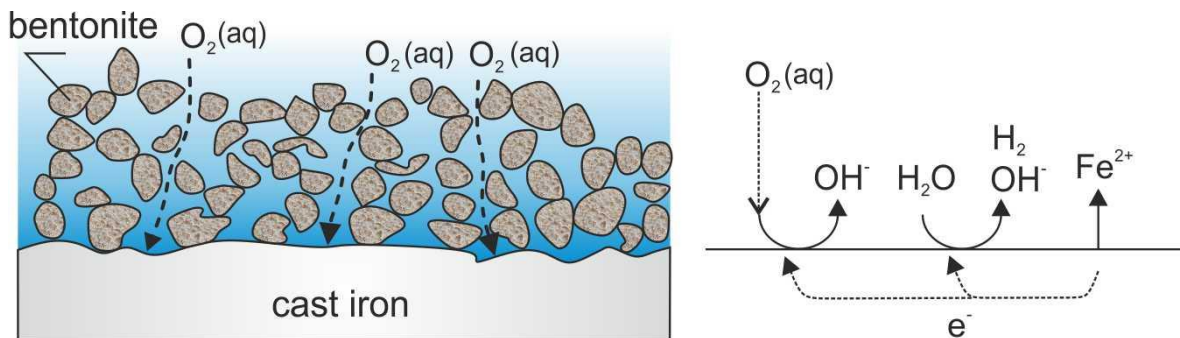
Figure 86 – Model of the cast iron-bentonite interface used for the interpretation of results of electrochemical experiments.

EURAD (Deliverable n° 15.12) – Identification on the effect of transient processes on corrosion
Dissemination level: Public
Date of issue of this report: 29/04/2024

Page 98

The extrapolation of the linear part of the transient to t $\rightarrow \infty$ yields a mean value of I_k = 0.73 µA. This current should correspond to the water reduction:

$$2\ H_2O + 2\ e^- \rightarrow H_2 + 2\ OH^- \qquad \qquad \text{Equation 5}$$

From the polarization curve in *Figure 85*a, the water reduction on GGG40 at 30°C can be described by:

$$I_w\ [\mu A] = 0.273 \times \exp\ [-38.287 \times 0.413 \times (V + 0.753)] \qquad \text{Equation 6}$$

considering a bentonite free area, A: 0.360 cm^2; the potential V is referred to Ag/AgCl (3M NaCl): +0.209 V (vs. NHE). Thus, the water reduction current for the bentonite covered electrode near the corrosion potential can be estimated as: $I_{water-red-bentonite}= I_w$ (V: -0.7 V) $\times$ [A_{geom} / 0.360 cm^2] = 0.09 µA, where I_w is the water reduction current calculated by Equation 6. This value is near that of the corrosion current.

3.1.3   Chemical changes of the liquid phase

The analysis of the supernatant solutions after the middle-term experiments performed at 30 °C and 50 °C are shown in *Table 18*. For 30°C the composition does not vary significantly compared with that after 4 weeks in contact with bentonite at room temperature. A concentration increase of most elements is observed, however, for 50 °C. This can a priori be explained by a larger intake of water by bentonite with temperature by formation of hydrates. The increase of the concentrations of Ca and Na could be ascribed to higher dissolution of minerals contained in the bentonite.

Table 18 – Elementary composition of artificial Opalinus Clay pore water contrasted with the ICP-OES results of solutions standing in contact with Wyoming bentonite. The pH of the pore water was 7.6. The analysed elements were selected regarding the elementary composition of bentonite.

Element	Opalinus-Clay water [mol/kg]	after 24 h [mol/l] pH: 8.09	after 4 weeks [mol/l] pH: 8.00	solution after experiment at 30 °C	solution after experiment at 50 °C
Na	0.240	0.262	0.261	0.269	0.305
K	0.00161	0.00201	0.0022	0.0023	0.0030
Mg	0.0169	0.0111	0.0114	0.0111	0.0148
Ca	0.0257	0.0073	0.0074	0.0074	0.0240
Sr	0.00065				
Cl	0.299	0.266	0.267	0.280	0.353
SO4	0.0140	0.0168	0.0174	0.0182	0.0195
HCO$_3$	0.00048				
Si		0.00033	0.00052	0.00070	0.00095
Al		< 1.5$\cdot$10^{-7}	< 1.5$\cdot$10^{-7}		
Fe		< 1.8$\cdot$10^{-8}	< 1.8$\cdot$10^{-8}		
P		< 3.2$\cdot$10^{-6}	< 3.2$\cdot$10^{-6}		

EURAD (Deliverable n° 15.12) – Identification on the effect of transient processes on corrosion
Dissemination level: Public
Date of issue of this report: **29/04/2024**

Page 99

Table 19 – Chemical composition of the used Wyoming bentonite (Kaufhold et al., 2008, 2015a).

%w/w	SiO$_2$	TiO$_2$	Al$_2$O$_3$	Fe$_2$O$_3$	MnO	MgO	CaO	Na$_2$O	K$_2$O	P$_2$O$_5$	LOI
Wyoming bentonite	59.2	0.2	19.2	3.7	0.0		1.3	2.3	0.5	0.1	10.7

3.1.4   Corrosion products

The surface chemistry after the experiments was analyzed by EDX and localized XPS: some results are presented in Figure 87 and *Figure 88.* According to the elemental analysis obtained with EDX, it can be suggested, that the corrosion products consist of iron oxides mixed with silicates. The similar atomic percentage of Si and Na lets us infer that silicates come from adhered bentonite particles. This is supported by local XPS core level spectra of Na, Si and Al. The EDX analysis also shows a strong Cl-signal associated to iron and oxygen signals, which cannot be assigned to NaCl crystals arising from drying of the solution contained in the bentonite slurry film retained on the sample surface. The deconvolution of XPS Fe 2p spectra indicate a ratio of Fe(III):Fe(II) of about 2:1 with particularly large satellite lines, which can be ascribed to Fe-OH bonds (Grosvenor et al., 2004). The O 1s signal indicates a similar among of O- and OH- bounds. Practically, the complexity of the composition of the corrosion products and the amorphous nature of corrosion precipitates formed at the initial stages of the steel-bentonite contact makes it difficult to identify them in terms of reference compounds. The following products or mixtures of them may be proposed:

- Goethite FeOOH
- Green rust [Fe(II)$_3$Fe(III)(OH$^-$)$_8$]$^+$ · [Cl$^-$·n H$_2$O]$^-$
- Fe$_2$O$_3$
- Fe(II) intercalated in Bentonite

element	% at 1 Iron	4 Iron oxide-chloride	3 Iron oxide-silicate	2 Steel phases	5 Steel phases
C	6.1		3.5	4.9	5.7
O	52.3	38.2	29.6	4.4	2.3
Na			2.1	2.0	
Mg		0.1	2.1	1.2	
Al	0.3	0.3	3.2		
Si	2.9	3.1	9.6	4.6	0.6
S	0.2		0.8	0.6	
Cl	5.8	29.4	0.4	0.4	
Cr					2.0
Mn					0.6
Fe	32.4	28.9	48.7	81.9	88.9
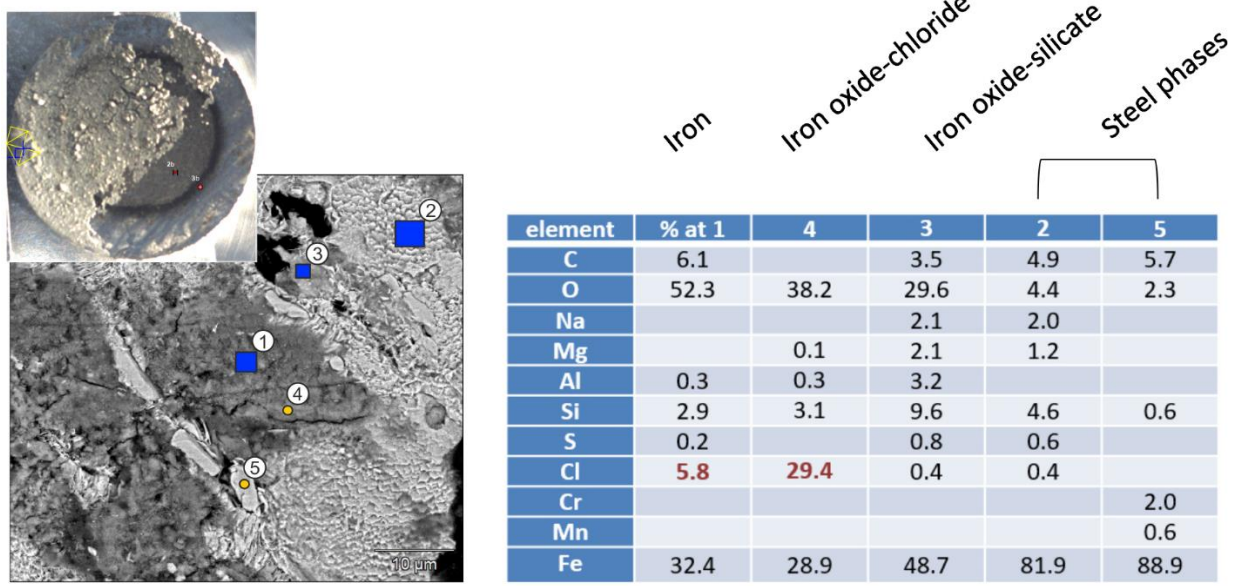
Figure 87 – SEM-EDX analysis performed inside the area free of bentonite.

EURAD (Deliverable n° 15.12) – Identification on the effect of transient processes on corrosion
Dissemination level: Public
Date of issue of this report: **29/04/2024**

Page 100
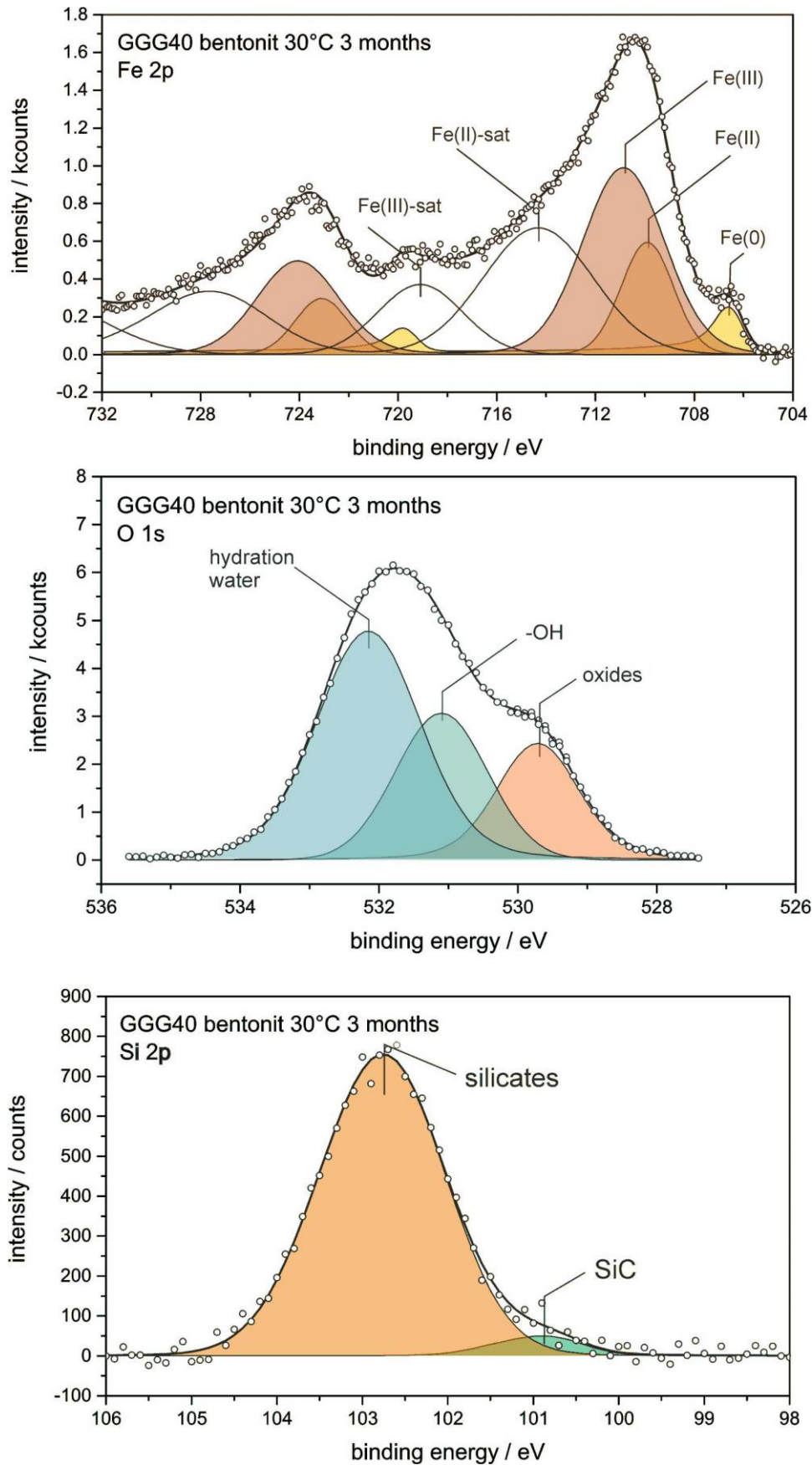
Figure 88 – XPS core level Fe2p, O 1s and Si 2p spectra obtained by focusing the X-ray spot on the area free of bentonite.

EURAD (Deliverable n° 15.12) – Identification on the effect of transient processes on corrosion
Dissemination level: Public
Date of issue of this report: **29/04/2024**

Page 101

3.2 Corrosion of cast iron GGG40 under γ-radiation

This experiment constitutes a cross-investigation as a collaboration with Task 3. It consists in the corrosion of cast iron GGG40 in saturated Wyoming bentonite in a ratio 1:10 using Opalinus Clay water, just the same conditions as initially in the electrochemical experiments described before. Four samples were put inside a liner manufactured with PEEK in a stainless-steel reactor (see *Figure 89*). This was closed tightly and γ-irradiated for 220 days in the Panoza-facility of UJV-Rez (Prague). The temperature was set to 50 ⁰C by an electric oven. The dose rate, measured with a dosimeter inside the reactor, was 130 kGy/ h.

The reactor was open in the glove box. The oxygen content measured in the supernatant solution was 0.03 mg l^{-1}, indicating the building of an anaerobic atmosphere. The ICP-OES analysis of a filtrate of the supernatant liquid indicated the formation of NO_3^- and NO_2^- by $6.45 \cdot 10^{-6}$ mol l^{-1} and $1.52 \cdot 10^{-5}$ mol l^{-1} respectively and $3.6 \cdot 10^{-3}$ mol l^{-1} of a sulfur compound different from SO_4^{2-}, probably HS^-. The pH of the solution was 8.

A preliminary analysis of the XPS spectra from the bentonite-free surface (see *Figure 90*) indicates the formation of fundamentally $Fe(OH)_2$ and silicates. The Fe2p was deconvoluted taking into account the multiple splitting (Grosvenor et al, 2004).

In addition, mass loss measurements were carried out, following the procedure described in the ASTM Standard G1 − 03 (Reapproved 2011). According to this, a corrosion rate of 52 μm y^{-1} was calculated considering a homogeneous degradation on the whole pellet. This value is ca 5 times larger than that determined electrochemically without radiation.
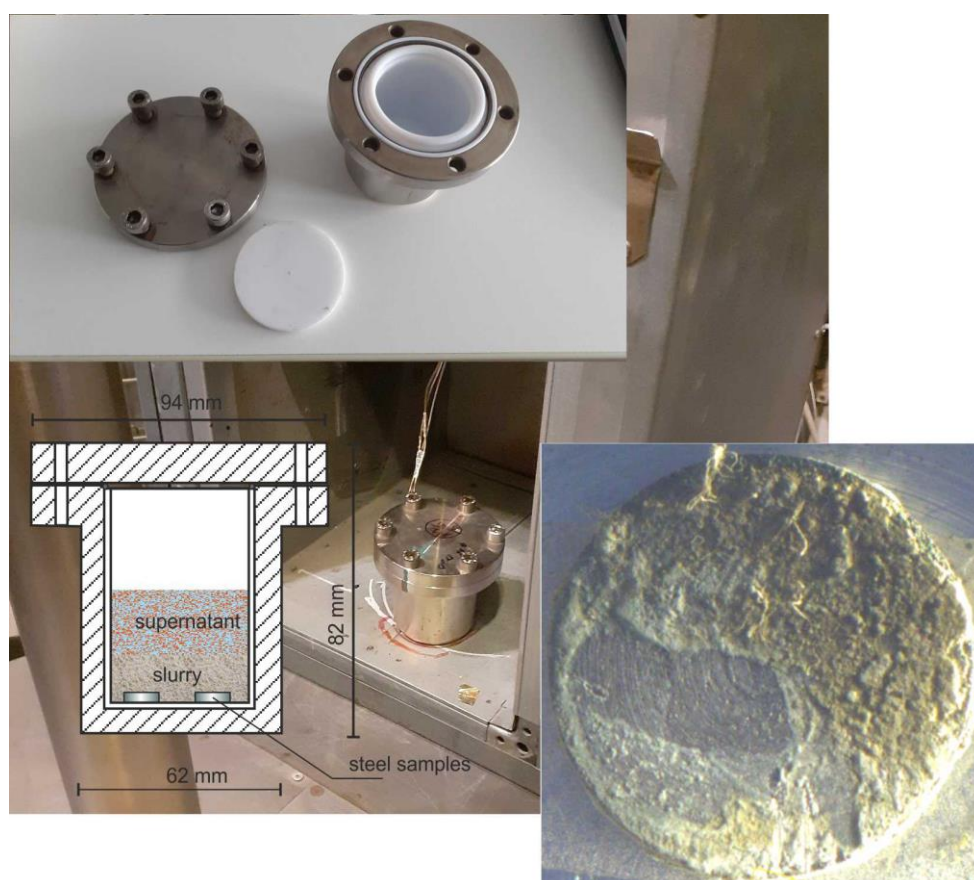
Figure 89 – Picture describing the experimental set up. Picture at the right-bottom corner shows the optical aspect of the sample after finalization of the experiment.

EURAD (Deliverable n° 15.12) – Identification on the effect of transient processes on corrosion
Dissemination level: Public
Date of issue of this report: 29/04/2024

Page 102
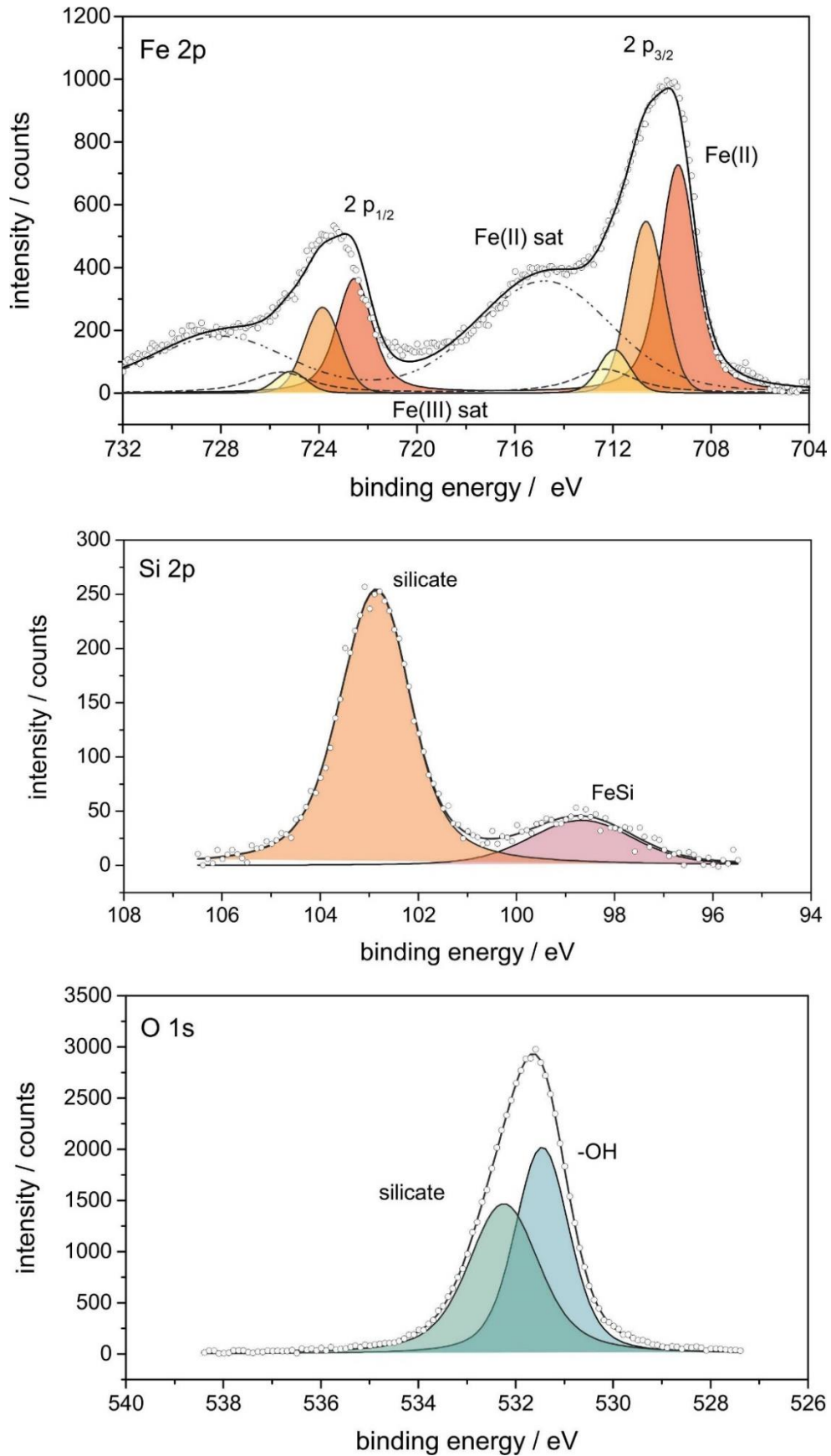
Figure 90 – XPS core level Fe2p, O1s and S2p performed on the corroded cast iron surface free of bentonite.

EURAD (Deliverable n° 15.12) – Identification on the effect of transient processes on corrosion
Dissemination level: Public
Date of issue of this report: **29/04/2024**

Page 103

3.3   Summary and conclusions

Electrochemical investigations of the first stages of corrosion of spheroidal graphite cast iron (GGG40) were carried out in contact with Wyoming bentonite oversaturated with artificial Opalinus Clay water (slurry) using a dedicated electrochemical cell. The corrosion rate was monitored by low current polarisation curves in runs of 3 months at temperatures of 30°C and 50°C. The corrosion rate and corrosion potential were observed to remain relative stable in this period of time with values of 6 and 13 μm a^{-1} for 30 °C and 50 °C, respectively. These values are in line with those obtained from coupons experiments in anoxic conditions carried out by other institutions (see next section). The electrochemical investigations have shown that at the corrosion potential, the oxygen reduction is mass controlled, the diffusion of oxygen being restrained by the slurry. Thus, the kinetically controlled water reduction seems to predominate. The polarisations were characterized by random current oscillations between two well-defined limits that are probably due to precipitation effects as a consequence of the stark local alkalization promoted by the closed spaces left by the slurry.

The effects of γ-radiation during the first stages of corrosion in the same slurry were analysed, this time by means of a coupon-experiment at 50 °C. The irradiation with a dose rate of 130 Gy h^{-1} increases the mean corrosion rate up to 52 μm y^{-1}. The enclosed oxygen was completely consumed inside the reactor and the iron (II) hydroxide predominates at the corroding surface. The causes of the acceleration of the corrosion rate are presently being pondered.

EURAD (Deliverable n° 15.12) – Identification on the effect of transient processes on corrosion
Dissemination level: Public
Date of issue of this report: **29/04/2024**

Page 104

4. KIT-INE experiments and results in Task 5

4.1 Motivation

The final disposal of high-level nuclear waste (HLW) in a stable deep geological repository (DGR) is the generally accepted strategy for dealing with this waste. In such a repository, the waste is foreseen to be emplaced in metallic containers and surrounded by various barriers in order to prevent or to significantly delay groundwater from reaching the HLW. However, during the long-term evolution of the repository system, water will move through the barriers and reach the containers which will start altering. Containers are usually proposed to be made of steel (i.e., Fe-based materials) and in some concepts, copper can be used as well because of its thermodynamic stability in anoxic environments characteristic of underground repositories located below the water table (in the absence of sulfide) (King, 2013). For the Safety Case of the DGR, detailed information regarding corrosion rate and mechanisms is needed. Such information can be obtained by performing corrosion experiments in the laboratory and also by performing or combining with *in situ* experiments in an underground research laboratory.

KIT-INE is currently partner of an *in-situ* corrosion experiment at the Grimsel Test Site in Switzerland, the Material Corrosion Test (MaCoTe) experiment (Reddy et al., 2020). In this experiment, selected candidate canister materials that may be of relevance in the context of deep disposal of HLW have been embedded within bentonite and exposed to natural borehole porewater. The goal of this experiment is to obtain information about corrosion rate and corrosion behavior of candidate canister materials for HLW under conditions representative of a DGR in granitic rock. KIT-INE selected six materials for the MaCoTe experiment, five Fe-based and one Cu-based materials.

The corrosion behaviour of materials typically envisaged in geological disposal is generally well understood, although some uncertainties exist (Padovani et al., 2017). Within the European Joint Programme on Radioactive Waste Management (EURAD), the Work Package 15 Container Corrosion under Disposal Conditions (ConCorD) aims at filling knowledge gaps related to coupled processes that can influence the accuracy of the Safety Case. One of these identified coupled processes is corrosion under transients, which is being tackled in Task 5 of CONCORD. The goal of this Task is to investigate about the effect of evolving e.g., chemical, mechanical and redox conditions on metallic corrosion. Indeed, the engineered barriers and the groundwater composition play a major role in the geochemical evolution of the DGR environment during the early repository closure phase, along with the thermal evolution. Unfortunately, the corrosion behaviour of canister materials has been usually studied under constant conditions, and thus for proper understanding of behaviour under expected conditions in the period following repository closure, dedicated experiments are needed.

KIT-INE is partner of Task 5 of ConCorD and selected two of the materials currently being tested in the MaCoTe experiment in order to identify the effect of specific transient conditions on their corrosion behavior. The goal of this study is to extend the knowledge regarding metallic corrosion of the selected materials by performing experiments under defined conditions in the laboratory. In the following, the selected materials and transient conditions will first be presented before the applied experimental approach will be described. Results will then be presented and discussed in the context of HLW disposal.

4.2 Definition of the systems

All experiments were performed with MX-80 bentonite and synthetic Grimsel groundwater (composition in *Table 20*) to have the same boundary conditions as in the *in situ* MaCoTe experiment at the Grimsel Test Site. Corrosion experiments were performed in 100 g/L bentonite suspension to allow *in situ* pH and E_h measurements at the end of the experiments, and thus deviate from compacted bentonite used in MaCoTe. It is expected that effects observed by changing one parameter using a bentonite slurry may still be transposable to experiments using compacted bentonite, for instance if increasing temperature increases the corrosion rate in slurry it would as well in compacted bentonite. Metallic coupons were used in all experiments and the ratio exposed metallic surface area to volume of suspension was kept constant.

EURAD (Deliverable n° 15.12) – Identification on the effect of transient processes on corrosion
Dissemination level: Public
Date of issue of this report: **29/04/2024**

Page 105

The first selected material is a spheroidal graphite cast iron (EN-GJS-400-15, abbreviated thereafter SGI, composition presented in *Table 21*). This material, often also referred to as nodular cast iron, was selected because it is among materials considered for the construction of canisters for a KBS-3V repository (Jonsson et al., 2018) and is also component of POLLUX® containers developed for direct final storage of heat generating nuclear waste. Owing to its high carbon content, using SGI as outer cask reduces the gamma and neutron dose rate.

Table 20 – Composition of the synthetic Grimsel groundwater (in mg/L) used in all experiments (*calculated from the amount of added salt). pH = 9.85 ± 0.10 and Eh = 115 ± 50 mV (vs S.H.E.) (pH and Eh measured in Ar-filled box).

Ion	Na	Ca	Si	F	Cl	SO$_4$	CO$_3$
mg/L	242.0	2.9	17.3	0.6	309.5	5.7	1.8*

Containers may undergo different degradation modes depending on their environment and their temperature (Terlain et al., 2001). When filled with HLW, they will be at the beginning at temperatures >100°C, and under these conditions dry oxidation is one possible degradation mode of container materials. Studies showed that under these conditions typical corrosion products are magnetite and hematite (Sewell and Cohen, 1964). Most reported study typically start with polished metallic coupons, and do not consider the presence of such oxic corrosion products. Thus, the effect of hematite presence on cast iron corrosion will be investigated in the present study. SGI will be prepared as polished coupon and exposed to bentonite suspension containing 0.5 wt.% hematite powder. Performing comparable experiments but in the absence of hematite will allow identifying the effect of hematite presence on cast iron corrosion.

The second material selected by KIT-INE in the present study is the cupronickel alloy UNS C71500 (or DIN 2.0882, abbreviated thereafter CuNi), which is mostly made of Cu with about 30 wt.% of admixed Ni (the exact composition is presented in *Table 21*). Countries such as Sweden, Finland and Canada envisage the use of copper in the construction of waste containers and the understanding of the degradation mechanism of this material is quite advanced. Interestingly, copper can be alloyed with nickel and some alloys, such as UNS C71500, find application in the construction of evaporators and heat exchange tubes, and also has an excellent corrosion behaviour in sea water. Copper corrodes under anoxic conditions in the presence of sulfide, but under repository conditions the amount of available sulfide will be limited and can be expected to increase progressively with time following repository closure in the very early stages owing to the development of bacterial activity. Unfortunately, in most laboratory Cu corrosion experiments reported in literature, a defined amount of sulfide is usually added at the beginning of the experiment, while under real repository conditions a continuous sulfide supply can be expected. In the present study, the corrosion behaviour of the selected alloy in the presence of a constant sulfide supply was investigated in order to mimic real case conditions.

Table 21 – Elemental composition in wt.%, as indicated on the inspection certificate DIN EN 10204/3.1, of the spheroidal graphite cast iron (SGI) and cupronickel alloy (CuNi) used in the corrosion experiments.

Element	C	Si	Mn	P	Mg	Cr	Fe	Cu	Ni
SGI	3.46	3.39	0.29	0.04	0.05	0.04	Bal.	0.04	-
CuNi	<0.01	-	0.95	<0.01	-	-	0.68	Bal.	30.43

EURAD (Deliverable n° 15.12) – Identification on the effect of transient processes on corrosion
Dissemination level: Public
Date of issue of this report: **29/04/2024**

Page 106

4.3   Experimental setup and details

4.3.1   Materials and experimental set-ups

All experiments, including analysis of the samples, were performed under anoxic condition using an Ar-filled or N_2-filled glove box, and airtight holders were used where needed. Solutions were prepared using ultrapure water (Milli-Q system, Millipore) and reagents of ACS grade or higher.

The source of sulfide was a commercial 1000 µg/mL IC certified standard solution (disodium sulfide nonahydrate in water, Sigma-Aldrich), and the used hematite was commercially available iron(III) oxide (Alfa Aesar). pH was measured using a combined electrode (LL Solitrode, Metrohm) that was calibrated on a daily basis, and redox potentials (E_h values) were measured using a Pt Ag/AgCl electrode (Radiometer Analytical) and corrected versus the standard hydrogen electrode (S.H.E.). All pH and E_h values in this study are those as recorded at room temperature and were not corrected for temperature.

The 100 g/L bentonite suspension was prepared in the glove box and homogenised mechanically on a daily basis, i.e., shaken by hand to obtain a homogeneous suspension. Suspensions were pre-equilibrated for 4 to 5 weeks to avoid parallel bentonite hydration and metallic corrosion. Coupons were first ground on SiC papers (P500, P800 and P1200) and then polished using a diamond-containing paste up to a roughness of 0.25 µm on all sides. Coupons were cleaned with ethanol, dried, weighed and placed inside the glovebox to avoid oxidation. The surface roughness was determined by atomic force microscopy using one coupon per material; results revealed a surface roughness of <50 nm. The composition of each material was assessed by SEM-EDX analyses using one polished coupon per material, values are in fairly good agreement with the certificate of analyses provided by the manufacturers.

Corrosion experiments were performed using two different setups. In the first more traditional approach, coupons were in contact with the bentonite suspension in a closed vessel and left to react. These experiments are referred to as under static conditions. Vessels are made of a stainless steel body and an inner liner and inner lid made of tantalum (Finck et al., 2023). The total inner volume is 90 mL and is filled with 50 mL suspension. Each vessel further contained 2 polished coupons (4 mm x 20 mm x 8 mm) placed on a PTFE stand (polytetrafluoroethylene, the stand was conditioned prior to use to avoid fluorine leaching).

A first series of experiments was performed at room temperature (thereafter also named 25°C) by simply leaving vessels in the glovebox following closure. A second series of experiments was performed at 50°C by using heating plates in order to identify any possible effect of temperature on corrosion processes. At both temperatures, contact times were 3 months and 6 months. In CuNi corrosion experiments using this setup, the sulfide content could not be changed over time so that a defined starting concentration of 3 µM was used. In SGI corrosion experiments, hematite was added as 0.5 wt.%. At the end of the experiments, vessels in experiments performed at 50°C were first allowed to cool down to room temperature before any further step.

Vessels were opened and pH and E_h values were measured *in situ* at room temperature. Coupons were subsequently taken out and the excess suspension was removed. The suspension was ultracentrifuged and the supernatant collected for analysis of the porewater composition.

The coupon was analysed by application of XRD, SEM/EDX and XPS. At last, the corrosion rate was calculated following determination of the weight loss according to the ASTM G1-03 (ASTM, 2011) standard practice. For samples corroded during 3 months, bentonite particles could not all be removed quantitatively from the coupons before determining the weight loss, implying that in some cases corrosion rates overestimate the actual value. For samples from 6 months experiments, care was taken to clean off all bentonite particles using isopropanol before determining the weight loss.

In the second approach, experiments were performed using a reactor having one inlet and one outlet and will be referred to as under dynamic conditions. Reactors are made of a stainless steel body and a PTFE inner liner, and are equipped at inlet and at outlet with metallic filters made of 316L stainless steel

European Joint Programme on Radioactive Waste Management

EURAD (Deliverable n° 15.12) – Identification on the effect of transient processes on corrosion
Dissemination level: Public
Date of issue of this report: **29/04/2024**

Page 107

(Tridelta Siperm GmbH, Germany) having a mean pore size of ~7 µm. Each reactor contained one coupon (4 mm x 8 mm x 8 mm) and ~3.1 mL of 100 g/L suspension. At inlet and at outlet, reactors were connected to tubing made of PEEK (polyether ether ketone) and a defined low water flow (2.5 ± 0.4 µL/min) was imposed using a peristaltic pump (Minipuls 3, Gilson) and calibrated tubing made of PVC having an inner diameter of 0.25 mm. The water was collected at specific time intervals at the outlet and weighed to determine the precise flow rate. pH and E_h were measured in the water that was then ultracentrifuged before being analysed by ICP-OES and IC. Only one series with a reaction time of 3 months could be performed and sampling times were 4, 5, 6, 8, 10 and 12 weeks. In CuNi corrosion experiments using this setup, the porewater initially contained no sulfide until week 6, then 1 µmol/L until week 8, subsequently 2 µmol/L until week 10 and finally 3 µmol/L until week 12. In SGI corrosion experiments, hematite was added as 0.5 wt.%. It should be noted that this design does not correspond to originally selected conditions in terms of amount of bentonite (initially planned were 35 cm^3 at a dry density of 1.25 g/cm^3) as presented in Deliverable 15.11, but it had to be selected because of technical reasons.

The list of all experiments performed in the present study is presented in Table 22 and Table 23.

Table 22 – List of corrosion experiments performed using spheroidal graphite cast iron (SGI), along with recorded pH (± 0.10) and Eh (± 50 mV) (values recorded at 25°C) and the determined corrosion rate (C.R., ± 15%) based on the measured weight loss (ASTM, 2011) (n.d. = not determined).

Condition	Applied transient	T (°C)	Duration (months)	pH	E_h (mV *vs* S.H.E.)	C. R. (µm/y)
Static	/	25	3	8.17	-441.	4.8
Static	0.5 wt.% α-Fe$_2$O$_3$	25	3	8.13	87	5.1
Static	/	50	3	8.13	-254	10.0
Static	0.5 wt.% α-Fe$_2$O$_3$	50	3	7.91	-149	10.6
Static	/	25	6	7.87	-47	2.6
Static	0.5 wt.% α-Fe$_2$O$_3$	25	6	7.74	-310	3.7
Static	/	50	6	7.73	-430	4.0
Static	0.5 wt.% α-Fe$_2$O$_3$	50	6	7.80	-420	6.9
Dynamic	/	25	3	9.2 to 9.7	-171 to -181	n.d.
Dynamic	0.5 wt.% α-Fe$_2$O$_3$	25	3	9.0 to 9.7	-167 to -179	n.d.
Dynamic	0.5 wt.% α-Fe$_2$O$_3$	50	3	9.0 to 9.7	-177 to -207	n.d.

4.3.2 Analytical techniques

In all experiments, the composition of the porewater was determined by ICP-OES (Optima8300DV, PerkinElmer) and IC (ICS 3000, Thermo Scientific) following ultracentrifugation (Beckman Coulter XL-90 K) for 1 hour at 50,000 rpm. For ICP-OES measurements, samples were acidified using nitric acid prior to measurements.

EURAD (Deliverable n° 15.12) – Identification on the effect of transient processes on corrosion
Dissemination level: Public
Date of issue of this report: **29/04/2024**

Page 108

The nature of crystalline phases was determined by X-ray diffraction analysis using a D8 Advance diffractometer (Bruker AXS) equipped with a Cu Kα source and a LynxEye XE-T detector. Anoxic conditions were ensured during measurements by using low background and air-tight holders. Phases were identified by comparison with the PDF-2 or COD (Grazulis et al., 2009) databases using the DIFFRAC.EVA v5.0 software (Bruker AXS).

Information on morphology and chemical composition of corroded coupons and secondary phases was provided by scanning electron microscopy (SEM, Quanta 650 FEG, FEI) and energy dispersive X-ray spectroscopy (EDXS, Thermo Scientific NORAN System 7 equipped with UltraDry™ silicon drift X-ray detector, Pathfinder X-ray microanalysis software v2.8). Electron micrographs were recorded either in backscattered electrons (BSE) or in secondary electrons (SE) mode. For selected corroded CuNi specimens, complementary electron backscatter diffraction (EBSD) analyses were carried out using a Crossbeam 350 KMAT (Zeiss) microscope equipped with an Oxford Instrument AZtec EDXS/EBSD system. Formed secondary phases having sizes ranging from 100 nm to 250 nm, no further specimen preparation method (e.g., surface coating) was used. EBSD patterns (Kikuchi patterns) were acquired by a Symmetry® S2 detector at a resolution of 622 x 512 pixels to ensure a good compromise between angular resolution and acquisition time.

The angle between surface sample and electron beam was set to 20°, and the working distance to 13 mm. An acceleration voltage of 15 kV was selected. Monte Carlo simulations (Casino 2.4.8 software (Drouin et al., 2007)) using 15 keV primary electrons showed that backscattered electrons are generated from a depth up to 150 nm at perpendicular incidence of electrons, which results in around 51 nm for the tilt angle of 20°, ensuring negligible contribution from the CuNi substrate. EBSD patterns were recorded and analyzed using the AZtec 6.1 (HF1) software (Oxford Instruments).

Table 23 – List of corrosion experiments performed using the cupronickel alloy (CuNi), along with recorded pH (± 0.10) and Eh (± 50 mV) (values recorded at 25°C) and the determined corrosion rate (C.R., ± 15%) based on the measured weight loss (ASTM, 2011) (n.d. = not determined).

Condition	Applied transient	T (°C)	Duration (months)	pH	E_h (mV *vs* S.H.E.)	C. R. (μm/y)
Static	/	25	3	8.17	225	1.2
Static	3 μM sulfide	25	3	8.09	271	1.1
Static	/	50	3	8.04	283	2.7
Static	3 μM sulfide	50	3	7.58	167	1.6
Static	/	25	6	8.09	287	0.1
Static	3 μM sulfide	25	6	7.94	245	0.1
Static	/	50	6	8.34	297	1.3
Static	3 μM sulfide	50	6	8.09	263	1.9
Dynamic	/	25	3	8.9 to 9.7	-166 to -179	n.d.
Dynamic	0-1-2-3 μM sulfide	25	3	9.4 to 9.5	-179 to -189	n.d.
Dynamic	/	50	3	8.9 to 9.5	-169 to -185	n.d.
Dynamic	0-1-2-3 μM sulfide	50	3	8.4 to 9.1	-171 to -183	n.d.

EURAD (Deliverable n° 15.12) – Identification on the effect of transient processes on corrosion
Dissemination level: Public
Date of issue of this report: **29/04/2024**

Page 109

Information on chemical composition and element speciation was provided by X-ray photoelectron spectroscopy (XPS) using a VersaProbe II from ULVAC-PHI (Al Kα monochromatic excitation, 1486.7 eV). The binding energy scale of the spectrometer was calibrated using well-established binding energies of pure metal (Cu $2p_{3/2}$ at 932.62 eV and Au $4f_{7/2}$ at 83.96 eV), and unless otherwise indicated the binding energy of elemental lines were charge-referenced to C 1s of adventitious hydrocarbon at 284.8 eV. The PHI MultiPak program v9.9 was used for data analysis. Curve fits to the Fe2p spectra were not applied because quantification of individual valence states is influenced by background function applied (Aronniemi et al., 2005). Spectra of Fe metal show asymmetric lines for Fe2p, whereas Fe(III)2p shows multiplet splitting and a shake-up satellite. Fits to Fe(III)2p spectra without knowing the parameters of the curve functions is not appropriate for exact quantification. Fe(II)2p spectra show a shake-up satellite at different binding energy than possible Fe(III)2p shake-up satellite. Fe2p spectra of the clay surface show predominantly Fe(II) exhibited by the Fe(II)2p shake-up satellite. A Fe(III)2p shake-up satellite is not clearly detected and Fe(III) concentration is thus expected within error margins of curve fits.

4.4   KIT-INE Results and discussion

4.4.1   SGI corrosion experiments under static conditions

The bentonite suspension was pre-equilibrated in the glovebox before starting the actual corrosion experiments. After 4 to 5 weeks of equilibration, pH was around 8.15 and E_h around 245 mV.

The *in situ* pH did not evolve much in SGI corrosion experiments carried out for 3 months (*Table 22*), and slightly decreased after 6 months. Overall, the presence of hematite only had a marginal effect. Metallic corrosion affected the redox potential that became clearly negative after 3 months except at 25°C with hematite present, and lower values were recorded after 6 months except in the experiment at 25°C in the absence of α-Fe₂O₃. Hematite is a pure Fe(III) compound and thus acts as an oxidizing agent. Indeed, after 3 months, the redox potential is systematically higher when hematite is present. Unfortunately, this trend is less clear after 6 months because at 50 °C the difference is within uncertainties and at 25 °C E_h is lower for SGI corroded in presence of hematite. Overall, reducing conditions developed as a consequence of steel corrosion, suggesting the formation of Fe(II)-bearing compounds. The absence of significant pH change may be related to bentonite acting as pH buffer.

Following *in situ* pH and E_h measurements, coupons were removed from the vessels for analyses. In some experiments, the SGI/suspension interface exhibited a slight blue/green colour indicating that some reaction had occurred. Colour is among properties of smectites that is greatly affected by redox reactions, especially for Fe-rich smectites (Stucki, 2011). Indeed, color changes appear because of changes in intra- and intervalence electron transfer transitions involving Fe(II), Fe(III), and O → Fe(III) charge transfer transitions. Structural iron in the starting MX-80 bentonite prevails as ferric ions, and metallic corrosion results in the formation of ferrous ions, which can interact with bentonite in suspension and result in electron transfer. The observed change of color may either suggest reduction of structural iron within the smectite component of the bentonite, or the formation of corrosion products (e.g., green rust compounds).

A fraction of the suspension was ultracentrifuged for application of ICP-OES and IC. The composition of the porewaters exhibits limited differences (data are presented in Milestone MS313) compared to that of the pre-equilibrated suspension used in the corrosion experiments, suggesting that metallic corrosion had only a negligible effect. Observed evolutions in contents are within experimental uncertainties. In the experiment for 3 months at 25°C in the absence of added hematite, the dissolved amounts of Fe reached 8.5 mg/L, while it was significantly lower in the other experiments. It is not yet entirely clear what caused this high Fe concentration, with the redox potential being very low (-441 mV, *Table 22*) in that experiment.

XRD analysis of the corroded specimens could only reveal the presence of structures characteristic of the coupon with its components iron, cementite and graphite (*Figure 91*). In addition, low amounts of

EURAD (Deliverable n° 15.12) – Identification on the effect of transient processes on corrosion
Dissemination level: Public
Date of issue of this report: **29/04/2024**

Page 110

bentonite components remaining on the surface could be detected (e.g., smectite, feldspars). No secondary phase presence could be detected, suggesting that either their amount was too low, that they are of too low crystallinity, or that they must have been removed when cleaning off the excess suspension.

Electron micrographs of the corroded SGI coupons show a non-uniformly corroded surface after 3 months. SGI has a pearlitic structure composed of alternating layers of ferrite (α-Fe) and cementite (Fe_3C), and contains graphite inclusions. Following exposure to the suspension, large fractions of the surface exhibit a lamellar morphology corresponding to cementite lamella, suggesting preferential removal of ferrite (*Figure 92*). The presence of hematite did not significantly affect the morphology of the surface damage of the exposed coupon, and no clear influence of temperature can be evidenced.

After 6 months of reaction, the surface is more damaged compared to 3 months, even at 25°C (*Figure 93*). The surface is particularly damaged within a small circular area surrounding graphite inclusions, suggesting preferential dissolution of iron without affecting the graphite. This observation may suggest the development of different electrochemical potentials at the surface of the conducting coupon between the inclusion and its immediately surrounding metal, whereby graphite would act as cathodic site. This spatial separation of anodic and cathodic sites results in the development of a galvanic cell (Schlegel et al., 2018), favourable to increasing the metallic corrosion, which thus can account for experimental observations. Interestingly, the presence of layered compounds can also be seen after 6 months at 25°C. Results from EDXS analysis indicate an Fe:O atomic ratio of 1:2 and rule out the presence of Cl or S, suggesting the most probable presence of $Fe(OH)_2$ but not green rust type compounds. This finding supports that conditions were clearly reducing at the coupon/suspension interface. Unfortunately, these layered compounds formed in too low amounts to be detected by XRD.
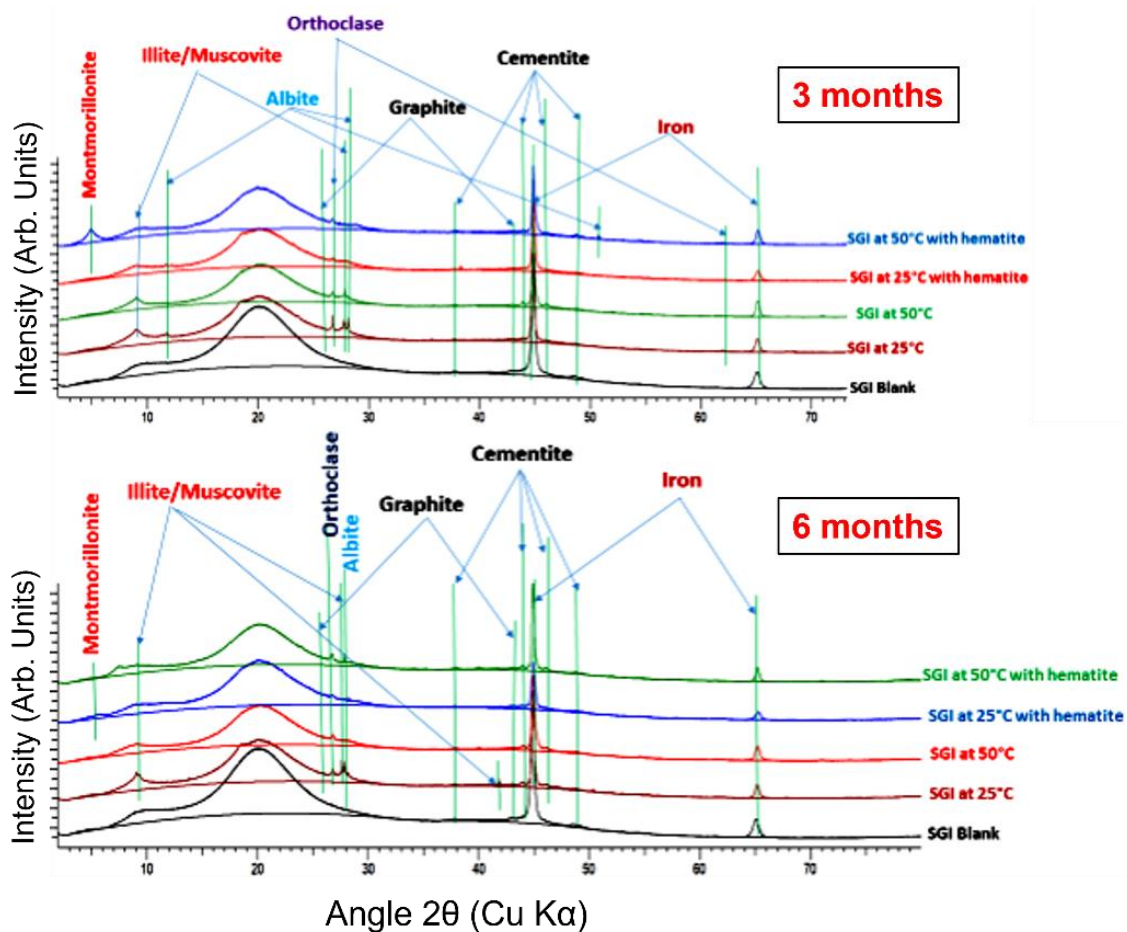
Figure 91 – X-ray diffractograms recorded on the corroded SGI specimens after 3 months (top) and 6 months (down) reaction time under static conditions.

EURAD (Deliverable n° 15.12) – Identification on the effect of transient processes on corrosion
Dissemination level: Public
Date of issue of this report: **29/04/2024**

Page 111

Figure 92 – Scanning electron micrographs (in BSE (left and centre) or SE (right) mode) of SGI coupons corroded for 3 months under static conditions (exact conditions are indicated above the micrographs).
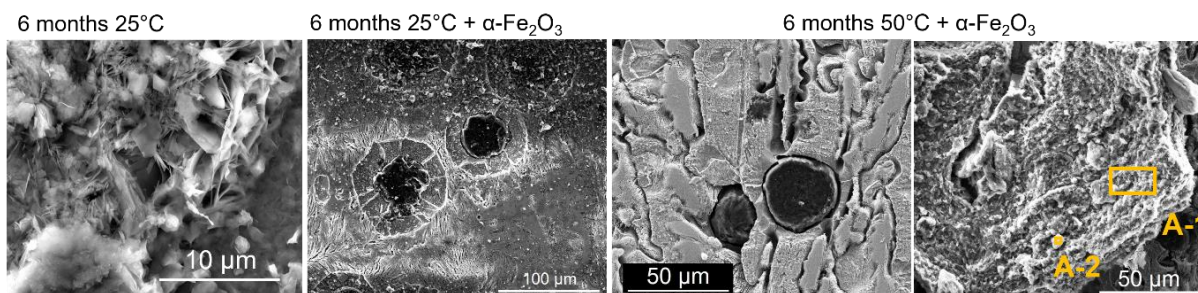
Figure 93 – Scanning electron micrographs (in SE mode) of SGI coupons corroded for 6 months under static conditions (exact conditions are indicated above the micrographs). Areas marked in orange were selected for EDXS analysis, quantitative results are provided in Table 24.

Information about chemical composition was provided by SEM-EDXS analysis at selected areas containing enough material to avoid probing simultaneously the adherent particles and the substrate underneath. This was for instance possible for SGI corroded for 6 months at 50°C with hematite present, at areas of the agglomerate shown on *Figure 93*. The compositions at both locations are very similar, containing substantial amounts of Si and Fe (14-19 at.%) with an atomic ratio close to ~1, and lower amounts of Al and Mg (*Table 24*). These values rule out the presence of only bentonite or hematite and instead may suggest the presence of Fe-rich secondary phases such as phyllosilicates of the kaolinite-serpentine group formed by condensation of one octahedral sheet with one tetrahedral sheet (TO type). This finding would be consistent with usually reported results for iron or steel corroded in contact with clay minerals (Lantenois et al., 2005; Lanson et al., 2012; Le Pape et al., 2015; Schlegel et al., 2018). According to reported findings from Pignatelli et al. (2013), together with the detection of Al presence in the present study, the formation of cronstedtite ($[Fe(II)_{3-x}Fe(III)_x][Fe(III)_xSi_{2-x}]O_5(OH)_4$) in the present work seems rather unlikely. Instead, results may suggest the formation of odinite ($[Fe(II),Fe(III),Mg,Al]_{2.5}[Si,Al]_2O_5(OH)_4$) or berthierine ($[Fe(II),Fe(III),Mg,Al]_3[Si,Al]_2O_5(OH)_4$). Unfortunately, neither of these compounds could be detected by XRD analysis, very likely due to their low amounts present.

EURAD (Deliverable n° 15.12) – Identification on the effect of transient processes on corrosion
Dissemination level: Public
Date of issue of this report: 29/04/2024

Page 112

Table 24 – Relative atomic concentrations by EDX analyses at selected areas shown in Figure 93. Relative errors are estimated to be within ± 10%.

Area	C	O	Na	Mg	Al	Si	Cl	Ca	Fe
A-1	3.1	52.1	1.0	0.9	4.1	19.1	0.2	0.5	19.0
A-2	6.9	59.2	0.6	0.8	1.4	16.8	0.4	/	13.9

XPS analyses provided complementary chemical information as well as speciation information. For all analysed samples, findings were very comparable. The Fe 2p spectrum recorded at the metal surface (*Figure 94*) evidenced the presence of metallic Fe, suggesting that no Fe-bearing secondary phase is attached to the surface. Low amounts of sulfide, indicated by the S $2p_{3/2}$ elemental line at 161.8 eV binding energy, were also detected at the coupon surface, most probably as iron sulfide (i.e., due to pyrite naturally present in the bentonite and sticking to the surface). Reference binding energies (Moulder et al., 1995) of the Fe $2p_{3/2}$ elemental line of Fe(0) (707.0 eV), FeO (709.4 eV) and FeS_2 (706.7 eV) are similar, whereas that of FeS (710.3 – 712.2) or Fe_3O_4 (708.2 eV and 710.4 eV), α-Fe_2O_3 (710.9 eV), and α-FeOOH (711.8 eV) clearly differ.
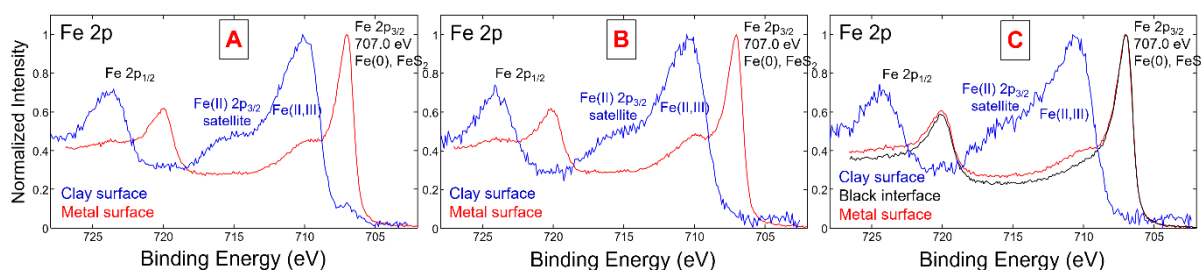
Figure 94 – X-ray photoelectron spectra recorded on the SGI corroded for 3 months at 25°C in absence of α-Fe_2O_3 (A), SGI corroded for 3 months at 50°C in presence of α-Fe_2O_3 (B) and SGI corroded for 6 months at 25°C in presence of α-Fe_2O_3 (C).

At the clay surface, Fe 2p spectra show shake-up satellites about 5 eV higher binding energies than the Fe 2p main lines, which is characteristic of Fe(II). Shake-up satellites of Fe(III), expected around 10 eV higher binding energy that the Fe 2p main lines are weak or not present. Interestingly, binding energy of Fe $2p_{3/2}$ lines are at about 710 eV, which is characteristic for iron oxides containing Fe(III), but also for Fe(II) in silicates. Even if Fe and Si have similar Pauling's electronegativity, the oxygen ion at Fe-O-Si may have stronger interaction with tetravalent Si than with Fe(II) or Fe(III) resulting in more positive charge on the Fe ion compared to iron oxides. Thus higher binding energy of Fe 2p photoelectrons emitted from Fe(II)-O-Si(IV) binding is expected (Seyama and Soma, 1987).

This finding would agree with the visual observation of a blue/green coloration at the coupon/suspension interface suggesting a possible reduction of structural Fe(III) within smectite. In addition, this finding would also agree with the presence of mixed Fe(II)/Fe(III)-bearing secondary phase such as odinite or berthierine suggested from SEM-EDX analysis. XPS data do not allow determining the nature of the compound(s) present at the interface but would in any case be consistent with the recorded negative redox potentials (*Table 22*). XPS data suggest that Fe prevails in divalent and in trivalent oxidation state at the coupon/bentonite interface in all experiments, and no significant impact due to the presence of hematite could be evidenced

EURAD (Deliverable n° 15.12) – Identification on the effect of transient processes on corrosion
Dissemination level: Public
Date of issue of this report: **29/04/2024**

Page 113

Following surface analyses, the corrosion rate was calculated based on the determined weight loss obtained following the ASTM G1-03 (ASTM, 2011) standard practice. After 3 months at 25°C in contact with the bentonite suspension, the corrosion rate of 4.8 µm/y (*Table 22*) is higher than that reported (~2 µm/y) for carbon steel embedded within compacted MX-80 and exposed to natural granitic porewater for 394 days in the MaCoTe experiment (Reddy et al., 2020). Both the difference in reaction time (90 days vs 394 days) and the difference in temperature (25°C vs rock temperature) can account for the different rates. In addition, the use of a suspension instead of compacted bentonite also plays a role because of the larger amount of water available. Increasing the temperature to 50°C significantly increased the corrosion rate in the present study, in agreement with reported findings (Hesketh et al., 2023). Corrosion rates increase with temperature because of decreased activation barrier for e.g., chemical and electrochemical reactions. Corrosion rates decreased systematically with increasing reaction time, for instance at 25°C from 4.8 µm/y after 3 months to 2.6 µm/y after 6 months. This result also agrees with reported corrosion rate evolutions in general and hint at the formation of a protective passivation layer at the coupon surface. The same trends were observed in experiments performed in the presence of hematite, thought the rates were systematically higher compared to experiments in the absence of added ferric compound. Hematite is a pure Fe(III) compound acting as oxidizing agent, as evidenced from measured E_h values (*Table 22*), thus increasing the corrosion rate.

The analyses of systems for SGI corrosion experiments performed under static conditions revealed that the presence of hematite affected the *in situ* redox potential and the corrosion rate. No other clear effect attributable to that ferric compound, in terms of surface morphology, surface Fe speciation or nature of secondary phases formed, could be evidenced. The formation of iron silicates could be detected in some samples, especially at 50°C. This finding suggests that dissolved silica must have been available in the system (Kaufhold et al., 2020), certainly favoured by the slightly elevated temperature and the prevailing pH/E_h conditions. Interestingly, data also indicate that neoformed iron silicates contain some aluminium meaning that the availability of dissolved silica alone cannot account for the observed secondary phases. Consequently, the reaction pathway may not simply consist in precipitation from dissolved species but may be more complex and possibly involve some kind of dissolution-reprecipitation mechanism.

Layered Fe-bearing compounds have also been detected at the coupon/suspension interface, suggesting that not enough silica must have been available for the formation of only Fe silicates. Most probably, steel corrosion resulted in larger amounts of dissolved Fe(II) than dissolved silica available, thus resulting in the simultaneous formation of Fe (hydr)oxides in addition to Fe silicates.

Fe(II) has a good affinity for hematite under the given pH conditions (Williams and Scherer, 2004; Larese-Casanova and Scherer, 2007) and reported data showed that ferrous ions uptake results in electron transfer with structural Fe(III) in hematite. In the long term, this may result in quantitative transformation of hematite into mixed Fe(II)/Fe(III) compounds.

4.4.2 SGI corrosion experiments under dynamic conditions

SGI corrosion experiments under dynamic conditions are finished, with data treatment in progress. In this report data interpretation should not be considered as final, at this stage some findings still require detailed evaluation.

At the outlet, the measured pH values increased from about 9.0 in the water collected after 4 weeks of reaction to 9.7 for the last collected water in all experiments (*Table 22*). These values are significantly higher than in experiments under static conditions (pH around 8), and the presence of hematite or increasing the temperature had no significant impact. The recorded E_h values were all within uncertainties similar and in the range -167 mV to -207 mV. These values suggest the development of reducing conditions, and thus steel corrosion, as in experiments under static conditions. The temperature or presence of hematite had no significant effect on measured E_h values, which seems rather unexpected because values would be expected to decrease with the extent of corrosion and higher values would be expected in experiments with added hematite.

EURAD (Deliverable n° 15.12) – Identification on the effect of transient processes on corrosion
Dissemination level: Public
Date of issue of this report: **29/04/2024**

Page 114

Consequently, the amount of added hematite must have been too low to have any effect already after 4 weeks of reaction time. Reactors have a PTFE inner liner and metallic filters made of stainless steel at inlet and outlet, these components are not expected to have any effect on pH and E_h values. In these experiments, pH and E_h were measured in the outlet water and not *in situ* in contact with bentonite and coupon. If both (bentonite and coupon) would act as buffers, measured values could deviate from the actual *in situ* values.

Results from ICP-OES and IC analyses of the outlet waters are presented in Milestone MS313. Dissolved amounts of Cl, Na, Si and Ca are rather constant and close to that in the inlet water. The Mg and Al contents decrease over time (the inlet water does not contain Mg or Al, *Table 20*), while values for Fe and K substantially scatter (these elements are also not present in the inlet water), suggesting possible problems occurred during measurements. Overall, results suggest a dilution of the suspension in contact with the coupon, which seems supported by the evolution of measured pH values approaching the value of the inlet water. Considering a mean flow rate of ~2.5 µL/mL over a period of 3 months results in ~300 mL of water going through the reactor containing 3.1 mL suspension. Under these conditions bentonite may not be able anymore to buffer pH, which increases to approach the pH of the inlet.

After 3 months exposure to bentonite suspension under dynamic conditions at 25°C (*Figure 95*), the coupon surface appears non uniformly corroded, with some areas having exposed cementite lamellas, comparable to the coupon corroded under static conditions at 25°C (*Figure 92*). In the presence of added hematite, the morphology seems comparable though with Fe removal going deeper at grain boundaries. At 50°C in the presence of added hematite, the iron removal from the surface seems larger: observations suggest that elevated temperature and presence of hematite both promote the surface degradation/corrosion. EDXS analyses corroborate the presence of steel, graphite inclusions and bentonite adhering to the surface. No formed secondary phase could be detected. Based on electron microscopic data, the steel degradation mechanisms under dynamic conditions seem not much different from that under static conditions, but the surface damage seems larger.

Iron is present in divalent and trivalent oxidation state at the surface exposed to the suspension for 3 months at 25°C with added hematite present (*Figure 96*). In the parallel experiment at 50°C, the Fe 2p spectrum recorded at the coupon surface agrees with the presence of metallic Fe, suggesting that no Fe-bearing secondary phase is attached to the surface. The sulfur 2p line (data not shown) hints at the presence of low amounts of sulfides at the surface of both coupons that may possibly be explained by the presence of admixed pyrite in the bentonite.

3 months 25°C   3 months 25°C + α-Fe$_2$O$_3$ 3 months 50°C + α-Fe$_2$O$_3$
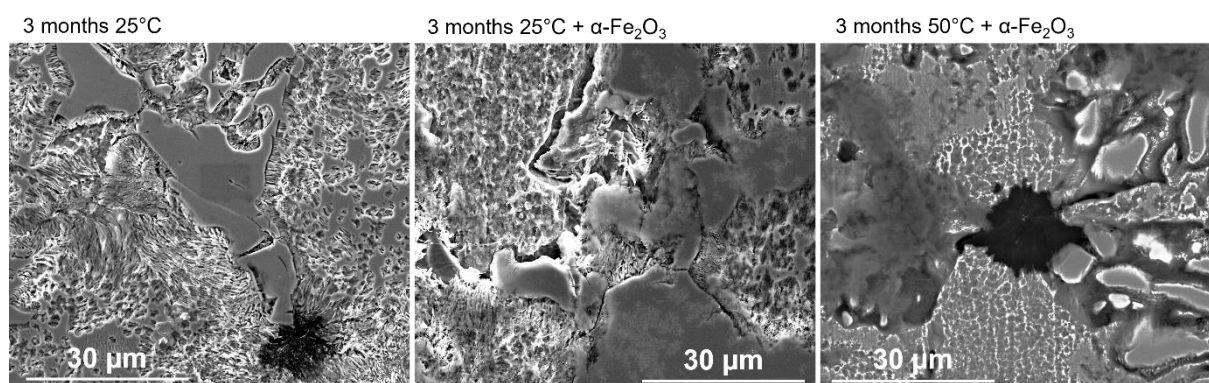
Figure 95 – Scanning electron micrographs (in SE (centre and left) or BSE (right) mode) of SGI coupons corroded for 3 months under dynamic conditions (exact conditions are indicated above the micrographs).

EURAD (Deliverable n° 15.12) – Identification on the effect of transient processes on corrosion
Dissemination level: Public
Date of issue of this report: 29/04/2024

Page 115

Figure 96 – X-ray photoelectron spectra recorded on SGI corroded under dynamic conditions for 3 months at 25°C in presence of α-Fe$_2$O$_3$ (A) and SGI corroded for 3 months at 50°C in presence of α-Fe$_2$O$_3$ (B).

At the clay surface, Fe is present as a mixture of Fe(II) and Fe(III), and this result is comparable to that from experiments under static conditions (*Figure 96*). This finding would suggest that Fe(II) formed upon steel corrosion reacted with the contacting bentonite, resulting either in the (partial) reduction of structural Fe(III) of bentonite or the formation of a mixed Fe(II)/Fe(III) compound. However, no presence of neoformed Fe-bearing phase could be detected by SEM-EDXS at the coupon/bentonite interface, suggesting a partial reduction of structural Fe of bentonite. This would also be consistent with the measured negative E$_h$ values (*Table 22*).

As corrosion rates are not yet available, the determination of the effect of static/dynamic conditions on the corrosion rates are yet to be evaluated. Outcomes suggest that the starting pre-equilibrated suspension was diluted during the 3 months reaction time, implying that dissolved amounts of Fe(II) formed upon steel corrosion very likely did not accumulate in significant amounts within the reactor. Though results showed that a fraction of formed Fe(II) reacted with the contacting bentonite, the remaining was transported away with the water. Under these conditions no protective passive layer may be able to develop and protect the coupon surface, resulting in corrosion progressing over time. The comparison of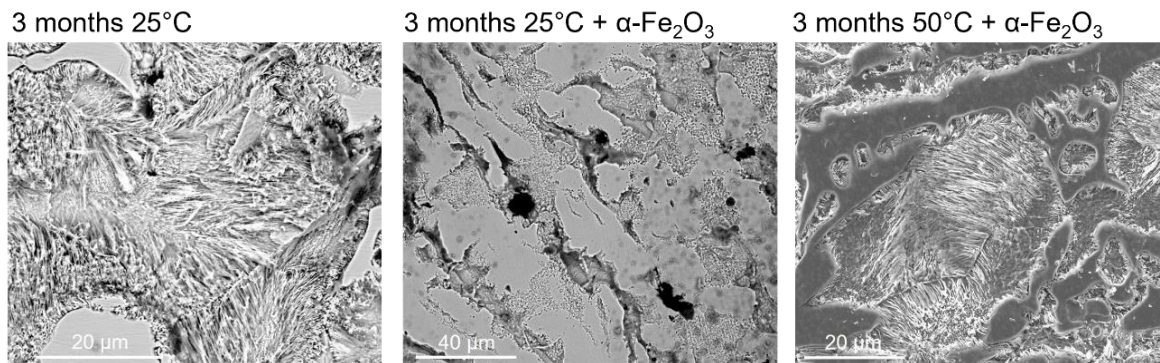 the corrosion rate for these experiments with that under static conditions will allow to confirm or to reconsider this hypothesis. In any case, no experimental finding supports the hypothesis of a steel degradation mechanism differing from that under static conditions.

4.4.3 CuNi corrosion experiments under static conditions

During 3 months reaction time under static conditions, the measured *in situ* pH and E$_h$ did not evolve much from the values of the starting pre-equilibrated bentonite suspension, except for the experiment at 50°C with 3 μM added sulfide. After 6 months, no significant difference in measured *in situ* pH and E$_h$ could be evidenced, with pH values ranging from 7.94 to 8.34 and E$_h$ values ranging from 245 mV to 297 mV (Table 20). Findings suggest that neither the presence of sulfide nor temperature had any significant effect on pH and E$_h$ evolutions and values remained almost within uncertainties unchanged compared to that of the starting pre-equilibrated suspension (pH = 8.15; E$_h$ = 245 mV). It is interesting to note that E$_h$ values are clearly positive, in contrast to experiments with the cast iron, suggesting that conditions did not become reducing not even in the presence of added sulfide.

Upon removal of the coupons from the suspension, the interface was brownish in some experiments performed at 50°C, and rather pale brown for experiments at 25°C, suggesting that reactions occurred at the coupon/suspension interface despite the absence of significant pH and E$_h$ evolutions. From the observed colors, a change in redox state of structural iron of bentonite may be excluded, also supported by the measured positive *in situ* E$_h$ values (*Table 23*). Instead, observations suggest the formation of secondary copper and/or nickel compounds accumulating at the coupon surface.

EURAD (Deliverable n° 15.12) – Identification on the effect of transient processes on corrosion
Dissemination level: Public
Date of issue of this report: 29/04/2024

Page 116

ICP-OES and IC analyses of the ultracentrifuged suspension could not reveal significant differences in compositions between the various experiments and observed differences may rather be attributed to experimental uncertainties. The Ni contents were below the quantification limits and the Cu contents were below or in rare cases at the quantification limit (data are presented in Milestone MS313).

No presence of corrosion products could be detected by XRD analysis of the corroded specimens (*Figure 97*). Diffractograms contain reflections attributable to the CuNi alloy and to components of the bentonite. Findings suggest that either secondary phases formed in too low amounts to be detected or that they may have been removed when cleaning off the excess suspension because electron microscopy showed the presence of particles at the coupon/suspension interface (see below).
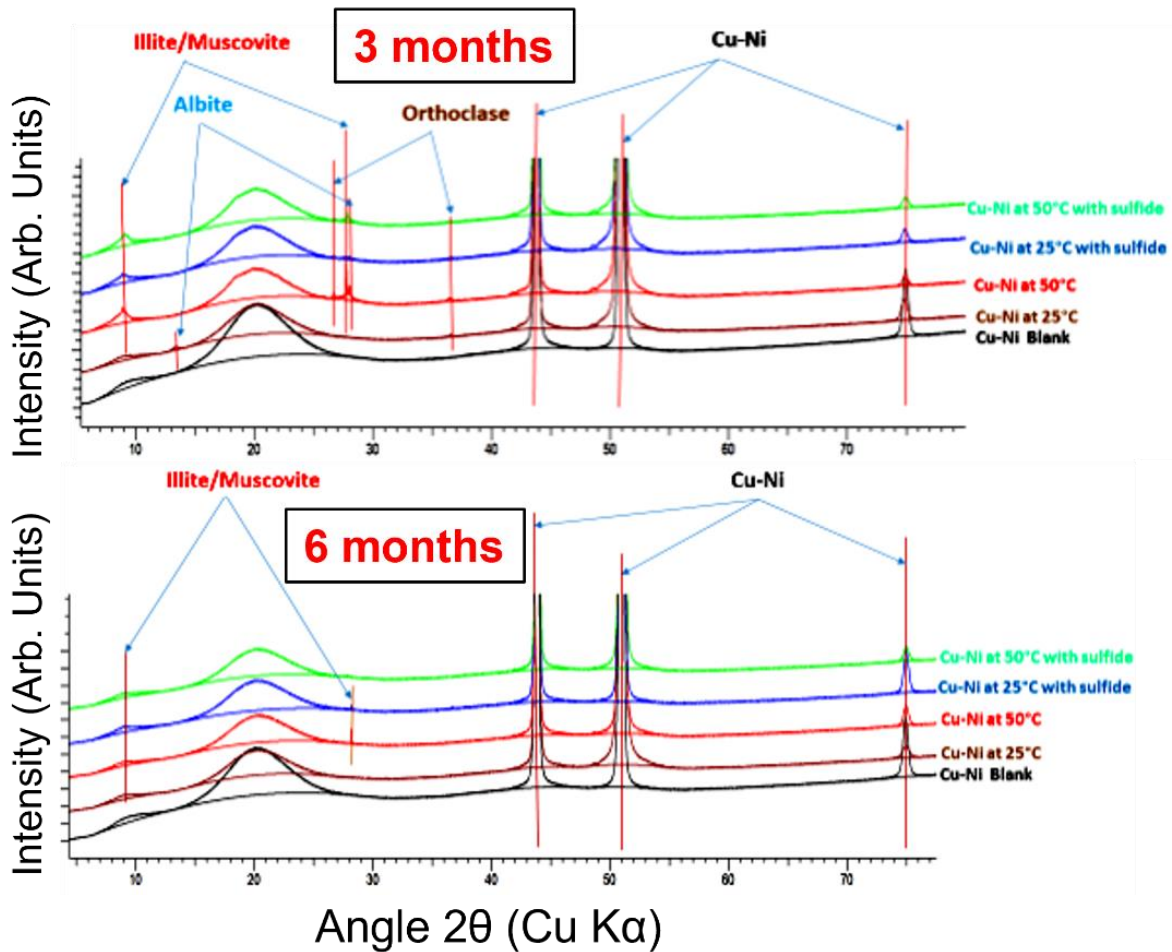
Figure 97 – X-ray diffractograms recorded on the corroded CuNi specimens after 3 months (top) and 6 months (down) reaction time under static conditions.

Scanning electron microscopy was subsequently applied to analyse the corroded coupons. Particles of octahedral morphology and sizes in the range 100 nm to 200 nm were detected at the surface of all coupons, and below the bentonite (*Figure 98* to *Figure 100*). The presence of sulfide had no significant effect on the morphology and increasing the temperature resulted in edges that seem more rounded. From 3 to 6 months, the size did not substantially evolve and observed differences in amounts of particles present may be attributed to the preparation of coupons (with bentonite removal also removing secondary phases).

EURAD (Deliverable n° 15.12) – Identification on the effect of transient processes on corrosion
Dissemination level: Public
Date of issue of this report: **29/04/2024**

Page 117

EDX analyses of the particles point at the presence of Cu-rich oxide particles in all samples, sometimes with low amounts of associated sulfur (*Figure 100*, *Table 25*). The Cu-rich particles have small sizes and are present at the surface of a substrate dominantly made of Cu, rendering complicated the exact determination of the elemental composition because of high contribution from the substrate underneath. However, EDXS spectra recorded on well separated particles allow concluding the absence of Fe and Ni associations with the particles. Sulfur is only detected in some samples, ruling out the compelling formation of Cu sulfide as corrosion products.
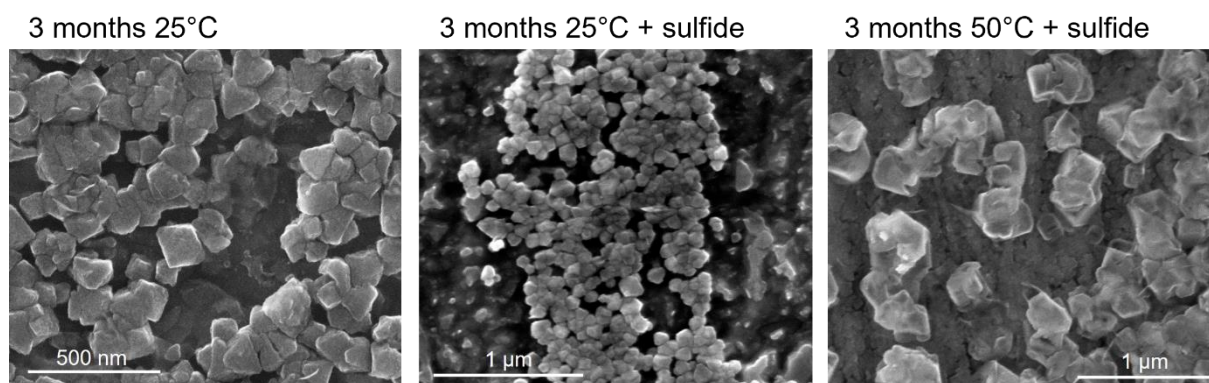
Figure 98 – Scanning electron micrographs (in SE mode) of CuNi coupons corroded for 3 months under static conditions (exact conditions are indicated above the micrographs).
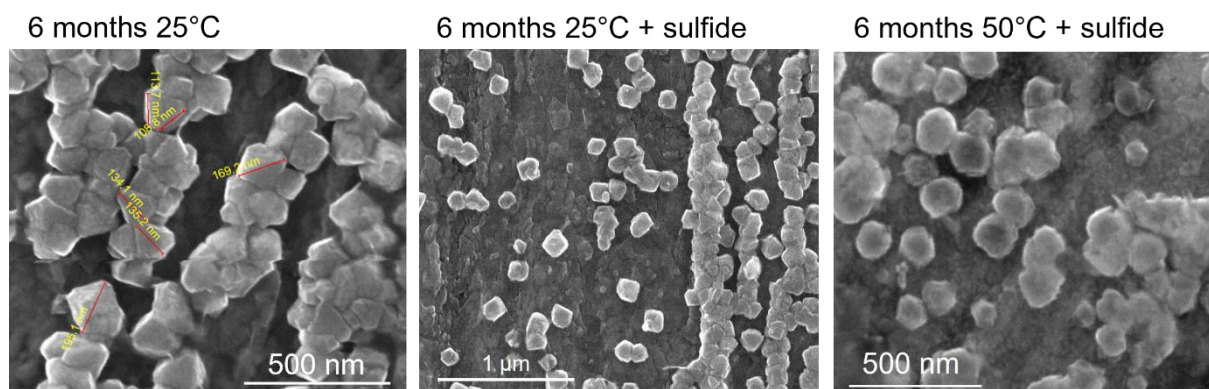
Figure 99 – Scanning electron micrographs (in SE mode) of CuNi coupons corroded for 6 months under static conditions (exact conditions are indicated above the micrographs).

SEM-EDX results showed above, and obtained using the FEI Quanta 650 FEG microscope, were complemented by electron backscatter diffraction (EBSD) using the sample corroded for 6 months at 25°C without added sulfide with the Zeiss Crossbeam 350 KMAT microscope. The acceleration voltage was set to 2.5 kV (compared to 15 kV using the FEI microscope) to record EDXS spectra, which will be free from substrate signal. This allowed revealing a Cu:O atomic ratio of 2:1, thus suggesting the presence of Cu_2O (cuprite) particles. For EBSD analysis, the acceleration voltage was subsequently increased to 15 kV, and EBSD scans were optimized in areas of 500 nm x 750 nm. By optimizing the indexing parameters, including the Hough transform parameters and number of reflections, a mean angular deviation of 0.29° was achieved, enabling to index 10 out of 11 bands (*Figure 101*).

The band indexing was consistent with a cubic crystal structure. Using this information, secondary phases could be identified as Cu_2O (Kirfel and Eichhorn, 1990), which is consistent with the EDXS

EURAD (Deliverable n° 15.12) – Identification on the effect of transient processes on corrosion
Dissemination level: Public
Date of issue of this report: **29/04/2024**

Page 118

quantitative analysis at 2.5 kV. Based on electron micrographs (*Figure 98*, *Figure 99*), it can be assumed that cuprite formed at the surface of coupons in all experiments.
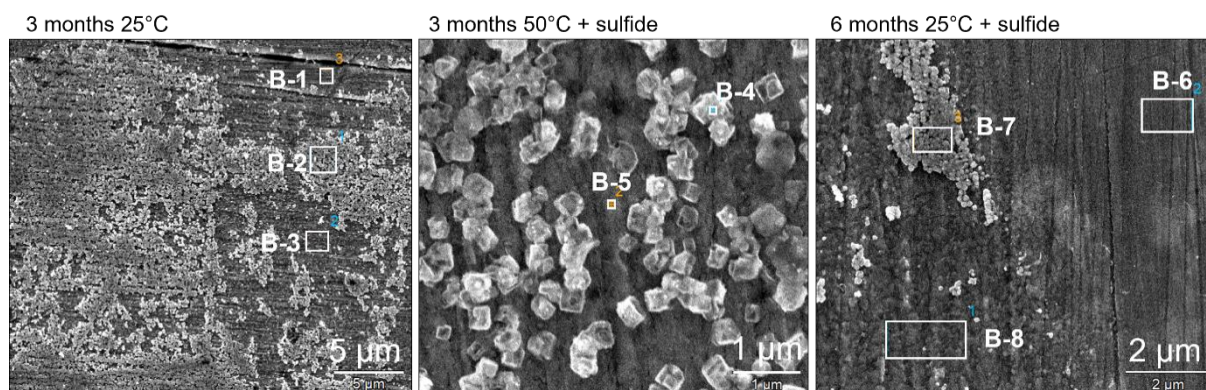
Figure 100 – Scanning electron micrographs (in SE mode) of CuNi coupons corroded for 3 or 6 months under static conditions (exact conditions are indicated above the micrographs). Marked areas were selected for EDXS analysis, quantitative results are provided in Table 25*.*

Table 25 – Relative atomic concentrations by EDXS analyses at selected areas shown in Figure 100. Relative errors are estimated to be within ± 10%.

Area	C	O	S	Al	Si	Mn	Fe	Ni	Cu
B-1	2.2	1.5	/	/	/	1.1	1.0	36.4	57.7
B-2	3.6	10.1	/	/	0.6	0.8	/	20.9	64.0
B-3	2.6	/	/	/	/	0.9	0.6	29.3	66.7
B-4	8.5	5.6	11.5	/	/	/	/	17.3	57.1
B-5	5.3	2.4	5.3	/	/	1.2	0.7	30.8	54.3
B-6	3.3	1.6	/	0.3	0.3	0.8	1.5	37.9	54.3
B-7	3.3	10.5	/	/	0.4	0.9	1.5	37.9	54.3
B-8	2.7	1.4	/	/	/	1.3	0.9	37.1	56.6

EURAD (Deliverable n° 15.12) – Identification on the effect of transient processes on corrosion
Dissemination level: Public
Date of issue of this report: **29/04/2024**

Page 119
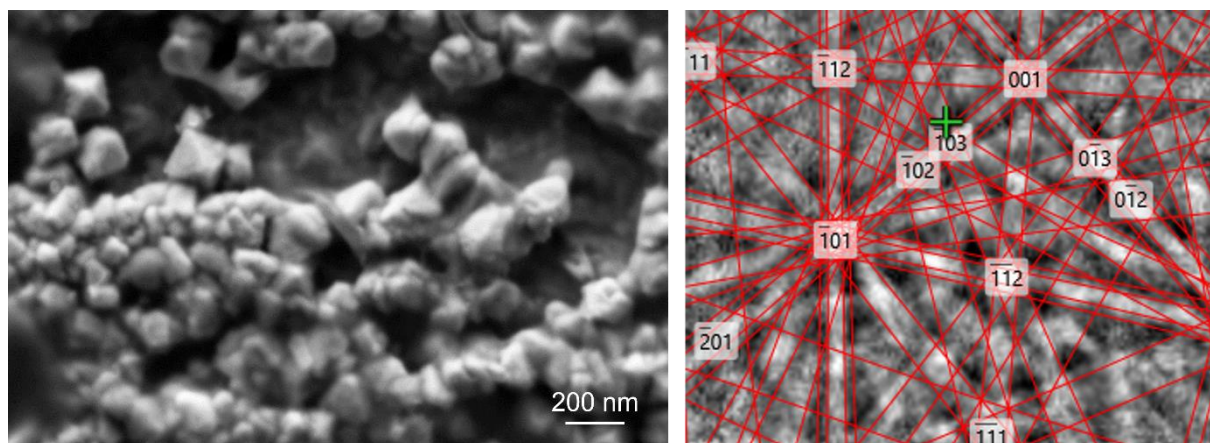
Figure 101 – Scanning electron micrograph recorded at 2.5 kV acceleration voltage (left), and Kikuchi pattern and indexing with Cu_2O (red) (right).

Complementary XPS measurements provided additional speciation information. Measurements were challenging especially for Cu because 2p narrow lines of metallic Cu and Cu_2O are very close. Recording Cu LMM and complementary O 1s narrow lines proved to be very helpful in the identification of the Cu speciation. After 3 months at 25°C, the presence of Cu_2O was detected at the coupon surface together with Ni(0), while Cu(0) and $Ni(OH)_2$ were detected in the parallel experiment at 50°C. The Cu speciation did not evolve between 3 and 6 months with the presence of Cu_2O at 25°C and Cu(0) at 50°C, but no Ni could be detected in samples after 6 months certainly because of its too low concentration at the surface. These findings may suggest that at 25°C Cu is oxidized to Cu(I) but not Ni, while at 50°C Ni would be oxidized to Ni(II) but not Cu. However, the presence of small Cu_2O particles was detected at the surface of all coupons at both temperatures by SEM, suggesting that their amount was very low or that particles were not homogenously distributed across the whole surface.

The presence of added sulfide had no significant impact on the Cu and Ni speciations at both temperatures and both exposure times, with comparable speciations found in all experiments (Figure 74). Sulfides could be detected at the surface of all coupons, with larger amounts detected in experiments at 50°C (data not shown). The position of the Cu $2p_{3/2}$ line (932.4-932.7 eV) would also agree with the presence of Cu_2S (Biesinger, 2017), suggesting that the presence of this compound in low amounts cannot be excluded. However, bentonite contains low amounts of pyrite that may stick to the surface and account for the detected low amounts of sulfides, at least for experiments performed in absence of added sulfide. The presence of NiS is excluded based on the position of Ni $2p_{3/2}$ line (Legrand et al., 1998). Finally, almost no Cu or Ni could be found associated with the clay surface, meaning that CuNi corrosion resulted in the formation of low soluble secondary phases at the coupon/suspension interface where the alloy is exposed.

EURAD (Deliverable n° 15.12) – Identification on the effect of transient processes on corrosion
Dissemination level: Public
Date of issue of this report: **29/04/2024**

Page 120
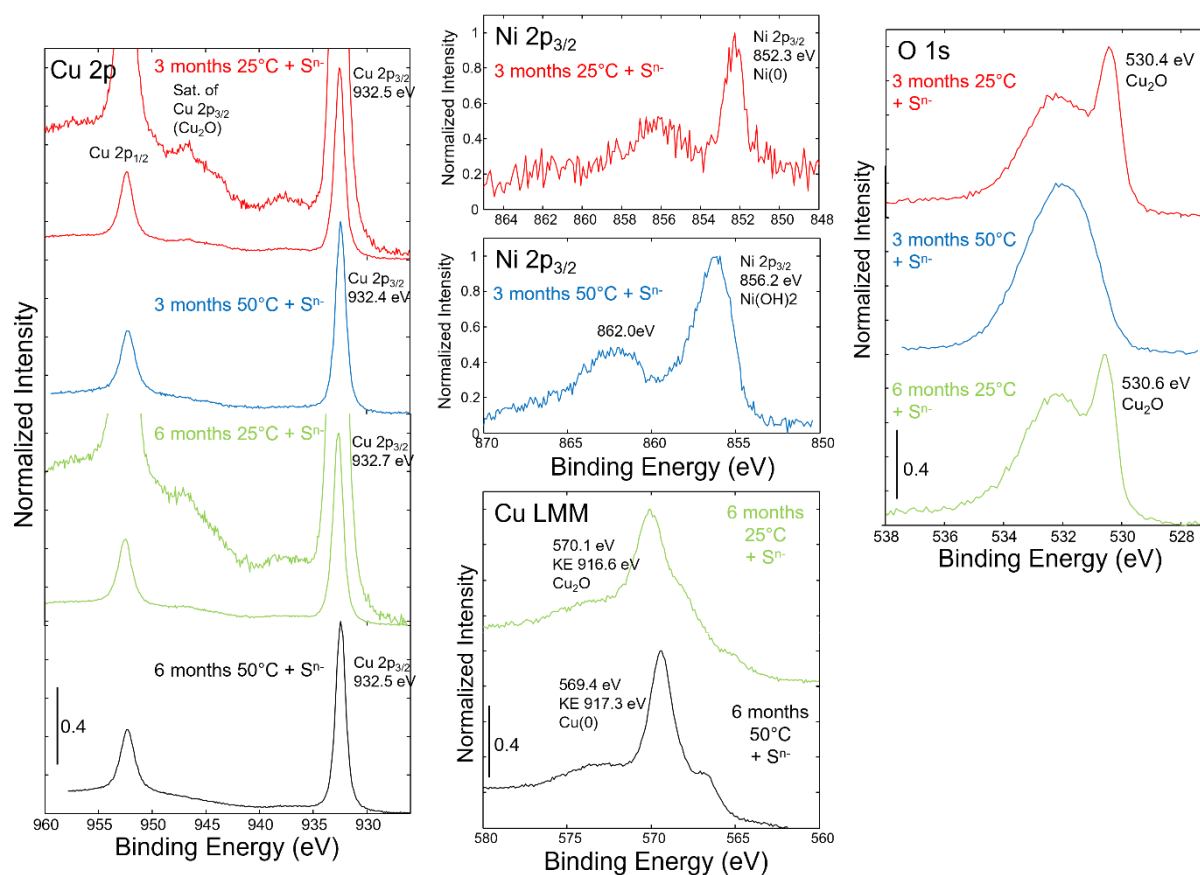
Figure 102 – X-ray photoelectron spectra recorded on CuNi corroded under static conditions (exact conditions are indicated on the individual graphs).

The exposure of CuNi to the MX-80 suspension hardly affected the *in situ* pH and E_h conditions, implying that no reducing conditions developed, in contrast to experiments with SGI. No significant amounts of Cu and Ni could be found associated with the contacting bentonite (based on XPS measurements) or in the porewater. Electron micrographs revealed the presence of secondary phases of comparable morphology and sizes in all experiments, and EDXS and EBSD analyses identified particles as Cu_2O (cuprite). XPS analyses corroborated the presence of cuprite in experiments at 25°C only but not at 50°C where only Cu(0) was detected. Sulfide has also been detected by XPS in all experiments, which may be explained by the presence of admixed pyrite within the bentonite. The presence of Cu sulfide such as Cu_2S at the surface of coupons in low amounts cannot be ruled out, but significant amounts can be excluded and certainly attributed to the low amount of added sulfide.

Nickel is the second major constituent of the alloy (~30 wt.%, *Table 25*), but could not be found associated with secondary phases. Similarly, no Si, Fe or Al, which are main elements of the bentonite could be found associated with corrosion products. This latter finding would agree with the reported existence of different reaction mechanisms at the Fe/bentonite interface compared to the Cu/bentonite interface (Kaufhold et al., 2017). In their study, Kaufhold et al. (2017) reported that Cu corrosion rates were significantly affected by the presence of pyrite (or sulfide) while in S-free bentonite experiments the observed Cu_2O formation was attributed to traces of oxygen.

The detection of compelling cuprite in the present study under the given positive redox conditions actually agrees well with reported thermodynamic data (Puigdomenech and Taxén, 2000). Indeed, on the reported Pourbaix diagram calculated considering 0.2 mmol/kg total sulfide, the pH ~8.1 and E_h ~220 mV conditions of the present study are located close to the Cu_2O/CuO boundary, well above the stability field of Cu(0) and Cu sulfides.

EURAD (Deliverable n° 15.12) – Identification on the effect of transient processes on corrosion
Dissemination level: Public
Date of issue of this report: **29/04/2024**

Page 121

The absence of detected Cu sulfides in significant amounts in the present study which may be attributed to the low initial sulfide content thus also agrees with thermodynamic data.

The alloy ued in the present study contains ~30 wt.% Ni with lower proportions (<1 wt.%) of Fe and Mn, but analyses revealed the dominant presence of Cu-bearing secondary phases, thus suggesting the degradation mechanism may involve copper. Since metallic Cu does not corrode in pure water (Hedin et al., 2018; Senior et al., 2019) not many possibilities may explain observed findings. Considering that only marginal amounts of S were found associated with secondary phases the only oxidant present is residual oxygen, which would agree with findings of Kaufhold et al. (2017) because the used MX-80 bentonite contains only low amounts of pyrite (0.6 wt.%, Karnland, 2010). Since cuprite was clearly detected at the surface of coupons, but not Cu sulfide, residual oxygen must have been in large excess compared to sulfide. Indeed, considering the starting sulfide concentration and the volume of suspension, only very low amount of Cu sulfide can be expected to form. In addition, under the prevailing conditions, i.e., excess of residual oxygen suggested from the observation of neoformed Cu_2O compared to added sulfide, the oxidation of sulfide to thiosulfide or other S species may also have happened. These considerations would also be in line with observed corrosion rates being hardly affected by the presence or absence of sulfide (*Table 26*).

4.4.4 CuNi corrosion experiments under dynamic conditions

Corrosion experiments with CuNi were performed in parallel with those using SGI, and samples for both materials are analysed in parallel. Consequently, CuNi corrosion experiments under dynamic conditions are finished, but data treatment is still in progress. Data obtained so far from analyses of the samples are presented and an interpretation is provided, but the interpretation is not yet considered final.

The pH measured at reactor outlet increased with time to values above 9 in all experiments (*Table 23*), the lowest increase being observed for the experiment at 50°C in the presence of added sulfide. Compared to experiments under static conditions, measured pH values are significantly higher. Measured E_h values are all very comparable and clearly negative, ranging from -166 mV to -189 mV, and do not exhibit any significant variation with time, temperature of sulfide presence. These outcomes suggest the development of reducing conditions, which contrasts with results from experiments under static conditions. As in experiments with SGI, reactors have a PTFE inner liner and metallic filters made of stainless steel at inlet and outlet, and these components are not expected to have any effect on pH and E_h values. pH and E_h were measured in the outlet water and not *in situ* in contact with bentonite and coupon. If both (bentonite and coupon) would act as buffers, measured values could deviate from the actual *in situ* values. It is currently unclear whether this played any role.

Interestingly, the observed pH and E_h values and their evolution with time compare well with those obtained in experiments under dynamic conditions with SGI. Though pH variations can be interpreted as dilution of the suspension by the inlet water, this may hardly explain observed E_h evolutions because the redox potential of the inlet water is positive (115 mV), suggesting that either the protocol used to measure E_h (i.e., in water at outlet) or the used setup may have an effect on these values. Results from the analysis of the corroded specimens will provide complementary information as the nature of formed corrosion products will allow drawing some conclusions regarding the possible development of reducing conditions.

The sample corroded for 3 months at 25°C looks covered by a thin layer of fine-grained material (*Figure 103*, left). EDXS analysis at 5 kV acceleration voltage of this fine-grained material allowed the detection of 73.3 at. % Cu and 18 at. % Ni, with only minor proportions of O and S, suggesting significant contribution from the underlying substrate. At 50°C, secondary phases exhibit a thin layered morphology (*Figure 103*, right), with up to several µm across, suggesting that temperature played a role in the morphology of the formed secondary phases. The measured elemental composition of the particles is consistent with a Cu oxide (Table 23), but without Ni present. Based on the formed corrosion products, findings suggest comparable degradation mechanisms occurred under static and under dynamic conditions.

EURAD (Deliverable n° 15.12) – Identification on the effect of transient processes on corrosion
Dissemination level: Public
Date of issue of this report: **29/04/2024**

Page 122

3 months 25°C   3 months 50°C

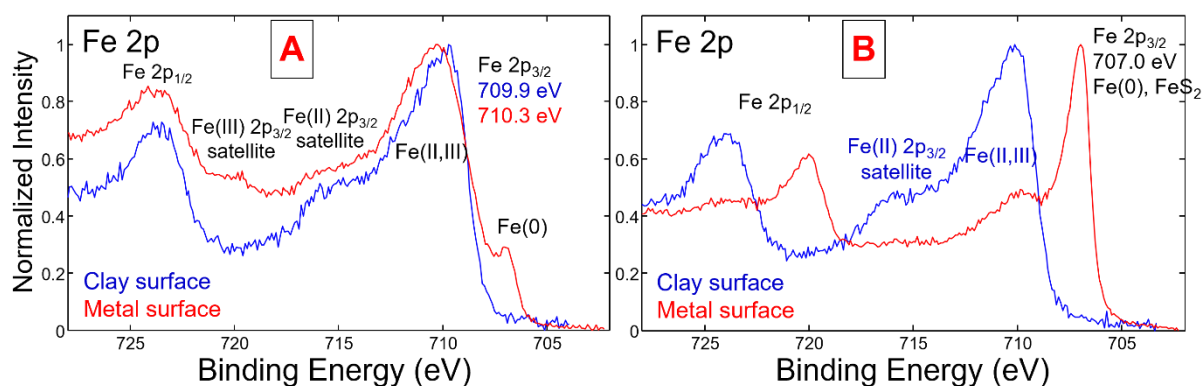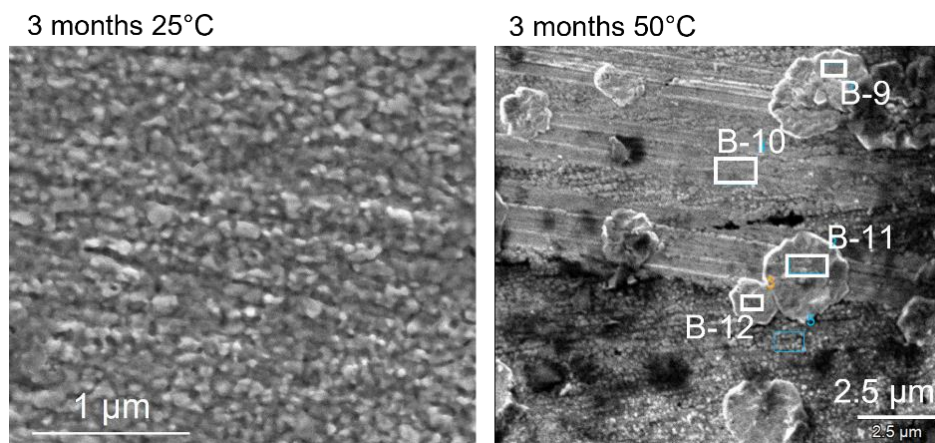*Figure 103* – Scanning *electron micrographs (in SE mode) of CuNi coupons corroded for 3 months under dynamic conditions (exact conditions are indicated above the micrographs). Marked areas were selected for EDXS analysis, quantitative results are provided in* Table 26.

Table 26 – Relative atomic concentrations by EDX analyses at selected areas shown in Figure 103. Relative errors are estimated to be within ± 10%.

Area	C	O	Al	Cu
B-9	1.5	28.3	/	70.2
B-10	5.8	9.3	/	84.9
B-11	1.3	34.0	5.0	59.7
B-12	1.5	33.6	4.7	60.2

The sample corroded for 3 months at 50°C in the presence of added sulfide was also selected for further EDXS mapping using the Zeiss Crossbeam 350 KMAT microscope (*Figure 104*). Since the surface coverage was low, two acceleration voltages were selected to provide information originating from different depths, i.e., near surface at low acceleration voltage and including substrate at higher acceleration voltage. At 15 kV Cu and Ni appear homogeneously distributed because at this acceleration voltage the elemental distribution is dominated by the substrate. Setting the acceleration voltage to 2.5 kV enabled to separate the surface signal from the CuNi substrate signal because of the decrease of the information depth from 400 nm at 15 kV to 25 nm at 2.5 kV. EDXS mapping at 2.5 kV suggests the formation of a Cu-rich interface, e.g., coexistence of Cu oxides along with Cu(0), on top of a Ni-rich interface, with the pristine coupon underneath. EDXS data further indicate that the Cu-rich layer contains O and S, suggesting the presence of Cu oxide and possibly sulfide (*Table 27*). The Ni-rich layer seems to be made of (hydr)oxide and contains only marginal amounts of S.

EURAD (Deliverable n° 15.12) – Identification on the effect of transient processes on corrosion
Dissemination level: Public
Date of issue of this report: **29/04/2024**

Page 123
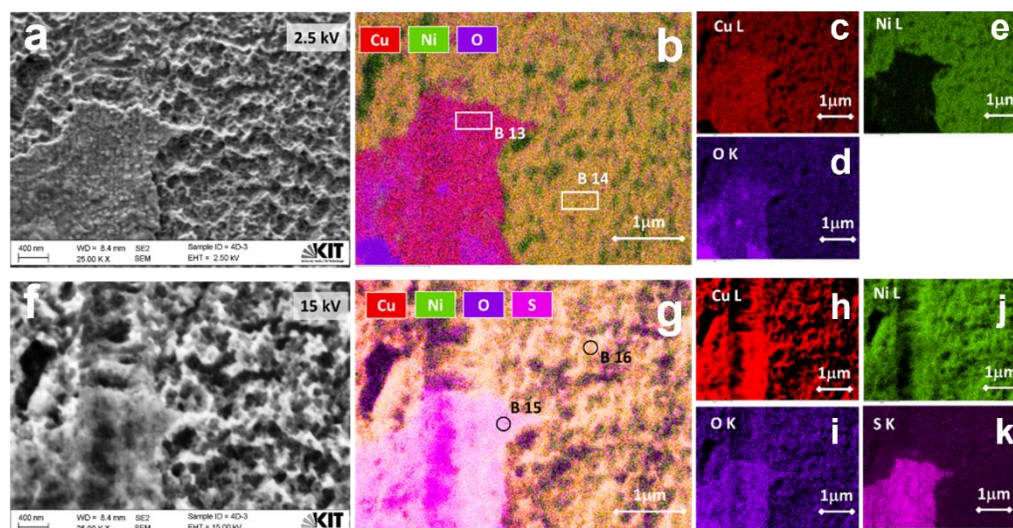
Figure 104 – Electron micrographs recorded at an acceleration voltage of either 2.5 kV (a) or 15 kV (f) *for the CuNi coupon corroded for 3 months under dynamic conditions with added sulfide present at 50°C together with corresponding elemental distribution maps: Cu (c), O (d) and Ni (e) distribution maps with the correlation map (b) at 2.5 kV; Cu (h), O (j), Ni (j) and S (k) distribution maps with the correlation map (b) at 15 kV. Marked areas were selected for local EDXS analysis, quantitative results are provided in* Table 27.

Table 27 – Relative atomic concentrations by EDXS analyses at selected areas shown in Figure 104. Relative errors are estimated to be within ± 10%.

Area	O	Mg	Al	Si	S	Ca	Mn	Fe	Ni	Cu
B-13	19.1	/	/	/	/	/	/	/	/	80.9
B-14	5.0	/	/	/	/	/	/	/	37.0	58.0
B-15	1.31	0.04	0.10	0.06	0.46	/	1.02	1.09	37.63	58.29
B-16	2.88	/	0.07	0.13	3.39	0.17	0.92	0.93	31.17	60.34

After 3 months at 25°C in the presence of added sulfide, XPS evidenced the presence of Cu(0) at the corroded coupon surface (Figure 77) but no Ni could be detected, corroborating the presence of a Cu-rich layer covering the surface. The Cu speciation is comparable in the experiment performed at 50°C, but the presence of low amounts of Ni, present as hydroxide, could be detected. The presence of sulfide species (data not shown) could be detected at the surface of both compounds, but in limited amounts, ruling out the presence of copper sulfides in significant amounts. This result compares well with that obtained in experiments under static conditions. The main difference between both approaches is the amount of sulfide present: a defined amount was added at the beginning of experiments under static conditions, in experiments under dynamic conditions (flow rate ~2.5 µL/min) no sulfide was present in the water until week 6, then 1 µmol/L until week 8, followed by 2 µmol/L until week 10, and 3 µmol/L until the end. Finally, almost no Cu or Ni could be detected at the clay surface, suggesting that CuNi corrosion resulted in the formation of secondary phase with only limited amounts of dissolved Cu or Ni available for interacting with the adjacent bentonite.

EURAD (Deliverable n° 15.12) – Identification on the effect of transient processes on corrosion
Dissemination level: Public
Date of issue of this report: **29/04/2024**

Page 124
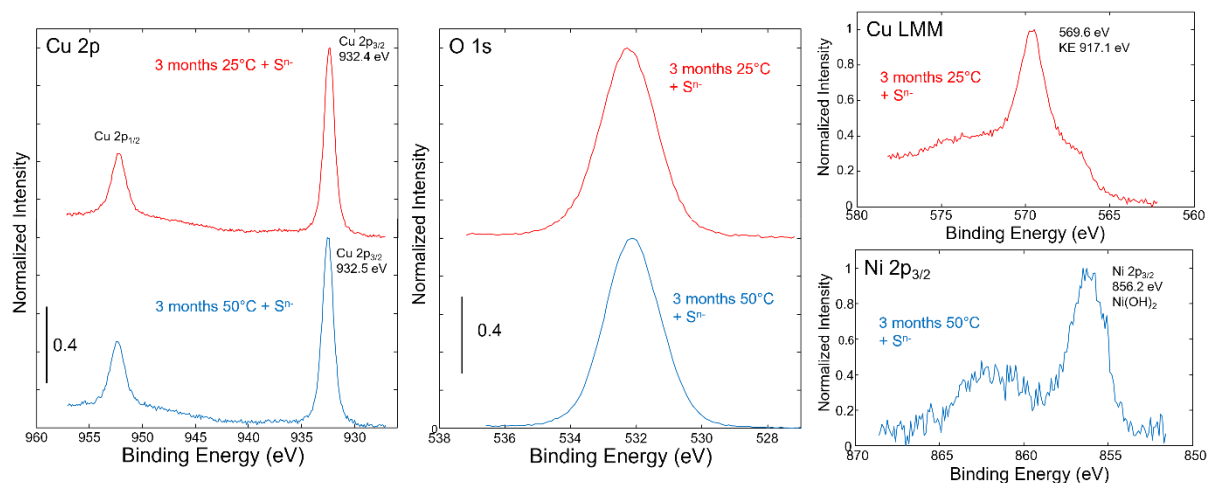
Figure 105 – X-ray *photoelectron spectra recorded on CuNi corroded under dynamic conditions (exact conditions are indicated on the individual graphs).*

X-ray diffractograms recorded on the corroded specimens (data not shown) only showed the presence of the underlying alloy, no crystalline secondary phase could be detected very likely because of the low amounts of formed compounds, as suggested from SEM-EDXS analysis. Corrosion rates are not yet available, but would be needed to assess the role of the applied conditions on the extent of surface damage.

Overall, results for experiments under dynamic conditions are very comparable to that obtained under static conditions, with the predominant formation of Cu oxide particles. With the formation of these secondary phases, a Ni-rich layer forms above the underlying coupon and Ni is not associated with the Cu oxides. Nickel is only found as hydroxide at the surface of some coupons. Finally, only limited amounts of S were found at the coupon surface. Based on the comparable secondary phases detected in experiments under static conditions, positive E_h values could be expected and not negative values as measured in the outlet water. One possible explanation could thus be the absence of bentonite and/or secondary phases acting as redox buffer of the system during E_h measurements.

4.5   KIT-INE conclusions

4.5.1   Effect of hematite presence on cast iron corrosion

In all experiments, SGI corroded upon exposure to the bentonite suspension. The pH hardly evolved, but the redox potential decreased in all experiments, suggesting the formation of Fe(II)-bearing secondary phases. The presence of hematite did not significantly alter the steel degradation mechanism, but served as a sink for Fe(II) which possibly retarded the formation of a protective layer of Fe(II)-bearing compounds which very likely caused an increase of the corrosion rate. Performing experiments under dynamic conditions did not significantly alter the steel degradation mechanisms.

For this steel, graphite inclusions may very likely serve as cathodic sites where water is reduced, and the coupled anodic reaction corresponds to the preferential ferrite oxidation:

$2 H_2O + 2 e^- \rightarrow H_2 + 2 OH^-$ Equation 7

$Fe(0) \rightarrow Fe^{2+} + 2 e^-$ Equation 8

EURAD (Deliverable n° 15.12) – Identification on the effect of transient processes on corrosion
Dissemination level: Public
Date of issue of this report: **29/04/2024**

Page 125

The formed Fe(II) can hydrolyze and precipitate as $Fe(OH)_2$, and with time can convert into magnetite according to the Schikorr reaction (Schikorr, 1933):

$$3\ Fe(OH)_2 \rightarrow Fe_3O_4 + 2\ H_2O + H_2 \qquad\qquad\qquad \text{Equation 9}$$

Fe(II) can also be transported away by the groundwater, which may only have occurred marginally under the present pH conditions. Alternatively, dissolved Fe(II) may react with dissolved Si and form iron silicates (e.g., berthierine, odinite, greenalite). The mechanism leading to the formation of such compounds may also be more complicated and involve dissolution/transformation reactions. In this sequence of reaction, hematite may only constitute an additional sorbent phase competing for Fe(II) uptake. The interaction of Fe(II) with hematite results in an electron transfer, with possible formation of mixed Fe(II)/Fe(III) compounds.

In the context of HLW, the formation of hematite at the container surface during the initial oxic period can result in a corrosion rate that is initially higher than it would be in the absence of α-Fe_2O_3. Outcomes did not evidence an alteration of the degradation mechanism, only the rate. With time and with metallic corrosion further proceeding, hematite is very likely to be converted into mixed Fe(II)/Fe(III) compound(s).

4.5.2 Effect of sulfide presence on cupronickel alloy corrosion

Copper oxides were the most abundant secondary phases observed in the CuNi corrosion experiments under all applied conditions. The presence of added sulfide had no significant effect and only minor amounts of sulfide species were detected, partly also attributable to the presence of pyrite naturally admixed within the bentonite. Interestingly, these findings parallel with outcomes from *in situ* corrosion experiments. Indeed, most of Cu corrosion products detected in the MaCoTe experiment are oxides, and only minor sulfide compounds (Reddy et al., 2020). It may thus be possible that longer exposure times, or higher sulfide concentrations, would be needed to observe unambiguously the formation of Cu sulfide species in substantial amounts.

Copper does corrode in the presence of sulfide, but not in pure water. In the present study, the only additional oxidant present is residual oxygen. Interestingly, under the prevailing pH and E_h conditions, the nature of detected corrosion products agree with reported Pourbaix diagrams (Puigdomenech and Taxen, 2000). These reported data further indicate that sulfides compounds would only be stable under lower, reducing conditions. It is also interesting to note that Ni, though present in substantial amounts in the alloy did certainly not play any significant role in the degradation mechanism because no Ni was found associated with the corrosion products.

In the context of HLW, the outcomes of the present study do not allow concluding on any negative effect of a progressive increase or constant supply of sulfide content on CuNi corrosion behaviour. No effect of Ni presence in the alloy on the corrosion behaviour could be evidenced either. During the long-term evolution under repository conditions, it can be hypothesized that CuNi would degrade and result in the formation of Cu sulfides (as product of copper oxide reacting with dissolved sulfides (Hollmark et al., 2012)) and separate Ni hydroxide, though the conversion of this latter compound into sulfide cannot be excluded.

EURAD (Deliverable n° 15.12) – Identification on the effect of transient processes on corrosion
Dissemination level: Public
Date of issue of this report: **29/04/2024**

Page 126

5. UJV-SURAO experiments and results in Task 5

5.1 Motivation

The degree of corrosion was investigated with respect to different dose rates, temperatures, and saturation. The experimental design consisted of bentonite with embedded carbon steel samples compacted and saturated in modules, inserted in sealed chambers (mounted in anaerobic box), irradiated (^{60}Co source) and constantly heated at 150 °C for 6, 9, 12 and 18 months.

The dose rate (0.4 Gy·h^{-1}) was calculated by simulating conditions, close to the fuel assembly at the defined temperature (Pospíšková et al. 2017). Modules were closed, keeping anaerobic conditions inside. The reference non-irradiated modules were allocated in the anaerobic box under corresponding temperature to compare irradiated and non-irradiated systems.

Complementary modules were designed and used for an estimation of microbial survivability after exposure at given conditions (EURAD ConCorD Task 4).

5.2 Test specimens

5.2.1 Carbon steel samples

The discs (10 mm in diameter, 1 mm thick) composed of carbon steel S355J2H (supplied by Škoda, *Figure 106*) were obtained by cutting a tube, which serves as the outer casing for the Czech canister concept (Pospíšková et al. 2017, Matulová et al. 2023). The steel discs were prepared out of the steel veld by steel crosscutting and grinding using grinding wheel with 46K grit.
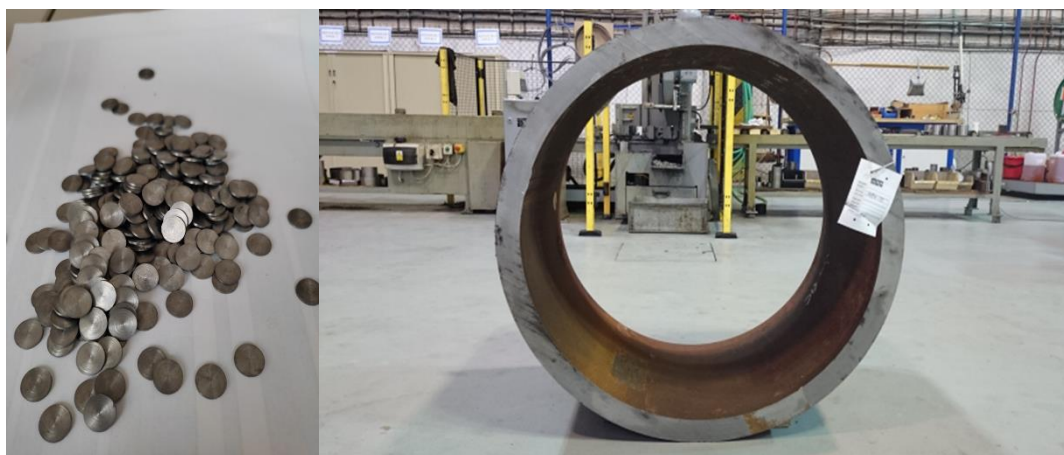
Figure 106 – Left – carbon steel disks, right – outer case of the canister in the Czech concept.

5.2.2 Bentonite samples

Two types of bentonites were used in the corrosion experiment: a calcium-magnesium bentonite (BCV) from the Czech Republic (provided by KERAMOST, Plc., Czech Republic) and a sodium bentonite (MX-80) that served as a reference material (provided by CIEMAT).

5.2.3 Saturation solution

A synthetic granitic water (SGW3, *Table 28*) was used as a saturation medium in all experiments designed by UJV. Chemical composition of SGW3 was calculated representing waters typical for the Rožná mine formation (the Bohemian Massif) layers located 1000–1200 m below the surface (Červinka et al. 2018).

EURAD (Deliverable n° 15.12) – Identification on the effect of transient processes on corrosion
Dissemination level: Public
Date of issue of this report: **29/04/2024**

Page 127

Table 28 – Chemical composition of synthetic granitic water (Červinka et al. 2018)

c (mg l⁻¹)	Na⁺	K⁺	Ca²⁺	Mg²⁺	F⁻	Cl⁻	SO₄²⁻	HCO₃⁻
SGW3	89.4	0.7	1.3	0.1	9.9	18.7	10.5	163.5

5.3   Experimental design, irradiation and loading conditions

The experiment consisted of 23 modules – each containing compacted bentonite with embedded steel coupons (*Figure 107*). According to the DGR concept (Pospíšková et al. 2017) initial bentonite moisture content was adjusted to 15 % (modules heated up at 150 °C) and 20 % (modules heated up at 90 °C). The dry density of compacted bentonite was 1600 kg·m⁻³. In each corrosion module, there are 12 carbon steel samples that are divided into three layers, each layer containing four steel samples.

The modules were compacted at hydraulic press machine MEGA 11-300 DM1S (Form+Test Seidner+Co GmbH, Germany).
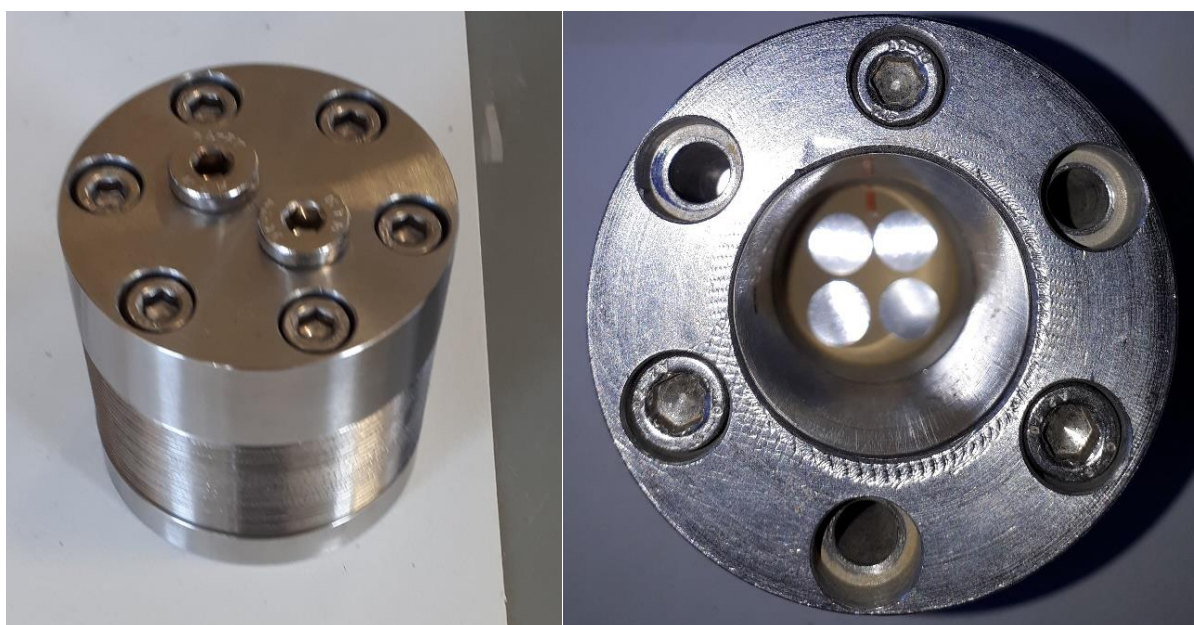
Figure 107 – Left – corrosion module, right – carbon steel samples inside of the corrosion module.

The modules were connected to capillaries and saturated under the pressure of 5 MPa for the whole loading period (*Figure 108*). The saturation pressure was applied through pressure exchanger in which a piston is pressurized by Ar. The water was de-oxidized in the glove box (GP CONCEPT, Jacomex, France) prior to its usage. All experimental modules were loaded in Ar atmosphere in the glove box or in the steel vessels filled by Ar prior to their welding. Nine modules were subjected to ⁶⁰Co irradiation (dose rate at samples ~ 0.4 Gy·h⁻¹, *Figure 108*). Nine modules were heated up without irradiation. The heating was adjusted to the appropriate temperatures (87–90 °C, 146–150 °C). The rest of the modules was saturated under Ar atmosphere in the glove box (reference modules) at ambient temperature (~ 21 °C). The complete list of experimental modules and loading conditions are summarised in Table 26.

EURAD (Deliverable n° 15.12) – Identification on the effect of transient processes on corrosion
Dissemination level: Public
Date of issue of this report: **29/04/2024**

Page 128

Table 29 – A list of experimental modules and loading conditions.

Modu le No.	Bentonite	w initial (%)	w final (%)	Loading period (months)	T (°C)	Radiation (Gy h^{-1})	Dismantling
1	BCV	15	21.14	6	150	0.4	2022-11-01
2	BCV	15	21.28	6	150	-	2022-11-01
3	BCV	15	25.06	9	150	0.4	2023-01-31
4	BCV	15	21.96	9	150	-	2023-01-31
5	BCV	15	20.54	12	150	0.4	2023-05-04
6	BCV	15	9.29	12	150	-	2023-05-04
7	BCV	15	22.61	18	150	0.4	2023-11-07
8	BCV	15	22.33	18	150	-	2023-11-07
9	MX80	15	16.57	18	150	0.4	2023-11-07
10	MX80	15	20.00	18	150	-	2023-11-07
11	MX80	15	19.58	18	RT	-	2023-11-07
12	BCV	20	20.86	9	90	0.4	2023-01-31
13	BCV	20	24.55	9	90	-	2023-01-31
14	BCV	20	23.24	12	90	0.4	2023-05-04
15	BCV	20	23.93	12	90	-	2023-05-04
16	BCV	20	18.34	18	90	0.4	2023-11-07
17	BCV	20	21.78	18	90	-	2023-11-07
18	MX80	20	20.57	18	90	0.4	2023-11-07
19	MX80	20	20.42	18	90	-	2023-11-07
20	BCV	20	22.58	6	RT	-	2022-11-01
21	BCV	20	24.54	9	RT	-	2023-01-31
22	BCV	20	23.77	12	RT	-	2023-05-04
23	BCV	20	23.94	18	RT	-	2023-11-07

EURAD (Deliverable n° 15.12) – Identification on the effect of transient processes on corrosion
Dissemination level: Public
Date of issue of this report: **29/04/2024**

Page 129

Figure 108 – Steel vessels containing steel modules connected by metal capillaries with saturation medium situated in the irradiation area.

5.4   Disassembly

The heating of heated modules was stopped 1 day prior to disassembly due to the safety reasons. The saturation and irradiation were stopped at the same time. After cooling the steel vessels were opened. The modules were disassembled in the glove box under Ar atmosphere. Bentonite and carbon steel samples were stored in the glove box and let dry under Ar atmosphere. After drying the carbon steel coupon were divided into three groups:

a) Ten carbon steel coupons – subjected to the mass loss analysis (Section 5.5.1.1). Following the mass loss analysis – one steel coupon was analysed using employing profilometry (Section 5.6.3).
b) A carbon steel coupon – subjected to light microscopy and scanning electron microscopy combined with energy dispersive analysis (SEM-EDX, Section 5.5.1.5). Following the SEM-EDX the cross section was analysed employing the Raman spectroscopy (Section 5.5.1.4).
c) A carbon steel coupon – subjected to X-ray diffraction analysis (Section 5.5.1.3)

All carbon steel coupons mentioned above were visually inspected using stereomicroscope. The visual inspection was done prior the analyses and after the mass loss analysis. The bentonites were subjected to the following analyses (Section 5.5.2): X-ray diffraction analysis, X-ray fluorescence, cation exchange capacity, water leachates and microbiological analyses (Concord Task 4).

EURAD (Deliverable n° 15.12) – Identification on the effect of transient processes on corrosion
Dissemination level: Public
Date of issue of this report: **29/04/2024**

Page 130

5.5   Post-test analysis

5.5.1   Post-test analysis of steel

5.5.1.1 Mass loss

Steel samples were subjected to decontamination according to the standard ČSN EN 10210-1. A solution of hydrochloric acid inhibited by urotropine was applied. The standard prescribes gradual immersion of steel samples in the solution for 10 minutes. After each immersion, the samples were washed with demineralised water and ethanol and dried. Immersion and washing were repeated twice. Immediately after decontamination the steel samples were weighed using Presica 240A analytical balances (Precisa Gravimetrics AG, Switzerland) with the 0.1 mg resolution, the same as before exposure. The weighting was done in triplicate. The corrosion rate was calculated as a mass loss divided by exposure time and surface area of the steel samples and multiplied by the steel density (7.85 g cm^{-3}, ČSN EN 10210-1).

5.5.1.2 Visual inspections

The surface of the steel samples was documented using an Olympus SZX10 stereomicroscope (Olympus Corporation, Japan). Images of both sides of the samples were taken.

5.5.1.3 XRD

Corrosion products on metal samples were determined by X-ray diffraction analysis with the PANalytical XPertPRO MPD (PANalytical, B. V., Almelo, Netherlands). The following measurement conditions were used: CoKα radiation (voltage 40 kV, current 30 mA), fast linear detector PIXCel 3D and reflective Bragg-Brentano arrangement. In the primary beam, we used an integrated iCore module with a Bragg-Brentano HD mirror, a 6 mm mask, a 0.03 rad Soller diaphragm, and a 0.25° divergence diaphragm. In the diffracted beam, we used an integrated dCore module with 0.25° anti-dispersion diaphragm and 0.02 rad Soller diaphragm. The measurement range was 4 to 80° 2theta with a step of 0.0131°. The measured diffractograms were evaluated using HighScorePlus, version 5.1.0b, Malvern PANalytical b.v., Almelo, NL (Degen et al. 2014) by comparison with database data contained in the PDF-4+ database (PDF-4+ database 2023).

5.5.1.4 Raman spectroscopy

Micro-Raman spectra of samples were measured by dispersive Raman spectrometer (Nicolet model DXR2-Raman microscopy, Thermo Electron Scientific Instruments LLC, USA) equipped with confocal microscope Olympus. As an excitation source, a laser having wavelength 532 nm and input power maximum 10mW was used. Full range grating (spectral range 3500–50 cm^{-1}), 25 μm confocal pinhole apertures and CCD detector (a multi-channel cooled CCD camera) were used. Samples were measured with following parameters: laser power: 0.5 mW–2 mW, aperture 25 pinhole, objective L50×, collect exposure time: 2 s, sample exposures 200, background exposure 200. All recorded spectra were analysed after fluorescence correction or baseline correction using OMNIC software (Thermo Electron Scientific Instruments LLC, USA).

5.5.1.5 SEM-EDX in cross-section

Microscopical analysis of corroded steel samples was conducted on stereomicroscope Nikon SMZ 745, light microscope Nikon Eclipse MA200 (Nikon Metrology, Ins.) and scanning electron microscope TESCAN AMBER (Tescan Group, a. s.) combined with energy dispersive spectrometer Oxford UltimMax 100 (SEM-EDS, Oxford Instruments plc.). A cross-section was prepared from the entire sample by grinding it to the plane of interest. The sample was secured in a Struers UniClip holder Struers GmbH) and embedded in Struers EpoFix epoxy resin under vacuum (pressure in the embedding chamber: 200 mbar) using the Struers Epovac device. The embedded sample was then ground and polished using the Struers Tegramin-25 automatic grinder. The grinding process was performed on a

EURAD (Deliverable n° 15.12) – Identification on the effect of transient processes on corrosion
Dissemination level: Public
Date of issue of this report: **29/04/2024**

Page 131

Struers Piano 220 disc with a pressure of 35 N, water lubrication, a disc rotation speed of 300 rpm, and simultaneous rotation of the specimen holder at a speed of 150 rpm. The grinding time was adjusted as needed to achieve the desired section in the area of interest. Subsequent polishing steps were carried out using Struers MD-Largo, Struers MD-Dac, and Struers MD-Nap cloths, which were wetted with diamond suspensions: Struers DiaPro Largo 9 µm, Struers DiaPro Dur 3 µm, and Struers Nap B 1 µm. In all polishing phases, a pressure of 30 N, a cloth rotation speed of 150 rpm, and simultaneous rotation of the specimen holder at 150 rpm were applied. Each polishing step lasted 5 minutes. Between individual preparation steps, the samples were cleaned in an ethanol bath using an ultrasonic cleaner Kraintek K 5LM. After the final polishing, the samples were cleaned with isopropanol. The microstructure of the base material was revealed by swab etching with a 2% Nital solution. Following examination using LOM, the sample was re-ground and re-polished, and it was further evaluated using SEM-EDS. For this purpose, a thin layer of approximately 10 nm of carbon was deposited on the sample surface using the Agar Turbo Carbon Coater (Agar Scientific Ltd.).

5.5.1.6 Profilometry

The profilometry was conducted employing 4-axes optical profilometer RedLux (RedLux Ltd., Southampton, UK). Laboratory of optical profilometry consisting of two sliding and two rotary axes. The rotary axes move with the sample and the shift axes move with the sensor. All axes use optical position sensors and linear motors. The sensor is a point confocal sensor. The principle of the analysis is based on the colour aberration of the lens (chromatic aberration) and is used to measure the distance from the measured object very accurately. According to the manufacturer's values, linear axes have a resolution of 100 nm, rotary axes 10" (arcsecond). The resolution of the point confocal sensor stated by the manufacturer is 20 nm. A profilometer records the position of individual points on a surface with a certain frequency. The frequency of point scanning can be set in both circumferential and longitudinal directions. The data were evaluated using the Matlab software (MathWorks, Inc.).

5.5.2 Post-test analysis of bentonite

5.5.2.1 Chemical composition

The chemical composition of bentonite was determined by X-ray fluorescence analysis (XRF). The spectrometer ARL 9400 (Thermo Fisher Scientific Inc.). The XRF method was chosen because of the small amount of sample needed to be analysed. The XRF analysis included the determination of the loss on ignition (LOI) at 850 °C. The total carbon content (C_{tot}) and the total sulphur content (Stot) were determined spectrophotometrically using the ELTRA CS 580 analyser (ELTRA GmbH, Germany) from a naturally wet sample.

5.5.2.2 XRD

X-ray powder diffraction patterns of bentonite samples was measured on the Empyrean, series III instrument, the same as corrosion products on steel samples (Section 5.5.1.3). For the bentonite samples, the loading time was 600 sec/step. This represented an analysis of about 4 hours. The samples were adjusted for measurement in back-loading cuvettes. The measured diffractograms were evaluated using HighScorePlus, version 5.1.0b, Malvern PANalytical b.v., Almelo, NL (Degen et al. 2014) by comparison with database data contained in the PDF-4+ database (PDF-4+ database 2023). Estimates of mass fractions (QPA) of individual crystalline phases were performed using the Rietveld method (Rietveld et al. 1969) using Profex 4.3.6/BGMN 4.2.23 (Bergmannet al. 1998, 2001; Döbelin and Kleeberg 2015). We used models obtained from ICSD (ICSD database 2022) and PDF-4+ (PDF-4+ database 2023). We used a structural model from BGMN (Bergmann et al. 1998).

5.5.2.3 Water leachates

The determination of leachable ions was performed by a series of batch experiments in different ratios of solid and liquid phase (s : l) into MilliQ water. The phase ratio (s : l) used in the interpretation indicates the ratio of dried bentonite to water. The samples were dried at 105 °C prior to the leaching. The phase

![eurad logo] European Joint Programme on Radioactive Waste Management

EURAD (Deliverable n° 15.12) – Identification on the effect of transient processes on corrosion
Dissemination level: Public
Date of issue of this report: **29/04/2024**

Page 132

interaction time (14 days) is considered long enough to achieve solid/liquid equilibrium (Roy et al. 1993; Hofmanová et al. 2019). The s : l ratio of MX-80 water leachates is lower comparing to those of the BCV bentonite due to restricted centrifugability and filterability. Subsequently, the liquid phase was separated by centrifugation, filtered through a 0.20 µm membrane filter (Millipore ®). The main cations (Na^+, K^+, Mg^{2+}, Ca^{2+}, Fe^{x+}) and anions (Cl^-, F^-, SO_4^{2-}, NO_2^-, NO_3^-, HCO_3^-) were analysed in all solutions. Anions were analysed employing capillary zone electrophoresis CE 7100 (Agilent Technologies, Santa Clara, USA) with UV detection. Cations were analysed employing double beam flame atomic absorption spectrophotometer SavantAA Σ (GBC Scientific Equipment Pty Ltd, Australia). The content of carbon dioxide forms (species) was analysed based on alkalimetric titration following the standard procedure ČSN 75 7373 (2001).

5.5.2.4 Cation exchange capacity

The CEC and exchangeable cations were determined by the Cu(II)-triethylenetetramine (Cu-trien) method (Meier and Kahr 1999; Ammann et al. 2005). Cu-trien (0.01 mol l^{-1}) was mixed with dried (105 °C) samples in the solid-to-liquid ratio of 25 g l^{-1}. After interaction for 30 minutes, the suspensions were centrifuged, and supernatants were analysed. The Cu^{2+} concentration was determined by UV/Vis spectrophotometer Specord 205 (Ana-lytik Jena, DEU). The concentration of displaced cations (Na^+, K^+, Ca^{2+}, Mg^{2+}) was determined by atomic absorption spectrometer SavantAA (GBC Scientific Equipment, AUS). Two values of cation exchange capacity were derived: CECVis from copper depletion and CECSUM by summing equivalent concentrations of displaced cations.

5.5.2.5 Scanning electron microscopy

The samples were studied using a JEOL SEM JSM 6510LV scanning electron microscope (JEOL, Ltd.) with an attached Oxford Instruments INCAx-actSN 55847 EDS analyser (Oxford Instruments plc.) operating at a resolution of 133 eV measured at 5.9 keV. The SEM microscope is equipped with a tungsten cathode, which allows work in the "low vacuum" mode. Due to the fact, that the studied materials were prepared from electrically non-conductive material and contained weakly bound water, the measurement was carried out in the "low vacuum" mode at an air pressure of 50 Pa. Under these conditions, there was neither charging of the surface of the samples by the action of the electron beam nor problems with achieving the necessary vacuum. The EDS analysis was carried out using a semi-quantitative method without standards using the company's software. Both microscopic images and EDS analyses were taken at an accelerating voltage of 25 kV.

EURAD (Deliverable n° 15.12) – Identification on the effect of transient processes on corrosion
Dissemination level: Public
Date of issue of this report: **29/04/2024**

Page 133

5.6   Results of tests performed by UJV

5.6.1   Mass loss

The steel samples were embedded in bentonite in three layers in each module. All experiments aimed to fully homogeneous saturation of experimental modules within the experiment. Thus, corrosion rate is expected to be comparable in all steel specimens in the module under certain conditions. Fully saturated modules exhibit very low confidence intervals (e.g., 0.1 µm y^{-1}) of corrosion rate indicating homogeneous saturation of the module within the experiment. The modules no. 2, 3, 15, 15 and 17 indicate higher corrosion rate of the steel samples located in two layers close to the source of saturation medium. The steel samples located in the third outermost layer in the module indicated lower corrosion rate. This heterogeneity in the individual layers is explained by inhomogeneous saturation of the module. Lower water content decreased a corrosion rate of the steel samples. The inhomogeneity of the saturation is reflected by higher confidence intervals of corrosion rate (2.1–4.1 µm y^{-1}) (*Table 30*).

The corrosion rates indicated small variation in the steel samples embedded at BCV bentonite heated up at 150 °C and irradiated for 6, 9, 12 and 18 months (10.1 ± 2.0☐12.3 ± 2.1 µm y^{-1}). Unirradiated samples indicated the highest corrosion rate after 6 months of thermal loading (24.3 ± 2.2 µm y^{-1}) and the corrosion rate decreased with loading time (13.3 ± 1.6☐18.0 ± 1.9 µm y^{-1}). The samples embedded at BCV bentonite heated up at 90 °C (both irradiated and unirradiated) indicate the highest corrosion rates after 6 months of loading (14.9 ± 1.7☐17.4 ± 4.1 µm y^{-1}). The lowest corrosion rates were observed in samples stored at laboratory temperature without any irradiation (*Table 30*, *Figure 109*).

Table 30 – Corrosion rates (µm/y) of steel samples. AVG – average, ± L – confidence interval of the Student's distribution at the significance level α = 0.05. IR – irradiated, NIR – unirradiated, 6 (resp. 9, 12 or 18) – the length of heating period in months, MX80 – MX-80 bentonite.

Module no.	Sample no.	Bentonite	AVG	± L
1	BCV150IR6	BCV	12	1.5
3	BCV150IR9	BCV	11.1	1.9
5	BCV150IR12	BCV	12.3	2.1
7	BCV150IR18	BCV	10.1	2
2	BCV150NIR6	BCV	24.3	3.2
4	BCV150NIR9	BCV	18	1.9
6	BCV150NIR12	BCV	13.3	1.6
8	BCV150NIR18	BCV	17.5	1.1
12	BCV90IR9	BCV	14.9	1.7
14	BCV90IR12	BCV	11.7	1.8
16	BCV90IR18	BCV	9.3	1.4
13	BCV90NIR9	BCV	17.4	4.1
15	BCV90NIR12	BCV	13.1	2.1
17	BCV90NIR18	BCV	12.9	2.3
20	BCVRTNIR6	BCV	6	0.8
21	BCVRTNIR9	BCV	4.7	0.2
22	BCVRTNIR12	BCV	3.6	0.6
23	BCVRTNIR18	BCV	2.6	0.1
9	MX80150IR18	MX80	17.2	0.3
10	MX80150NIR18	MX80	18.9	0.3
11	MX80RTNIR18	MX80	2.2	0.1
18	MX8090IR18	MX80	4.7	0.1
19	MX8090NIR18	MX80	4.5	0.7

EURAD (Deliverable n° 15.12) – Identification on the effect of transient processes on corrosion
Dissemination level: Public
Date of issue of this report: **29/04/2024**

Page 134

Different corrosion rates were observed when steel samples were embedded at MX80 bentonite (*Figure 110*). The highest corrosion rates were observed when steel samples were embedded at MX-80 bentonite and heated up at 150 °C (both irradiated and unirradiated, 17.2 ± 0.3 μm y^{-1}, resp. 18.9 ± 0.3 μm y^{-1}). The steel samples embedded at MX-80 bentonite heated up at 90 °C indicate much lower corrosion rates (2.2 ± 0.1 μm y^{-1} resp. 4.7 ± 0.1 μm y^{-1}) comparable to those of thermally unloaded samples (4.5 ± 0.7 μm y^{-1}) *Figure 110*).
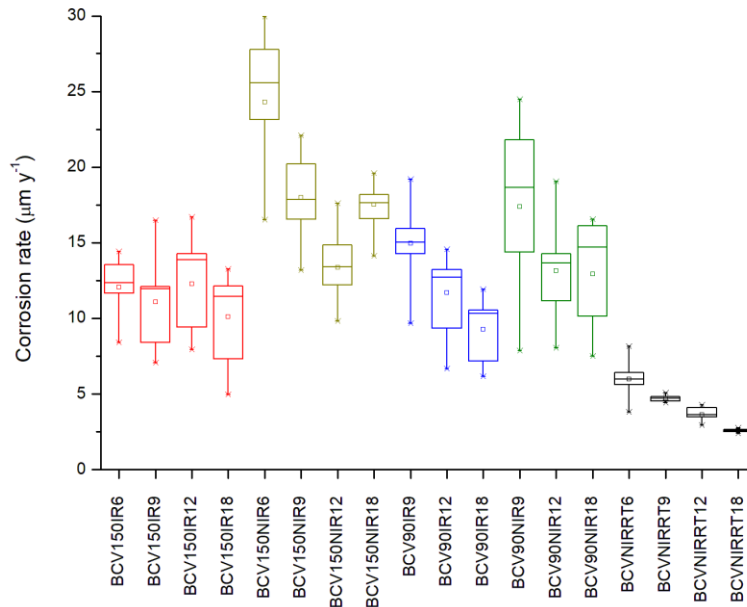
Figure 109 – Corrosion rate of steel samples loaded at BCV bentonite at 150 °C (red – irradiated, dark yellow – unirradiated), 90 °C (blue – irradiated, green – unirradiated) and at laboratory temperature (black). The loading period is indicated by last 1–2 digits in the title of the samples (6, 9, 12 or 18).
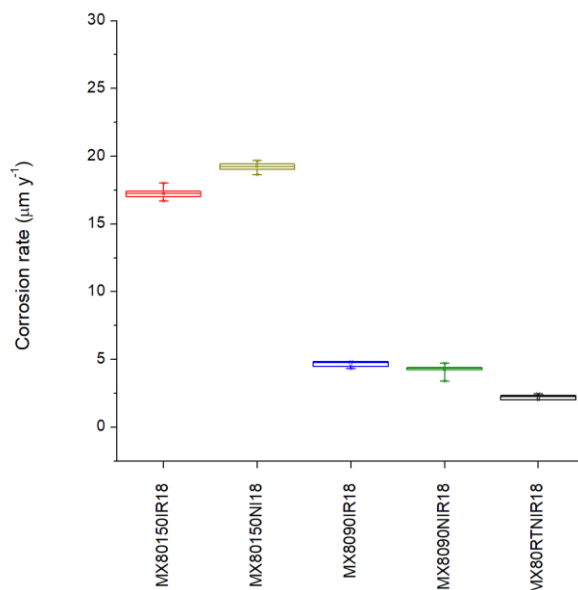
Figure 110 – Corrosion rate of steel samples embedded at MX80 bentonite heated up at 150 °C (red – irradiated, dark yellow – unirradiated), 90 °C (blue – irradiated, green – unirradiated) and at laboratory temperature (black). The loading period – 18 months.

EURAD (Deliverable n° 15.12) – Identification on the effect of transient processes on corrosion
Dissemination level: Public
Date of issue of this report: 29/04/2024

Page 135

5.6.2 SEM-EDX and LOM

Light optical microscopy (LOM) analysis confirmed ferritic-pearlitic microstructure of steel samples (*Figure 111*). The transition from ferritic-pearlitic microstructure to spheroidal microstructure was observed only in one steel sample in BCV bentonite in the module no. 2 heated up at 150 °C without irradiation for 6 months. Pearlite was found forming lamellae up to 30 μm thick in all steel samples. The steel's surface roughness revealed the presence of surface depressions, which were approximately 25□30 μm deep and filled with corrosion products.

The corrosion products formed a layer partially covering the steel surface for samples loaded for 6□9 months or completely covering it (12-18 m) in the BCV bentonite. Thinner corrosion layer and deeper depression are typical for steel samples heated in MX-80 bentonite. The thickness of the corrosion layer varied, ranging from 10 to 43 μm (*Table 31*), and was directly correlated with the duration of loading. Irradiation and thermal loading at 150 °C led to the formation of thinner corrosion layers, typically ranging from 10 to 20 μm.

Similar thickness of corrosion layer (5 to 20 μm) was found in the steel samples that remained unirradiated (*Figure 113*). More extensive corrosion layers (20 to 45 μm thick) were identified in the steel samples heated up at 90 °C (*Figure 114*, *Figure 115*) showing no difference regarding to the irradiation.
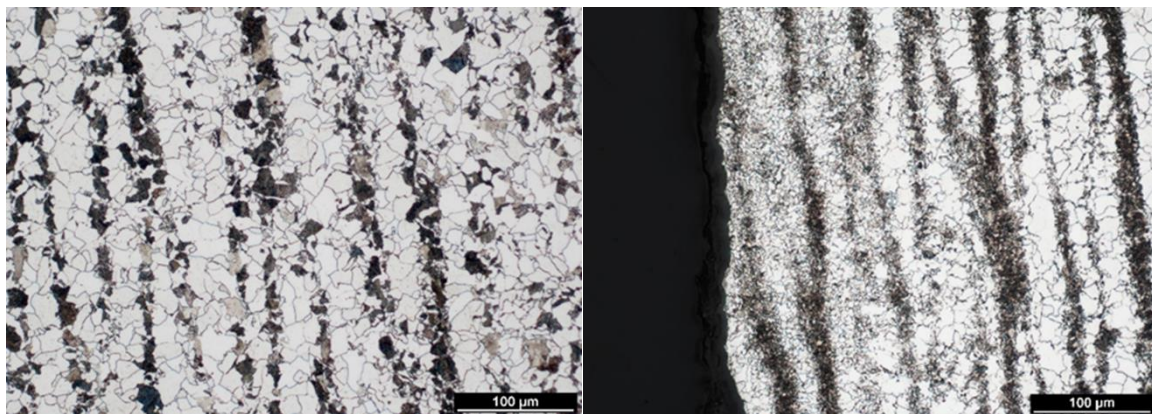
Figure 111 – Steel microstructure ferritic-pearlitic (left) and ferritic-pearlitic with spheroidal areas (right) (module no. 2).

EURAD (Deliverable n° 15.12) – Identification on the effect of transient processes on corrosion
Dissemination level: Public
Date of issue of this report: **29/04/2024**

Page 136

Table 31 – Composition and maximum thickness of corrosion layer measured employing SEM-LOM analysis in the cross-section.

Module no.	Composition of corrosion/alteration layer	Max. thickness (μm)	Module no.	Composition of corrosion/alteration layer	Max. thickness (μm)
1	Fe-O, Fe-Si-O, Ca-Fe-(Mg-Mn)-O	15.7	13	Fe-O, Fe-Ca-Mn-Mg-O, Ca-Fe-Mg-Mn-O	43.0
3	Fe-O, Fe-Si-O, Ca-Fe-(Mg-Mn)-O	21.7	15	Fe-O, Fe-Ca-Mn-Mg-O, Ca-Fe-Mg-Mn-O	42.8
5	Fe-O, Fe-Si-O, Ca-Fe-(Mg-Mn)-O	22.1	17	Fe-O, Fe-Ca-Mn-Mg-O, Ca-Fe-Mg-Mn-O	-
7	Fe-O, Fe-Si-O, Ca-Fe-(Mg-Mn)-O	42.0	23	Fe-O, Ca-Fe-O	10.0
2	Fe-O, Fe-Si-O, Ca-Fe-(Mg-Mn)-O	15.0	9	Fe-O, Fe-Si-O, Fe-Si-(S-Mn)-O	12.2
4	Fe-O, Fe-Si-O, Ca-Fe-(Mg-Mn)-O	34.6	10	Fe-O, Fe-Si-O, Fe-Ca-(Mn)-O	40.0
6	Fe-O, Fe-Si-O, Ca-Fe-(Mg-Mn)-O	23.5	18	Fe-O, Fe-Ca-(Mn)-O	-
8	Fe-O, Fe-Si-O, Ca-Fe-(Mg-Mn)-O	31.2	19	Fe-O, Fe-Ca-(Mn)-O	-
12	Fe-O, Fe-Ca-Mn-Mg-O, Ca-Fe-Mg-Mn-O	24.5	11	Fe-O, Fe-Ca-(Mn)-O	10.0
14	Fe-O, Fe-Ca-Mn-Mg-O, Ca-Fe-Mg-Mn-O	38.0		-	
16	Fe-O, Fe-Ca-Mn-Mg-O, Ca-Fe-Mg-Mn-O	-			

Employing SEM-EDS analysis it was found different composition of corrosion products dependent on the temperature of thermal loading. Two discrete layers originated at 90 °C: a layer of Fe-oxide (Fe-oxy-hydroxide) and a layer of carbonates mixed with minerals coming from bentonite (*Figure 114*, *Figure 115*). On the other hand, the steel samples heated up at 150 °C contain: a layer composed of Fe-Si-O(OH) and a layer of carbonates mixed with minerals coming from bentonite (*Figure 111* to *Figure 113*). The formation of Fe-Si-O(OH) layer is more obvious in samples heated at 150 °C and irradiated (*Figure 112*). These results partially correlate with the composition of corrosion products determined through XRD analysis. These included magnetite, Fe-rich carbonates, and a mixture of magnetite and clay minerals originating from the bentonite. The presence of Fe-Si-rich phases was not identified.

Corrosion layers are dominated by Fe-O and Fe-Si-O phases in the MX-80 bentonite (*Figure 116*). The thickness of the corrosion layer is comparable or slightly higher comparing to those embedded in BCV bentonite and loaded under similar conditions. Only very thin corrosion layer (5-10 μm thick) composed of Fe-O and Ca-Fe-O was analysed on unheated and unirradiated steel sample loaded in the BCV bentonite (*Figure 117*).

Fe-S phases were detected on the steel samples loaded in MX-80 bentonite, both heated and unheated (*Figure 118*). They are explained as a mixture of steel corrosion and Fe-S phases. Their morphology and poor bordering indicate their possible corrosion/alteration. On the other hand, pyrite was analysed employing XRD in the MX-80_input.

EURAD (Deliverable n° 15.12) – Identification on the effect of transient processes on corrosion
Dissemination level: Public
Date of issue of this report: **29/04/2024**

Page 137
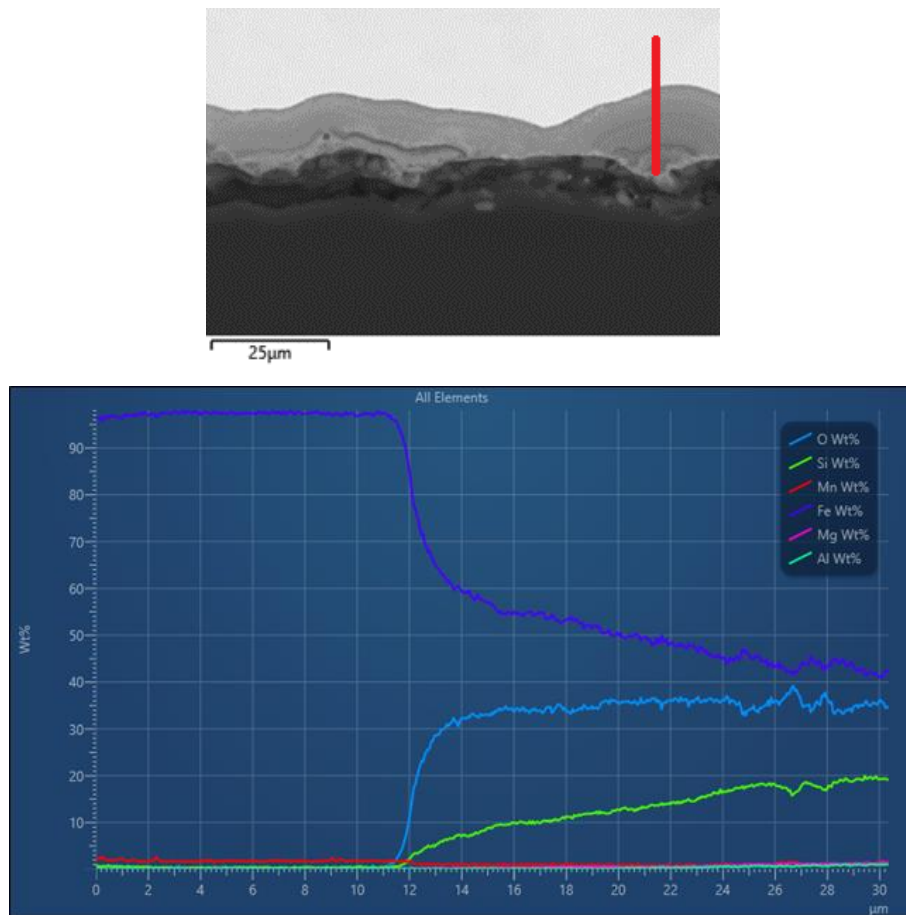
Figure 112 – Corrosion layer on the surface of irradiated steel samples embedded in BCV bentonite heated at 150 °C for 12 months (module no. 5). SEM images including red line indicating position of the profile analysed by EDS (above) and the profile analysis.

EURAD (Deliverable n° 15.12) – Identification on the effect of transient processes on corrosion
Dissemination level: Public
Date of issue of this report: **29/04/2024**

Page 138
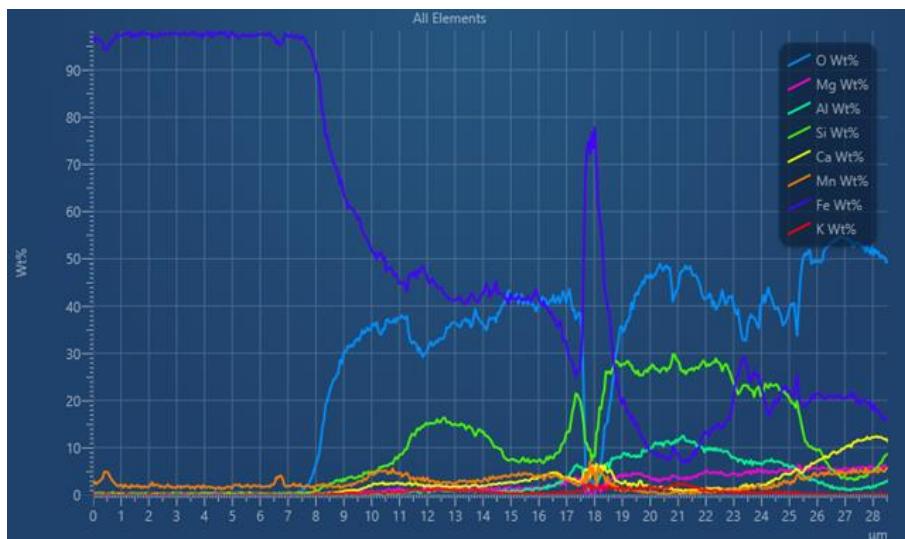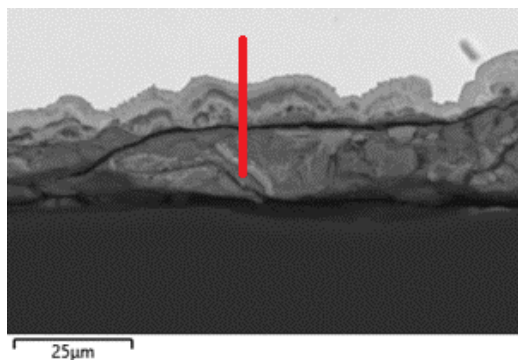
Figure 113 – Corrosion layer on the surface of unirradiated steel samples embedded in BCV bentonite heated up at 150 °C for 12 months (module no. 6). SEM images including red line indicating position of the profile analysed by EDS (above) and the profile analysis.

EURAD (Deliverable n° 15.12) – Identification on the effect of transient processes on corrosion
Dissemination level: Public
Date of issue of this report: **29/04/2024**

Page 139
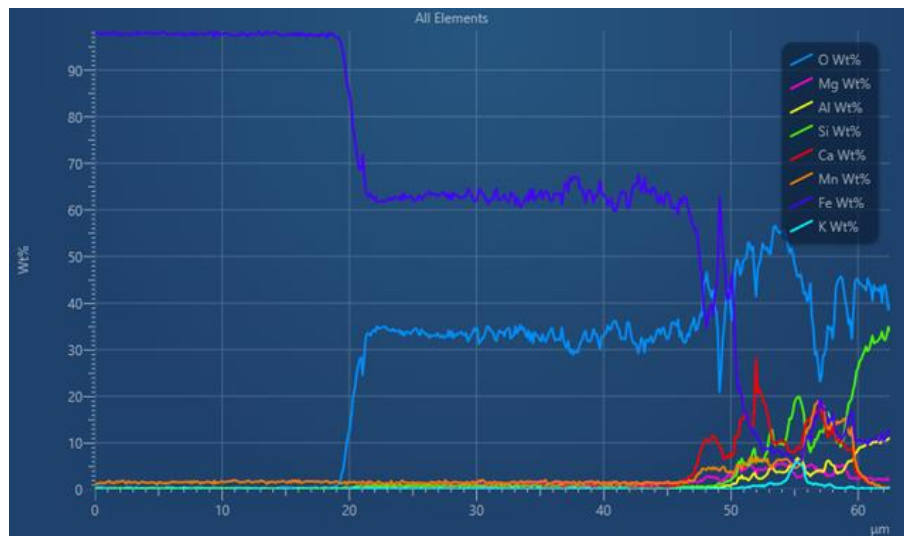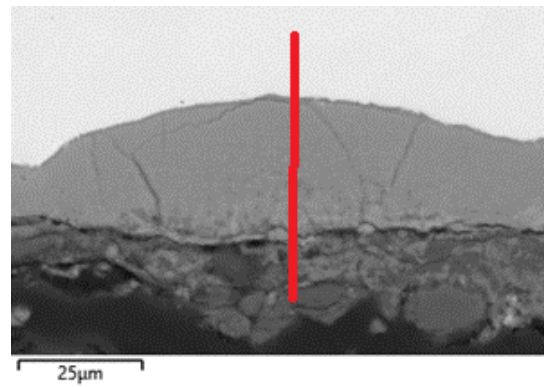
Figure 114 – Corrosion layer on the surface of irradiated steel samples embedded in BCV bentonite heated up at 90 °C for 12 months (module no. 14). SEM images including red line indicating position of the profile analysed by EDS (above) and the profile analysis (right).

EURAD (Deliverable n° 15.12) – Identification on the effect of transient processes on corrosion
Dissemination level: Public
Date of issue of this report: **29/04/2024**

Page 140
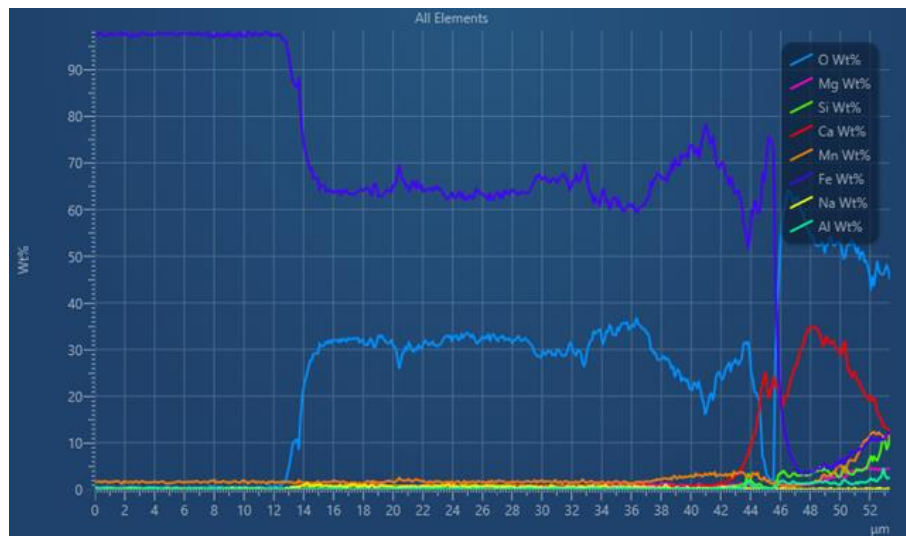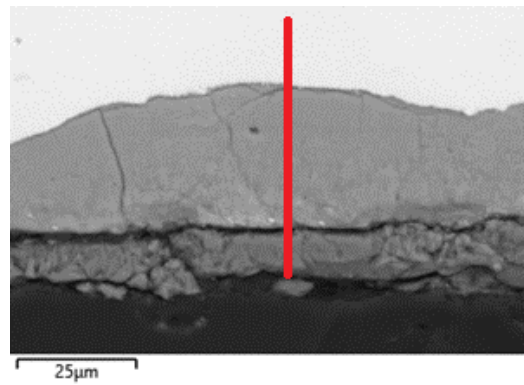
Figure 115 – Corrosion layer on the surface of unirradiated steel samples embedded in BCV bentonite heated up at 90 °C for 12 months (module no. 15). SEM images including red line indicating position of the profile analysed by EDS (above) and the profile analysis (right).

EURAD (Deliverable n° 15.12) – Identification on the effect of transient processes on corrosion
Dissemination level: Public
Date of issue of this report: **29/04/2024**

Page 141
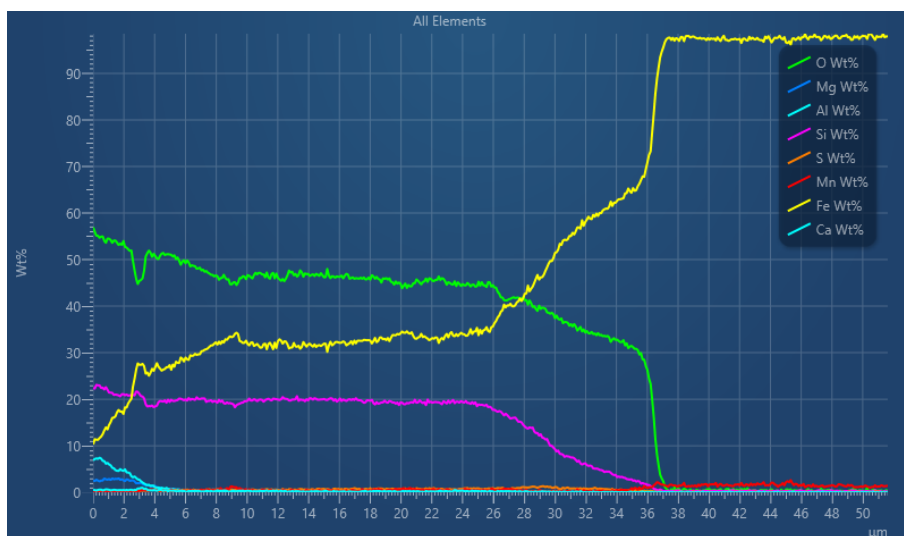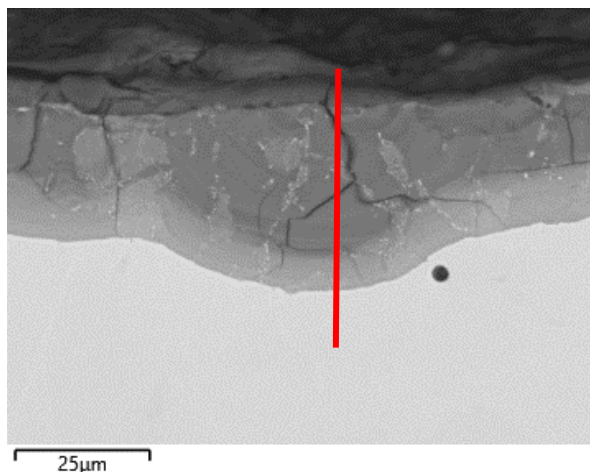
Figure 116 – Corrosion layer on the surface of irradiated steel samples embedded in MX-80 bentonite heated at 150 °C for 18 months (module no. 9). SEM images including red line indicating position of the profile analysed by EDS (above) and the profile analysis.

EURAD (Deliverable n° 15.12) – Identification on the effect of transient processes on corrosion
Dissemination level: Public
Date of issue of this report: **29/04/2024**

Page 142
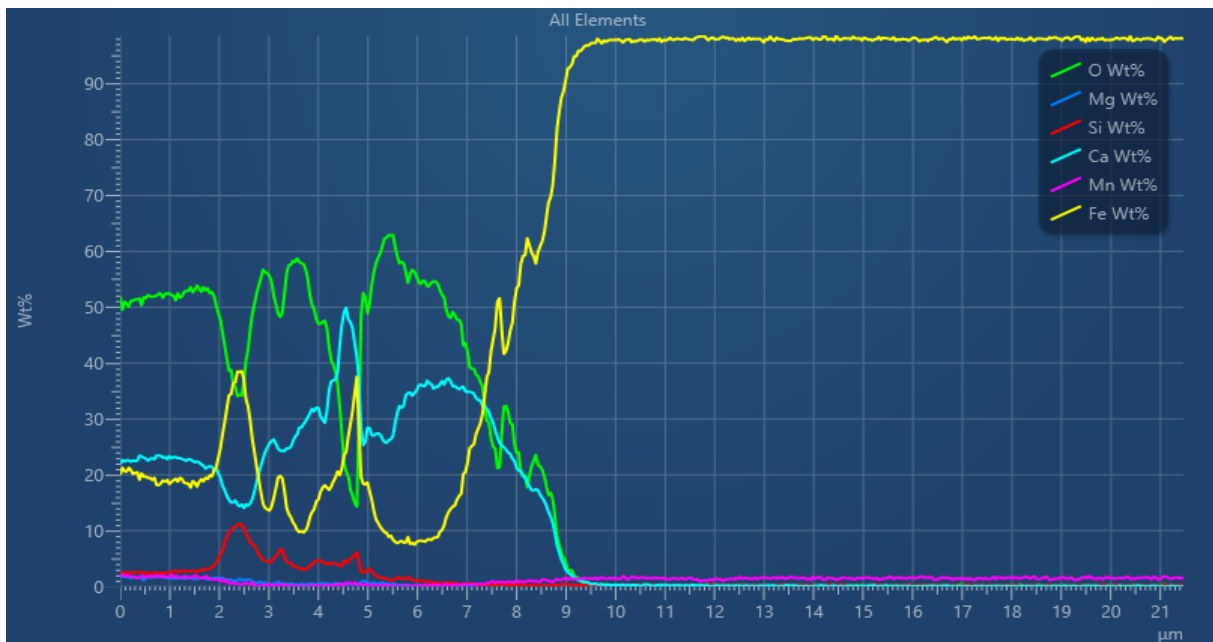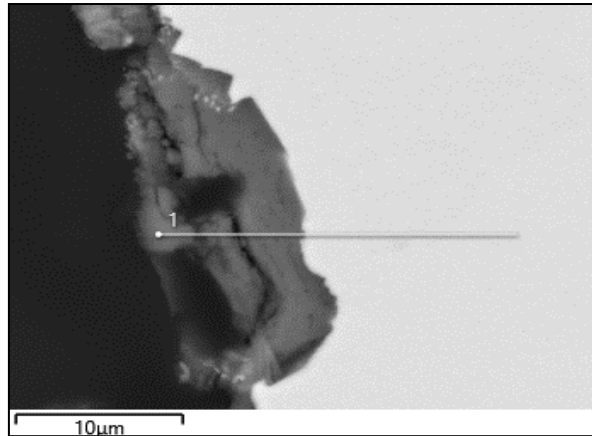
Figure 117 – Corrosion layer on the surface of unirradiated steel sample embedded in BCV bentonite stored at ambient temperature for 18 months (module no. 23). SEM images including red line indicating position of the profile analysed by EDS (above) and the profile analysis.

EURAD (Deliverable n° 15.12) – Identification on the effect of transient processes on corrosion
Dissemination level: Public
Date of issue of this report: **29/04/2024**

Page 143

Table 32 – Chemical composition of Fe-Ca-O corrosion products as analysed b EDX on the steel samples embedded in the BCV and MX-80 bentonite heated up to 90 °C (90), 150 °C (150) or at ambient temperature (RT), irradiated (IR) or unirradiated (NIR) for 12 (12m) and 18 months (18m).

Loading conditions	Spectrum	O	Mg	Al	Si	S	K	Ca	Mn	Fe
MX80_RT_NIR_18m	1	48.7	/	/	/	0.8	/	45.6	/	3.6
MX80_RT_NIR_18m	2	47.8	0.4	/	/	0.9	/	29.3	1.1	20.6
MX80_RT_NIR_18m	7	34.1	/	/	/	0.5	/	33.4	4.1	26.6
MX80_RT_NIR_18m	8	38.2	/	/	/	0.5	/	31.7	3.6	24.7
MX80_90_IR_18m	3	37.3	/	/	1.0	0.6	/	7.8	1.2	52.0
MX80_90_IR_18m	4	39.0	/	/	0.7	0.6	/	8.6	1.3	49.8
MX80_90_IR_18m	12	29.1	/	/	0.8	0.6	/	6.3	3.4	60.0
MX80_90_IR_18m	3	29.9	1.5	/	0.4	1.0	/	15.3	2.9	49.1
MX80_90_IR_18m	4	43.5	2.1	/	1.3	1.2	/	22.2	2.6	27.3
BCV_RT_NIR_18m	2	33.7	/	/	0.4	/	/	52.4	/	13.5
BCV_RT_NIR_18m	3	49.6	/	/	0.4	/	/	46.3	/	3.8
BCV_RT_NIR_18m	4	39.4	/	/	0.4	/	/	49.9	/	10.4
BCV_150_IR_18m	2	36.2	6.3	/	0.4	/	/	42.1	11.9	3.2
BCV_90_IR_12m	4	48.2	4.3	/	0.5	/	/	20.5	4.7	21.8
BCV_90_IR_12m	5	51.2	3.4	/	/	/	/	15.5	4.3	25.7
BCV_90_IR_12m	6	43.6	1.4	/	/	/	/	26.2	2.8	26.0

EURAD (Deliverable n° 15.12) – Identification on the effect of transient processes on corrosion
Dissemination level: Public
Date of issue of this report: **29/04/2024**

Page 144

Table 33 Chemical composition of Fe-Si-O corrosion products as analysed b EDX on the steel samples embedded in the BCV and MX-80 bentonite heated up to 90 °C (90), 150 °C (150) or at ambient temperature (RT), irradiated (IR) or unirradiated (NIR) for 12 (12m) and 18 months (18m).

Loading conditions	Spectrum	O	Na	Si	S	K	Ca	Mn	Fe
MX80_150_NIR_18m	3	44.3	/	20.9	0.6	/	/	/	34.3
MX80_150_NIR_18m	4	44.8	/	20.8	0.5	0.6	0.3	/	33.0
MX80_150_NIR_18m	5	41.6	0.8	20.1	0.8	0.6	0.3	0.5	35.2
MX80_150_NIR_18m	6	35.1	/	17.3	0.4	/	/	2.3	44.9
MX80_150_NIR_18m	7	34.7	/	17.3	0.4	/	/	2.6	44.7
MX80_150_IR_18m	11	43.1	0.6	20.2	0.6	0.2	0.3	/	34.7
MX80_150_IR_18m	12	43.0	0.6	20.1	0.6	0.2	0.3	/	34.8
MX80_150_IR_18m	14	30.6	/	6.4	0.8	/	/	/	62.2
MX80_150_IR_18m	15	30.7	/	6.1	0.7	/	/	/	62.5
MX80_150_IR_18m	16	26.2	/	5.0	0.8	/	/	1.9	66.2
BCV_150_IR_12m	17	38.4	/	7.1	/	0.6	0.2	0.9	52.7
BCV_150_IR_12m	18	35.6	/	6.7	/	0.3	/	1.0	56.4
BCV_150_IR_12m	19	33.7	/	3.6	/	/	/	0.8	61.8
BCV_150_NIR_18m	18	37.2	/	5.3	/	/	1.0	2.3	54.2
BCV_150_NIR_18m	19	39.3	/	6.0	/	/	1.7	3.3	49.6
BCV_150_NIR_18m	20	36.9	/	9.3	/	/	0.4	1.0	52.5

EURAD (Deliverable n° 15.12) – Identification on the effect of transient processes on corrosion
Dissemination level: Public
Date of issue of this report: **29/04/2024**

Page 145
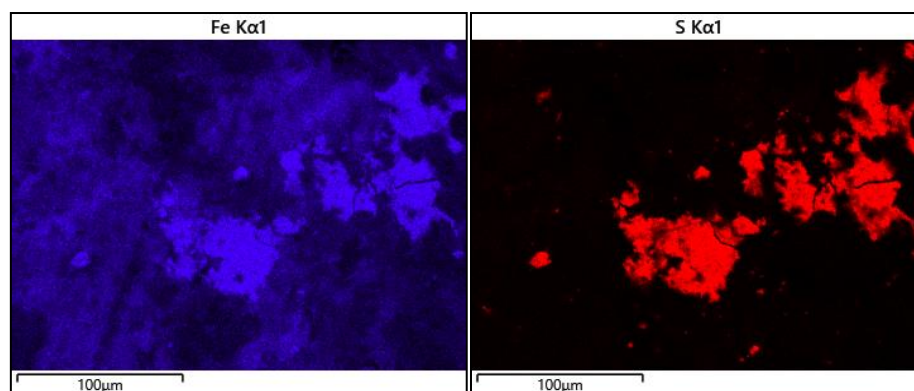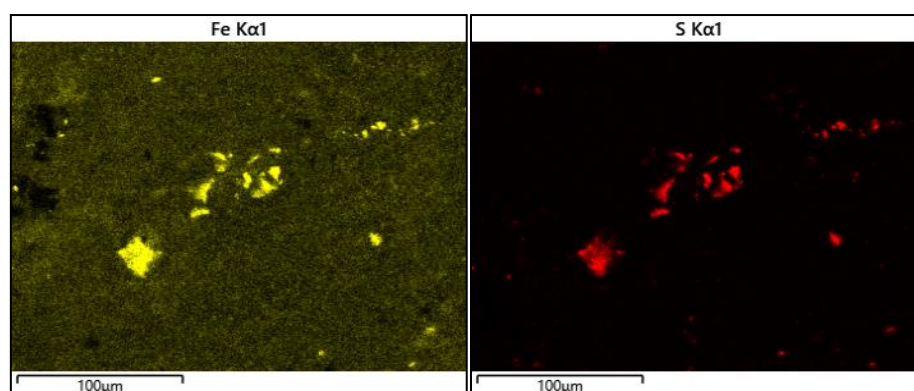
MX80_150_NIR_18m

MX80_150_IR_18m

Figure 118 – EDX element maps of corrosion products originating on the irradiated steel samples embedded in MX-80 bentonite heated at 150 °C for 18 months (module no. 9).

Table 34 – Chemical composition of Fe-S corrosion products as analysed by EDX on the steel samples embedded in the BCV and MX-80 bentonite heated up to 90 °C (90), 150 °C (150) or at ambient temperature (RT), irradiated (IR) or unirradiated (NIR) for 12 (12m) and 18 months (18m).

Loading conditions	Spectrum	O	Al	Si	S	Fe
MX80_RT_NIR_18m	1	13.6	0.9	2.0	43.2	40.4
MX80_RT_NIR_18m	2	12.1	0.9	1.8	44.4	40.0
MX80_150_IR_18m	3	3.3	0	1.1	34.3	61.0
MX80_150_IR_18m	7	8.6	0.4	2.3	33.1	55.6
MX80_150_NIR_18m	1	3.0	/	0.8	35.7	60.6
MX80_150_NIR_18m	2	2.6	/	0.5	33.8	63.1
MX80_150_NIR_18m	3	2.6	/	0.5	33.9	63.1
MX80_150_NIR_18m	4	9.0	0.4	1.6	31.8	57.2

EURAD (Deliverable n° 15.12) – Identification on the effect of transient processes on corrosion
Dissemination level: Public
Date of issue of this report: **29/04/2024**

Page 146

5.6.3 Profilometry

Based on the profilometry analysis it was confirmed surface corrosion of the steel samples heated in the BCV and MX80 bentonite. The degree of the corrosion was quantified based on the mean value and variation, both related to the reference plane. The mean value and colour map of the BLANK sample (*Figure 119*,

EURAD (Deliverable n° 15.12) – Identification on the effect of transient processes on corrosion
Dissemination level: Public
Date of issue of this report: **29/04/2024**

Page 147

) reflect roughness of the surface related to the steel preparation and grinding prior to the experiment. Lower mean values of the selected steel samples (e.g., modules nos. 1–5) comparing to the BLANK steel sample reflect limitations connected to the profilometry analysis as well as surface smoothing connected to the corrosion (

EURAD (Deliverable n° 15.12) – Identification on the effect of transient processes on corrosion
Dissemination level: Public
Date of issue of this report: **29/04/2024**

Page 148

).

Corrosion of the steel sample in the BCV bentonite at laboratory temperature indicates minor corrosion propagating along the initial surface inhomogeneities (*Figure 119*). Corrosion indicating pitting character was observed in steel samples stored in the MX-80 bentonite at laboratory temperature (*Figure 119*).

Blank   BCV_RT_NIR_18m   MX-80_RT_NIR_18m
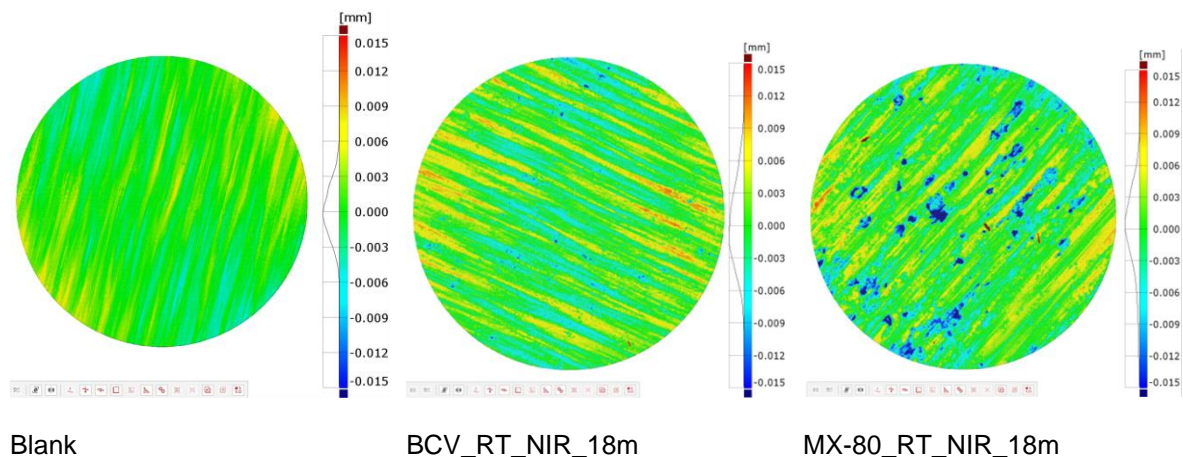
Figure 119 – Comparison of the profilometry analysis of the BLANK steel sample (on the left) with unirradiated steel sample loaded at laboratory temperature in the BCV (in the middle) and MX-80 bentonite (on the right) for 18 months.

Longer loading period and high heating temperature (90 and 150 °C) caused more extensive corrosion (*Figure 120* , *Figure 121*). The extent of corrosion correlates with the standard mean deviation and variation coefficient calculated based on profilometry. The most extensive corrosion located in the boundary parts of steel samples. After 12 and 18 months of heating corrosion affected a major part of the steel surface. Less corrosion was observed on steel samples heated and irradiated in MX-80 bentonite compared to steel sampled heated under similar conditions in the BCV bentonite (*Figure 122* and *Figure 123*).

EURAD (Deliverable n° 15.12) – Identification on the effect of transient processes on corrosion
Dissemination level: Public
Date of issue of this report: **29/04/2024**

Page 149

Table 35 – Deviation from the reference Mean value and variance from reference point based on profilometry.MX80 – MX-80 bentonite, RT – ambient temperature, 90 (resp. 150) – 90 °C (resp. 150 °C), IR – irradiated, NIR – unirradiated.

Sample no.	Module no.	Side A			Side B		
		Mean value (µm)	Standard mean deviation (µm)	Variation (µm²)	Mean value (µm)	Standard mean deviation (µm)	Variation (µm²)
BCV_150_IR_6m	1	0.00	3.35	11.24	n.a.	n.a.	n.a.
BCV_150_IR_9m	3	0.00	3.72	13.85	-0.02	4.21	17.74
BCV_150_IR_12m	5	0.16	4.95	24.46	0.18	4.54	20.61
BCV_150_IR_18m	7	-1.04	8.03	64.41	0.24	6.71	45.04
BCV_150_NIR_6m	2	0.02	3.29	10.85	n.a.	n.a.	n.a.
BCV_150_NIR_9m	4	-0.03	4.43	19.59	0.08	4.21	17.71
BCV_150_NIR_12m	6	0.36	4.76	22.63	0.03	5.51	30.33
BCV_150_NIR_18m	8	0.01	6.61	43.72	-0.02	4.34	18.85
BCV_90_IR_9m	12	0.28	5.54	30.66	1.15	8.64	74.65
BCV_90_IR_12m	14	-2.00	9.71	94.30	-0.64	6.73	45.25
BCV_90_IR_18m	16	0.50	13.09	171.37	-0.63	12.04	145.08
BCV_90_NIR_9m	13	-1.35	11.08	122.72	-0.46	8.13	66.07
BCV_90_NIR_12m	15	-2.39	10.59	112.23	-1.11	9.31	86.67
BCV_90_NIR_18m	17	1.37	8.08	65.36	1.03	7.67	58.78
BCV_RT_NIR_12m	22	0.24	4.01	16.05	0.49	3.98	15.82
BCV_RT_NIR_18m	23	-0.11	3.40	11.54	0.13	3.81	14.51
MX80_150_IR_18	9	0.16	6.91	47.74	0.05	5.41	29.24
MX80_150_NIR_18	10	-0.03	6.56	43.00	-0.46	5.70	32.47
MX80_90_IR_18	18	-0.14	4.05	16.41	-0.18	5.23	27.37
MX80_90_NIR_18	19	-0.36	4.26	18.19	-0.21	4.29	18.44
MX80_RT_NIR_18	11	-0.58	4.90	24.01	-0.47	3.23	10.44
/	BLANK	0.27	3.76	14.15	0.04	2.19	4.80

![eurad logo] European Joint Programme on Radioactive Waste Management

EURAD (Deliverable n° 15.12) – Identification on the effect of transient processes on corrosion
Dissemination level: Public
Date of issue of this report: **29/04/2024**

Page 150
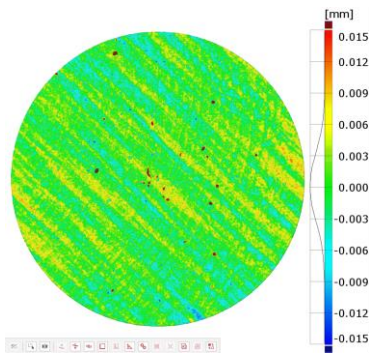
BCV_150_IR_6m (module no. 1)
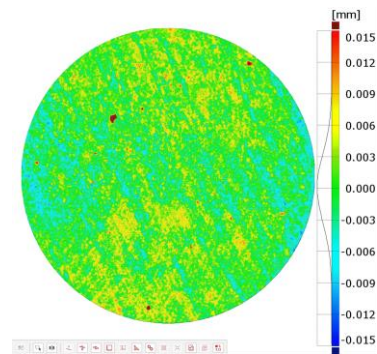
BCV_150_NIR_6m (module no. 2)
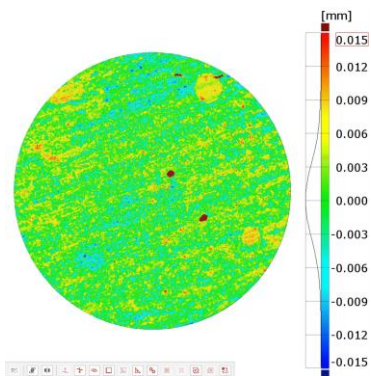
BCV_150_IR_9m (module no. 3)
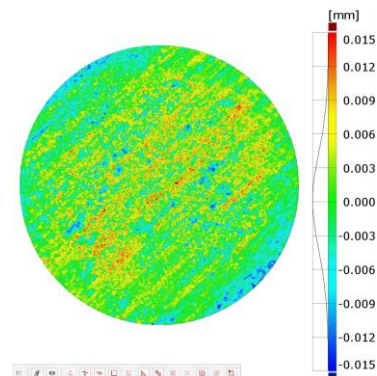
BCV_150_NIR_9m (module no. 4)
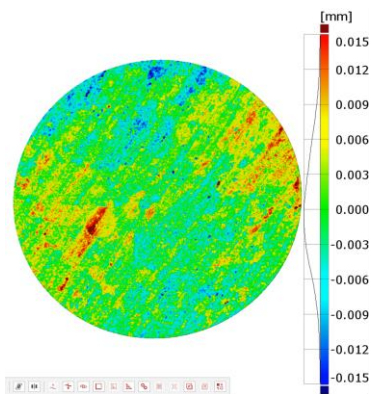
BCV_150_IR_12m (module no. 5)
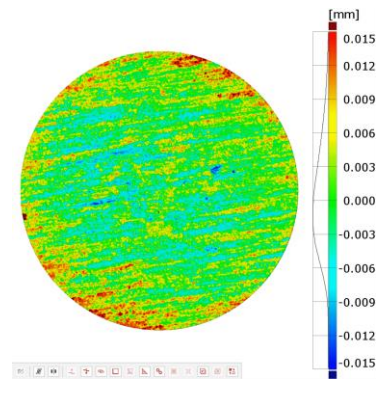
BCV_150_NIR_12m (module no. 6)
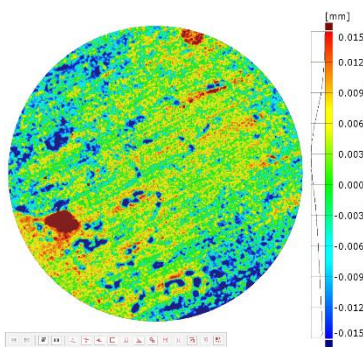
BCV_150_IR_18m (module no. 7)

BCV_150_NIR_18m (module no. 8)

EURAD (Deliverable n° 15.12) – Identification on the effect of transient processes on corrosion
Dissemination level: Public
Date of issue of this report: **29/04/2024**

Page 151
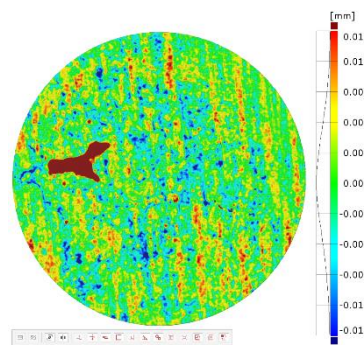
Figure 120 – Comparison of the profilometry analysis of steel samples in the BCV bentonite heated up at 150 °C and irradiated for 6 (module no. 1), 9 (module no. 3), 12 (module no. 5) and 18 months (module no. 7) with the unirradiated ones (modules no. 2, 4, 6 and 8).

BCV_90_IR_9m (module no. 12)

BCV_90_NIR_9m (module no. 13)

BCV_90_IR_12m (module no. 14)

BCV_90_NIR_12m (module no. 15)

BCV_90_IR_18m (module no. 16)

BCV_90_NIR_18m (module no. 17)
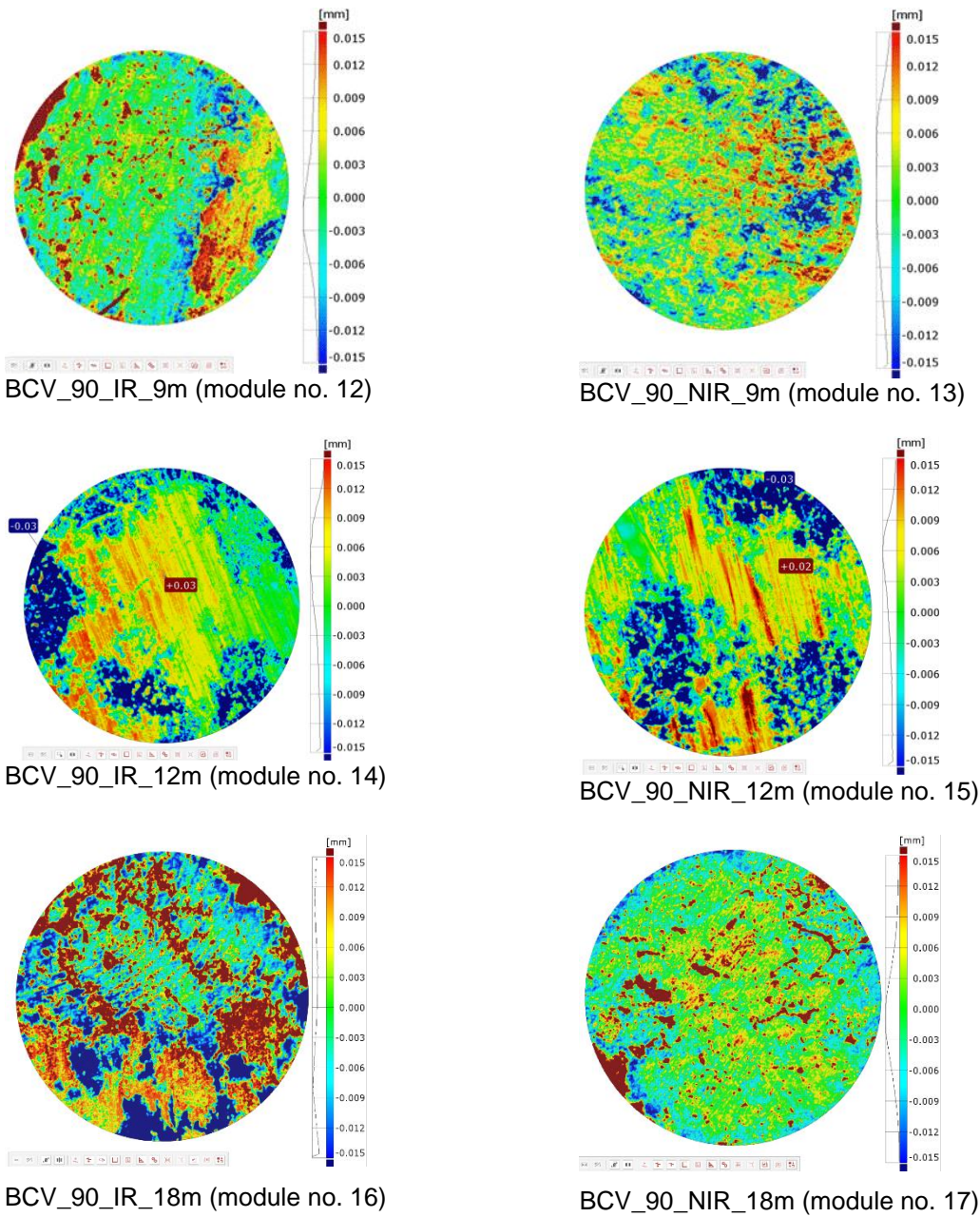
Figure 121 – Comparison of the profilometry analysis of steel samples in the BCV bentonite heated up at 90 °C and irradiated for 9 (module no. 12), 12 (module no. 14) and 18 months (module no. 16) with the unirradiated ones (modules no. 13, 15 and 17).

EURAD (Deliverable n° 15.12) – Identification on the effect of transient processes on corrosion
Dissemination level: Public
Date of issue of this report: **29/04/2024**

Page 152

MX-80_150_IR_18m (module no. 9)   MX-80_150_NIR_18m (module no. 10)

MX-80_90_IR_18m (module no. 18)   MX-80_90_NIR_18m (module no. 19)
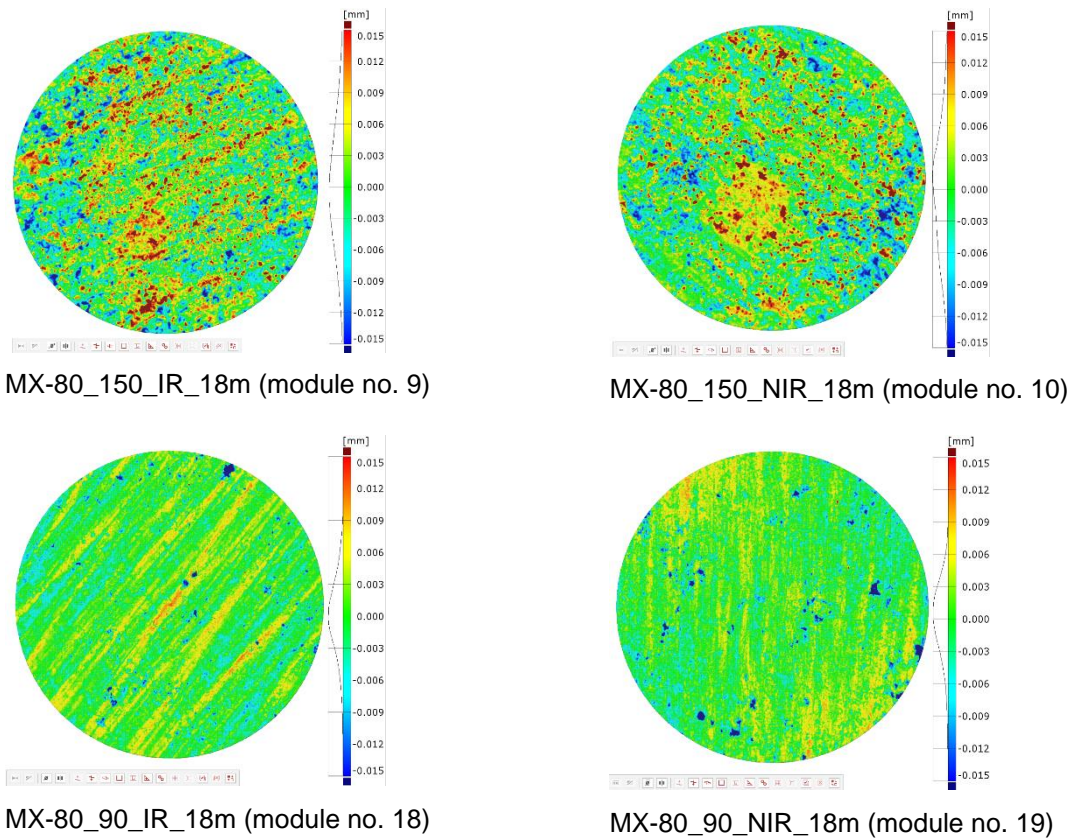
Figure 122 – Comparison of the profilometry analysis of steel samples irradiated in the MX-80 bentonite heated up at 150 °C (module no. 9) and 90 °C (module no. 18) for 18 months with the unirradiated ones (modules no. 10 and 19).

.
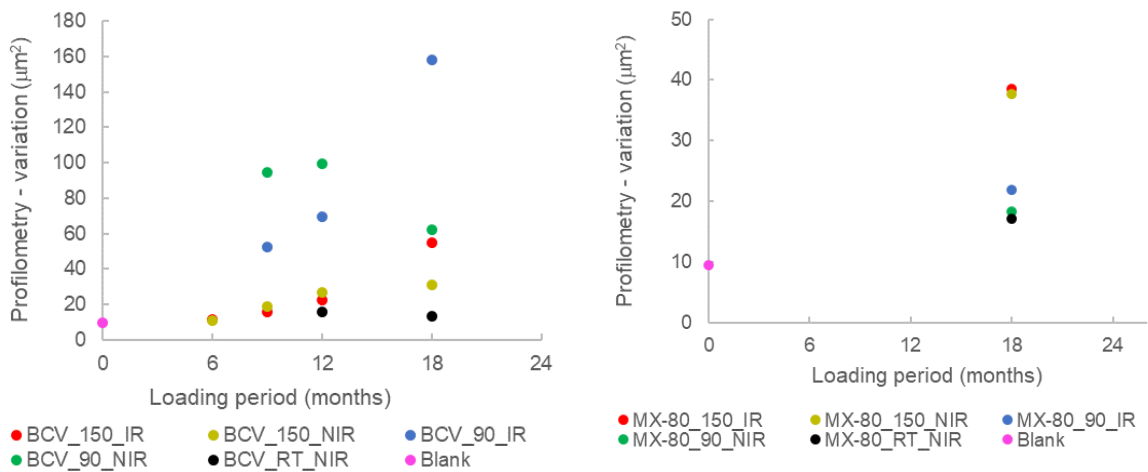
Figure 123 – Comparison of variation values of steel samples in the BCV bentonite (on the left) and in the MX-80 bentonite (on the right) heated at 90 °C, 150 °C and at ambient temperature (RT).

![eurad logo] EURAD (Deliverable n° 15.12) – Identification on the effect of transient processes on corrosion
Dissemination level: Public
Date of issue of this report: **29/04/2024**

Page 153

5.6.4 XRD and Raman spectroscopy

Bulk mineralogical composition of the BCV and MX-80 bentonite is shown in *Table 36*. The BCV_input bentonite is dominated by dioctahedral smectite (montmorillonite, d_{060} ~ 1.50 Å, d_{001} ~ 15.18 Å), accompanied by quartz and kaolinite. Illite, and goethite were analysed in amount < 5 wt.%. anatase, calcite, aragonite, ankerite, siderite, fluorapatite, augite, rutile and sanidine were analysed in amount < 1 wt.%.

There is expected ~ 7–10 wt.% of amorphous phases in the BCV bentonite (Červinka et al. 2018). Amorphous phases were not included in the analysis due to inaccuracy connected to its quantification in the bentonite analyses (e.g., Ufer et al. 2008; Heuser 2018). MX-80 bentonite is dominated by dioctahedral smectite (Na-montmorillonite, d_{060} ~ 1.49 Å, d_{001} ~ 11.46 Å) followed by albite. Muscovite (2M1), SiO_2-phases (quartz + cristobalite) and microcline were analysed in amount < 5 wt.%. Calcite, pyrite, siderite and gypsum were analysed in amount < 1 wt.%. The MX-80 semiquantitative composition is in accordance with previously published data (e.g., Ufer et al. 2008).

No changes were observed in d_{006} values of montmorillonite in both types of bentonites connected to loading conditions *Figure 124*). The effect of heating was observed mainly on the position of d_{001} basal diffraction reflecting both hydration and substitution of exchangeable cations (*Figure 125*). The d_{001} basal diffraction of the BCV bentonite shifted from 15.18 Å to 14.41 Å, both values typical for montmorillonite with 2-layer hydrate (e.g., de Pablo et al. 2005). Contrary the shape and the d_{001} value (d_{001} ~ 11.46 Å) of basal diffraction of the MX-80_input is typical for montmorillonite with 1-layer hydrate (e.g., de Pablo et al. 2005). Thermal loading and saturation with SGW3 water caused splitting of MX-80 basal diffraction into two: the major diffraction typical with the d_{001} ~ 12.24–12.61 Å, and the minor one with the d_{001} ~ 13.80–14.68 Å. The splitting is explained by the substitution of Na^+ by Ca^{2+}/Mg^{2+} in the montmorillonite crystal lattice.

Muscovite (2M1) including illite content of the heated BCV bentonite is comparable to those in the BCV_input bentonite which excludes effect of illitization (e.g., Inoue et al. 1988; Madsen et al. 1988, Pusch and Karnland 1988). No changes in illite content reflect very low K^+ content in SGW3 used as a saturation medium. Increasing K^+ content combined with increasing temperature and time is regarded as a main factor affecting illitization of smectite (e.g., Mosser-Ruck et al. 1999; Pusch et al. 2010).

EURAD (Deliverable n° 15.12) – Identification on the effect of transient processes on corrosion
Dissemination level: Public
Date of issue of this report: **29/04/2024**

Page 154

Table 36 – Semiquantitative XRD of randomly oriented powder mounts..

Sample no.	Smc (Ca-Mg)	Kaol	Msc (2M1)	Qz	Arg	Cal	Ank	Sd	Gth	Snd	Ant	Others
BCV_input	72.5	6.2	2.2	10.0	0.6	1.1	0.3	0.6	2.6	2.0	1.9	nd
BCV_150_IR_6m	72.5	3.6	3.0	9.7	nd	1.2	0.5	0.2	4.0	1.2	2.1	2.1
BCV_150_IR_9m	73.1	3.3	2.8	10.2	0.1	0.4	0.5	0.1	4.2	1.1	2.1	2.3
BCV_150_IR_18m	60.9	2.6	7.4	12.7	nd	1.8	0.4	0.1	9.1	nd	0.3	nd
BCV_150_6m	73.9	2.9	3.1	9.8	nd	0.3	0.5	0.2	3.7	1.7	2.1	1.9
BCV_150_9m	69.7	5.2	2.6	10.8	0.3	1.0	0.5	0.3	3.8	1.7	2.3	1.8
BCV_150_18m	60.7	2.4	8	10.4	nd	2.1	0.2	0.2	10.6	nd	0.1	nd
BCV_90_IR_9m	70.7	4.9	2.7	11.2	0.1	0.8	0.4	0.2	3.6	1.6	2.2	1.6
BCV_90_IR_18m	66.6	2.8	6.3	10.6	nd	2.4	0.5	0.3	4.7	nd	0.7	nd
BCV_90_9m	70.9	5.0	2.6	10.6	0.5	1.1	0.4	0.2	3.2	1.6	2.3	1.8
BCV_90_18m	58.3	4.2	6.6	12	nd	2.1	1.1	0.5	8.5	nd	nd	nd
BCV_RT_6m	68.4	6.0	2.8	10.3	1.0	1.1	0.5	0.3	3.5	1.7	2.2	2.2
BCV_RT_9m	70.3	5.2	2.6	11.2	0.4	0.8	0.5	0.0	2.6	1	2.0	0.9
BCV_RT_18m	64.4	1.8	5.6	11.3	nd	2.8	0.4	0.6	6.0	nd	0.6	nd
	Smc (Na)	Smc (Ca)	Msc (2M1)	Qtz+Crs	Cal	Ab	Mc	Gp	Py	Sd		
MX80_input	88.0	nd	1.4	3.8	0.6	1.8	2.5	0.4	0.6	1.1		-
MX80_150_IR_18m	60.4	21.4	2.4	3.8	0.9	3.4	4.7	nd	nd	nd		
MX80_150_NIR_18m	54.6	23.8	2.0	3.0	0.0	7.5	5.7	0.2	nd	nd		
MX80_90_IR_18m	53.2	26.4	1.1	4.4	2.0	7.1	3.7	0.6	nd	nd		
MX80_90_NIR_18m	60.4	20.2	1.8	3.6	0.7	4.5	5.3	0.2	nd	nd		
MX80_RT_NIR_18m	67.6	12.0	1.7	3.6	0	6.3	3.8	0.4	nd	nd		

Ab – albite, Ank – ankerite, Ant – anatase, Arg – aragonite, Aug – augite, bql – bellow quantification limit, Cal – calcite, Crs – cristobalite, F-apt – fluorapatite, Gp – gypsum, Gth – goethite, Kaol – kaolinite, Mc – microcline, Msc – muscovite (including illite), nd – not detected, nq – not quantified, Qz – quartz, Rtl – rutile, Sd – siderite, Smc – smectite, Snd – sanidine

EURAD (Deliverable n° 15.12) – Identification on the effect of transient processes on corrosion
Dissemination level: Public
Date of issue of this report: **29/04/2024**

Page 155
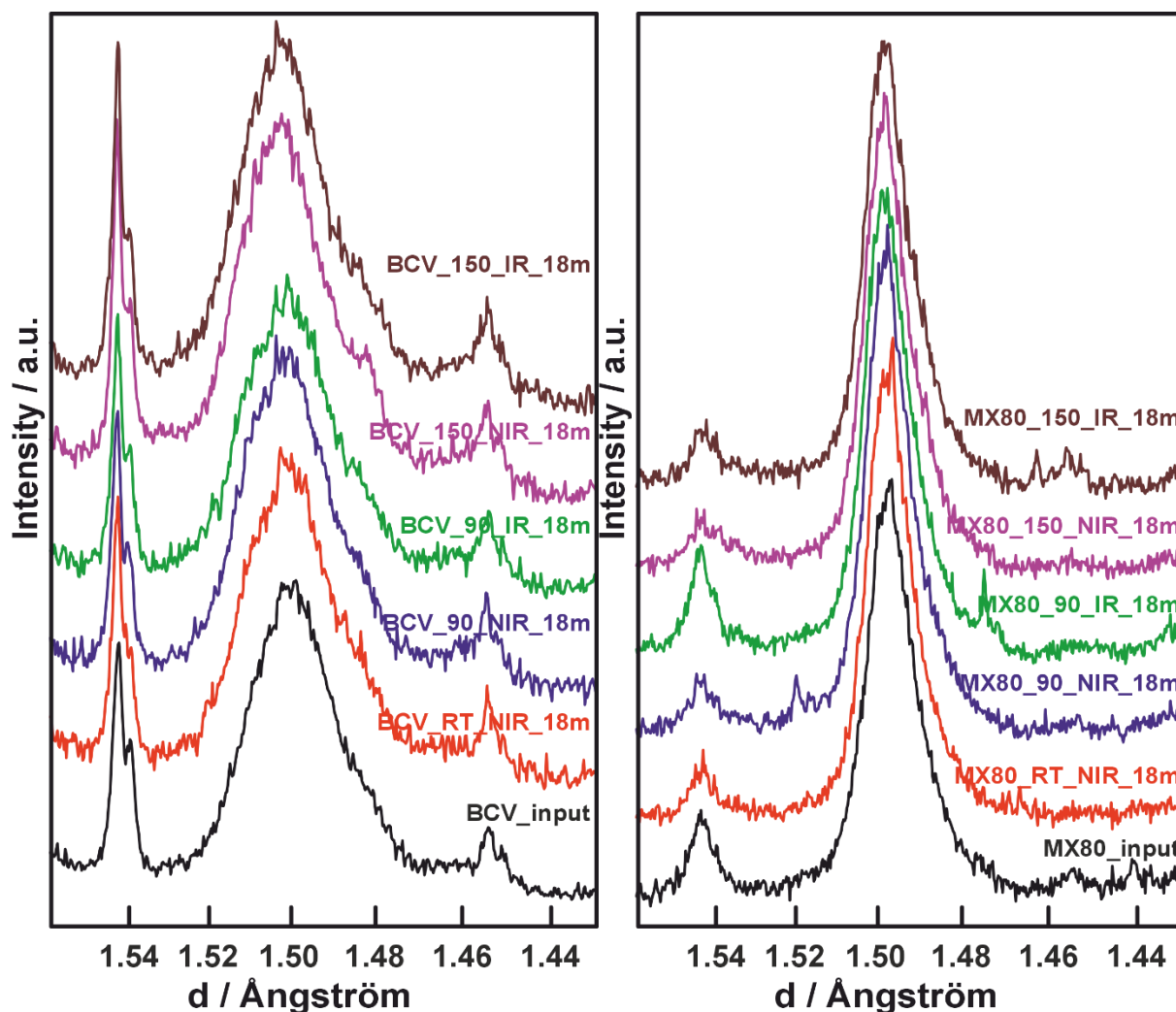
Figure 124 – d$_{006}$ difraction lines of BCV_input bentonite (left) and MX-80_input bentonite (right) – comparison with samples heated up to 90 °C (90), 150 °C (150) or stored at ambient temperature (RT), irradiated (IR) or unirradiated (NIR) for 18 months (18m).

EURAD (Deliverable n° 15.12) – Identification on the effect of transient processes on corrosion
Dissemination level: Public
Date of issue of this report: **29/04/2024**

Page 156
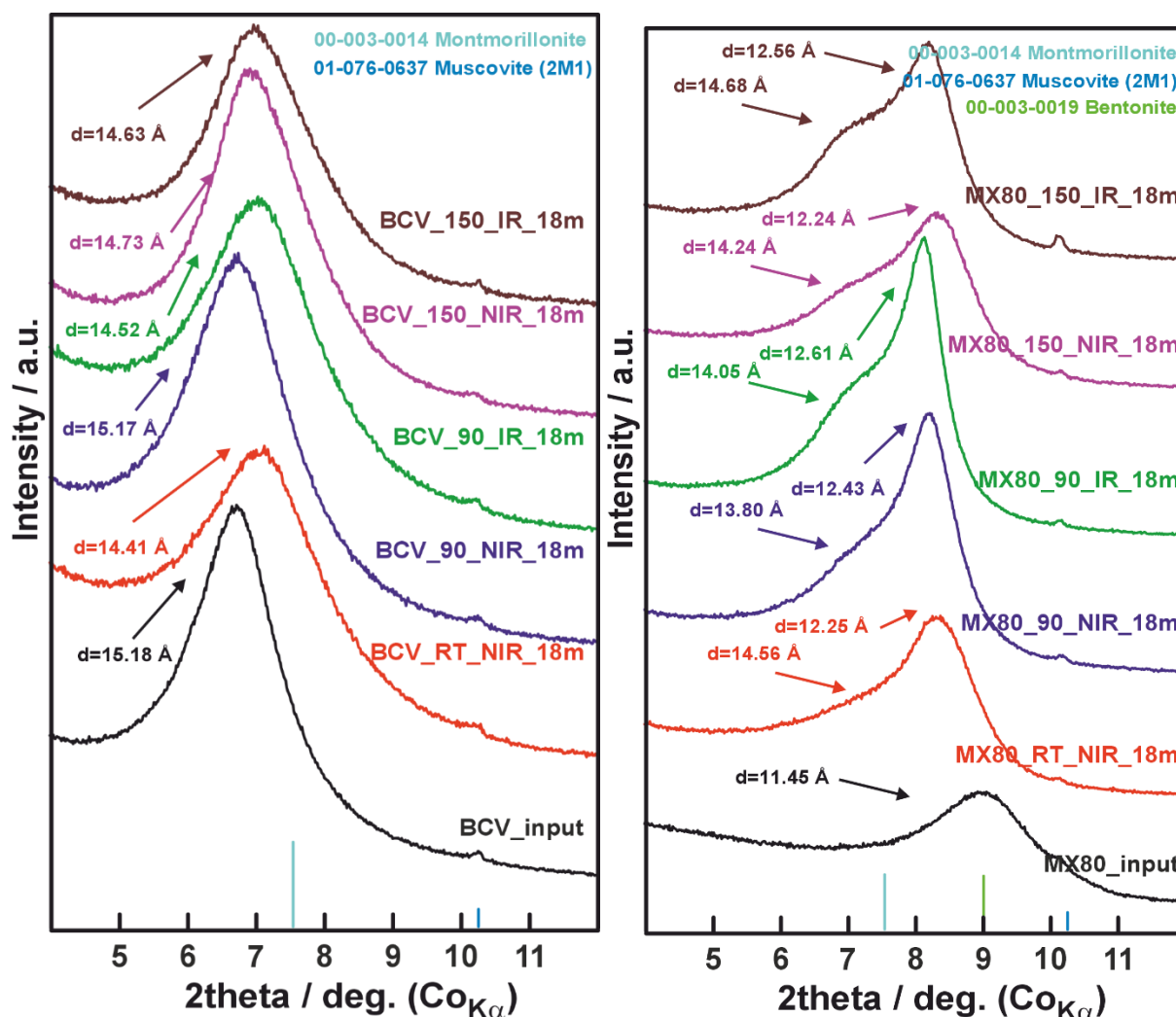
Figure 125 – Basal d_{001} diffraction peak of the BCV_input bentonite (left) and the MX-80_input bentonite (right) – comparison with samples heated up to 90 °C (90), 150 °C (150) or stored at ambient temperature (RT), irradiated (IR) or unirradiated (NIR) for 18 months (18m).

Fe-rich carbonates (siderite), Fe-hydroxy-carbonates (chukanovite) and magnetite were identified as a main corrosion product in the steel samples embedded in BCV bentonite heated up at 90 °C and 150 °C by XRD (*Figure 126*). Siderite was identified as a main corrosion product in the steel samples embedded in MX-80 bentonite heated up at 90 °C and 150 °C (*Figure 127*). Presence of chukanovite and siderite confirmed anoxic conditions of the experiment. Ankerite and aragonite were detected on the surface of steel samples heated up at 90 °C in MX-80 bentonite. These minerals may be the results of corrosion and primarily precipitation from saturation medium.

In all analyses iron and minerals coming from bentonite (montmorillonite, illite, quartz and calcite) were detected as a relic of surrounding material. Presence of silicate-based corrosion products was not confirmed by XRD. The main reason is regarded in very low amount of corrosion products and their possible amorphous character which complicates their identification.

EURAD (Deliverable n° 15.12) – Identification on the effect of transient processes on corrosion
Dissemination level: Public
Date of issue of this report: **29/04/2024**

Page 157
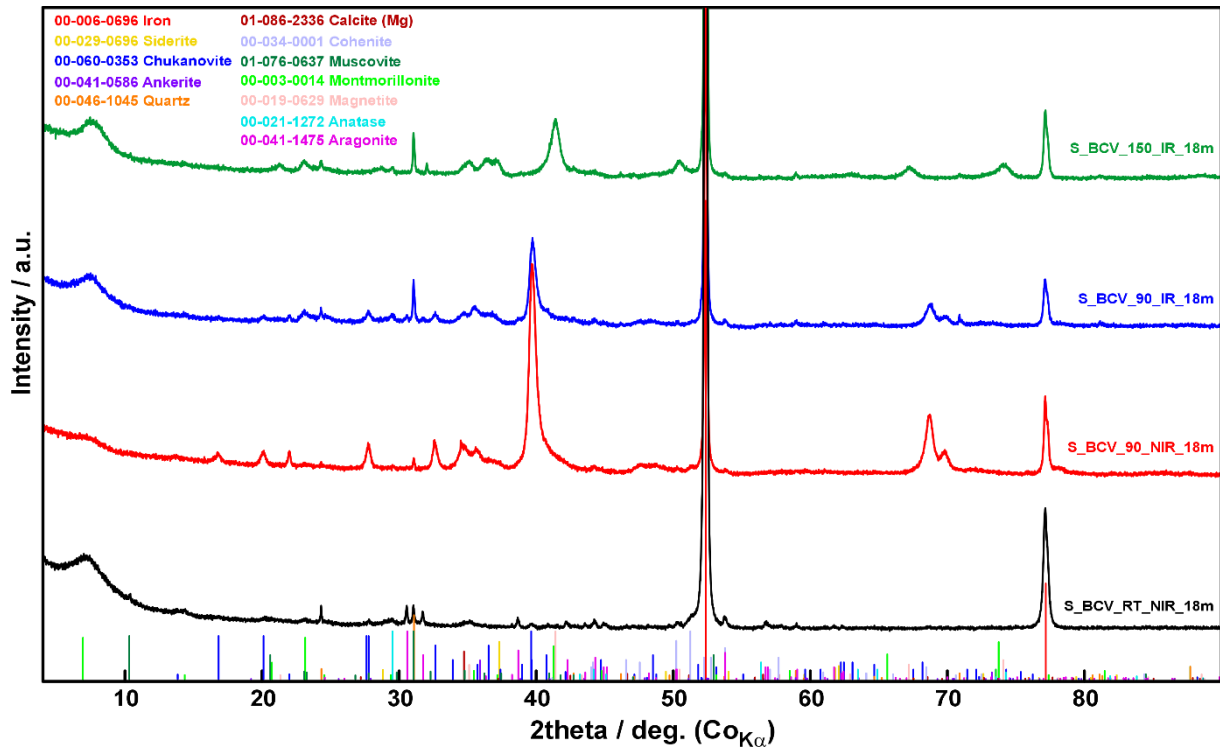
Figure 126 – XRD pattern of carbon steel (S) heated in the BCV bentonite at 90 °C (90), 150 °C (150) or stored at ambient temperature (RT), irradiated (IR) or unirradiated (NIR) for 18 months (18m).
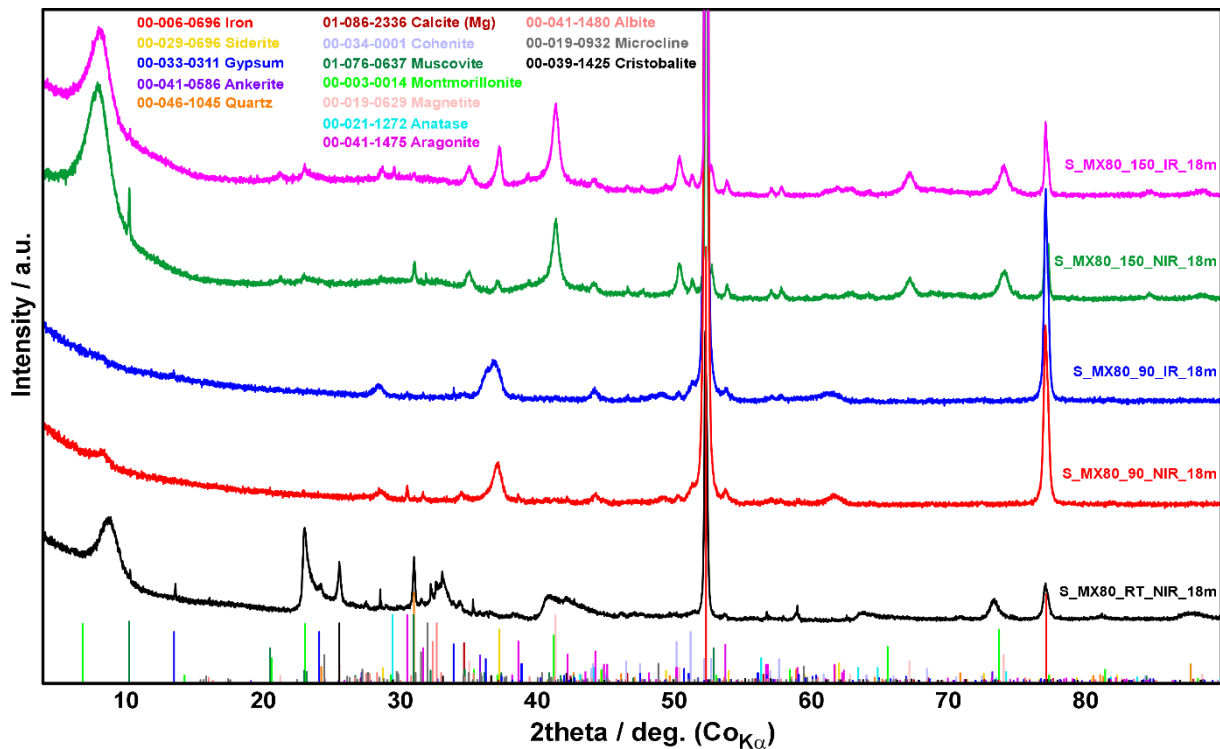
Figure 127 – XRD pattern of carbon steel (S) heated in the MX-80 bentonite (MX80) at 90 °C (90), 150 °C (150) or stored at ambient temperature (RT), irradiated (IR) or unirradiated (NIR) for 18 months (18m).

EURAD (Deliverable n° 15.12) – Identification on the effect of transient processes on corrosion
Dissemination level: Public
Date of issue of this report: **29/04/2024**

Page 158

5.6.5 Bentonite chemical composition

The chemical composition of both types of bentonites (*Table 37*) indicated higher content of Fe_2O_3 in all loaded samples (*Figure 128*a, *Figure 129*a) and increased content of MnO in all heated samples (*Figure 128* – b, *Figure 129* – b) compared to the input bentonites. The main source of both species is regarded in the carbon steel. Due to alteration of steel samples the corrosion products originate forming mixed structures with bentonite.

The CaO content (*Figure 128*c, *Figure 129*c) decreased after 6 and 18 months in all heated samples. The CaO decrease is more obvious in bentonite samples heated up to 90 °C compared to those heated up 150 °C. The MgO content decreased in all samples heated at 150 °C (*Figure 128*d, *Figure 129*d). The MgO decrease is more obvious in the BCV bentonite. The K_2O content increased only in the heated BCV bentonite and in the MX-80 bentonite heated at 150 °C.

Variations of Na_2O content were mainly dependent on the type of bentonite. The BCV bentonite indicated higher Na_2O content when heated up at 150 °C. The MX-80 bentonite indicated slightly lower Na_2O content at the same temperature. No changes in Na_2O content were observed when both types of bentonites were heated up at 90 °C or at ambient temperature. Variable loss of ignition reflects partial drying of the samples during the bentonite pulverizing.

EURAD (Deliverable n° 15.12) – Identification on the effect of transient processes on corrosion
Dissemination level: Public
Date of issue of this report: **29/04/2024**

Page 159

Table 37 (I/II) – Chemical composition of the BCV and MX-80 bentonite heated up at 150 °C (150), 90 °C (90) and at ambient temperature (RT), irradiated (IR) or unirradiated (NIR) (in wt.%). The data were recalculated to the 0.00 wt.% of loss of ignition (LOI).

Sample no.	BCV_input	BCV_150_IR_6				BCV_150_NIR				BCV_90_IR			
Months	0	6	9	12	18	6	9	12	18	9	12	18	
Na_2O	0.35	0.42	0.40	0.35	0.42	0.42	0.39	0.42	0.42	0.33	0.33	0.36	
MgO	3.34	3.24	3.27	3.02	3.05	3.32	3.20	3.13	3.17	3.27	3.22	3.36	
Al_2O_3	20.31	19.47	19.00	18.80	19.21	19.05	19.08	18.73	18.84	19.10	18.92	19.51	
SiO_2	54.44	55.13	54.99	54.34	54.46	54.64	54.54	54.19	53.72	54.22	54.42	54.25	
P_2O_5	0.56	0.58	0.56	0.62	0.62	0.57	0.58	0.60	0.58	0.54	0.58	0.55	
SO_3	0.04	0.07	0.06	0.08	0.08	0.06	0.06	0.12	0.06	0.07	0.09	0.13	
K_2O	1.04	1.12	1.18	1.18	1.15	1.14	1.20	1.17	1.19	1.15	1.15	1.15	
CaO	3.29	3.15	3.18	3.28	3.11	3.16	3.20	3.32	3.03	3.17	3.09	2.95	-
TiO_2	2.92	2.64	2.71	3.02	2.95	2.61	2.86	3.00	2.91	2.96	3.03	2.82	
Cr_2O_3	0.07	0.08	0.08	0.09	0.08	0.09	0.08	0.08	0.08	0.08	0.08	0.08	
MnO	0.21	0.23	0.22	0.24	0.23	0.24	0.25	0.26	0.25	0.23	0.23	0.21	
Fe_2O_3	13.19	13.46	13.97	14.78	14.34	14.16	14.41	14.83	15.42	14.42	14.71	14.31	
NiO	0.02	0.03	0.03	0.03	0.03	0.03	0.03	0.03	0.03	0.03	0.03	0.03	
BaO	0.08	0.23	0.24	0.05	0.15	0.31	0.00	0.00	0.17	0.13	0.00	0.17	
Others	0.14	0.15	0.13	0.12	0.12	0.20	0.13	0.12	0.12	0.31	0.12	0.12	
	100.0	100.0	100.0	100.0	100.0	100.0	100.0	100.0	100.0	100.0	100.0	100.0	
LOI	15.95	23.50	20.70	8.02	17.80	20.20	18.70	10.30	18.30	19.20	9.37	23.10	

EURAD (Deliverable n° 15.12) – Identification on the effect of transient processes on corrosion
Dissemination level: Public
Date of issue of this report: **29/04/2024**

Page 160

Cont. Table 37(II/II) – Chemical composition of the BCV and MX-80 bentonite heated up at 150 °C (150), 90 °C (90) and at ambient temperature (RT), irradiated (IR) or unirradiated (NIR) (in wt.%). The data were recalculated to the 0.00 wt.% of loss of ignition (LOI).

Sample no.	BCV_90_NIR			BCV_RT_NIR				MX-80_input	MX-80_150_IR	MX-80_150_NIR	MX-80_90_IR	MX-80_90_NIR	MX-80_RT_NIR
Months	9	12	18	6	9	12	18	0	18	18	18	18	18
Na_2O	0.35	0.33	0.34	0.32	0.31	0.28	0.28	2.28	1.93	1.94	2.23	2.20	1.98
MgO	3.29	3.23	3.34	3.30	3.28	3.25	3.25	2.62	2.41	2.53	2.65	2.62	2.69
Al_2O_3	19.18	18.93	19.35	19.31	19.38	19.01	18.87	23.27	22.01	22.84	23.13	23.01	23.06
SiO_2	54.09	54.47	53.89	54.60	54.91	54.82	52.95	64.02	64.02	64.01	64.81	64.89	64.98
P_2O_5	0.55	0.57	0.56	0.54	0.54	0.59	0.54	0.04	0.04	0.04	0.04	0.04	0.04
SO_3	0.08	0.10	0.09	0.07	0.07	0.08	0.06	0.84	1.03	1.03	0.71	0.71	0.87
K_2O	1.14	1.15	1.16	1.19	1.18	1.17	1.25	0.59	0.67	0.72	0.45	0.48	0.51
CaO	3.12	3.09	2.93	3.17	3.14	3.18	3.23	1.49	1.42	1.37	1.21	1.17	1.38
TiO_2	3.07	2.94	2.96	2.93	2.83	3.05	3.29	0.16	0.17	0.16	0.15	0.15	0.17
Cr_2O_3	0.08	0.08	0.08	0.08	0.08	0.08	0.09	0.00	0.01	0.00	0.00	0.00	0.00
MnO	0.22	0.23	0.20	0.20	0.20	0.26	0.28	0.00	0.04	0.04	0.01	0.01	0.01
Fe_2O_3	14.48	14.72	14.93	14.14	13.91	14.04	15.58	4.34	5.97	5.18	4.49	4.41	4.01
NiO	0.03	0.03	0.03	0.03	0.03	0.03	0.03	0.00	0.00	0.00	0.00	0.00	0.00
BaO	0.19	0.00	0.00	0.00	0.00	0.04	0.16	0.03	0.15	0.04	0.03	0.03	0.00
Others	0.13	0.13	0.13	0.12	0.13	0.13	0.15	0.32	0.12	0.11	0.10	0.27	0.30
	100.0	100.0	100.0	100.0	100.0	100.0	100.0	100.0	100.0	100.0	100.0	100.0	100.0
LOI	19.20	9.66	20.90	18.70	19.50	9.51	17.90	9.98	0.00	18.20	19.10	17.90	19.30
The analytical errors estimated of the bentonite materials are following: Na_2O 0.03; MgO 0.08; Al_2O_3 0.19; SiO_2 0.25; P_2O_5 0.04; SO_3 0.01; K_2O 0.01; CaO 0.08; TiO_2 0.08; Cr_2O_3 0.01; MnO 0.02; Fe_2O_3 0.16; NiO 0.01; BaO 0.03.													

EURAD (Deliverable n° 15.12) – Identification on the effect of transient processes on corrosion
Dissemination level: Public
Date of issue of this report: **29/04/2024**

Page 161
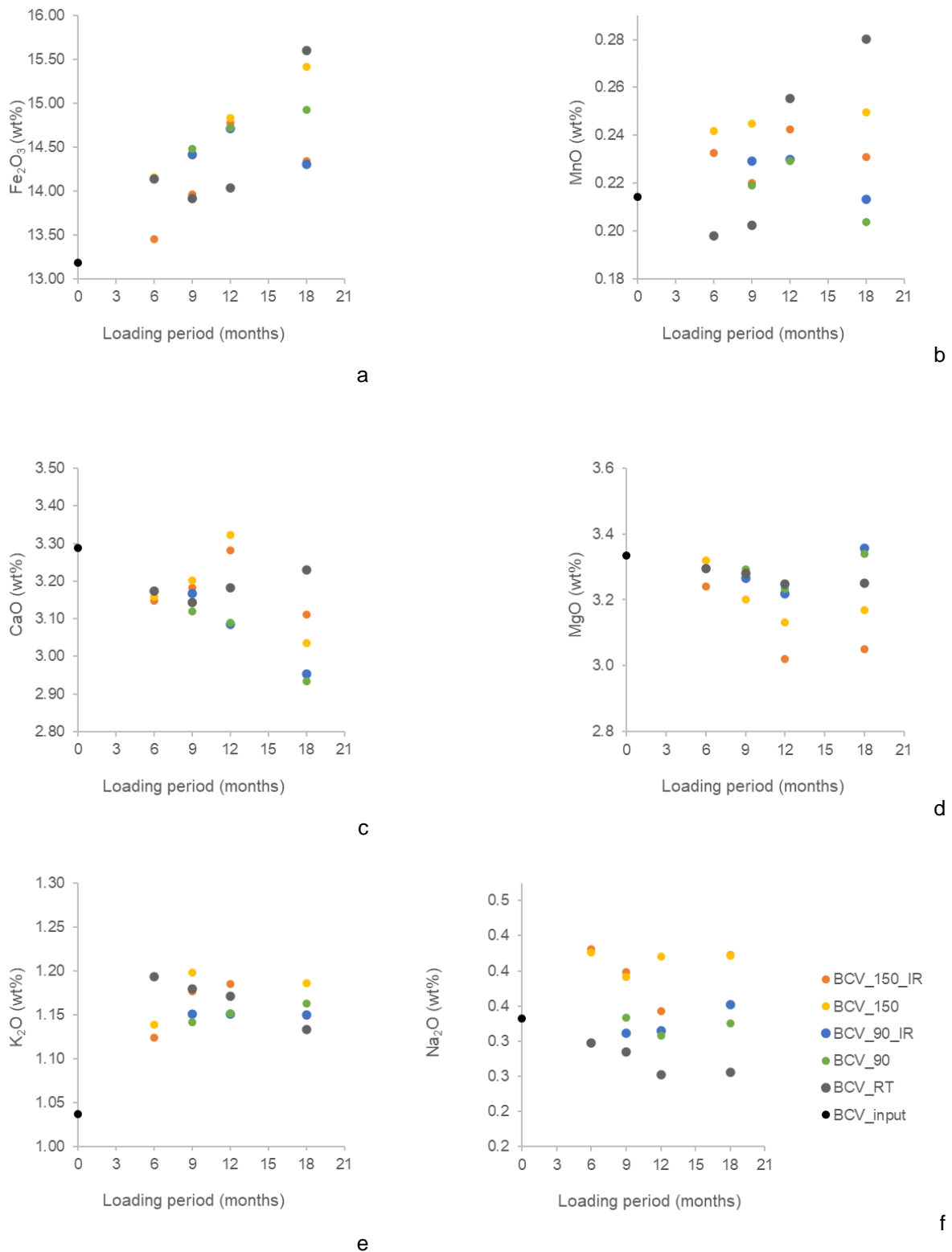
Figure 128 – Fe$_2$O$_3$ (a), MnO (b), CaO (c), MgO (d), K$_2$O (e) and Na$_2$O (f) content in original bentonite (BCV_input) and bentonite heated up at 150 °C (150), 90 °C (90) and at ambient temperature (RT), irradiated (IR) or unirradiated (NIR).

EURAD (Deliverable n° 15.12) – Identification on the effect of transient processes on corrosion
Dissemination level: Public
Date of issue of this report: **29/04/2024**

Page 162
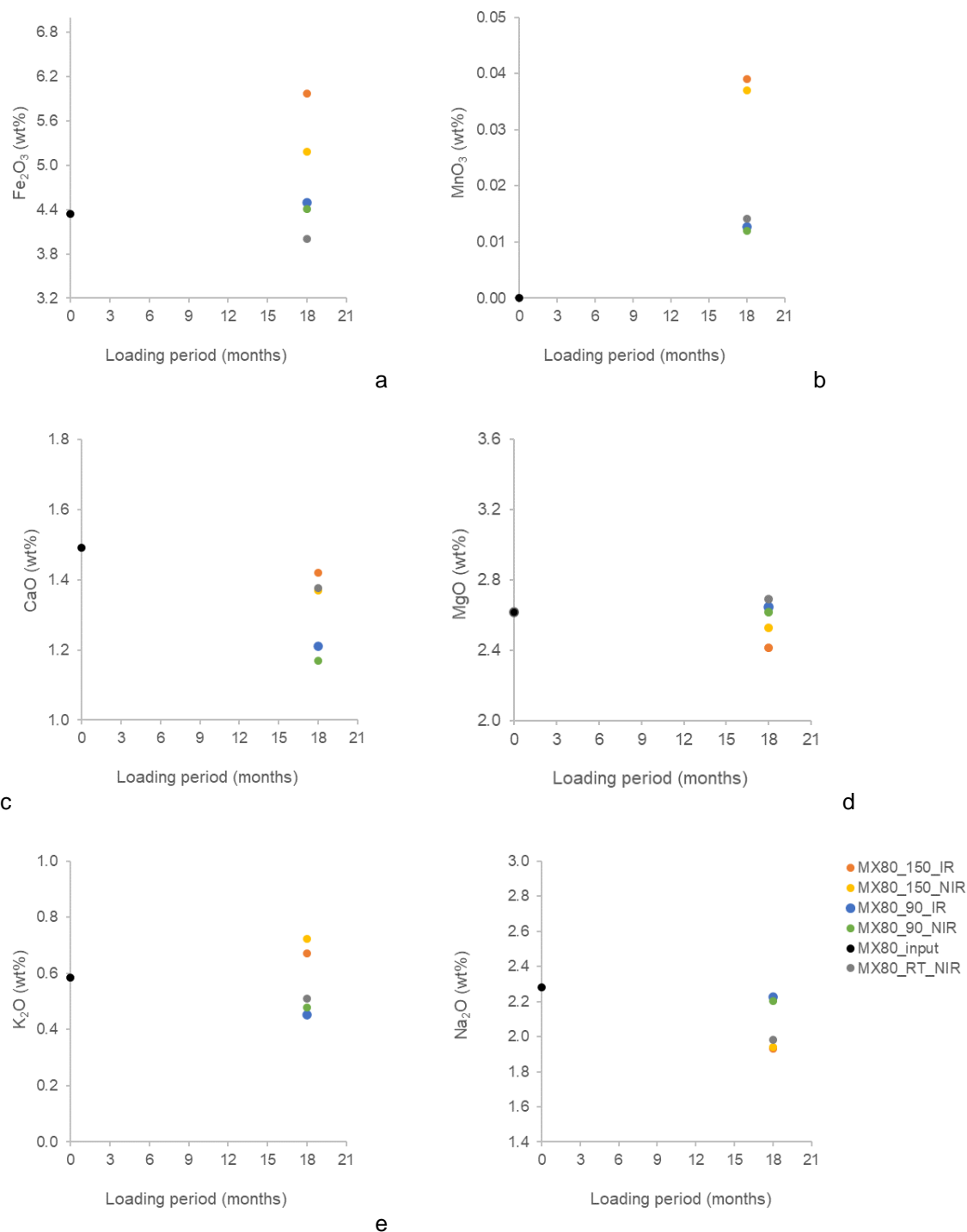
Figure 129 – Fe₂O₃ (a), MnO (b), CaO (c), MgO (d), K₂O (e) and Na₂O (f) content in original bentonite (MX80_input) and bentonite heated up at 150 °C (150), 90 °C (90) and at ambient temperature (RT), irradiated (IR) or unirradiated (NIR).

5.6.6   Cation exchange capacity

The BCV input bentonite is dominated by Mg^{2+} followed by Ca^{2+} in the position of exchangeable cations (*Table 38*). The CEC analysed spectroscopically (CEC_{vis}) of the BCV_input bentonite equals to 59.4 ± 2.4 meq $100g^{-1}$. The sum of exchangeable cations CEC_{sum} is comparable (59.3 ± 0.5 meq $100g^{-1}$).

EURAD (Deliverable n° 15.12) – Identification on the effect of transient processes on corrosion
Dissemination level: Public
Date of issue of this report: **29/04/2024**

Page 163

Heated BCV bentonite exhibited increasing CEC_{sum} and CEC_{vis} values when heated up to 150 °C. Heating led to higher proportion of exchangeable Ca^{2+} and a lower proportion of Mg^{2+} (*Figure 130*) which are phenomena typical for thermal loading of Ca-Mg bentonites (e.g., Kašpar et al. 2021). A slight increase in Na^+ in exchangeable cation in heated bentonite is explained by higher content of Na^+ in SGW3. This may be related to CEC_{vis} and CEC_{sum} increase.

The MX-80_input bentonite is dominated by Na^+ followed by Ca^{2+} in the position of exchangeable cations (*Table 38*, *Figure 131*). There is minimum content of K^+ and Mg^{2+} in the position of exchangeable cations. The CEC analysed spectroscopically (CEC_{vis}) of the BCV_input bentonite equals to 76.9 ± 1.2 meq 100g^{-1}. The sum of exchangeable cations CEC_{sum} is comparable (88.8 ± 1.7 meq 100g^{-1}). Heated MX-80 bentonite exhibited increasing CEC_{sum} and CEC_{vis} values when heated up to 150 and 90 °C. Heating led to higher proportion of exchangeable Mg^{2+}, Ca^{2+} and K^+ and a lower proportion of Na^+. Changes in the composition of exchangeable cations are explained because of thermal loading combined with an influence of chemical composition of saturation medium.

Table 38 – The CEC analysed spectroscopically (CECvis), the sum of exchangeable cations (CECsum) and the proportions of exchangeable cations in the BCV_input bentonite, MX-80 bentonite and bentonites heated up to 90 °C (90), 150 °C (150) or at ambient temperature (RT), irradiated (IR) or unirradiated (NIR) for 6 (6m), 9 (9m), 12 (12m) and 18 months (18m).

Sample no.	CECvis (meq 100g^{-1}) AVG	± L	CECsum (meq 100g^{-1}) AVG	± L	Ca^{2+} (%) AVG	± L	Mg^{2+} (%) AVG	± L	Na$^+$ (%) AVG	± L	K$^+$ (%) AVG	± L
BCV_input	59.4	2.4	59.3	0.5	24.3	0.3	63.9	0.7	9.4	0.5	2.3	0.2
BCV_150_IR_6m	66.4	1.8	63.2	1.1	60.8	0.8	22.9	0.6	13.9	0.2	2.3	0.1
BCV_150_IR_9m	67.2	1.4	64.2	2.9	59.1	0.8	27.0	0.6	11.2	0.3	2.8	0.1
BCV_150_IR_12m	66.4	2.4	69.8	1.1	70.3	0.6	16.3	0.4	10.5	0.1	2.9	0.1
BCV_150_IR_18m	68.4	1.7	70.1	2.6	70.3	0.1	15.2	0.5	12.1	0.6	2.3	0.0
BCV_150_NIR_6m	67.7	4.2	63.5	3.1	66.8	0.8	16.3	0.5	14.3	1.0	2.5	0.1
BCV_150_ NIR_9m	67.4	3.1	61.5	1.6	69.1	1.0	15.5	0.2	12.5	0.7	3.0	0.2
BCV_150_ NIR_12m	66.7	17.2	70.9	1.7	73.1	0.3	10.5	0.2	13.3	0.0	3.2	0.1
BCV_150_ NIR_18m	69.7	1.5	72.3	1.1	78.6	0.3	7.7	0.2	11.1	0.2	2.6	0.1
BCV_90_IR_9m	56.8	8.3	61.9	7.6	32.3	1.0	55.4	1.7	10.0	1.3	2.3	0.2
BCV_90_IR_12m	56.8	0.5	58.4	2.4	37.3	1.5	48.0	1.6	10.9	0.8	3.8	0.2
BCV_90_IR_18m	63.9	2.0	62.4	1.3	29.7	0.7	56.7	0.9	11.2	0.9	2.5	0.1
BCV_90_ NIR_9m	57.8	4.1	60.2	2.2	40.9	2.5	44.6	1.9	10.8	0.5	3.8	0.1
BCV_90_ NIR_12m	57.3	0.4	56.9	1.4	37.1	1.4	48.4	1.1	10.6	0.3	3.9	0.0
BCV_90_ NIR_18m	63.6	2.3	61.6	3.2	35.2	2.2	51.6	1.7	10.7	0.7	2.5	0.0
BCV_RT_ NIR_6m	59.4	0.8	60.4	3.3	30.0	1.2	57.7	1.4	9.0	0.5	3.3	0.3
BCV_RT_ NIR_9m	58.6	-	59.3	-	31.2	-	57.5	-	7.8	-	3.6	-
BCV_RT_ NIR_12m	55.7	1.5	59.6	2.6	34.6	1.3	53.3	1.5	7.6	0.2	4.5	0.1
BCV_RT_ NIR_18m	60.6	0.9	60.9	0.3	30.6	3.2	57.8	2.0	7.3	1.2	4.4	0.3
MX80_input	76.9	1.2	88.8	1.7	31.1	0.8	3.9	0.3	63.0	1.1	1.9	0.0
MX80_150_IR_18m	92.7	2.7	101.3	2.4	35.6	0.4	10.1	0.6	49.9	0.9	4.4	0.1
MX80_150_NIR_18m	94.2	1.9	100.7	3.9	36.5	1.7	9.7	0.5	48.2	1.5	5.7	0.2
MX80_90_IR_18m	85.2	0.1	90.9	2.8	31.3	1.0	11.4	0.4	54.8	0.8	2.4	0.0
MX80_90_NIR_18m	95.8	1.7	98.0	1.1	31.2	2.1	11.0	0.1	56.1	2.2	1.7	0.0
MX80_RT_NIR_18m	94.6	0.3	95.3	0.8	31.9	1.9	11.6	0.3	54.9	1.7	1.6	0.1

EURAD (Deliverable n° 15.12) – Identification on the effect of transient processes on corrosion
Dissemination level: Public
Date of issue of this report: **29/04/2024**

Page 164
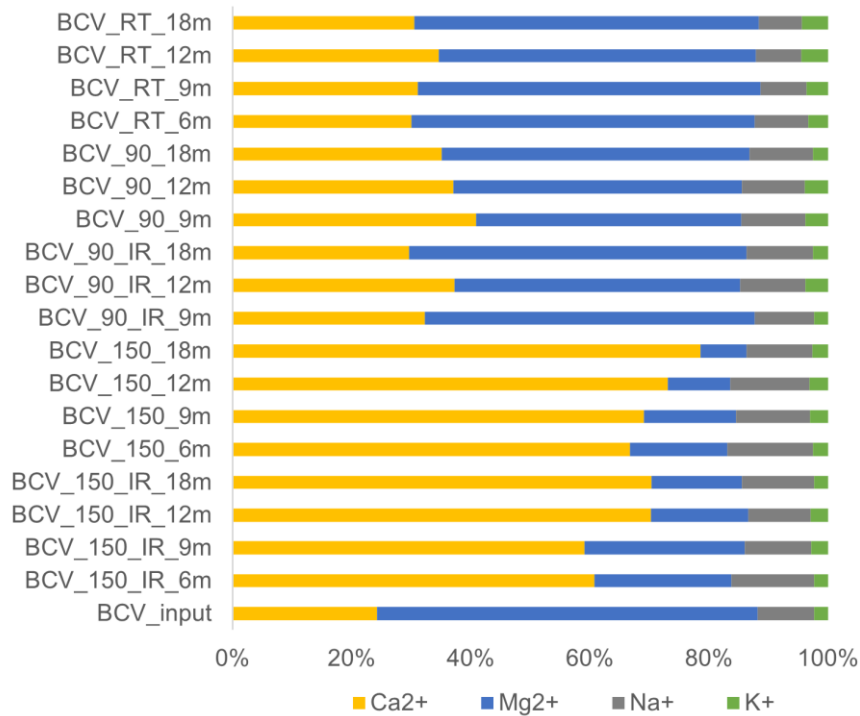
Figure 130 – *Exchangeable cations of BCV bentonite heated up to 90 °C (90), 150 °C (150) or at ambient temperature (RT), irradiated (IR) or unirradiated (NIR) for 6 (6m), 9 (9m), 12 (12m) and 18 months (18m).*
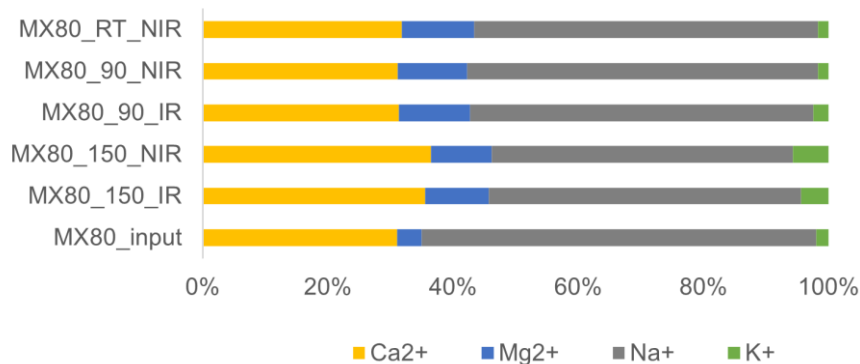
Figure 131 – *Exchangeable cations of MX-80 bentonite heated up to 90 °C (90), 150 °C (150) or at ambient temperature (RT), irradiated (IR) or unirradiated (NIR) for 6 (6m), 9 (9m), 12 (12m) and 18 months (18m).*

5.6.7 Water leachates

The chemical composition of water leachates of BCV_input bentonite and bentonite heated up at 90 and 150 °C indicates prevailing Na-HCO$_3$ type (*Table 39*). The concentration is dependent on solid-to-liquid (s : l) ratio (

Figure 132). There was observed significant effect of both temperature and irradiation on the concentration of water leachable species. Thermal loading at 90 and 150 °C decreased a concentration of water leachable Na$^+$, K$^+$, and Mg^{2+} and slightly increased a concentration of Ca^{2+} and Cl$^-$ (

EURAD (Deliverable n° 15.12) – Identification on the effect of transient processes on corrosion
Dissemination level: Public
Date of issue of this report: **29/04/2024**

Page 165

Figure 132). Similar trends were observed in water leachates of MX-80 bentonite (*Figure 133*). A concentration of SO_4^{2-} increased significantly only in the BCV bentonite heated up to 90 °C (

*Figure 132*g). This increase is more obvious in unirradiated BCV bentonite. In contrast a concentration of SO_4^{2-} in water leachates of the MX-80 is higher when heated up to 150 °C (*Figure 133*g). A concentration of HCO_3^- decreased in all heated up samples. Irradiated samples indicate similar concentration of water leachates after 18 months of loading comparing to those of unirradiated.

Table 39 – Concentration of water leachates in BCV_input, MX-80_input (MX80) and the bentonites heated up at 150 °C (150), 90 °C (90), ambient temperature (RT), irradiated (IR) and unirradiated (NIR).

Sample no.	s : l (g / l)	Na$^+$	K$^-$	Ca^{2+}	Mg^{2+}	Fe^{x+}	Cl$^-$	SO$_4^{2-}$	NO$_3^-$	F$^-$	HCO$_3^-$
BCV_input	25.18	1.41	0.13	0.06	0.11	bdl	0.01	0.06	bdl	0.03	1.73
	114.03	3.80	0.26	0.10	0.23	bdl	0.03	0.25	bdl	0.09	4.19
	201.94	4.95	0.33	0.13	0.29	bdl	0.05	0.44	bdl	0.10	5.17
BCV150IR6	23.82	1.51	0.12	0.04	0.03	bdl	0.04	0.09	bdl	bdl	1.54
	115.97	3.14	0.16	0.06	0.04	bdl	0.10	0.29	bdl	bdl	2.81
	209.18	4.09	0.20	0.10	0.05	bdl	0.16	0.45	bdl	bdl	3.52
BCV150IR9	118.10	2.73	0.22	0.06	0.04	bdl	0.06	0.28	bdl	bdl	2.56
BCV150IR12	21.82	1.17	0.15	0.07	0.03	bdl	0.01	0.08	bdl	bdl	1.36
	109.75	2.76	0.22	0.11	0.04	bdl	0.03	0.21	bdl	bdl	2.82
	196.70	3.41	0.23	0.13	0.04	bdl	0.06	0.30	bdl	bdl	3.31
BCV150IR18	22,28	1.17	0.13	0.10	0.02	bdl	0.02	0.07	0.01	bdl	1.37
	111,10	2.63	0.17	0.10	0.03	bdl	0.07	0.22	0.01	0.11	2.42
	198,96	3.35	0.20	0.12	0.03	bdl	0.12	0.33	0.01	0.16	2.89
BCV150NIR6	23.55	1.56	0.12	0.05	0.02	bdl	0.04	0.11	bdl	bdl	1.57
	113.39	3.36	0.18	0.08	0.03	bdl	0.12	0.28	bdl	bdl	3.06
	203.69	4.47	0.22	0.12	0.03	bdl	0.20	0.43	bdl	bdl	3.93
BCV150NIR9	22.67	1.31	0.14	0.04	0.02	bdl	0.05	0.10	bdl	bdl	1.32
	113.22	2.64	0.19	0.07	0.02	bdl	0.11	0.27	bdl	bdl	2.36
	203.12	3.50	0.22	0.11	0.02	bdl	0.13	0.38	bdl	bdl	3.09
BCV150NIR12	21.93	1.50	0.14	0.07	0.02	bdl	0.08	0.11	0.04	bdl	1.48
	109.47	3.46	0.21	0.10	0.03	bdl	0.07	0.28	bdl	bdl	3.28
	196.60	4.64	0.25	0.16	0.04	bdl	0.16	0.42	bdl	bdl	4.30
BCV150NIR18	23,14	1.17	0.13	0.09	0.01	bdl	0.03	0.07	0.01	0.14	1.19
	111,30	2.79	0.18	0.13	0.01	bdl	0.07	0.26	0.01	0.19	2.45
	198,17	3.46	0.21	0.15	0.02	bdl	0.13	0.39	0.02	0.28	2.79
BCV90IR9	117.54	3.20	0.29	0.11	0.21	bdl	0.11	0.31	bdl	bdl	3.39
BCV90IR12	22.81	1.29	0.20	0.08	0.13	bdl	0.02	0.09	bdl	bdl	1.72
	107.29	3.16	0.25	0.11	0.19	bdl	0.13	0.29	bdl	bdl	3.29
	194.58	4.05	0.38	0.15	0.27	bdl	0.19	0.45	bdl	bdl	4.16
BCV90IR18	22,44	1.04	0.15	0.07	0.11	bdl	0.03	0.10	bdl	bdl	1.33
	111,67	2.38	0.24	0.10	0.15	bdl	0.12	0.36	0.01	0.10	2.16
	199,09	3.22	0.29	0.13	0.21	bdl	0.24	0.59	0.03	0.13	2.62
BCV90NIR9	119.87	3.19	0.26	0.11	0.19	bdl	0.14	0.42	bdl	bdl	3.06

EURAD (Deliverable n° 15.12) – Identification on the effect of transient processes on corrosion
Dissemination level: Public
Date of issue of this report: **29/04/2024**

Page 166

Cont. Table 39 – Concentration of water leachates in BCV_input, MX-80_input (MX80) and the bentonites heated up at 150 °C (150), 90 °C (90), ambient temperature (RT), irradiated (IR) and unirradiated (NIR).

Sample no.	s : l (g / l)	Na^+	K^-	Ca^{2+}	Mg^{2+}	Fe^{x+}	Cl^-	SO_4^{2-}	NO_3^-	F^-	HCO_3^-
BCV90NIR12	22.89	1.18	0.20	0.08	0.14	bdl	0.07	0.12	bdl	bdl	1.53
	108.48	3.04	0.33	0.11	0.21	bdl	0.18	0.33	bdl	bdl	3.18
	194.33	4.30	0.40	0.17	0.29	bdl	0.30	0.52	bdl	bdl	4.27
BCV90NIR18	23,20	0.98	0.15	0.09	0.10	bdl	0.05	0.12	0.01	bdl	1.21
	112,59	2.37	0.24	0.13	0.14	bdl	0.20	0.43	0.03	0.11	1.94
	202,72	3.30	0.29	0.18	0.19	bdl	0.33	0.71	0.03	0.13	2.42
BCVRTNIR6	116.32	2.91	0.39	0.11	0.27	bdl	0.05	0.26	bdl	bdl	3.49
BCVRTNIR9	22.77	1.19	0.25	0.10	0.22	bdl	0.04	0.11	bdl	bdl	1.83
	112.12	2.86	0.39	0.11	0.29	bdl	0.05	0.26	bdl	bdl	3.51
BCVRTNIR12	22.03	1.11	0.28	0.12	0.24	bdl	0.02	0.10	bdl	bdl	1.88
	107.87	3.03	0.49	0.16	0.37	bdl	0.01	0.19	bdl	bdl	4.18
	194.91	4.26	0.53	0.20	0.50	bdl	0.02	0.28	bdl	bdl	5.64
BCVRTNIR18	22,58	0.77	0.28	0.09	0.14	bdl	0.02	0.07	bdl	bdl	1.68
	110,66	1.99	0.42	0.16	0.28	bdl	0.04	0.23	0.02	0.09	2.69
	200,53	2.75	0.47	0.17	0.31	bdl	0.08	0.41	0.03	0.10	3.17
MX80_input	1,62	0.84	0.02	0.03	0.05	0.01	0.02	0.05	bdl	bdl	0.92
	3,94	1.50	0.03	0.03	0.08	0.01	0.02	0.09	0.01	bdl	1.56
MX80150IR18	1,68	0.54	0.03	bdl	0.01	bdl	bdl	0.12	bdl	bdl	0.36
	4,43	0.87	0.04	bdl	0.02	0.01	0.02	0.19	bdl	bdl	0.57
MX80150NIR18	1,85	0.48	0.03	bdl	0.01	bdl	0.02	0.09	bdl	bdl	0.33
	4,28	0.84	0.05	bdl	0.02	bdl	0.02	0.19	0.01	bdl	0.51
MX8090IR18	1,64	0.65	0.01	0.03	0.03	0.01	0.03	0.07	0.01	bdl	0.64
	4,15	1.05	0.02	0.04	0.06	0.01	0.05	0.13	0.01	bdl	1.01
MX8090NIR18	1,34	0.48	0.01	0.03	0.03	0.02	0.02	0.04	0.01	bdl	0.53
	3,33	0.86	0.02	0.03	0.06	0.01	0.04	0.09	0.01	bdl	0.86
MX80RTNIR18	1,58	0.57	0.02	bdl	0.02	bdl	0.03	0.06	0.01	bdl	0.47
	4,25	1.03	0.03	0.03	0.03	0.01	0.04	0.12	0.01	bdl	0.91

EURAD (Deliverable n° 15.12) – Identification on the effect of transient processes on corrosion
Dissemination level: Public
Date of issue of this report: **29/04/2024**

Page 167
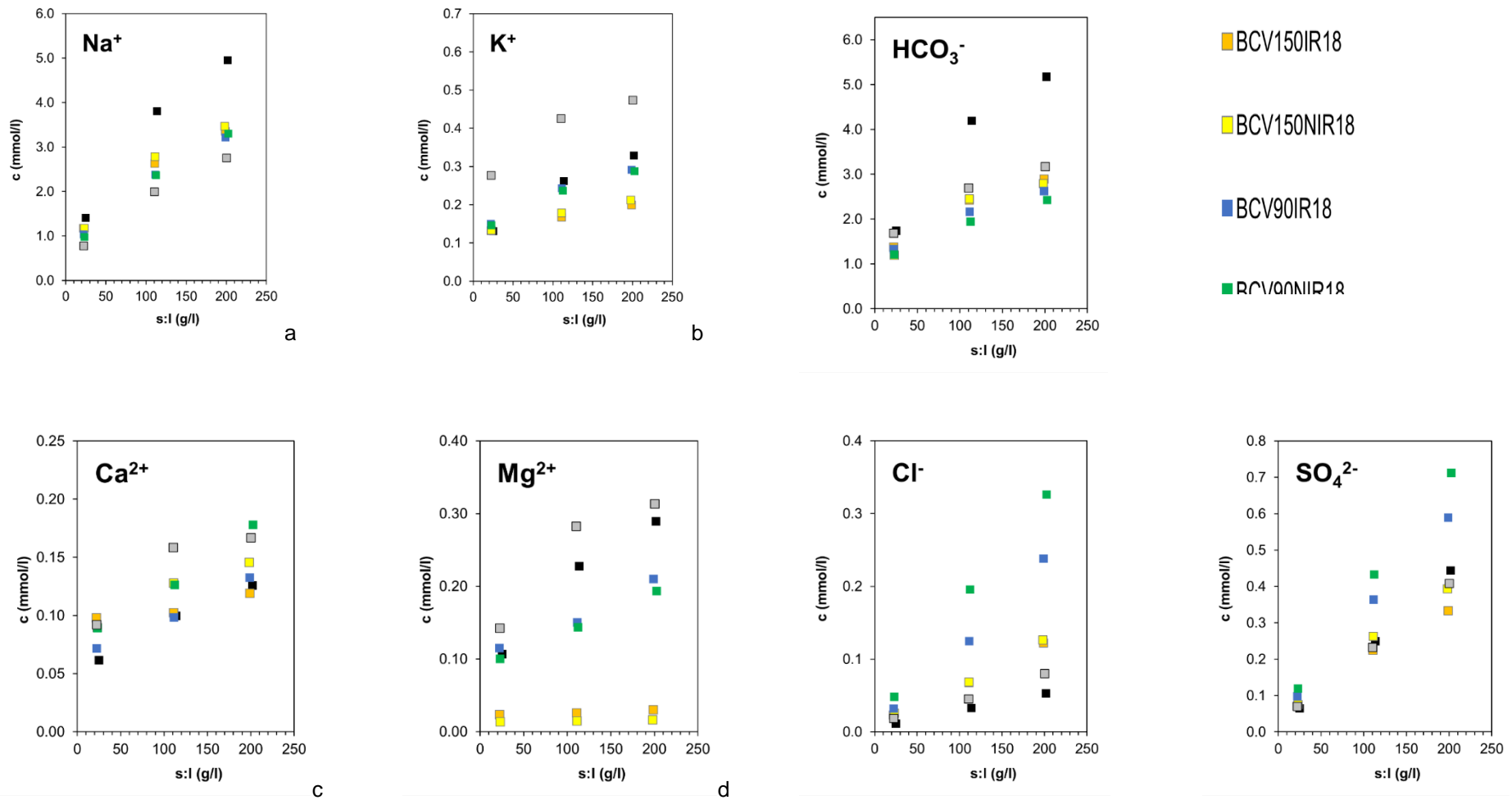
Figure 132 – Concentration of Na+ (a), K+ (b), Ca2+ (c), Mg2+ (d), HCO3- (e) Cl- (f) a SO42- (g) in water leachates from BCV bentonite heated up at 150 °C (150), 90 °C (90) or laboratory temperature (RT), irradiated (IR) or unirradiated (NIR), loaded for 18 months.

EURAD (Deliverable n° 15.12) – Identification on the effect of transient processes on corrosion
Dissemination level: Public
Date of issue of this report: **29/04/2024**

Page 168

Figure 133 – Concentration of Na+ (a), K+ (b), Ca2+ (c), Mg2+ (d), HCO3- (e), Cl- (f) a SO4 2- (g) in water leachates from MX-80 bentonite heated up at 150 °C (150), 90 °C (90) or laboratory temperature (RT), irradiated (IR) or unirradiated (NIR), loaded for 18 months.

EURAD (Deliverable n° 15.12) – Identification on the effect of transient processes on corrosion
Dissemination level: Public
Date of issue of this report: **29/04/2024**

Page 169

5.7   Discussion and conclusions

5.7.1   Influence of temperature and degree of saturation

Temperature and degree of saturation are the main factors affecting corrosion rates of steel samples embedded in bentonite. Heterogeneous saturation of experimental modules increased confidence intervals of corrosion rate of steel embedded in several modules. Non uniform corrosion connected to heterogeneous saturation was observed previously in various clay/bentonite environments (e.g., King 2008; Zuna et al. 2023). Corrosion rates in model environments range from units to tens of µm·y^{-1} for most authors (e.g., Neff at al. 2010, Smart et al. 2012). It well corresponds to the corrosion rates analysed in the heated BCV and MX-80 bentonite.

There wasn´t verified an effect of initial humidity on the steel corrosion rate Increasing initial humidity of bentonite seems to have inhibiting effect on the steel corrosion rate (*Figure 134*). The effect of low final humidity on decreasing corrosion rate is partially visible in the set of modules containing BCV bentonite, heated at 150 °C and unirradiated (modules nos. 2, 4, 6, and 8) (*Figure 135*). The module no. 6 indicates the lowest corrosion rate (13.3 ± 1.6 µm y^{-1}) and its moisture content was only 9.29 % after disassembly. Other modules loaded under the same conditions exhibit higher corrosion rates while their moisture content varies between 21.28-22.33 % (*Figure 135*). Due to technical difficulties the module was not fully saturated, and its humidity decreased from initial 15 wt.% to final 9.2 wt.%. The steel samples embedded in the module no. 6 indicate lower corrosion rate compared the other modules load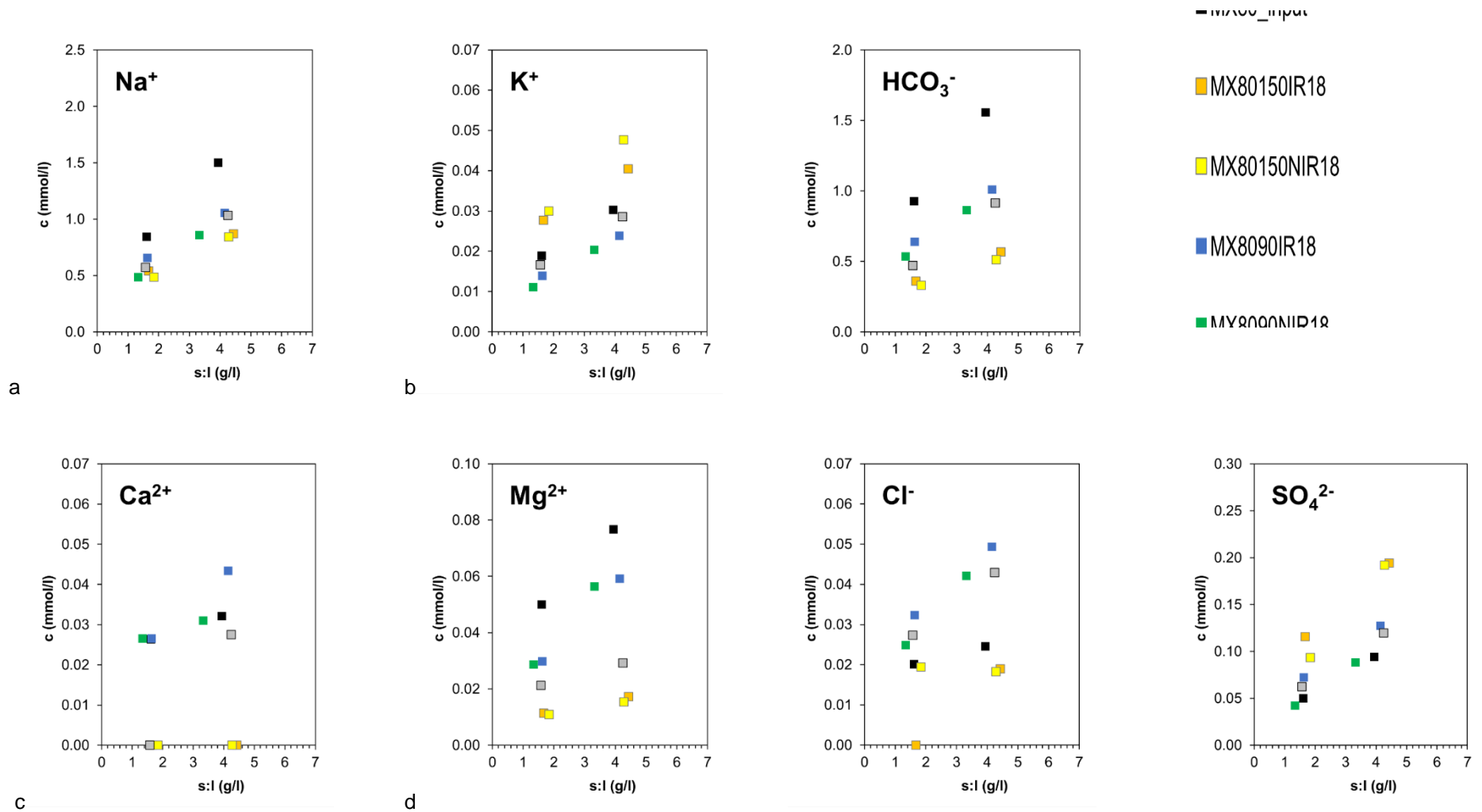ed under similar conditions (*Figure 135*). Parallel influence of temperature, irradiation and humidity makes it impossible to distinguish which effect is dominating. The possible explanation may be in the insufficient pressure used in the saturation of irradiated cells. The insufficient pressure causes corrosion in water vapour conditions instead of corrosion in contact with pore solution. Corrosion products originating in vapour conditions are conventionally more compact and thinner.
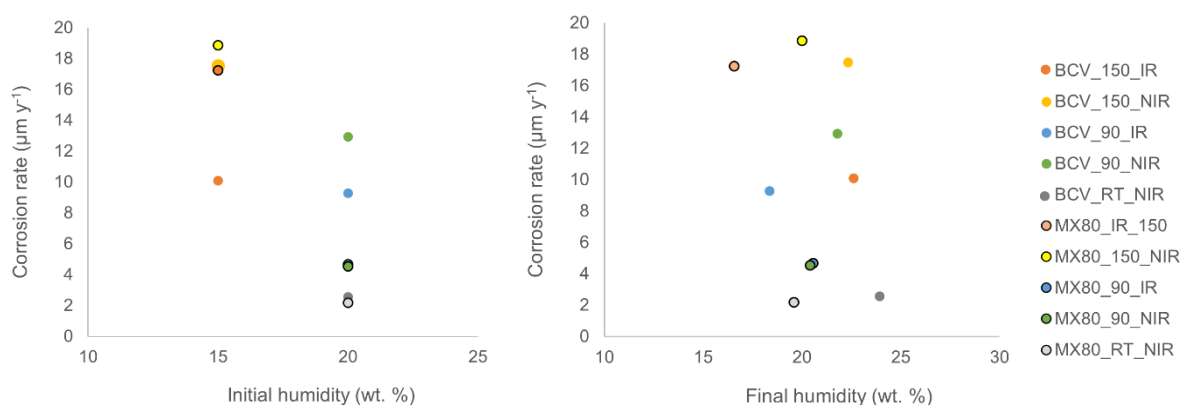

Figure 134 – Correlation of steel corrosion rate with initial (left) and final (right) humidity of bentonite.

EURAD (Deliverable n° 15.12) – Identification on the effect of transient processes on corrosion
Dissemination level: Public
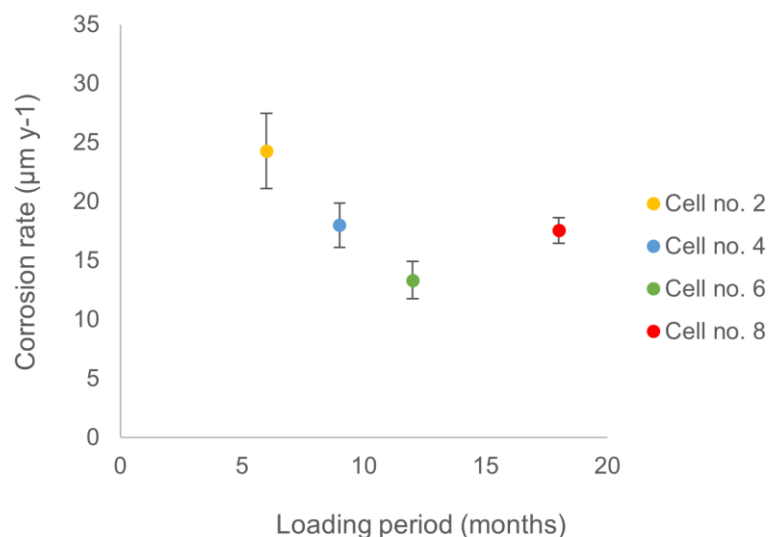Date of issue of this report: **29/04/2024**

Page 170

Figure 135 – Corrosion rate of steel heated in the BCV bentonite at 150 °C, unirradiated.

Fe-oxide and Fe-carbonates were analysed on steel-BCV bentonite surface heated up at 90 °C. A formation of Fe-Si-O(OH) layer was analysed in samples heated up at 150 °C. The thickness of the corrosion layer well correlated with the heating temperature and length of loading period. More extensive and thicker layer was identified on steel samples heated up at 90 °C. This feature is explained by higher saturation of bentonite and higher water content, which can facilitate formation of corrosion products.

Amorphous or poorly-crystalline Fe-rich corrosion products were analysed by Ishidera et al. (2008) in the experiment simulating carbon steel corrosion under aerobic conditions in compacted bentonite after 3–4 years at room temperature. The corrosion products were distributed into compacted bentonite from carbon steel as Fe^{2+} and amorphous, noncrystalline or poorly ordered Fe compounds ($Fe(OH)_2$, $Fe(OH)_3$). No content of silica was detected in these products. Temperature of 150 °C is regarded as a main factor affecting dissolution of amorphous silica and its incorporation into corrosion/alteration products.

Lower corrosion rate of Fe-pellets embedded in the Na-bentonites compared to those embedded in Ca-bentonites was observed by Kaufhold et al. (2015b). The initial expectation was that Na-bentonites would be more corrosive due to formation of voluminous water-rich gels hence leaving more water at interface. However, experiments showed less corrosion in Na-bentonites. Fe-rich bentonites were also not more corrosive than others. The lower corrosion rate in Na-bentonite compared to Ca-bentonites was explained by possible effect of different pH.

Formation of Fe-Si-rich corrosion layers was found dependent on heating temperature up to 150 °C. Comparable Si-rich phases were detected neither in natural nor in archaeological analogues (Stoulil et al. 2022). The source of silica is regarded in the amorphous phases in bentonite. Theoretical models of corrosion product formation (Gondolli et al. 2018) predict the formation of magnetite as the main corrosion product, as well as siderite and chukanovite as minor corrosion products in the early stages of environmental development. Greenalite, chamosite and Fe-illite should be present in the system according to the long-term models. Magnetite, chukanovite and siderite were confirmed in the experiments. This is in accordance with the expected model. Absence of silicate-based corrosion products is explained by short duration of the experiments (e.g., King et al. 2008; Stoulil et al. 2013, 2022).

Regarding to the bentonite parameters high temperature and saturation changed the position of smectite d_{001} basal diffraction line (*Figure 125*). Thermal loading and saturation with SGW3 water caused splitting

EURAD (Deliverable n° 15.12) – Identification on the effect of transient processes on corrosion
Dissemination level: Public
Date of issue of this report: **29/04/2024**

Page 171

of MX-80 basal diffraction line into two: the major diffraction line typical for 1-layer hydrate, and the minor one typical for 2-layer hydrate. The splitting is explained by the substitution of Na^+ by Ca^{2+}/Mg^{2+} in the montmorillonite crystal lattice and well correlates the proportions of exchangeable cations.

Thermal effect (150 °C) is well visible on the proportions of Ca^{2+} and Mg^{2+} as exchangeable cations. High temperature caused an increase in Ca^{2+} content and decrease in Mg^{2+} content. Bentonite heated at 90 °C indicates comparable values to those of unheated one (*Figure 136*).
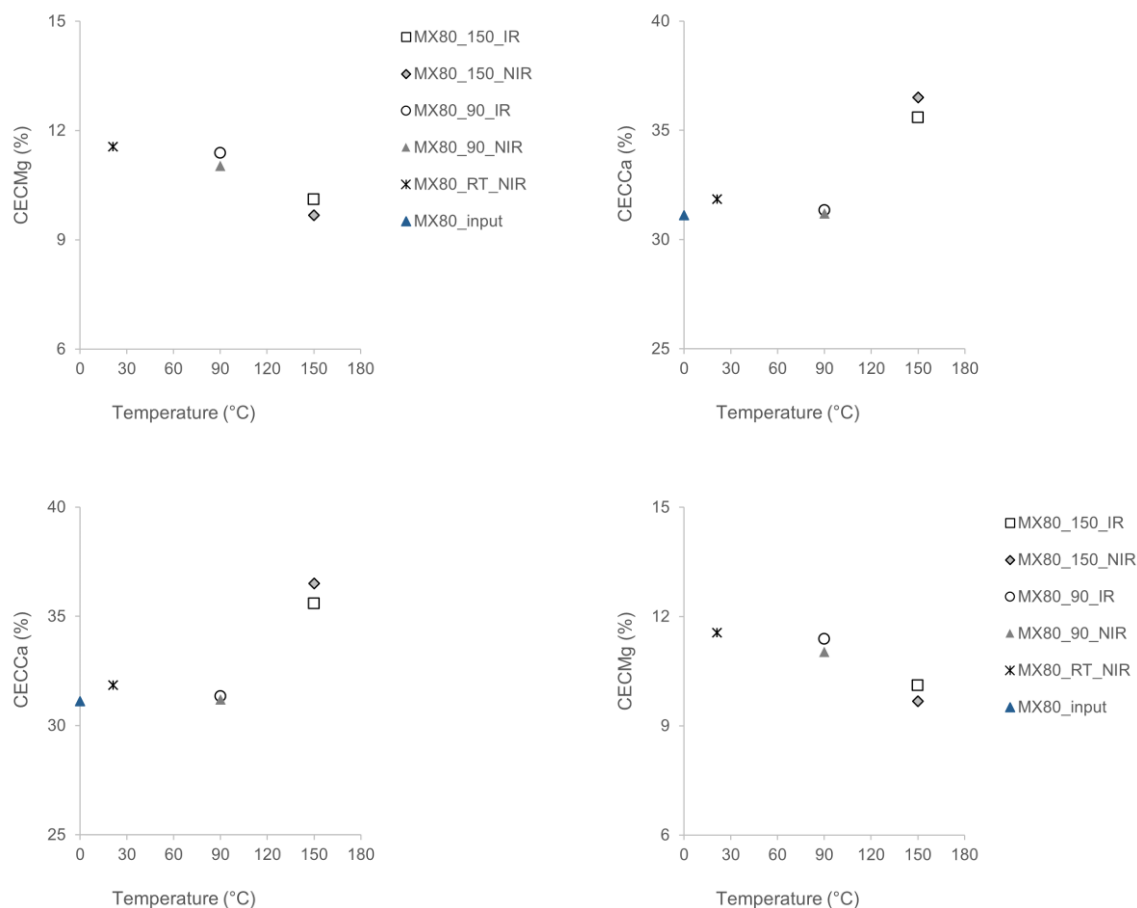
Figure 136 – Proportions of Ca^{2+} and Mg^{2+} in exchangeable cations in the MX-80 bentonite.

Thermal loading at 150°C induced an increase in Ca^{2+} and a decrease in Mg^{2+} levels in the BCV bentonite. (*Figure 137*), like those observed in the MX-80 bentonite. The same trend connected to thermal loading was previously discussed by Kašpar et al. (2021). An increase of Na^+ in the position of exchangeable cation was observed in the BCV bentonite heated up to 150 °C. There is expected a combined effect of heating and Na^+ input from SGW3.

EURAD (Deliverable n° 15.12) – Identification on the effect of transient processes on corrosion
Dissemination level: Public
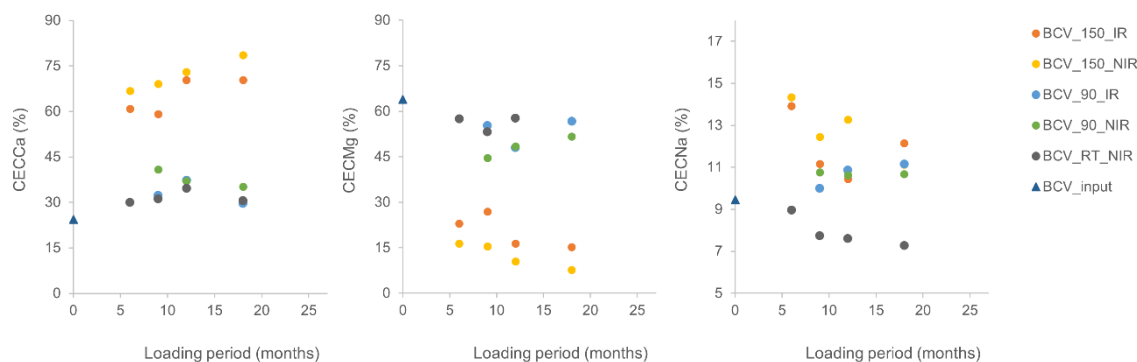Date of issue of this report: **29/04/2024**

Page 172

Figure 137 – Proportions of Ca^{2+}, Mg^{2+} and Na^+ in exchangeable cations in the BCV bentonite.

Enrichment of bentonite by Fe^{x+} was confirmed by XRF. Charpentier et al. (2006) documented transformation of montmorillonite caused by interaction of MX-80 bentonite with Fe-powder in the presence of alkaline solutions and elevated temperatures. Montmorillonite was still dominant clay phase at 80 and 150 °C but enriched in Fe and depleted in Si. Fe-vermiculite predominated at 300 °C and was associated with zeolite and saponite. The montmorillonite transformation led to significant modification of the material properties exhibited by decreasing swelling connected to the origin of less swelling vermiculite and non-swelling of zeolite. On the other hand, zeolite (mordenite) indicated high cation exchange capacity and high adsorption capacity, comparable to the initial bentonite.

Formation of magnetite was documented by XRD in all steel samples. El Mendili et al. (2014) discussed inhibiting effect of magnetite precipitation on carbon steel corrosion in clay environment. The presence of iron sulphide was detected as the result of the SRB (sulphate-reducing bacteria) activity. These bacteria use lactate added to COx water and hydrogen formed by steel dissolution as an energy source for sulphate reduction. However, the 70 % of the steel surface was still covered by magnetite, the corrosion products contained less than 3 % of the sulphide compounds. The siderite, chukanovite and β-Fe2-(OH)3Cl were detected after 6 months. In current experiments influence of sulphate-reducing bacteria (SRB) was minimal due to high temperature. The main conclusions connected to the microbiological analyses of BCV and MX-80 bentonites sampled in the current experiments were reported in Concord Task 4 (Černá et al. (submitted).

5.7.2 Influence of irradiation

No or very minor effect of irradiation on corrosion rate was observed when the steel samples were heated in the MX-80 bentonite. This can be explained by low dose rates used in the experiment. On the other hand, corrosion rates and profilometry data indicate lower corrosion of carbon steel when it was embedded in the BCV bentonite and unirradiated at 150 °C compared those subjected to irradiation. This phenomenon is more attributed to the degree of saturation (see Section 5.7.1), less to the influence of radiation.

5.8 UJV summary and conclusions

The steel samples heated up at 150 °C in the BCV bentonite indicate lower corrosion rate when irradiated compared to unirradiated samples. Combination of 150 °C and irradiation lead to the surface corrosion indicating almost constant corrosion rate for the whole testing period. Unirradiated samples heated up to 150 °C showed the highest corrosion rate after 6 months with decreasing tendency when the loading period was prolonged up to 18 months. The decreasing corrosion rate was observed in both irradiated and unirradiated steel samples heated up at 90 °C correlating with increasing loading period. Longer loading period minimised the difference in the corrosion rate of irradiated and unirradiated steel samples. No or very minor effect of irradiation on corrosion rate was observed when the steel samples

EURAD (Deliverable n° 15.12) – Identification on the effect of transient processes on corrosion
Dissemination level: Public
Date of issue of this report: 29/04/2024

Page 173

were heated in the MX-80 bentonite. Minimum corrosion rate was found in steel samples embedded in water saturated BCV bentonite stored under laboratory temperature without irradiation.

Longer loading period led to the formation of higher amount of corrosion products facilitating their identification. Hematite and Fe-rich carbonates (chukanovite, siderite) were confirmed forming corrosion layers on the steel surface. The thickness of the corrosion layer varied, ranging from 10 to 45 μm, and was directly correlated with the duration of loading. Steel samples that remained unirradiated and were heated up at 90 °C exhibited corrosion layers up to 45 μm in thickness after 12 months of loading. In contrast, irradiation, and thermal loading at 150 °C led to the formation of thinner corrosion layers, typically ranging from 10 to 20 μm. Corrosion layer composed of Fe-Si-O was identified on the surface of steel subjected to thermal loading of 150 °C. The layer was identified only by SEM-EDS indicating amorphous or poorly crystalline structure. The origin of Fe-Si-rich corrosion products needs to be confirmed by future research.

Combination of high temperature and saturation of SGW3 water led to the partial transformation of Na-smectite into Ca/Mg-smectite in the MX-80 bentonite. This transformation was indicated by proportions of exchangeable cations and by splitting of montmorillonite basal diffraction line. The heated BCV bentonite indicated partial cation exchange of Ca^{2+}/Mg^{2+} by Na^+ coming from saturation medium and enrichment in Fe^{x+} and Mn^{2+} coming from carbon steel.

EURAD (Deliverable n° 15.12) – Identification on the effect of transient processes on corrosion
Dissemination level: Public
Date of issue of this report: **29/04/2024**

Page 174

6. Common conclusions

Laboratory scale corrosion studies have been conducted with four different types of materials that are considered candidates for radioactive waste containers: C-steel, Cu-OFP, spheroidal graphite cast iron (SGI) and cupronickel alloy (CuNi).

All laboratory experiments simulated the conditions the container/bentonite barrier interface in the initial stages after the repository closure, reproducing different repository scenarios of coupled thermo-hydraulic gradients and thermo-hydraulic-chemical interactions. Metal samples separately subjected to different types of bentonites, hydrated with waters of different salinity and nature, form low saline granitic waters, bentonite porewater and sedimentary clay groundwater of high salinity. Samples were subject to temperatures from 25⁰c up to 150⁰C, and in some cases to gamma-irradiation.

All studies once again confirmed that corrosion depends fundamentally on the nature of the container material, and on the specific environmental conditions to which the metal is subjected or loaded.

C-steel corrosion values were increased at higher temperatures, and were enhanced combining temperature and irradiation (24.3 µm/y corrosion rate with Ca-Mg bentonite at 150⁰C and γ-irradiated 0.4 Gy·h^{-1}). However, the highest C-steel corrosion values measured in all experiments were in C-steel samples in contact with compacted Ca-Mg bentonite at a density 1.4 g/cm^3, hydrated with high salinity water and subjected to a temperature of 80 ⁰C (413 µm/year). This seems to indicate that the bentonite and the salinity of its porewater salinity played a major role.

Cu-OFP corrosion subjected to the same coupled thermo-hydraulic gradients were significantly lower that of C-steel upon the same conditions (ranging from 3 to 9 µm/year)

Spheroidal graphite cast iron (SGI) corrosion behaviour contacted to a slurry of Na-bentonite hydrated with synthetic Opalinus clay or granitic water, was analysed by different approaches. SGI corrosion rates were lower upon exposure to the bentonite suspension hydrated with low saline granitic water (4.8 µm/y) than to Opalinus clay saline pore water (6 and 13 µm y^{-1} for 30 °C and 50 °C) and higher values were determined combining a γ-radiation dose 130 Gy h^{-1} and temperature, up to 52 µm y^{-1}.

CuNi corrosion was significantly lower than any of the other materials tested, being the highest corrosion rate measured of 2.7 µm/y at 50⁰C. The presence of added sulfide had no significant effect on corrosion but may have an effect at longer exposure times, or higher sulfide concentrations.

In all experiments, the main corrosion products were identified, being very diverse and highly dependent on the specific material and environmental conditions established at equilibrium.

In general, the impact of metal corrosion on the bentonite was limited. For instance, the main changes observed in all bentonites analysed form m the in-situ Äspö- ABM5 experiment were the modification of exchangeable cation composition and the Fe increase in bentonites as a function of the distance to heater contact, due to heater corrosion.

The studies carried in Task 5 out provide quantitative data on corrosion rates of four different metal materials (C-steel, Cu-OFP, spheroidal graphite cast iron (SGI) and cupronickel alloy (CuNi)), measured under specific conditions, which can be used in studies to evaluate the performance of storages. The identification of corrosion products, changes in chemical conditions and identified gases production, provide a better understanding of the mechanisms involved in the corrosion of metals subjected to coupled thermo-hydraulic gradients and thermo-hydraulic-chemical, reproducing transient repository conditions,.

The evaluation of the impact of chemical perturbances, temperature and irradiation on the stability of different materials (metals and bentonites) contributes to a better selection of materials for future repositories.

EURAD (Deliverable n° 15.12) – Identification on the effect of transient processes on corrosion
Dissemination level: Public
Date of issue of this report: **29/04/2024**

Page 175

References

Ammann L., Bergaya F., Lagaly G. (2005) Determination of the Cation Exchange Capacity of Clays with Copper Complexes Revisited. Clay Min. 40: 441–453, doi:10.1180/0009855054040182.

ASTM, 2011. ASTM-G1: Standard Practice for Preparing, Cleaning, and Evaluating Corrosion Test Specimens. ASTM International, West Conshohocken, PA, USA.

Bergmann J., Friedel P., Kleeberg R. 1998. BGMN – a new fundamental parameters-based Rietveld program for laboratory X-ray sources, its use in quantitative analysis and structure investigations. CPD Newsl. (Commission of Powder Diffraction, International Union of Crystallography) 20: 5–8.

Bergmann J., Monecke T., Kleeberg R. 2001. Alternative algorithm for the correction of preferred orientation in Rietveld analysis. J. Appl. Crystallogr. 34: 16–19.

Biesinger, M.C., 2017. Advanced analysis of copper X-ray photoelectron spectra. Surf. Interface Anal. 49, 1325-1334.

Černá K. (submitted) Deliverable 15.9 and 15.10: Integration of the findings on the impact of irradiation, dry density, and particle size on the microbial community of deliverable D15.9 &15.10 of the HORIZON 2020 project EURAD. EC Grant agreement no: 847593.

Červinka R., Gondolli J., Havlová V., Rukavičková L. 2016. Selection of representative groundwater and preparation of its synthetic equivalents (in Czech). SURAO Technical report no. 41/2016, SURAO, Prague, Czech Republic.

Červinka R., Vašíček R., Večerník P., Kašpar V. 2018. SÚRAO report no. 419/2019: Complete characterization of the BCV 2017 bentonite (in Czech). SURAO, Prague, Czech Republic.

Charpentier D., Devineau K., Mosser-Ruck R., Cathelineau M., Villiéras F. (2006): Bentonite–iron interactions under alkaline condition: An experimental approach. Applied Clay Science, 32, 1–13.

Cloet, V., Pekala, M., Smith, P., Wersin, P., Diomidis, N., 2017. An evaluation of sulphide fluxes in the near field of a HLW repository. NAGRA Technical Report 17-04, Wettingen, Switzerland.

ČSN 75 7373 (757373) Water quality - Calculation of carbon dioxide forms (species). Czech Normalization Institute.

ČSN EN 10210-1 Hot finished structural hollow sections of non-alloy and fine grain steels - Part 1: Technical delivery conditions. Czech Normalization Institute.

de Pablo L., Chávez M.L., de Pablo J.J. 2005. Stability of Na-, K-, and Ca-Montmorillonite at High Temperatures and Pressures: A Monte Carlo Simulation. Langmuir 2005, 21, 23, 10874–10884, https://doi.org/10.1021/la051334a.

Degen T., Sadki M., König E. U., Nénert G. 2014. The HighScore suite. J. Pow. Diff. 29 (sup. S2): S13-S18, doi: 10.1017/S0885715614000840

Döbelin N., Kleeberg R. 2015 Profex: a graphical user interface for the Rietveld refinement program BGMN. J. Appl. Cryst. 48: 1573-1580. doi:10.1107/S1600576715014685

Drouin, D., Réal Couture, A., Joly, D., Tastet, X., Aimez, V., Gauvin, R., 2007. CASINO V2.42 – A fast and easy-to-use modeling tool for scanning electron microscopy and microanalysis analysis users. Scanning 29, 92-101.

El Mendili Y., Abdelouas A., Ait Chaou A. Bardeau J.-F., Schlegel M. L. (2014): Carbon steel corrosion in clay-rich environment. Corrosion Science, 88, 56–65.

Farmer, V.C., 1974. The infrared spectra of minerals. Mineralogical Society Monograph 4, 539 pp. Mineralogical Society, London.

EURAD (Deliverable n° 15.12) – Identification on the effect of transient processes on corrosion
Dissemination level: Public
Date of issue of this report: **29/04/2024**

Page 176

Fernandez, A.M., Rivas. P. 2005. Pore water chemistry of saturated FEBEX bentonite compacted at different densities. Advances in Understanding Engineered Barriers. Alonso & Ledesma (eds). Taylor and Francis Group, London. Pp 505- 514 ISBN 04-1536-544-9 (2005).

Fernández, A.M.; Sánchez-Ledesma, D.M.; Melón, A.; Robredo, L.M.; Rey, J.J.; Labajo, M.; Clavero, M.A.; Fernández, S.; González, A.E., 2018. Thermo-hydro-chemical (THC) behaviour of a Spanish Bentonite after dismantling Heater#1 and Heater#2 of the FEBEX in situ test at the Grimsel Test Site. Nagra Working Reports. NAB 16-25, 583 pp. NAGRA, 2018.

Féron, D., Crusset, D., Gras, J.M., 2008. Corrosion issues in nuclear waste disposal. Journal of Nuclear Materials 379, 16-23.

Finck, N., Morelová, N., Schlegel, M.L., Schild, D., Reguer, S., Dardenne, K., Geckeis, H., 2023. Corrosion of austenitic stainless steel at 90°C under highly saline and anoxic conditions: A microscopic study. Corros. Sci. 220, 111265.

Grazulis, S., Chateigner, D., Downs, R.T., Yokochi, A.F.T., Quiros, M., Lutterotti, L., Manakova, E., Butkus, J., Moeck, P., Le Bail, A., 2009. Crystallography Open Database – an open-access collection of crystal structures. J. Appl. Cryst. 42, 726-729.

Grosvenor, A.P., Kobe, B.A., Biesinger, M.C., McIntyre, N.S. Investigation of multiplet splitting of Fe 2p XPS spectra and bonding in iron compounds, Surf. Interface Anal. 2004, 36, 1564-1574.

Han, P., Bartels, D.M. Temperature Dependence of Oxygen Diffusion in H2O and D2O, J. Phys. Chem. 1996, 110, 5597-5602.

Hausmannová L, Dohnálková M., Matušková E., Lahodová Z., Augusta J. (2023): Technical Design of the Deep Geological Repository 2023, SÚRAO technical report no. TZ 711/2023/ENG, Prague.

Hedin, A., Johansson, A.J., Lilja, C., Boman, M., Berastegui, P., Berger, R., Ottosson, M., 2018. Corrosion of copper in pure O_2-free water? Corros. Sci. 137, 1-12.

Hesketh, J., Haynes, H., Reddy, B., Rance, A., Bevas, C., Padovani, C., Diomidis, N., 2023. Carbon steel corrosion in a bentonite buffer: A comparison between in situ exposure and lab based experiments. Mater. Corros. 74, 1728-1745.

Heuser M. (2018) The interaction between bentonite and water vapor. Ph.D. thesis. RWTH Aachen University, Aachen, Germany.

Hofmanová E., Červinka R., Vopálka D., Baborová L., Brázda L., Pecková A., Vetešník A., Viglašová E., Vašíček R. (2019): Transport of radionuclides from a repository / Input parameters and process models for evaluation of radionuclide transport across engineering barriers: Final report of the project. Technical report no. 420/2019, SÚRAO, Prague, Czech Republic.

Hollmark, H.M., Keech, P.G., Vegelius, J.R., Werme, L., Duda, L.-C., 2012. X-ray absorption spectroscopy of electrochemically oxidized Cu exposed to Na_2S. Corros. Sci. 54, 85-89.

Huertas, F., Fariña, P., Farias, J., García-Siñeriz, J.L., Villar, A.M., Fernández, A.M., Martín, P.L., Elorza, F.J., Gens, A., Sánchez, M., Lloret, A., Samper, J., Martínez, M.A., 2006. FEBEX Project. Full-scale engineered barriers experiment for a deep geological repository for high level radioactive waste in crystalline host rock. Updated Final Report 1994-2004. Technical Publication ENRESA 5-0/2006, 590 pp. Madrid.

ICSD database FIZ Karlsruhe, Germany, release 2022/2, 2022

Inoue A., Velde B., Meunier A., Touchard G. 1988. Mechanism of illite formation during smectite to illite conversion in a hydrothermal system. Am. Miner. 73: 1325–1334.

Ishidera T., Xia X., Idemitsu K., Kikuchi Y. (2008): Corrosion products from carbon steel formed in compacted bentonite under reducing conditions. J. Nuclear. Sc. Technol., 45, 8, 763–772.

EURAD (Deliverable n° 15.12) – Identification on the effect of transient processes on corrosion
Dissemination level: Public
Date of issue of this report: **29/04/2024**

Page 177

Jonsson, M., Emilsson, G., Emilsson, L., 2018. Mechanical design analysis for the canister. Posiva SKB Report 04, July 2018. SKB ID 1524476, Posiva ID RDOC-104919. ISSN 2489-2782.

Karnland, O., 2010. Chemical and mineralogical characterization of the bentonite buffer for the acceptance control procedure in a KBS-3 repository. Technical Report TR-10-60. Svensk Kärnbränslehantering AB, Stockholm, Sweden.

Kaufhold, S., Dohrmann, R (2008). Detachment of colloidal particles from bentonites in water, Appl. Clay Sci. 2008, 39, 50-59.

Kaufhold, S., Dohrmann, R., Klinkenberg, M., Noell , U (2015a). Electrical conductivity of bentonites, Appl. Clay. Sci. 2015, 114, 375-385.

Kaufhold S., Hassel A. W., Sanders D., Dohrmann R. (2015b): Corrosion of high-level radioactive waste iron-canisters in contact with bentonite. Journal of Hazardous Materials, 285, 464–473.

Kaufhold, S., Dohrmann, R., Gröger-Trampe, J. (2017). Reaction of native copper in contact with pyrite and bentonite in anaerobic water at elevated temperature. Corros. Eng. Sci. Technol. 52, 349-358.

Kaufhold, S., Klimke, S., Schloemer, S., Alpermann, T., Renz, F., Dohrmann, R. (2020). About the corrosion mechanism of metal iron in contact with bentonite. ACS Earth Space Chem. 4, 711-721.

King F. (2008). Corrosion of carbon steel under anaerobic conditions in a repository for SF and HLW in Opalinus Clay, Nagra Technical Report 08-12, Nagra, Switzerland.

King, F., (2009). Microbiologically influenced corrosion of nuclear waste containers. Corrosion, 65(4), 233-251.

King, F. (2013). Container materials for the storage and disposal of nuclear waste. Corros. 69, 986-1011.

Kirchfel, A., Eichhorn, K., 1990. Accurate structure analysis with synchrotron radiation. The electron density in Al_2O_3 and Cu_2O. Acta Crsyt. A46, 271-284.

Kloprogge, J.T. 2005. The application of vibrational spectroscopy to clay minerals and layered double hydroxides. CMS Workshop Lectures 13. The Clay Minerals Society. 285 pp.

Lanson, B., Lantenois, S., van Aken, P.A., Bauer, A., Plancon, A., 2012. Experimental investigation of smectite interaction with metal iron at 80°C: Structural characterization of newly formed Fe-rich phyllosilicates. Am. Mineral. 97, 864-871.

Lantenois, S., Lanson, B., Muller, F., Bauer, A., Jullien, M., Plancon, A., 2005. Experimental study of smectite interaction with metal Fe at low temperature: 1. Smectite destabilization. Clays Clay Miner. 53, 597-612.

Larese-Casanova, P., Scherer, M.M., 2007. Fe(II) sorption on hematite: New insights based on spectroscopic measurements. Environ. Sci. Technol. 41, 471-477.

Legrand, D.L., Nesbitt, H.W., Bancroft, M.G., 1998. X-ray photoelectron spectroscopic study of a pristine millerite (NiS) surface and the effect of air and water oxidation. Am. Mineral. 83, 1256-1265.

Le Pape, P., Rivard, C., Pelletier, M., Bihannic, I., Gley, R., Mathieu, S., Salsi, L., Migot, S., Barres, O., Villiéras, F., Michau, N., 2015. Action of a clay suspension on an Fe(0) surface under anoxic conditions: Characterization of neoformed minerals at the Fe(0)/solution and Fe(0)/atmosphere interfaces. Appl. Geochem. 61, 62-71.

Mackenzie, R.C., 1957. The differential thermal investigation of clays. Mineralogical Society. Clay minerals group. London.

Madejová, J., Komadel, P., 2001. Baseline studies of the Clay Minerals Society Source Clays: Infrared methods. Clays and Clay Minerals 49, pp. 410-432.

EURAD (Deliverable n° 15.12) – Identification on the effect of transient processes on corrosion
Dissemination level: Public
Date of issue of this report: **29/04/2024**

Page 178

Madsen F.T. (1998): Clay mineralogical investigations related to nuclear waste disposal. Clay Miner. 33? 109–129.

Matulová M., Hausmannová L., Malina J., Šatura L. (2023): Waste disposal package for spent nuclear fuel in the Czech Republic - MS SÚRAO, TZ 665/2023, Prague.

Meier L.P., Kahr G. 1999. Determination of the Cation Exchange Capacity (CEC) of Clay Minerals Using the Complexes of Copper(II) Ion with Triethylenetetramine and Tetraethylenepentamine. Clays Clay Miner. 47: 386–388, doi:10.1346/CCMN.1999.0470315

Mosser-Ruck R., Cathelineau M., Baronnet A., Trouiller A. 1999. Hydrothermal reactivity of K-smectite at 300 C and 100 bar: dissolution–crystallisation process and non-expandable dehydrated smectite formation. Clay Miner. 34: 275–290.

Moulder, J.F., Stickle, W.F., Sobol, P.E., Bomben, K.D., 1995. Handbook of X-Ray Photoelectron Spectroscopy; ULVAC-PHI, Inc., Physical Electronics USA, Inc.

Neff D., Saheb M., Monnier J., Perrin S., Descostes M., LHostis V., Crusset D., Millard A., Dillmann P. 2010. A review of the archaeological analogue approaches to predict the long-term corrosion behaviour of carbon steel overpack and reinforced concrete structures in the French disposal systems, J. Nucl. Mat. 402: 196–205.

Newman, A.C.D., 1987. Chemistry of Clays and Clay Minerals. Mineral Society. Monograph Nº 6. Longman Scientific & Technical, 480 pp.

Patel R, Punshon C, Nicholas J, Bastid P, Zhou R, Schneider C, Bagshaw N, Howse D, Hutchinson E, Asano R & King F, 2012, 'Canister design concepts for disposal of spent fuel and high level waste', NAGRA Technical Report 12-06.

Padovani, P., King, F., Lilja, C., Féron, D., Necib, S., Crusset, D., Deydier, V., Diomidis, N., Gaggiano, R., Ahn, T., Keech, P.G., Masdonald D.D., Asano, H., Smart, N., Hall, D.S., Hänninen, H., Engelberg, D., Nöel, J.J., Shoesmith, D.W., 2017. The corrosion behaviour of candidate canister materials for the disposal of high-level waste and spent fuel – a summary of the state of the art and opportunities for synergies in future R&D. Corros. Eng. Sci. Technol. 52, 227-231.

PDF-4+ database, International Centre for Diffraction Data, Newtown Square, PA, U.S.A. release 2023.

Pignatelli, I., Mugnaioli, E., Hybler, J., Mosser-Ruck, R., Cathelineau, M., Michau, N., 2013. A multi-technique characterization of cronstedtite synthesized by iron-clay interaction in a step-by-step cooling procedure. Clays Clay Miner. 61, 277-289.

Pospiskova I., Dobrev D., Kouril M., Stoulil J., Novikova D., Kotnour P., Matal O. 2017. Czech national programme and disposal canister concept. Corrosion Engineering, Science and Technology 52(sup.1): 6-10, DOI: 10.1080/1478422X.2017.1300379

Puigdomenech, I., Taxén, C., 2000. Thermodynamic data for copper. Implications for the corrosion of copper canister under repository conditions. Technical Report TR-00-13. Svensk Kärnbränslehantering AB, Stockholm, Sweden.

Pusch R., Karnland O. 1988. Hydrothermal effects on montmorillonite. A preliminary study. SKB Technical Report 88-15, Svensk Kärnbränslehantering AB, Stockholm, Sweden.

Pusch R., Kärnland O., Lajudie A., Decarreau A. 1992. MX 80 clay exposed to high temperatures and gamma radiation. SKB Technical Report P3-03, Svensk Kärnbränslehantering AB, Stockholm, Sweden.

Pusch R., Kasbohm J., Thao H.T.M. 2010. Chemical stability of montmorillonite buffer clay under repository-like conditions—A synthesis of relevant experimental data. Appl. Clay Sci. 47: 113–119.

Reddy, B., Padovani, C., Rance, A.P., Smart, N.R., Cook, A., Haynes, H.M., Milodowski, A.E., Field, L.P., Kemp, S.J., Martin, A., Diomidis, N., 2020. The anaerobic corrosion of candidate disposal

EURAD (Deliverable n° 15.12) – Identification on the effect of transient processes on corrosion
Dissemination level: Public
Date of issue of this report: **29/04/2024**

Page 179

canister materials in compacted bentonite exposed to natural granitic porewater containing native microbial populations. Mater. Corros. 72, 361-382.

Rietveld H.M. 1969. A profile refinement method for nuclear and magnetic structures, J. Appl. Crystallogr. 2: 65–71.

Roy W. R. 1993. Adsorption-Desorption Methodologies and Selected Estimation Techniques for Transport-Modeling Parameters. Migration and Fate of Pollutants in Soils and Subsoils. In: (Petruzzelli D., Helfferich F.G., Eds.) NATO ASI Series G 32: 169–188, doi:10.1007/978-3-642-77862-9_8

Schlegel, M.L., Necib, S., Daumas, S., Labat, M., Blanc, C., Foy, E., Linard, Y., 2018. Corrosion at the carbon steel-clay borehole interface under anoxic alkaline and fluctuating temperature conditions. Corros. Sci. 136, 70-90.

Senior, N.A., Newman, R.C., Artymowicz, D., Binns, W.J., Keech, P.G., Hall, D.S., 2019. Communication – A method to measure extremely low corrosion rates of copper metal in anoxic aqueous media. J Electrochem. Soc. 166, C3015-C3017.

Sewell, P.B., Cohen, M., 1964. The oxidation of iron single crystals around 200°C. J. Electrochem. Soc. 111, 501-508.

Seyama, H., Soma, M., 1987. Fe 2p spectra of silicate minerals. J. Electron Spectrosc. Relat. Phenom. 42, 97-101.

Smart N. R., Rance A., Reddy B., Fennell P., Winsley R. 2012. Analysis of SKB MiniCan Experiment 3. SKB TR-12-09, Svensk Kärnbränslehantering AB, Stockholm, Sweden.

Stoulil J., Kaňok J., Kouřil M., Parschová H., Novák P. 2013. Influence of temperature on corrosion rate and porosity of corrosion products of carbon steel in anoxic bentonite environment. J. Nucl. Mat. 443(1–3): 20-25, DOI:10.1016/j.jnucmat.2013.06.031.

Stoulil J., Mukhtar S., Lhotka M., Bureš R., Kašpar V., Šachlová Š., Dobrev D., Večerník P., Zuna M., Němeček J., Němeček J.2023. Processing of samples from corrosion experiments – Corrosion products 2, SÚRAO technical report TZ 700/2022.

Stucki, J.W., 2011. A review of the effects of iron redox cycles on smectite properties. C. R. Geoscience 343, 199-209.

Terlain, A., Desgranges, C., Gauvain, D., Feron, D., Galtayries, A., Marcus, P., 2001. Oxidation of materials for nuclear waste containers under long term disposal. Corrosion, paper 01119, (NACE International, 2001: Houston, TX).

Ufer K., Stanjek H., Roth G., Dohrmann R., Kleeberg R., Kaufhold S. 2008. Quantitative phase analysis of bentonites by the rietveld method. Clays Clay Min. 56: 272–282.

Van der Marel, H.W., Beutelspacher, H., 1976. Atlas of infrared spectroscopy of clay minerals and their mixtures. Elsevier, Amsterdam, 396 pp.

Wallis I., Idiart A., Dohrmann R., Post V. 2016. Reactive transport modelling of groundwater-bentonite interaction: Effects on exchangeable cations in an alternative buffer material in-situ test. Applied Geochemistry 73: 59-69, doi.org/10.1016/j.apgeochem.2016.07.005.

Wersin, P, Birgersson, M., Olsson, S., Karnland, O., Snellman, M. (2007). Impact of Corrosion-derived iron on the bentonite buffer within the KBS-3H disposal concept – The Olkiluoto Site as Case Study. Posiva Working Report 2007-11, 70 pp.

Williams, A.G.B., Scherer, M.M., 2004. Spectroscopic evidence for Fe(II)-Fe(III) electron transfer at the iron oxide-water interface. Environ. Sci. Technol. 38, 4782-4790.

Zuna M., Steinová J., Šachlová Š., Dobrev D., Mendoza Miranda A. N., Kolomá K., Kašpar V., Jankovský F., Večerník P. (2023): Corrosion test in natural granitoid environment – involvement in

EURAD (Deliverable n° 15.12) – Identification on the effect of transient processes on corrosion
Dissemination level: Public
Date of issue of this report: **29/04/2024**

Page 180

the MaCoTe project. Final report. SURAO Technical report no. 712/2023, SÚRAO, Prague, Czech Republic.

EURAD (Deliverable n° 15.12) – Identification on the effect of transient processes on corrosion
Dissemination level: Public
Date of issue of this report: **29/04/2024**

Page 181